Supermagnetism in magnetic nanoparticle systems

(Supermagnetismus in magnetischen Nanoteilchensystemen)

Subhankar Bedanta

aus Jignipur, Cuttack, Indien

Dedicated to my parents

Abstract

Nanoscale magnetic materials are of interest for applications in ferrofluids, high-density magnetic storage, high-frequency electronics, high performance permanent magnets, and, magnetic refrigerants. Magnetic single-domain nanoparticles ("superspins) are very interesting not only for potential applications, e.g. high density storage devices, but also for fundamental research in magnetism. In an ensemble of nanoparticles in which the inter-particle magnetic interactions are sufficiently small, the system shows superparamagnetic (SPM) behavior as described by the Néel-Brown model. On the contrary, when inter-particle interactions are non-negligible, the system eventually shows collective behavior, which overcomes the individual anisotropy properties of the particles. In order to address the effect of interactions, we have investigated two different magnetic nanoparticle systems.

The first part of this thesis focuses on the magnetic properties of ensembles of magnetic single-domain nanoparticles in an insulating matrix. The samples have a granular multilayer structure prepared as discontinuous metal-insulator multilayers (DMIM) $[Co_{80}Fe_{20}$ $(t_n)/Al_2O_3$ $(3nm)]_m$ where the nominal thickness of CoFe is varied in the range $0.5 \pounds t_n \pounds 1.8$ nm, and the number of bilayers m is varied between $1-10$. The DMIMs represent a model system to study the effect of inter-particle interactions by varying the nominal thickness which corresponds to the magnetic particle concentration. The structural properties are investigated by transmission electron microscopy, small angle X-ray reflectivity and electric conductivity measurements. It is found that CoFe forms well-separated and quasi-spherical nanoparticles in the Al_2O_3 matrix, and the samples exhibit a regular multilayer structure. The magnetic properties are investigated by means of *dc* magnetization, *ac* susceptibility, polarized neutron reflectometry (PNR), magneto-optic Kerr effect and ferromagnetic resonance. The DMIM system with the lowest $t_n = 0.5$ nm, in which the inter-particle interaction is almost negligible, single particle blocking has been observed. When increasing the nominal thickness to $t_n = 0.7$ nm and, hence, increasing the inter-particle interaction, the system shows spin glasslike cooperative freezing of magnetic moments at low temperatures. Superspin glass properties have been evidenced by static and dynamic criticality studies such as memory and rejuvenation. With further increase of nominal thickness and hence stronger interaction, the system shows a superferromagnetic (SFM) state, e.g., at $t_n = 1.3$ nm. A SFM domain state has been evidenced by Cole-Cole

analysis of the *ac* susceptibility and polarized neutron reflectivity measurements. Finally, the SFM domains have been imaged by synchrotron based photoemission electron microscopy (PEEM) and magneto-optic Kerr microscopy. Stripe domains stretched along the easy in-plane axis, but exhibiting irregular walls and hole-like internal structures ("domains in domains") are revealed. They shrink and expand, respectively, preferentially by sideways motion of the long domain walls as expected in a longitudinal field. The SFM domain state is explained by dipolar interaction and tunneling exchange between the large particles mediated by ultrasmall atomically small magnetic clusters. These have been evidenced by their sizable paramagnetic contributions, first in systems referring to $t_n = 0.5$ nm and 0.7 nm, but later on also at SFM coverages, $t_n = 1.3$ nm and at higher coverages. These ultrasmall particles (atoms?) are undetectable in transmission electron microscopy.

At $t_n = 1.4$ nm, physical percolation occurs and a conventional three-dimensional (3D) ferromagnetic phase with Ohmic conduction is encountered. Polarized neutron reflectivity and magnetometry studies have been performed on the DMIM sample with $t_n = 1.6$ nm which exhibits dominant dipolar coupling between the ferromagnetic layers. Our PNR measurements at the coercive field reveal a novel and unexpected magnetization state of the sample exhibiting a modulated magnetization depth profile from CoFe layer to layer with a period of five bilayers along the multilayer stack. With the help of micromagnetic simulations we demonstrate that competition between long and short-ranged dipolar interactions apparently gives rise to this unusual phenomenon.

In the second part of the thesis the structural and magnetic properties of FeCo nanoparticles in liquid hexane will be analyzed for two different concentrations of the ferrofluids. Inter-particle SFM ordering between FeCo nanoparticles are evidenced by magnetization measurements and *ac* susceptibility measurements. Mössbauer spectroscopy measurements are shown to evidence collective inter-particle correlations between the nanoparticles.

Kurzfassung

Magnetische Materialien auf der Nanoskala sind von hohem Interesse in zahlreichen Anwendungen, wie z.B. Ferrofluiden, Speichermedien, Hochfrequenzelektronik, Permanentmagneten und magnetischen Kühlmitteln. So sind insbesondere magnetisch eindomänige Nanopartikel ("superspins") nicht nur für Anwendungen, wie z.B. in der Speichertechnologie interessant, sondern auch für das Grundlagenverständnis im Magnetismus. In einem Ensemble von Nanopartikeln mit genügend kleiner magnetischer Wechselwirkung zwischen den Partikeln, zeigt das System superparamagnetisches (SPM) Verhalten, welches durch das Néel-Brown- Modell beschrieben werden kann. Umgekehrt, wenn die Inter-Partikel-Wechselwirkungen nicht vernachlässigbar sind, zeigt es kollektives Verhalten, welches dabei die individuellen Anisotropieeigenschaften der Partikel überwindet. Um diesem Effekt der Wechselwirkungen nachzugehen, haben wir zwei unterschiedliche Nanopartikelsysteme untersucht.

Der erste Teil dieser Arbeit behandelt die Eigenschaften von Ensembles von magnetisch eindomänigen Nanopartikeln in einer isolierenden Matrix. Die Proben haben eine granulare Multilagenstruktur, die als diskontinuierliche Metall-Isolator-Vielfachschichten (DMIMs) der Form $[Co_{80}Fe_{20}\,(t_n)/Al_2O_3(3nm)]_m$ hergestellt werden. Die nominelle Dicke der CoFe-Schicht liegt dabei im Bereich 0.5 £ t_n £ 1.8 nm und die Anzahl der Bilagen im Bereich 1 £ m £ 10. Diese DMIMs stellen ein hervorragendes Modell-System zum Untersuchen des Effekts der Inter-Partikel-Wechselwirkungen dar. Die nominelle Dicke entspricht hierbei der Partikelkonzentration. Die strukturellen Eigenschaften wurden mit Hilfe von Transmissionselektronenmikoskopie (TEM), Kleinwinkel-Röntgen-Streuung und elektrischen Transportmessungen studiert. So findet man, dass das CoFe getrennte und nahezu sphärische Nanopartikel in der Al_2O_3-Matrix bildet, und das ganze System eine exzellente Multilagenstruktur aufweist. Die magnetischen Eigenschaften wurden mittels DC-Magnetisierung, AC-Suszeptibilität, DC-Relaxation, magneto-optischem Kerr-Effekt (MOKE) und ferromagnetischer Resonanz untersucht. Im DMIM-System mit der niedrigsten nominelle Dicke, $t_n = 0.5$ nm, und somit kleinster Inter-Partikel-Wechselwirkung wurde individuelles Blocking (SPM-Verhalten) gefunden. Bei einem größeren Wert von $t_n = 0.7$ nm, und somit stärkeren Wechselwirkungen, zeigt das System spinglas-artiges kooperatives Einfrieren der magnetischen Partikelmomente bei niedrigen Temperaturen. Diese 'Superspinglas'-

Eigenschaften wurden nachgewiesen durch statische und dynamische Untersuchungen, wie z.B. den Memory- und Rejuvenation-Effekt. Bei weiterer Vergrößerung der nominellen Dicke und somit stärkeren Wechselwirkungen zeigt das Ensemble einen superferromagnetischen (SFM) Zustand. Dieser SFM-Domänen-Zustand wurde nachgewiesen durch eine Cole-Cole-Plot-Analyze der AC-Suszeptibilität und durch polarisierte Neutronenreflektometrie (PNR). Es ist sogar gelungen diese SFM-Domänen direkt durch Photoelektronen-Emissionsmikroskopie (PEEM) an einem Synchrotron und MOKE-Mikroskopie darzustellen. Sichtbar sind Streifendomänen entlang der leichten planaren Achse, jedoch mit unregelmäßigen Wänden und loch-artigen Strukturen ("Domänen in Domänen") Wie erwartet wachsen bzw. schrumpfen die Domänen vorzugsweise durch seitliche Bewegung der langen Wände in einem longitudinalen Feld. Der SFM-Domänenzustand kann erklärt werden durch Dipol- und Tunnelaustausch-Wechselwirkung der Partikel sowie Wechselwirkungen über atomare magnetische Cluster. Diese extrem kleinen Cluster wurden durch deren paramagnetischen Beitrag zunächst in Systemen mit $t_n = 0.5$ nm und 0.7 nm nachgewiesen, dann aber auch in SFM-Systemen mit $t_n = 1.3$ nm. In beiden Fällen sind sie nicht durch TEM nachweisbar.

Bei $t_n = 1.4$ nm findet strukturelle Perkolation der Partikel statt und es wird eine gewöhnliche drei-dimensionale (3D) ferromagnetische Phase mit Ohm'schen Widerstand gefunden. PNR und Magnetisierungs-Messungen an der DMIM-Probe mit $t_n = 1.6$ nm zeigen dominante dipolare Kopplung der ferromagnetischen Lagen. So zeigen die PNR-Daten nahe der Koerzitivfeldstärke einen neuartigen und unerwarteten Zustand, bei dem ein moduliertes Magnetisierungs-Profil im Multilagenstapel vorzufinden ist. Mit Hilfe von mikromagnetischen Simulationen konnten wir zeigen, dass eine Konkurrenz zwischen langreichweitiger und kurzreichweitiger (Néel-) Dipol-Kopplung für diesen Zustand verantwortlich ist.

Im zweiten Teil meiner Arbeit wurden die strukturellen und magnetischen Eigenschaften von FeCo-Nanopartikel in flüssigem Hexan mit zwei unterschiedlichen Konzentrationen untersucht. Eine Inter-Partikel SFM-Ordnung wurde mittels Magnetisierungs- und AC-Suszeptibilitäts-Messungen nachgewiesen. Mössbauer-Spektroskopieuntersuchungen zeigen ebenso kollektive Inter-Partikel-Korrelationen.

List of acronyms and abbreviations

ANNNI	Axial-Next-Nearest-Neighbour-Ising
C	Creep
CEMS	Conversion Electron Mössbauer
CIP	Current-In-Plane
DM	Dzyaloshinsky-Moriya
DMIM	Discontinuous Metal Insulator Multilayer
DW	Domain Wall
EA	Edwards-Anderson
EDX	Energy-Dispersive X-ray
EFG	Electric Field Gradient
FC	Field Cooling (Cooled)
FIB	Focused Ion-Beam
FM	Ferromagnetic
FMR	Ferromagnetic Resonance
H_c	Coercive field
LCP	Left- Circularly Polarized
LLG	Landau–Lifshitz–Gilbert
MLs	Multilayers
MOKE	Magneto-Optic Kerr Effect
MRAM	Magnetic Random Access Memory
M_{ref}	Reference Magnetization
N	Non-magnetic
NSF	Non-Spin-Flip
OOMMF	Object-Oriented Micromagnetic Modeling Framework
PNR	Polarized Neutron Reflectivity
R	Relaxation
RCP	Right- Circularly Polarized
RF	Radio Frequency
RFDS	Random-Field Domain State
RKKY	Rudermann-Kittel-Kasuya- and Yosida
S	Switching

SAF	Superantiferromagnetic
SANS	Small Angle Neutron Scattering
SF	Spin-Flip
SFM	Superferromagnetic
SK	Sherrington-Kirkpatrick
SL	Slide
SPM	Superparamagnetic
SQUID	Superconducting Quantum Interference Device
SSG	Superspin Glass
SW	Stoner-Wohlfarth
T_a	Annealing temperature
T_b	Blocking temperature
T_c	Curie temperature
TEM	Transmission Electron Microscopy
T_f	Freezing temperature
t_n	Nominal thickness
TRM	Thermoremanent Magnetization
T_s	Stop temperature
XMCD	X-ray Magnetic Circular Dichroism
X-PEEM	Photoemission Electron Microscopy
XRD	X-Ray Diffraction
ZFC	Zero Field Cooling (Cooled)

Contents

Chapter 1

Introduction

Nanoscale magnetic materials have attracted widespread interest because of novel effects arising due to the reduction of their spatial extension. This has a major impact on modern magnetic storage technology [1] as well as on the basic comprehension of magnetism on the mesoscopic scale [2, 3]. As first predicted by Frenkel and Dorfman [4] a particle of a ferromagnetic material is expected to consist of a single magnetic domain below a critical particle size. Rough estimates of this critical particle sizes, have first been made by Kittel [5]. An approximate radius of 15 nm is estimated for a spherical sample of a common ferromagnetic material. The magnitude of the magnetic moment m of a particle is proportional to its volume. Such monodomain ferromagnetic particles can be viewed as large magnetic units, each having a magnetic moment of thousands of Bohr magnetons. Usually an ellipsoidal shape of the particles is assumed, where the magnetic moments have the tendency to align along the longest axis, which defines the direction of largest "shape" anisotropy energy [6].

Since the pioneering theoretical study made by Stoner and Wohlfarth [7] on the magnetization reversal mechanism in single-domain particles, intensive theoretical and experimental work has been carried out in last few decades. The magnetization reversal can occur via the rotation of the magnetization vector from one magnetic easy axis to another via a magnetically hard direction. As a consequence of this rotation mechanism, the coercivities of magnetic nanoparticles can be controlled. They lie between those of soft magnetic materials and normal permanent magnet materials. This unique property to control coercivity in such magnetic nano-materials has led to a number of significant technological applications, particularly in the field of information storage. Small magnetic particles are promising candidates for further increase the density of magnetic storage devices toward the 100 Gbit/inch^2 to a few Tbit/inch^2. Apart from data storage they are potential candidates for other applications such in ferrofluids, high-frequency electronics, high performance permanent magnets, and, magnetic refrigerants. Also magnetic particles are potential candidates to be used in biology and medical uses such as drug-targeting, cancer therapy, lymph node imaging or hyperthermia.

In a system consisting of widely spaced ("isolated"), hence, non-interacting single domain particles ("superspins" for short), the magnetic moments of the particles act independently. They are characterized by the instability of the magnetization due to thermal agitation that results in the phenomenon of superparamagnetism because each particle behaves like a paramagnetic atom having a magnetic moment $\boldsymbol{m} \approx 10^3 - 10^5 \, \boldsymbol{m_B}$. Although in an ensemble of isolated particles, direct exchange between them may be neglected, the magnetic properties may be determined by the dipole field energy along with the thermal and magnetic anisotropy energies [8]. At sufficient high packing densities the interparticle interactions have profound effects on the spin dynamical properties of the particle assembly. Firstly, they modify the energy barrier arising from the anisotropy contributions of each particle. In this case individual priority is given to the total free energy of the assembly, while single particle energy barriers are no longer solely relevant. The reversal of one particle moment may change all energy barriers within the assembly. Secondly, they may produce a low temperature collective state that is completely different from individual blocked one. The collective state sometimes shares most of the phenomenology attributed to magnetic glassy behavior [9, 10, 11]. However, at increasing interparticle correlations the collective state can form a distinct long range ordered superferromagnetic (SFM) state, which is different from the spin glasslike state in many respects [12, 13].

The present thesis is devoted to understand the effect of interaction in two different kinds of ensembles of nanoparticles. In the first part of the thesis, we have studied ensemble of ferromagnetic nanoparticles dispersed in an insulating matrix in a form of metal insulator multilayer thin films. In this system the effect of interparticle interaction is tuned by varying the concentration. At very low concentration where interparticle interaction is negligible, single particle blocking is encountered. However with increase of concentration and, hence, of interaction between the particles, the systems show collective behaviours. At intermediate concentrations, there is strong evidence of a collective "superspin glass" behaviour and at higher concentrations, but prior to physical percolation, a ferromagnetic collective domain state is encountered which is termed as "superferromagnetism". Furthermore beyond physical percolation the system behaves as a conventional ferromagnet like in a continuous thin film. However, these percolated films show a peculiarly structured magnetization depth profile from layer to layer at the demagnetized state or coercive field.

In the second part of the thesis, we have studied the effects of interparticle interactions between ferromagnetic nanoparticles with heavily disordered surface dispersed in a liquid carrier and prepared as ferrofluids.

The thesis is organized as follows.

In **Chapter 2**, an introduction to general properties of magnetic particles together with some theoretical background related to the present work will be discussed. Also a brief discussion of the domain structures observed in thin film elements will be addressed. In **Chapter 3**, various experimental techniques used to prepare the samples and for structural and magnetic characterizations will be described. **Chapter 4** presents the structural and magnetic properties of the discontinuous metal-insulator multilayers (DMIMs) with the general formula $[Co_{80}Fe_{20}(t_n)/Al_2O_3(3nm)]_m$ where t_n and m represent the nominal thickness and the number of layers, respectively. Starting from single particle blocking (superparamagnetism) with negligible interactions to different collective states due to strong interparticle interactions will be presented in this chapter. Finally we report how the competition between dipolar interaction and Néel coupling can lead to a modulated magnetization depth profile in a strongly dipolarly coupled percolated DMIM sample. In **Chapter 5** structural and magnetic properties of ferrofluids with the general formula $[Fe_{55}Co_{45}/n\text{-hexane}]$ for two different volume ratios [such as (1:1) and (1:5)] will be presented. Here a collective superferromagnetic state will be evidenced between the ferromagnetic cores while the single nanoparticles have a heavily disordered surface. The summary of the present work is presented in **Chapter 6** with an outlook.

Chapter 2

Fundamentals

This chapter gives an introduction to magnetic nanoparticles, different relevant interactions in a magnetic system as well as different collective states observed in ensembles of nanoparticle systems. First the general properties of nanoparticles will be discussed along with the phenomenon of superparamagnetism. Afterwards different anisotropy contributions in nanoparticles will be discussed. Then magnetic domains in thin films will be briefly addressed. Magnetization reversal in single domain nanoparticles via coherent rotation and via domain wall motion in thin films will be discussed. Towards the end of this chapter, the effect of inter-particle interaction will be discussed and observed collective states such as the superspin glass and superferromagnetism ones will be discussed.

2.1. Magnetic nanoparticles and Superparamagnetism

2.1.1. Generalities

The physics of nanoscale magnetic materials has been a vivid subject for researchers within the last few decades not only for technological reasons, but also from the fundamental research point of view. In the last decade thorough investigations have been made in the field of nanosized magnetic particles, because of their potential for biomedical applications such as improving the quality of magnetic resonance imaging (MRI), hyperthermic treatment for malignant cells, site-specific drug delivery and also the recent research interest of manipulating cell membranes [14]. In a bulk ferromagnetic specimen the magnetization, M, measured as a function of the applied field, H, displays hysteresis loops at temperatures below its corresponding Curie temperature. The hysteresis behavior was first explained by Pierre Weiss in 1907 by the assumption that ferromagnetic materials consist of domains [15]. These domains are separated by domain walls and try to minimize the net energy of the system. The magnetostatic energy increases proportionally to the volume of the material, while the domain wall energy increases proportionally to the surface area. Thus a critical size may be reached, below which formation of domains may

become energetically unfavourable due to the domain wall energy, such that the sample consists of a single uniformly magnetized domain. Then the system is in a state of uniform magnetization and it behaves like a small permanent magnet. The size of the single-domain particle depends on the material and contributions from different anisotropy energy terms. The critical radius r_c below which a particle acts as a single domain particle is given by [16]

$$r_c \approx 9 \frac{(AK_u)^{1/2}}{m_0 M_s^2}$$ (2.1)

where A is the exchange constant, K_u is the uniaxial anisotropy constant, m_0 is called constant of permeability, and M_s is the saturation magnetization. Typical values for r_c are about 15 nm for Fe and 35 nm for Co, for g-Fe_2O_3 it is 30 nm, while for $SmCo_5$ it is as large as 750 nm [17]. Depending on the size and material, the magnetic moments of single-domain particles can be $10^2 - 10^5$ m_B where $m_B = e\hbar/2m_e = 9.274 \times 10^{-24}$ Am^2 is the Bohr magneton [18].

There are various models for the magnetization reversal of single-domain particles. A model for the coherent rotation of the magnetization was developed by Stoner and Wohlfarth [7]. They assumed non-interacting particles with uniaxial anisotropy in which the spins are parallel and rotate at unison. This model will be described briefly in section 2.4. Furthermore, at any finite temperature, thermal activation can overcome the anisotropy energy barrier leading to switching of the particle moment. This relaxation process was first proposed by Néel in 1949 [19] and further developed by Brown in 1963 [20]. This model will also be briefly discussed in section 2.4. However, in larger particles approaching the critical size for single-domain behaviour, magnetization reversal occurs via incoherent modes such as fanning and curling [21]. More complicated switching mechanisms like nucleation with subsequent domain wall motion occur in nanowires [22].

2.1.2. Superparamagnetism

As mentioned before in this section, small enough ferromagnetic particles will be single-domain because the energy cost of domain wall formation does not outweigh any saving of demagnetizing energy. In these single-domain ferromagnetic particles the magnetization is often considered to lie parallel or antiparallel to a particular direction called an *easy axis*. This can be due to different anisotropy contributions, which will be described in section 2.2. Let us consider an assembly of uniaxial, single-domain particles, each with an

anisotropy energy density $E = KV \sin^2 q$, where q is the angle between the magnetization and the easy axis and K is the anisotropy energy density and V is the volume of the particle. For a particle, the energy barrier $\left(\mathbf{D}E = E_B = E_{\max} - E_{\min} = KV \right)$ separates the two energy minima at $q = 0$ and $q = p$ corresponding to the magnetization parallel or antiparallel to the easy axis as shown in Fig. 2.1. Néel pointed out that, if single-domain particles become small enough, KV would become so small that energy fluctuations could overcome the anisotropy energy and spontaneously reverse the magnetization of a particle from one easy direction to the other, even in the absence of an applied field.
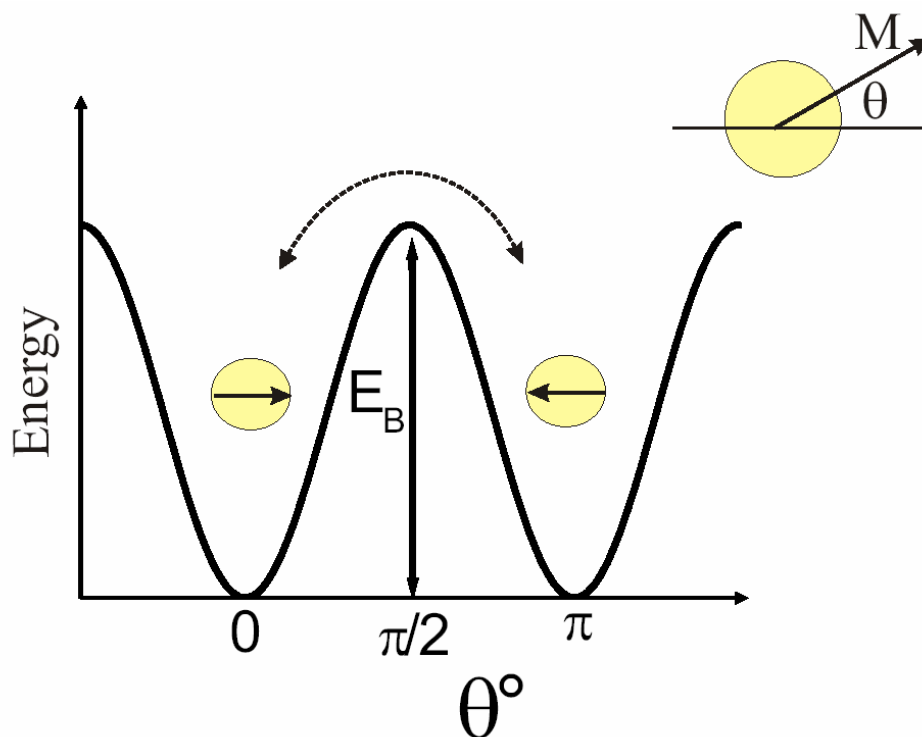
Figure 2.1: Schematic picture of the energy of a single-domain particle with uniaxial anisotropy as a function of magnetization direction. E_B is the energy barrier needed for the rotation of the magnetization and q is the angle between the magnetization M and the easy axis.

Let us consider a distribution of single-domain ferromagnetic particles in a non-magnetic matrix and assume that the particles are separated far enough such that no inter-particle interactions exist between the particles. Then for $k_B T \gg KV$, where k_B is the Boltzmann constant and T is the temperature, the system will behave like a paramagnet, with one notable exception that the independent moments are not that of a single atom, but rather of a single domain ferromagnetic particle, which may contain more than 10^5 atoms

ferromagnetically coupled by exchange forces. The system is then called **superparamagnetic**.

For small particles at high temperatures the anisotropy energy becomes comparable to or smaller than the thermal energy. Thus the magnetization will fluctuate between the two energy minima. The direction of the magnetization then fluctuates with a frequency f or a characteristic relaxation time, $t^{-1} = 2\pi f$. It is given by the Néel-Brown expression

$$t = t_0 \exp\left(\frac{KV}{k_B T}\right) \qquad (2.2)$$

where k_B is Boltzmann´s constant and $t_0 \sim 10^{-10}$ s is the inverse attempt frequency. The fluctuations thus slow down (t increases) as the sample is cooled (Fig. 2.2) to lower temperatures and the system appears static when t becomes much longer than the experimental measuring time t_m. When the relaxation time becomes comparable to experimental measurement time the particle is said to be blocked. The magnetic behavior of the particle is characterized by the so-called "blocking" temperature, T_b, below which the particle moments appear frozen on the time scale of the measurement, t_m. This is the case, when $t_m \approx t$. Using Eq. (2.2) one obtains

$$T_b \approx KV / k_B \ln(t_m / t_0). \qquad (2.3)$$

The above equation is valid for individual particles or a system of non-interacting particles with the same size and anisotropy. If the particles are not monodisperse, the distribution of particle sizes results in a blocking temperature distribution. The experimental measuring time t_m is in the range 10^{-12}–10^{-10}s for inelastic neutron scattering, 10^{-10}–10^{-7}s for Mössbauer spectroscopy (comparable to the decay time of the nuclear Mössbauer transition), 10^{-10}–10^{-5}s for mSR (a measurable fraction of muons live for up to $\sim 10 t_m$ where $t_m = 2.2$ ms is the average muon lifetime), while *ac* susceptibility typically probes 10^{-1}–10^{-5} s.

Brown [23] has shown that t_0 depends on the material parameters (size and anisotropies), field and even on temperature. From Eq. (2.2), it is clear that t depends on V and T so that by varying the volume of the particles or the measurement temperature, t can be in the order of 10^{-9} s to several years.

The treatment of the thermal equilibrium magnetization properties of an assembly of isotropic single domain particles is analogous to the Langevin treatment of atomic paramagnetism. If we denote the magnetic moment of such a particle by m and ignore the

anisotropy energy and suppose that an assembly of such particles has come to equilibrium at a given temperature T under the influence of an applied magnetic field H, then the mean dipole moment in the field direction is $\boldsymbol{mH} = \boldsymbol{mL}(x)$, where $L(x) = \coth(x) - 1/x$ is the Langevin function and $x = \dfrac{\boldsymbol{mH}}{k_BT}$ [24]. However it differs only in that the moments m we are dealing with is not that of a single atom, but rather large group of moments, each inside a ferromagnetic particle.
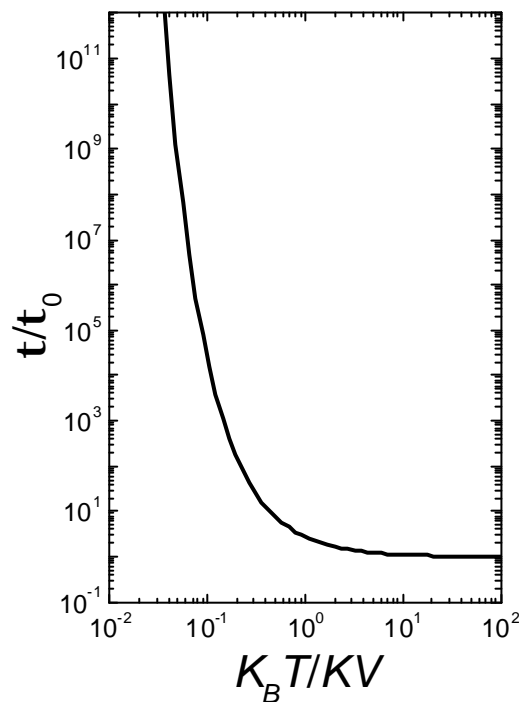
Figure 2.2: The dependence of the relaxation time t as a function of temperature T (scaled by k_B/KV) according to Eq. 2.2. When the temperature is reduced, the fluctuations slow down (t increases).

The magnetization behavior of single domain particles in thermodynamic equilibrium at all fields is identical with that of atomic paramagnetic except that an extremely large moment is involved, and thus large susceptibilities are involved. Because of these similarities, such thermal equilibrium behavior has been termed "superparamagnetism". This behavior has also been discussed in the literature under several other names, including "apparent paramagnetism" [25], collective paramagnetism, [26], "quasiparamagnetism" [27], and subdomain behavior [28].

An operational definition of superparamagnetism would include at least two requirements. In the thermodynamical limit and at infinite time scales, the magnetization curve must show no hysteresis (i.e., no coercivity H_c). Second, except for particle interaction effects which will be discussed later, the magnetization curve for an isotropic sample must be temperature dependent to the extent that curves taken at different temperatures must approximately superimpose when plotted against H/T after correction for the temperature dependence of the spontaneous magnetization.

2.2 Magnetic anisotropy

The term magnetic anisotropy is used to describe the dependence of the internal energy on the direction of the spontaneous magnetization, creating *easy* and *hard* directions of magnetization. The total magnetization of a system will prefer to lie along the easy axis. The energetic difference between the easy and hard axis results from two microscopic interactions: the spin-orbit interaction and the long-range dipolar coupling of magnetic moments. The anisotropy energy arises from the spin-orbit interaction and the partial quenching of the angular momentum. The spin-orbit coupling is responsible for the intrinsic (magnetocystalline) anisotropy, surface anisotropy, and magnetostriction, while the shape anisotropy is a dipolar contribution and is calculated *e.g.* by assuming a uniform distribution of magnetic poles on plane surfaces. Anisotropy energies are usually in the range 10^2–10^7 Jm^{-3}. This corresponds to energy per atom in the range 10^{-8}–10^{-3} eV. The anisotropy energy is larger in lattices (of magnetic ions) of low symmetry and smaller in lattices of high symmetry. In bulk materials, magnetocrystalline and magnetostatic energies are the main source of anisotropy whereas in fine particles, thin films and nanostructures, other kinds of anisotropies such as shape and surface anisotropy are relevant in addition to these usual anisotropies. In the following we will discuss four different contributions to magnetic anisotropy: magnetocrystalline anisotropy, shape anisotropy, strain anisotropy and surface anisotropy.

2.2.1. Magnetocrystalline anisotropy

Magnetic anisotropy is meant as the dependence of the internal energy on the direction of spontaneous magnetiation. An energy term of this kind is called as magnetic anisotropy energy. Generally the magnetic anisotropy energy term possesses the crystal symmetry of

the material, and known as crystal magnetic anisotropy or magnetocrystalline anisotropy [18].

The simplest forms of crystal anisotropies are the *uniaxial* anisotropy in the case of a hexagonal and the cubic anisotropy in the case of a cubic crystal. For example, hexagonal cobalt exhibits uniaxial anisotropy, which makes the stable direction of internal magnetization (or easy direction) parallel to the *c* axis of the crystal at room temperature. For uniaxial symmetry the energy is given by

$$E_a^{uni} = K_1 V \sin^2 q + K_2 V \sin^4 q + \text{.......} \qquad (2.4)$$

where K_1 and K_2 are anisotropy constants, V is the particle volume and q is the angle between the magnetization and the symmetry axis. The K's are dependent on temperature [29, 16], but at temperatures much lower than the Curie temperature of the material they can be considered as constants. Usually in case of ferromagnetic materials K_2 and other higher order coefficients are negligible in comparison with K_1 and many experiments may be analyzed by using the first term only. In the convention of Eq. (2.4), $K_1 > 0$ implies an easy axis. For single-domain particles with uniaxial anisotropy most of the calculations are performed also by neglecting K_2 and the magnetocrystalline anisotropy energy is written as

$$E_a^{uni} = KV \sin^2 q \qquad (2.5)$$

where K is usually considered as the uniaxial anisotropy constant. This expression describes two local energy minima at each pole ($q = 0$ and p) separated by an equatorial ($q = 90$) energy barrier KV.

For crystals with cubic symmetry, the anisotropy energy can be expressed in terms of the direction cosines (a_1, a_2, a_3) of the internal magnetization with respect to the three cube edges [30]

$$E_a^{cubic} = K_1 V \left(a_1^2 a_2^2 + a_2^2 a_3^2 + a_3^2 a_1^2 \right) + K_2 V a_1^2 a_2^2 a_3^2 + \text{........}, \qquad (2.6)$$

where the a_i are defined through $a_1 = \sin q \cos f$, $a_2 = \sin q \sin f$ and $a_3 = \cos q$, q is the angle between the magnetization and the Z-axis and f is the azimuthal angle.

2.2.2. Shape Anisotropy

Another source of magnetic anisotropy results from the shape of the specimen. A uniformly magnetized single domain spherical particle has no shape anisotropy, because the demagnetizing factors are isotropic in all directions. However, in the case of a non-spherical sample it will be easier to magnetize along a long axis than along a short direction. This is due to the demagnetizing field which is smaller in the long direction,

because the induced poles at the surface of the sample are further apart. Demagnetizing factors for the general ellipsoid were calculated by Osborn [31]. For example, the shape anisotropy energy of a uniform magnetized ellipsoid can be written as [29]

$$E_a^{shape} = \frac{1}{2} \boldsymbol{m}_0 V \left(N_x M_x^2 + N_y M_y^2 + N_z M_z^2 \right) \tag{2.7}$$

where M_x, M_y and M_z are the components of magnetization and N_x, N_y, and N_z are the demagnetization factors relative to the X, Y, and Z axes, respectively and they satisfy the relation $N_x + N_y + N_z = 1$.

The magnetostatic energy, for an ellipsoid of revolution, is equal to

$$E_a^{shape} = \frac{1}{2} \boldsymbol{m}_0 V M_s^2 \left(N_z \cos^2 \boldsymbol{q} + N_x \sin^2 \boldsymbol{q} \right) \tag{2.8}$$

where $\boldsymbol{q}$ is the angle between the magnetic moment and the polar Z-axis, M_s is the saturation magnetization, N_z is the demagnetization factor along the polar axis, and $N_x = N_y$, the demagnetization factor along the equatorial axis.

Both the magnetostatic energy for an ellipsoid and the uniaxial magnetocrystalline anisotropy energy [Eq. 2.8] up to first order can be written as

$$E_a^{shape} = \frac{1}{2} \boldsymbol{m}_0 V M_s^2 \left(N_x - N_z \right) \sin^2 \boldsymbol{q} , \tag{2.9}$$

where a constant energy term has been omitted which does not change the calculations because a constant energy term only means a shift in the definition of the zero energy. Eq. 2.9 can be written as

$$E_a^{shape} = A \sin^2 \boldsymbol{q} \tag{2.10}$$

where $A = KV$ is the anisotropy energy barrier and the uniaxial anisotropy constant $K = \frac{1}{2} \boldsymbol{m}_0 M_s^2 (N_x - N_z)$ in the case of shape anisotropy. For a prolate ellipsoid, $K_s > 0$ and the effective anisotropy is of *easy axis* type, since there exist two minima of the anisotropy energy along the polar $\pm z$ axis. For an oblate ellipsoid, $K_s < 0$ and the anisotropy energy has its minimum in the equatorial XY plane. In this case the anisotropy is of *easy plane* type.

2.2.3. Strain Anisotropy

The secondary effect due to the surface is related to strains. Strain anisotropy is essentially a magnetostrictive effect and because of magnetostriction, strains are effective in the

magnetization direction. This kind of anisotropy often described by a magnetostatic energy term

$$E_a^{strain} = -\frac{3}{2} l_s s \, S \cos^2 q',$$

(2.11)

where l is the saturation magnetostriction, s is the strain value by surface unit, S is the particle surface, and q' the angle between magnetization and the strain tensor axis.

2.2.4. Surface Anisotropy

The surface anisotropy is caused by the breaking of the symmetry and a reduction of the nearest neighbour coordination. Surface effects in small magnetic nanoparticles are a major source of anisotropy [32, 33]. This can easily be understood, because with decreasing particle size, the magnetic contributions from the surface will eventually become more important than those from the bulk of the particle, and, hence, surface anisotropy energy will dominate over the magnetocrystalline anisotropy and magnetostatic energies. Therefore the change in symmetry of atoms at the surface of a thin film has an impact on the magnetic anisotropy and the easy direction of magnetization.

To lowest order, the anisotropy energy of a ferromagnetic layer may be written as

$$E_{an} = K \sin^2 q$$

(2.12)

where q is the angle between the magnetization and the surface normal and K is the effective anisotropy constant and can be described as the sum of three terms

$$K = \frac{2K_s}{t} + K_v - m_0 M^2$$

(2.13)

where t is the thickness of the film, K_s is the surface contribution, and K_v is the volume anisotropy consisting of magnetocrystalline, magnetostriction and shape anisotropy. In the case of small spherical particles with diameter d the effective magnetic anisotropy can be expressed as:

$$K_{eff} = K_v + \frac{S}{V} K_s = K_v + \frac{6}{d} K_s$$

(2.14)

where $S = p d^2$ and $V = \frac{1}{6} p d^3$ are the surface and the volume of the particle respectively [34].

2.3. Magnetic domains

A ferromagnet of macroscopic size contains numerous regions called "*magnetic domains*" in the demagnetized state. Within each domain, all the atomic moments are aligned in one of the easy directions leading to spontaneous magnetization. The direction of spontaneous magnetization, however, varies from domain to domain so as to minimize the magnetostatic energy. On a purely statistical basis, all available easy directions will be used equally in the material. For instance, if there are *n* domains of approximately equal volume in a demagnetized iron specimen, the number of domains spontaneously magnetized in each of the six <100> easy directions will be *n*/6. Hence the specimen as a whole will not show a net magnetization in the absence of an applied field.

The principal factors affecting domain distribution and magnetic behavior may be listed as follows:

1. magnetocrystalline anisotropy, which determines the natural easy axis of the crystallites;

2. induced anisotropy, produced by strain or magnetic annealing (as for ´permalloy´) which produces an easy axis over-riding the magnetocrystalline contribution;

3. shape anisotropy, in which the easy axis is determined by minimization of magnetostatic energy (this applies to small particles);

4. size and orientation of the crystallites composing the specimens.

Once domains form, the orientation of *M* in each domain and the domain size are determined by magnetostatic, crystal anisotropy, magnetoelastic, and domain wall energy. All domain structure calculations involve minimization of the appropriately selected energies.

2.3.1. Domain walls

Domain walls are interfaces between regions in which the spontaneous magnetization has different directions. At or within the wall the magnetization must change direction. A simplistic picture of a domain wall which makes an abrupt change between two domains is shown in Fig. 2.3. For this ferromagnetic specimen the easy axis is $\pm y$ and a row of atoms is shown parallel to *x*-axis, with the 180° domain wall lying in the *y-z* plane. In this case the domain wall will have a large exchange energy associated with it because the spins adjacent to the wall are anti-parallel and the exchange energy in a ferromagnet is a

minimum only when adjacent spins are parallel. Let us first calculate the exchange energy and then see the structure of a domain wall to minimize it.
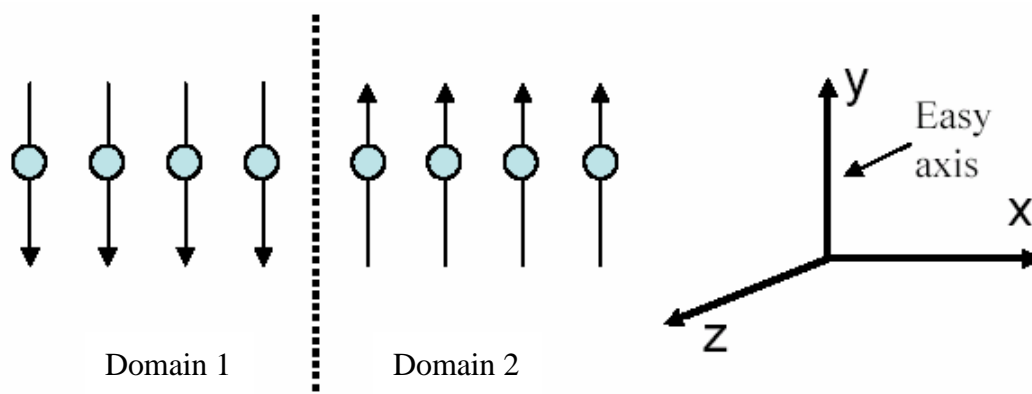

Figure 2.3: Hypothetical infinitely thin 180° wall.

The exchange energy for a pair of atoms with the same spin S is

$$E_{ex} = -2JS^2 \cos f \tag{2.15}$$

where J is an exchange intergral and f is the angle between adjacent spins as shown in Fig. 2.4 (c). The series expansion of $\cos f$ is

$$\cos f = 1 - \frac{f^2}{2} + \frac{f^4}{24} - \cdots \tag{2.16}$$

Dropping the term in f^4 and higher powers, because f is small, and substituting in Eq. (2.15), we have

$$E_{ex} = JS^2 f^2 - 2JS^2 . \tag{2.17}$$

The second term in Eq. (2.17) is independent of angle and has the same value within a domain as within the wall, and it can therefore be dropped. The extra exchange energy per spin pair exisiting within the wall is given by the first term, $JS^2 f^2$.

Now going back to Fig. 2.3 in order to decrease the exchange energy, a 180° change in spin direction to take place gradually over N atoms is necessary so that the angle f between adjacent spins will be π/N. The total exchange energy is then reduced because, from Eq. (2.17), it varies as f^2 rather than as f. Fig. 2.4 illustrates the two simplest cases of a 180° domain wall, (a) a Bloch wall and (b) a Néel wall, in both of which the magnetization rotates from one domain to the other in different ways.
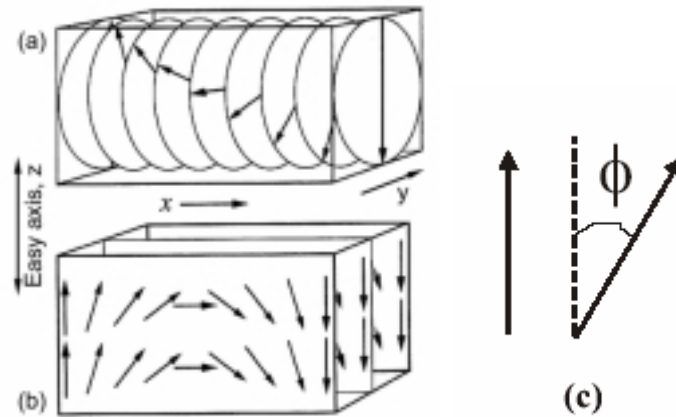
Figure 2.4: Rotation of the magnetization vector between two adjacent domains through a 180° wall in an infinite uniaxial material. Two different rotation modes are shown, (a) a Bloch wall, which is the optimum mode and (b) a Néel wall, which is less favorable here, but can be preferred in ultrathin films and in applied fields. The opposite rotation is equally possible for both modes. [From Ref. 35] Schematic of the angle (f) between two adjacent spins (c).

If the wall plane contains the anisotropy axis, the domain magnetizations are parallel to the wall and there will be no global magnetic charge, meaning that the component of magnetization perpendicular to the wall is the same on both sides of the wall. However if the magnetization rotates parallel to the wall plane (*y-z* plane in Fig. 2.4(a)), there will be no charges inside the wall, either. Then the stray field energy will assume its minimum zero value. This wall mode, first proposed and calculated by Landau and Lifshitz [36] and the first theoretical examination of the structure of a domain wall was made by Felix Bloch [37] in 1932, and domain walls are accordingly called as *Bloch walls*.

In ultrathin films where the film thickness becomes comparable to the wall width, Bloch walls cannot occurr. Because with decrease of sample thickness, the magnetostatic energy of the wall that extends through the thickness of the sample increases as a result of the free poles at the top and bottom of the wall. The spins inside the wall may execute their 180° rotation in such a way as to minimize their magnetostatic energy. If the spins were to rotate in the plane of the surface, a smaller magnetostatic energy at the internal face of the wall is accepted as the price for removing the larger magnetostatic energy at the top surface. Such a wall is called *Néel wall* in which the magnetization rotates in a plane perpendicular to the plane of the wall (see Fig. 2.4 (b)).

Similar to 180° domains walls in which the spins rotate by 180° from one domain to the other, there is also 90° domain walls exist in which the spins rotate by 90°. In short, a 180° domain wall separates domains of opposite magnetization whereas a 90° domain wall separates domains of perpendicular magnetization. There are also 71° and 109° domain walls observed in negative-anisotropy cubic materials. Details of different kinds of domain walls can be found in reference [35].

The spins within the wall of Fig (2.4) are not pointing in easy directions, so that the crystal anisotropy energy within the wall is higher than it is in the adjoining domains. While the exchange energy tries to make the wall as wide as possible, in order to make the angle f between adjacent spins as small as possible, the anisotropy energy tries to make the wall thin, in order to reduce the number of spins which are not pointing in the easy direction. As a result of this competition, the wall has a certain finite width and a certain structure. Since domain walls form a continuous transition between two domains, therefore there can be no unique definition of a domain wall width. The classical definition of domain wall width introduced by Lilley [38] is given by

$$W_L = p\sqrt{A/K} \qquad\qquad (2.18)$$

where A and K are the exchange stiffness and anisotropy constants for the ferromagnet resepectively. In another definition the wall width W_L is given by [35]

$$W_L = 2\sqrt{A/K} . \qquad\qquad (2.19)$$

For many practical ferromagnets, A is of the order 10^{-11} Jm^{-1}, so the wall width depends mainly on the anisotropy constant, which ranges from 10^3 Jm^{-3} in soft magnets with induced anisotropy to 10^7 Jm^{-3} in rare-earth permanent magnets. The corresponding range of W_L is from 2 to 200 nm.

2.3.2. Domain nucleation

Next is to focus on how domain formation occurs in an initially saturated specimen. In general this process constitutes a very considerable resistance to the process of demagnetization in many specimens. Saturation is expected in a magnetic specimen when the demagnetizing fields can be overcome in certain magnetic fields. However, the real demagnetizing fields are non-uniform over the volume of the specimen. Usually the end regions are much more difficult to saturate than the bulk of the crystal, and residual domains persist near the ends until external magnetic fields can completely make saturation [21]. The demagnetizing effect of the end surfaces can be eliminated assuming a

ring-shaped specimen, however residual domains are still expected to be stabilized by pores, inclusions and grain boundaries. Considerable demagnetizing fields can arise from grain boundaries and this requires higher fields which are considerably higher than bulk saturation.

A critical field designated as H_n (nucleation fields) may be needed sometime to start nucleation of domains. However it is quite possible that critical fields may represent the initiation of wall motion rather than the nucleation of the walls, and in this case they may be designated as starting fields (H_s).

2.4. Magnetization reversal

In this section we will discuss the magnetization reversal process in single domain nanoparticles and in bulk thin films. First we will discuss the Stoner-Wohlfarth model of coherent rotaion in single domain nanoparticles and then magnetization reversal via domain wall motion will be discussed briefly.

2.4.1. Magnetization reversal via coherent magnetization rotation

The magnetization reversal in single-domain particles was examined in great detail by Stoner and Wohlfarth (SW) [7] in a classic paper published in 1948. Their calculations have an important bearing on the theory of permanent-magnet materials, because some of these materials are thought to consist of single-domains. The SW model describes the magnetization curves of an aggregation of single-domain particles with uniaxial anisotropy either as a result of particle shape or from the magnetocrystalline anisotropy. The main assumptions of the model are: (i) coherent rotation of the magnetization of each particle (i.e., no internal degrees of freedom) and (ii) negligible interaction between the particles. In the SW model, the calculations were made for ellipsoidal particles, because the ellipsoidal shape of evolution includes all the particle shapes of physical interest such as rod (prolate spheroid), sphere, and disk (oblate spheroid).
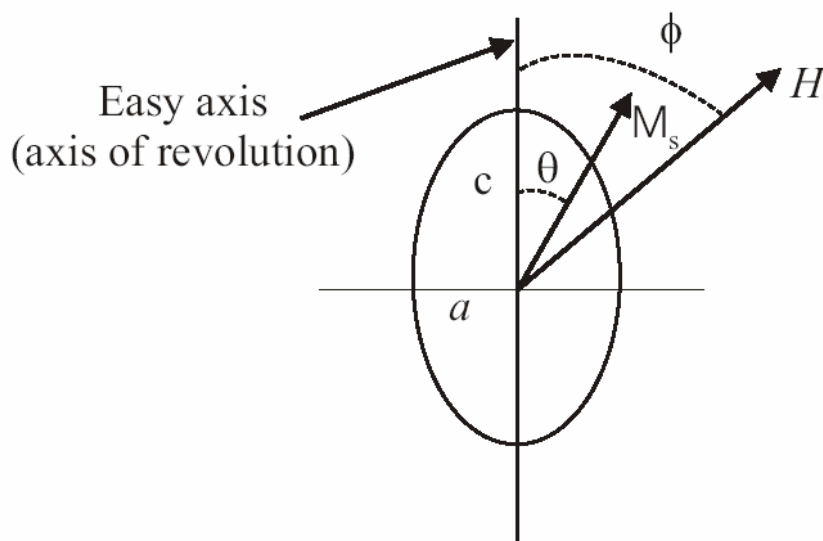

Figure 2.5: Coordinate system for magnetization reversal process in a single-domain particle in which the shape and crystallographic easy axis coincide. An externally applied field at an angle f relative to the easy axis causes a net magnetization to lie at some angle q relative to the easy axis.

The coordinate system of SW model is shown in Fig. 2.5. The equilibrium direction of the particle magnetization vector is determined by the easy anisotropy (EA) axis and the direction of the applied field. As shown in Fig. 2.5 when a magnetic field H is applied at an angle f to the easy axis of the uniaxial anisotropy of the particle, the magnetization vector then lies under an angle q relative to the easy axis. The free energy density of the system may be written in terms of anisotropy energy density as

$$E = K \sin^2 q - m_0 H M_s \cos(f - q) \tag{2.20}$$

The equilibrium position of M is given by

$$\frac{dE}{dq} = 2K \sin q \cos q - m_0 H M_s \sin(f - q) = 0, \tag{2.21}$$

and the magnetization resolved in the field direction is given by

$$M = M_s \cos(f - q). \tag{2.22}$$

Let us consider magnetic field is normal to the easy axis, so that f is 90°. Then

$$2K \sin q \cos q = m_0 H M_s \cos q$$

and $M = M_s \sin q$.

Therefore,

$$2K(M/M_s) = m_0 H M_s .$$

Put $M/M_s = m$ = reduced magnetization. Then,

$$m = m_0 H (M_s/2K). \tag{2.23}$$

From above it is clear that the magnetization is a linear function of H, with no hysteresis. Saturation is achieved when $H = H_k = 2K_u/M_s$ = anisotropy field. If we define the reduced field as

$$h = H/H_k = m_0 H M_s/2K_u$$

then $m = h$ when f is 90°.

Now Eqs. (2.21) and (2.22) can be may be written as

$$\sin q \cos q - h \sin(f - q) = 0, \tag{2.24}$$

$$m = \cos(f - q). \tag{2.25}$$

Let us consider the case when the magnetic field is along the easy axis ($f = 0$) and H and M_s both point along the positive direction of this axis. Then let H be reduced to zero and then increased in the negative direction ($f = 180°$). In this case H and M_s are antiparallel

and the field exerts no torque on M_s, but the magnetization will become unstable at $\boldsymbol{q} = 0$ and will flip over to $\boldsymbol{q} = 180°$ (parallelism with H) when H reaches a sufficient high value in the negative direction.

To find the equilibrium energy states, we need the second derivative of total energy E

$$\frac{1}{2K_u}\frac{d^2E}{d\boldsymbol{q}^2} = \cos^2\boldsymbol{q} - \sin^2\boldsymbol{q} + h\cos(\boldsymbol{f}-\boldsymbol{q}) = 0. \tag{2.26}$$

When $d^2E/d\boldsymbol{q}^2$ is positive, the equilibrium is stable, if it is negative, the equilibrium is unstable, and if it is zero, that means a condition of stability is just changing to one of the unstable position. Now the critical field h_c and the critical angle $\boldsymbol{q}_c$, at which the magnetization will flip may be calculated from the solutions of Eqs. (2.24) and (2.26):

$$\tan^3\boldsymbol{q}_c = -\tan\boldsymbol{f}, \tag{2.27}$$

$$\text{and } h_c^2 = 1 - \frac{3}{4}\sin^2 2\boldsymbol{q}_c. \tag{2.28}$$
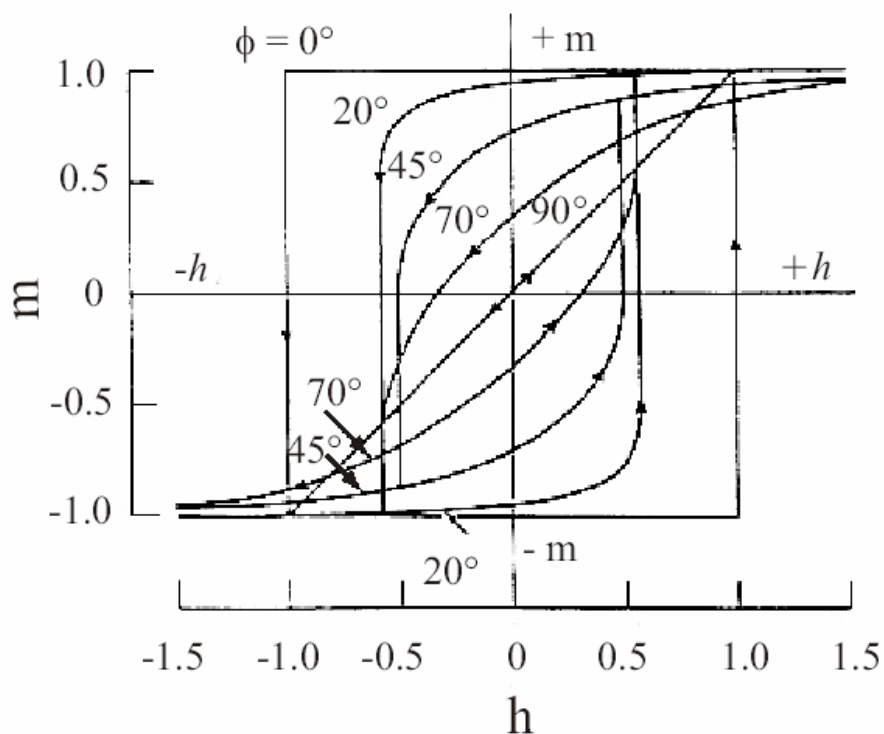
Figure 2.6: Hysteresis curves of a spherical single domain particle for different angles between anisotropy axis and external field in the framework of Stoner-Wohlfarth model [7].

For $f = 180°$, $q_c = 0$ and $h_c = 1$ or $H = H_k$. In this case the hysteresis loop is rectangular as shown in Fig. 2.6 The way in which the total energy E varies with the angular position q of the M_s vector for $f = 180°$ is shown in Fig. 2.7 for various field strengths. It is understandable how the original energy minimum at $q = 0$ changes into a maximum when $h = h_c$.
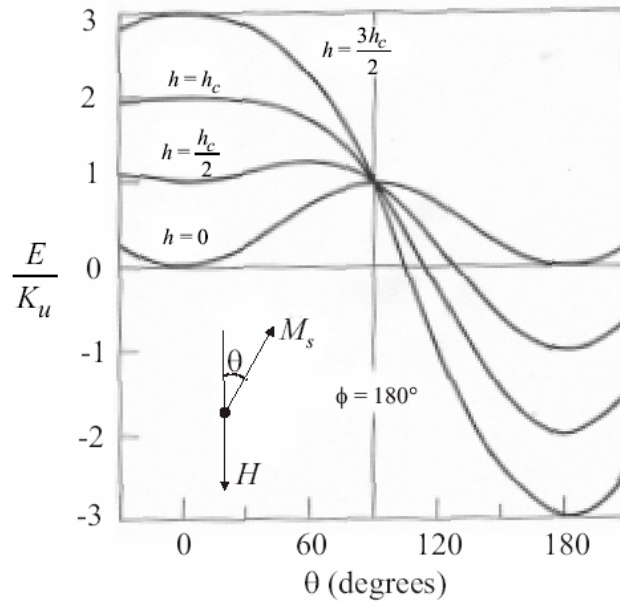
Figure 2.7: Variation of the total energy E with the angular position q of a Stoner-Wohlfarth particle.

Figure 2.8: Hysteresis loop of an assembly of uniaxial single domain particles having their easy axes randomly oriented showing remanence of 0.5 M_s.

The reduced magnetization m as a function of reduced field h for any intermediate angles ($q \neq 0$) can be solved numerically from Eqs. (2.24) and (2.25). The hysteresis loops calculated for various values of f are shown in Fig. 2.6.

Stoner and Wohlfarth [7] and Rhodes [39] also calculated the hysteresis loop of an assembly of noninteracting particles, with their easy axes randomly oriented in space so that the assembly 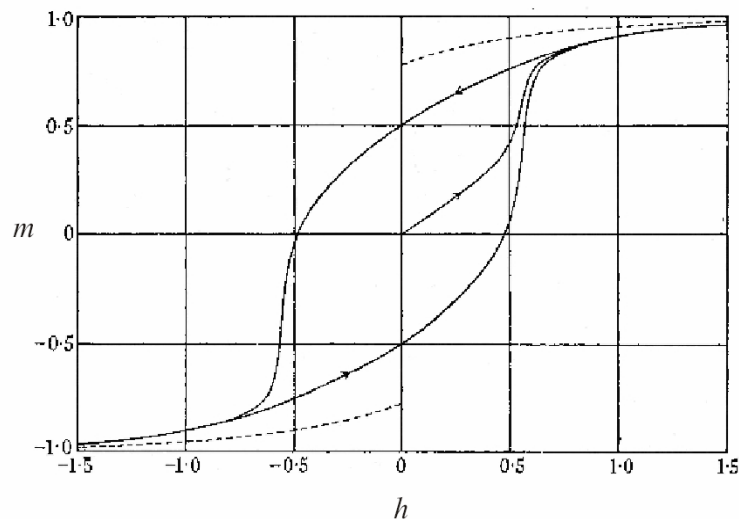as a whole is magnetically isotropic. In this case they found that the hysteresis loop (Fig. 2.8) is characterized by a remanence m_r of 0.5 and a coercive field h_{ci} of 0.48.

2.4.2. Magnetization reversal in thin films

Above we have seen how magnetization reversal based on coherent rotation of all spins in the magnetic sample is described by the Stoner-Wohlfarth model. However magnetization reversal process in thin films can occur either via coherent rotation and or via domain wall motion. In this section we will consider samples in which domain walls are present and move with complete freedom in the weakest field.

The behaviour of a ferromagnet in a magnetic field is considered the primary factor in the practical evaluation of the material. For this evaluation, the magnetization M or the induction B is plotted against the magnetizing field H. Such magnetization curves are not only useful for technical puposes, but also indispensable in elucidating the process of magnetization under different conditions. A typical hysteresis loop for a ferromagnetic sample is shown in Fig. 2.9. However, easy axis magnetization curves in thin films typically exhibit square-like hysteresis-loops [16].

If the system is magnetized to the saturation magnetization M_s by an applied field, then by reducing the field to zero, the magnetization reduces to the remanent magnetization M_r. A magnetic field equal to the coercive field H_c is needed to switch the magnetization into the opposite direction and to bring the magnetization to zero from remanence. The parameters M_r and H_c can be used to characterize a ferromagnet. Previously we have evidenced if a specimen exceeds a certain critical size, it would divide into *domains*, in each of which M_s is everywhere parallel, separated by *domain walls* where the direction of M_s varies with position.
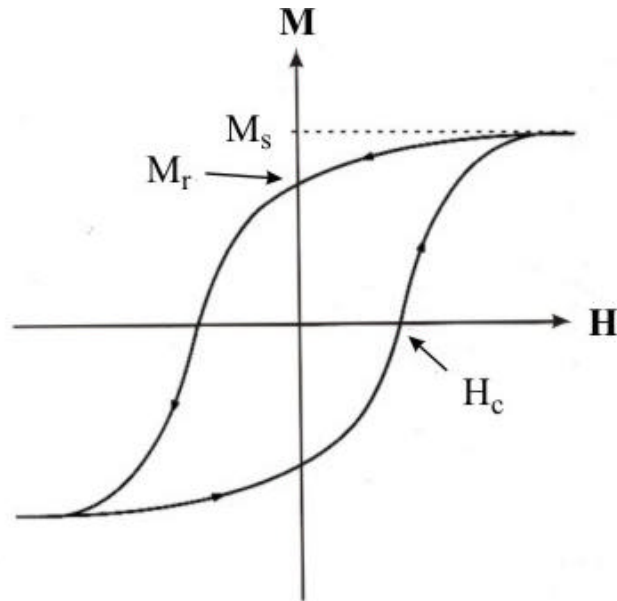
Figure 2.9: Magnetization *M* vs. applied field *H* for a typical ferromagnet.

When a demagnetized ferromagnet is magnetized, various processes occur. First the applied field is increased from zero, domain wall motion starts to occur which requires least magnetic energy. In this process, domains which are aligned favourably with the magnetic field will grow at the expense of domains which are unfavourably aligned. At small applied fields the domain walls move through small distances and return to their original positions on removal of the field; these are termed reversible displacements and correspond to the initial curved part of the magnetization curve. Here the domain walls expand like an elastic membrane under the action of the magnetic field. When the field is removed the wall returns to its original position. This reversible process is called as *domain-wall bowing* or one can also call it *domain-wall relaxation*. Wall bowing becomes irreversible once the domain wall is sufficiently deformed that the expansion continues without further increase of field. The bending of the domain wall which begins as reversible can also become irreversible if during this process the wall encounters further pinning sites which prevent it relaxing once the field is removed. At intermediate to high field amplitudes, there is an irreversible mechanism, namely domain rotation can occur in which the anisotropy energy can be outweighed and the magnetization can suddenly rotate away from the original direction of magnetization to the crystallographic easy axis which is nearest to the field direction. The final domain process at highest magnetic fields is coherent rotation of the domains to a direction aligned with the magnetic field, irrespective of the easy and hard axis. The magnetization of a ferromagnet also changes by a series of

discontinuous steps due to domain boundary motion, so that very small steps are sometimes seen on the magnetization curves. This is known as **Barkhausen effect**. In case of a finite average activation energy, the wall proceeds in so-called Barkhausen jumps from local minimum to local minimum of the domain-wall potential. [40] The time for a jump, t_B, can be expressed by an Arrhenius law [41]

$$t_B = t_0 \cdot \exp \frac{E_A - \mu_0 V_B M_s H}{k_B T} .$$ (2.29)

The numerator of the exponent represents the average activation energy, with E_A the activation energy in the absence of a magnetic field, and the second term representing its reduction due to gain in Zeeman energy. V_B is the activation or Barkhausen volume whose magnetization is reversed in a single Barkhausen step. The characteristic time t_0 is basically given by the spin-precession period time, which is in the order of $t_0 \approx 10^{-10}$ s.

A pinned domain wall in a random ferromagnet can exhibit four different dynamic modes namely *relaxation*, *creep*, *slide* and *switching* [13, 42, 43, 44]. Relaxation means a kinetic state of motion, where the external field is not able to displace the center of gravity of the domain walls, but merely gives rise to local hopping between adjacent free energy double wells. Creep refers to thermally activated nonadiabatic motion of a DW. In the creep regime, i.e. in small external magnetic fields, the total free energy of the system more or less follows the potential. After the wall has surpassed a maximum in the potential there is no substantial gain in kinetic energy because the spin precession is damped within the wall due to spin-lattice relaxation or magnon excitations. Consequently, the wall is pinned at positions where the potential has a local minimum. The domain wall can only proceed if either sufficient activation energy, E_A, is provided (thermal excitations) or if the external magnetic field is strong enough so that the potential minimum disappears due to the superimposed position-dependent Zeeman energy. So domain wall pinning increases coercivity. In the creep regime, the domain-wall speed v is inversely proportional to the time for a Barkhausen step, t_B, and thus depends exponentially on the magnetic-field strength H. (above equation). An analogous magnetic-field dependence is assumed for the thermally-activated nucleation processes [45]:

$$v(H) = v_0 \exp \frac{\mu_0 M_s V_B H}{k_B T}$$ (2.30)

$$R(H) = R_0 \exp \frac{\mu_0 M_s V_N H}{k_B T}$$ (2.31)

Here, V_N denotes the average volume of the nucleated domains. The constants R_0 and v_0 depend on the respective activation energies for domain nucleation and Barkhausen step. Slide is known as the adiabatic viscous motion of the DW. And finally in switching the magnetization flips from negative to positive saturation and vice versa. We will discuss these dynamic modes of domain wall in detail in section 4.3.2.1.2.

Apart from static measurements, dynamic hysteresis can be measured by applying an *ac* field. Dynamic hysteresis is another way to characterize ferromagnetic thin films. One can scale the area of the hysteresis loop as a function of applied field amplitude and frequency. If the applied magnetic field varies periodically in time, $H(t) = H_0 \sin \boldsymbol{w} t$, the system is driven back and forth across a first-order phase transition at $H = 0$. Due to this $m(t)$ lags behind $H(t)$, and hysteretic effects take place. The areas of the hysteresis loop, $A = \oint m(H)\, dH$, as functions of the amplitude H_0, frequency $\boldsymbol{w}$ and temperature T have been studied theoretically [46, 47, 48] and experimentally [49, 50]. The simulated average hysteresis-loop area showed a power scaling law, $A \propto H_0^a \boldsymbol{w}^b T^{-g}$, where $\boldsymbol{a}$, $\boldsymbol{b}$ and $\boldsymbol{g}$ are the exponents depending on the dimensionality and symmetry of the system [50].

From above we understood that in a non-interacting single domain particle system, the magnetization reversal can occur via coherent rotation and in bulk films, the reversal takes place via coherent domain rotation or domain wall motion. However in an interacting nanoparticle system, magnetization reversal can also occur via domain wall motion like in thin films and only with the exception that the domains consist of many single domain nanoparticle. This is a point of interest to be further discussed in section 2.7.

2.5. Magnetic interparticle interactions

In all fine-particle systems, different kinds of magnetic interparticle interactions exist and the interaction strength varies with the volume concentration x_v. The different types of magnetic interactions which can be important in allowing the magnetic moments in a solid to interact with each other and may lead to long range order are explained in the following:

i) **dipole-dipole interaction**: Two magnetic dipoles m_1 and m_2 separated by a distance r will have potential energy

$$E = \frac{m_0}{4\pi r^3}\left[m_1 \times m_2 - \frac{3}{2}\left(m_1 \times r\right)\left(m_2 \times r\right)\right].$$ (2.32)

This interaction is long-range and anisotropic in nature. From Eq. 2.32, it is seen that the strength of this interaction depends between their separation and their degree of mutual alignment. One can easily estimate the order of magnitude of dipolar effect for two moments each of $m_1 \gg m_2 \approx 1$ m_B separated by $r \approx 0.1$ nm that turns out to be $m^2/4\pi r^3 \sim 10^{-23}$ J, which is equivalent to about 1 K in temperature. Therefore dipolar interaction is much too weak to account for the ordering of most magnetic materials, since most of the magnetic materials order at much higher temperature. However, in magnetic nanoparticle systems where each nanoparticle has a moment $m \approx 10^3$-10^4 m_B, the energy may correspond to an ordering temperature of a few tens of Kelvins.

(ii) **exchange interaction:** The exchange interaction is actually an effect that arises from the interplay of electromagnetism with quantum mechanics. This interaction lies at the heart of the phenomenon of long-range magnetic order.

When the electrons on neighboring magnetic atoms undergo exchange interaction, this is known as direct exchange. Hence direct exchange interaction plays a big role in nanoparticle assemblies where the surfaces of the particles are in close contact.

(iii) **tunneling exchange interaction:** Another kind of interaction in fine particle system is tunneling exchange interaction where nanoparticles are only few nanometers apart from each other [51].

(iv) **RKKY interaction:** In a nanoparticle assembly where the matrix and particles are both metallic, RKKY (*Rudermann-Kittel-Kasuya- and Yosida*) interaction occurs and depends on $1/d_{ij}^3$, where d_{ij} is the distance between particles similar to dipolar interaction.

(v) **Superexchange interactions**: When the matrix is insulating, superexchange interaction can exist depending on the structure and the nature of the matrix and the bonding at the

particle matrix interface. Exchange interactions are short ranged in insulating magnetic materials, but if the bonding is favorable, superexchange interactions may extend over large distances.

2.5.1. Effects of interparticle interaction

These above mentioned interparticle interactions have significant effects on the magnetic properties of the nanoparticle assemblies. The energy barrier E_B, which depends on the symmetry of the anisotropy of the single particle, is modified because of the interaction effects. In this case individual priority is given to the total free energy of the assembly, while single particle energy barriers are no longer solely relevant. The reversal of one particle moment may change all energy barriers within the assembly.

As mentioned earlier an ensemble of single domain nanoparticles is denoted as superparamagnetic (SPM), when the particles are separated far enough apart so that inter-particle interactions can be neglected [11]. When the thermal energy ($k_B T$) is higher than the activation energy ($\Delta E = KV$), then the ensemble will behave like a paramagnet, with the only difference that the independent moments are not atomic moments but consist of large group of moments and each group inside a ferromagnetic particle. Usually in the case of small concentrations of particles, only SPM behavior is observed because of negligible interparticle interactions.

However, for increasing concentrations the strength of inter particle interaction is not negligible. For example assuming only dipolar interaction between two particles each with a moment of $\boldsymbol{m} = 3000\boldsymbol{m}_B$ and a center-to-center distance of $D = 6$ nm, the mean (point) dipolar energy will be be $E_{d-d}/k_B = (\boldsymbol{m}_0/4\pi k_B)\, \boldsymbol{m}^2 / D^3 = 26$ K. However, taking into account all neighbours, the mean dipolar energy can be around 100 K in a dense nanoparticle assembly. Furthermore, higher-order multipole terms can become relevant in case of imperfectly spherical particles [52]. Thus in a dense ensemble of single domain nanoparticles, the inter-particle interaction can dominate over single particle blocking and may lead to a collective freezing [2, 53, 11]. Two kinds of collective states can be distinguished namely superspin glass and superferromagnetism. Superspin glass behavior has been observed in many nanoparticle systems with intermediate strength of dipolar interactions [54, 10, 55]. Here the superspins of the nanoparticles freeze collectively into a spin glass phase below a critical temperature, T_g [54, 10, 55]. Increasing the particle density and, hence, the interaction between the particles, collective ferromagnetic-like

correlations or a so called superferromagnetic [12, 56, 51, 57, 58] state can be observed with properties being different from those of a spin glass.

In real systems the particle sizes usually vary and so do their magnetic moments. This "polydispersivity" leads to a more complex behavior of the whole system already in the border case of strong dilution. First of all, the sharp features to be expected in the M vs. T curves at T_B become smeared. Further, decay curves of the magnetization after switching off the aligning field are described by stretched exponentials, $M(t) \propto \exp[-(t/t)^{-b}]$, rather than by simple exponential ones. Such systems may easily be confounded with spin glasses [59, 60].

In such questionable cases tests for prototypical spin glass properties have to be carried out. Spin glasses typically show a divergence of the non-linear part of the susceptibility at the spin glass temperature T_g or aging and memory effects at $T < T_g$ [61 62]. All of these features cannot occur in superparamagnetic, *viz.* strongly diluted magnetic nanoparticle systems, in which the interaction of the particles can be neglected. This assertion does not change, if the systems are not ideally diluted, but non-negligible inter-particle interactions (*e. g.*, of dipolar origin) are still weak enough. In that case the nanoparticle system merely reveals a change of both the relaxation times and the activation energies [2].

In granular systems, dipolar and exchange interactions (interaction between two particles by surface contact) may exist simultaneously. In this case the density of the particles and their position (frozen fluid agglomerates, multilayer structures etc.) should have a large effect on the physical properties of the particles. Ulrich *et al.* [63] have studied the influence of dipolar interactions and polydispersivity on the isothermal magnetization relaxation of a random ensemble of magnetic nanoparticles after switching off a saturating external magnetic field. They found that the relaxation of magnetization (i) decays by a stretched exponential law at low concentration, (ii) decays by a power law at intermediate concentration, and (iii) retains a nonvanishing remanent magnetization at very high densities. Undoubtedly, the results of steps (i) and (ii) are indicative of a spin glass phase. However, the finite value of the remanent magnetization as observed in step (iii) seems to imply the existence of some long-range ordered state beyond the spin glass state with zero remanence. The conjectured [12, 13, 43] superferromagnetic (SFM) domain state was supported by the results of Monte Carlo (MC) simulations [64] on a model very similar to the preceding one [63]. It was concluded that collective behavior governs the dynamics of

the system at low temperatures as demonstrated by the occurrence of aging phenomena and a remarkable broadening of the distribution of relaxation times as compared to the non-interacting case.

Further hints at both spin glass freezing and short-distance ferro- and antiferromagnetic correlations of randomly distributed supermagnetic moments was found by Chantrell *et al.* [65] within precise Monte-Carlo investigations. To investigate very large systems, the dipolar interaction was cut off in order to overcome time consumption by complete Ewald summations. Even when neglecting this far distance ordering tendency the ferromagnetic correlations become so strong on cooling at particle volume densities $x_v > 0.2$ that no demagnetized states can be prepared anymore. This concentration range showing "non-equilibrium artifacts" was not further investigated and we argue that the authors of Ref. [65] must thus have missed the opportunity to evidence SFM ordering.

Let us remind that the dipolar interactions being always present in a magnetic nanoparticle system and being most relevant due to their long-range nature may favour both ferromagnetic or antiferromagnetic alignments of the moments in magnetic nanoparticle systems. For example it has been predicted that dipolar interactions can give rise to ferromagnetic and antiferromagnetic ground states, if the particles are positioned in face centered and body centered cubic lattice sites, respectively [66]. In a system of randomly distributed magnetic particles one may expect a competition of different spin alignments. Thus, the nature of the low temperature state of such a frustrated system will resemble that of a spin glass state in many respects. Indeed, very recently the seemingly clear indication of a remanent moment in a random superspin ensemble after FC [63] has been cast in doubt by Bunde and Russ [67], who found that finite size artifacts might have been responsible for the SFM signature in their previous calculations [63]. In this new situation we should remember that the suspected glassiness of the ground state of a concentrated dipolarly coupled spin system [65] can be lifted when adding, *e.g.*, a small ferromagnetic interaction between the particles. This was shown by Kretschmer and Binder [68], who predicted a ferromagnetic ground state in a simple cubic dipolarly coupled Ising system upon introducing weak positive nearest neighbor exchange, $J > 0$, in addition to the dipolar long-range interactions.

2.6. Superspin glass

In this section spin glass systems in bulk materials as well as in nanoparticle systems will be discussed. Finally different models of spin glass properties will be briefly addressed.

The key parameters to have a spin glass state are randomness and frustration. Fig. 2.10 (b) depicts how frustration can arise in a triangular lattice. There is no magnetic frustration as shown in Fig. 2.10 (a), because all the spins on the square lattice are anti-parallel satisfying nearest neighbour antiferromagnetic interactions. However in a triangular lattice as shown in Fig. 2.10 (b) geometrical frustration occurs because it is not possible to orient the spin on the third site to satisfy the requirement of antiferromagnetic nearest-neighbour interactions with the other two spins.
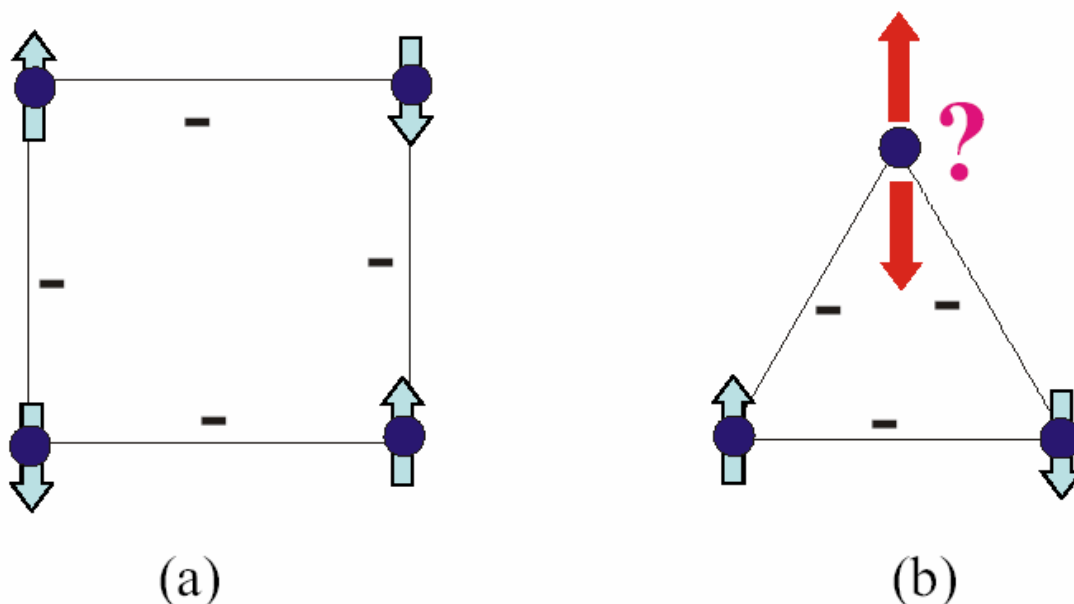

(a)   (b)

Figure 2.10: (a) Unfrustrated antiferromagnetic nearest-neighbour configuration on a square lattice. (b) Frustrated antiferromagnetic nearest-neighbour configuration on a triangular lattice. The triangular lattice shows frustration because it is not possible to orient the spin on the third site to satisfy the requirement of antiferromagnetic nearest–neighbour interactions with the other two spins [69].

If one starts with a non-magnetic lattice and sparsely populate it with a dilute, random distribution of magnetic atoms, then the system might show disorder which would not be likely to exhibit a phase transition from a high temperature disordered state to a low temperature ordered state. Indeed such systems do show something resembling a phase

transition at a particular temperature to a state, while not ordered, is distinctly different from the high temperature disordered state. This kind of magnetic system with mixed interactions characterized by a random, yet cooperative, freezing of spins at a well defined temperature T_f (the *freezing temperature*) below which a metastable frozen state appears without a regular magnetic long-range ordering is called a spin glass. Obviously at high temperatures the magnetic behaviour is dominated by thermal fluctuations, i.e., all the spins are virtually independent. But when the system is cooled down to lower temperatures, the independent spins slow down and form locally correlated units, denoted *clusters*. As the system is further cooled down to T_f the fluctuations in the clusters also progressively slow down and the glassy corelations between the spins become more long range. Thus at this state each spin becomes aware of its spins in a progressively growing region around it. Therefore at T_f the system finds one of its many ground states and freezes. Below T_f the system approaches a glassy kind of ground state, but still possesses metastability and slow relaxation behaviour. Let us discuss some of the relevant interactions for spin glass state and some examples of spin glass material.

One class of spin glass materials is called the canonical spin-glass materials and some examples of this are noble metals (Au, Ag, Cu or Pt) weakly diluted with 3d transition metal ions, such as Fe or Mn. Since 4d or 5d transition metals are non-magnetic i.e., do not form local moments, they cannot be used as impurities in a noble metal to form a spin glass. A commonly studied spin glass is $Cu_{1-x}Mn_x$ with $x \ll 1$ in which the substitution of small amounts of Mn into the Cu matrix occurs completely randomly with no short-range ordering. In canonical spin-glass systems the magnetic interaction is due to the scattering of the conduction electrons at the spins, leading to an indirect exchange interaction- the RKKY interaction which oscillates strongly with distance d between spins,

$$J(d) = J_0 \frac{\cos(2k_F d + \boldsymbol{j}_0)}{(k_F d)^3}, \qquad (2.33)$$

where J_0 and $\boldsymbol{j}_0$ are constants and k_F is the Fermi wave vector of the host metal. Since the spins are randomly placed in the host metal, some spin-spin interaction will be positive ($J_{i,j} = J > 0$) and favour parallel alignment, while others will be negative ($J_{i,j} = J < 0$), thus favouring anti-parallel alignment. Therefore the required factor of competition or frustration among parallel and anti-parallel alignment is governed via the oscillating nature of $J(d)$.

As we know pure RKKY interaction is isotropic, and the canonical spin glass systems are therefore often referred to as **Heisenberg spin glasses**. However, dipolar interaction and interaction of the Dzyaloshinsky-Moriya (DM) [70] type can lead to some anisotropy in these systems. The DM type interaction is due to spin-orbit scattering of the conduction electrons by non-magnetic impurities and reads as

$$E_{DM} = -\overrightarrow{D_{i,j}} \cdot \left(\overrightarrow{S_i} \times \overrightarrow{S_j} \right), \ \overrightarrow{D_{i,j}} \propto \overrightarrow{d_i} \times \overrightarrow{d_j} \tag{2.34}$$

where $\overrightarrow{D_{i,j}}$ is a random vector due to the randomness of the spin positions $\vec{d_i}$.

Other categories of spin glass systems are based on magnetic dopants in amorphous metals (*e.g.*, a-$La_{80-x}Gd_xAu_{20}$), in semiconductor ($Eu_xSr_{1-x}Te$), and in dilute insulating material (*e.g.*, $Fe_xMg_{1-x}Cl_2$, $x \leq 0.4$).

As we have already discussed, randomness is the most important ingredient as well the competing interactions for the spin glass state. The distribution of distances between moments in a random-site spin glass can lead to competing interactions and depending on the distances their sign (ferromagnetic or antoferromagnetic) will change. However, competing interactions are always present in a random-bond spin-glass, because different bonds try to order the system in different ways. Thus frustration arises because of these competing interactions.

At very high concentrations of magnetic ions, the system approaches the percolation limit, at which long-range magnetic order can exist, because nearest-neighbour links are possible through the whole sample along which each ion is magnetic. This kind of system is called as a **re-entrant spin glass**. In these systems the cluster-glass phase develops from a ferromagnetic state, and thus re-enters the frozen (disordered) phase out of another, not paramagnetic, state [61].

Analogously to the spin glass state in bulk materials, this kind of collective state can also occur in ensembles of single domain nanoparticles in which the inter-particle interaction is non-negligible. As already mentioned due to their single domain nature, the nanoparticles are abbreviated as *superspins*, therefore the collective glassy state of the nanoparticle assembly is called *superspin glass* (SSG). In ferromagnetic fine-particle systems such SSG state has been observed in frozen ferrofluids [54, 71] and also in our DMIMs [55]. Different crucial criterion can be checked to interpret the spin glass or superspin glass state as follows.

One of the most crucial signatures of spin glass behaviour is to study the criticality of the non-linear susceptibility, c_3, as defined by the expansion of the magnetization M with respect to a weak magnetic field H [54],

$$M = c_1 H - c_3 H^3 + c_5 H^5 - \cdots\cdots \tag{2.35}$$

where c_1 is the linear and c_3, c_5, etc are the nonlinear susceptibilities. At the glass transition temperature T_g (= freezing temperature T_f in the limit $t \circledR ¥$, i.e., in thermal equilibrium) c_1 is non-divergent, whereas the higher-order terms diverge, *e.g.*

$$c_3 = c_3^0 \left(T/T_g - 1\right)^{-g} \tag{2.36}$$

$$\text{and } c_5 = c_5^0 \left(T/T_g - 1\right)^{-(-2g+b)}, \tag{2.37}$$

with the critical exponents g and b. Also dynamic critical scaling can be used to test the universality of the system. That means the imaginary part of the susceptibility, $c''(w,T)$, measured at various angular frequencies $w = 2pf$ is expected to yield a data collapse onto a single function $H(w,t)$ according to [72]

$$c''/c_{eq} = \left(T/T_g - 1\right)^b H(wt), \quad T > T_g, \tag{2.38}$$

where b is the order parameter exponent and c_{eq} denotes the equilibrium susceptibility in the limit $w \rightarrow 0$.

There are also some other important characteristics like aging, memory, and rejuvenation, which characterize the collective spin glass state. Details of these phenomena can be found in references [73, 55, 62, 74].

There are different spin glass models such as the Edwards-Anderson (EA) model, Sherrington-Kirkpatrick (SK) model, hierachical model, droplet model and fractal-cluster model [75]. EA model is based on the mean field approach and the important assumption is that the system has quenched disorder, i.e., the randomness of spin sites (sample structure disorder is frozen-in) and only the spin orientation can vary [76]. The SK model is an extended approach to EA mean-field approximation model in which the interaction is considered as infinite-range where every spin couples equally with every other spin [75]. The Hamiltonian in SK model can have an infinite number of solutions and each solution can be regarded as an equilibrium state: metastable if separated by finite barriers from others and stable if separated by infinite barriers [77, 78]. At any temperature below T_g

these states are hierarchically organized with respect to their mutual overlaps in a multi-valley landscape. This is called the hierarchical model. Fischer and Huse [79, 80] presented the droplet model in which the spin glass state can be mapped as a distribution of droplets or dynamic domains of correlated spins. The definition of a droplet in the ground state is a compact cluster of lowest-energy at a certain length scale around a particular point. The assumption of this theory is that an understanding of the spin glass phase (which should exist at $T = 0$) can be obtained from its ground-state properties. In the fractal-cluster model [81] a scaling theory of the spin glasses is proposed by considering clusters of correlation length x, which diverge as $\left[\left(T - T_f\right)\big/T_f\right]^{-u}$. These coherent regions have a cluster size s_x on which all relevant physical quantities depend. The volume of these clusters is x^D, where D is the fractal dimension because the clusters are expected to be highly irregular and branched. Details of all these models can be found in references [73, 61].

2.7. Superferromagnetism

Superparamagnetism (SPM) in an ensemble of nanoparticles occurs when the inter-particle interactions are sufficiently small. In the SPM state no collective inter-particle order exists, while the intra-particle spin structure is FM ordered. However for increasing concentration of particles, the magnetic inter-particle interactions become non-negligible and one may find a crossover from single-particle blocking to collective freezing. As described above for an intermediate strength of magnetic interactions, randomness of particle positions and sufficiently narrow size distribution, one can observe a superspin glass state. With further increase of concentration but prior to physical percolation, the inter-particle interactions become even stronger and this can lead to a kind of ferromagnetic (FM) domain state. These FM like correlations will consist of "supermoments" of the nanoparticle instead of atomic moments. This FM state in nanoparticle ensembles is being called "*superferromagnetism*". Therefore a superferromagnetic (SFM) domain can be defined as a ferromagnetic domain, the only difference being that the atomic moments are replaced by supermoments of the individual nanoparticles. This concept implies that the FM nanoparticles remain single-domain whereas the ensemble shows collective SFM behaviour.

The term "superferromagnetism" was introduced by Morup in 1983 [56] when he studied microcrystalline goethite by Mössbauer spectroscopy. Afterwards this terminology

has been used in different magnetic systems [82]. However the SFM domain state in nanoparticle systems has been evidenced only a few times up to now. For example Sankar *et al*. [83] have studied non-percolated Co-SiO$_2$ granular films and evidenced FM like correlations between the nanoparticles measured by small-angle-neutron scattering. They have studied different concentrations of nanoparticles and found that the magnetic correlations disappear for lower metallic volume fractions, i.e. for weaker dipolar interactions. The FM like correlations can be illustrated as in Fig. 2.11.
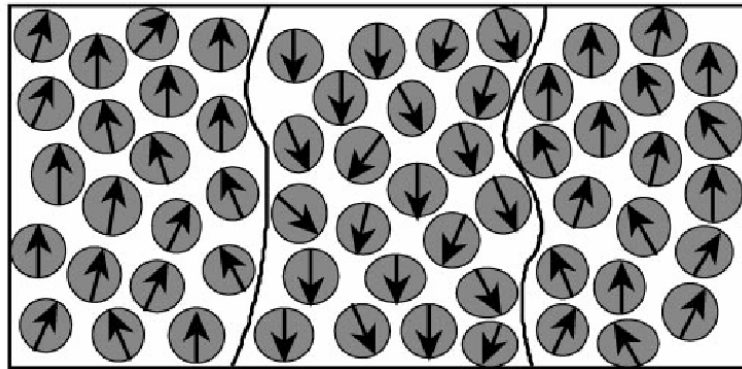

Figure 2.11: Schematic of superferromagnetic domains consisting of singe-domain nanoparticles [From Ref. 83].

As can be seen from the above figure drawn by Sankar *et al*., the magnetic (Co in their case) particles are coupled ferromagnetically in these correlated regions and the neighbouring FM regions are antiferromagnetically aligned. In their case the observed magnetic correlations were extracted from the zero-field cooled state in zero magnetic field, therefore they attribute the FM correlations resulting from magnetic interactions among the nanoparticles. In another 2D system of Fe dots on an insulator substrate, long-range order has been found [51] that has been attributed to a contribution of superexchange coupling between the dot supermoments. Long-range ferromagnetic order has also been found in one- and two-dimensional (1D and 2D, respectively) self-organized (i.e., quasi-periodic) arrays of nanosized transition-metal dots [84, 85, 86, 57]. Puntes *et al*. have studied two-dimensional self-assembly of Co nanoparticles and observed correlated areas (similar to domains) by magnetic force microscopy [58].

Similar domain structures have been found in polycrystalline permanent magnetic materials. It was found that the domain patterns obtained represent magnetically coherent

regions in which the smaller oriented particles are uniformly magnetized in the same direction. In fine-grained permanent magnet materials *e.g.* in $Sm_2Fe_{17}N_3$ [87], the grains are usually strongly correlated, and therefore cannot be treated as an ensemble of independent particles. In these materials the magnetic interactions (via exchange coupling and/or stray fields) between the particles are non-negligible and therefore collective phenomena become important which are described *e.g.* by the concept of "*Interaction domains*" [88, 89, 90, 87]. In these permanent magnetic materials the single domain size is around 200-300 nm and the grains studied were in the range of 100 nm [87]. Therefore any possibility of domain walls inside the grains was excluded. Also in polycrystalline Alnico V [91], similar interaction domains with spike-like shape were observed. An intuitive explanation on these interaction domains was given by the authors of these works. After thermal demagnetization the random selection of one of the two easy directions in each grain leads to a relatively high degree of frustration between the magnetization of neighbouring grains. However at saturation the sample selects the direction in each grain which is closest to the field direction. Thus subsequent demagnetization in an opposite field of well-defined amplitude creates a configuration with regions (interaction domains) magnetized around the directions parallel and anti-parallel to the applied field which results a smaller degree of frustration [87]. In this model, it has been simply assumed that dipolar interaction is responsible for these interaction domains.

In this thesis, CoFe nanoparticles embedded in insulating Al_2O_3 are studied similar to the permanent magnetic material only with the difference that our samples are very soft magnetic and there are no grain boundaries which may possess a large angle domain wall [92]. As discussed previously, only dipolar interaction is not sufficient to produce a ferromagnetic state. Later in this thesis it will be shown that additional tunnelling exchange interaction might be a crucial ingredient to produce this superferromagnetic state.

Chapter 3

Experimental Techniques

In this chapter, the experimental techniques employed to prepare the samples and also different techniques used for the structural and magnetic characterization will be discussed. Two different kinds of magnetic systems have been investigated in this thesis. First, we studied soft ferromagnetic $Co_{80}Fe_{20}$ nanoparticles embedded in an amorphous alumina (Al_2O_3) matrix prepared as **D**iscontinuous **M**etal **I**nsulator **M**ultilayers (DMIMs) represented by $[Co_{80}Fe_{20}(t_n)/ Al_2O_3 (3nm)]_m$, where t_n and m are the nominal thickness of the ferromagnetic layer and number of bilayers, respectively. The DMIMs with $t_n = 0.5 - 1.8\,nm$ and $m = 1 - 10$ were prepared by focused Xe-ion beam sputtering on glass substrate by the group of Prof. P. P. Freitas at INESC, Lisbon, Portugal. The microstructure and the layer quality are investigated by X-ray diffraction (XRD) and diffuse X-ray scattering under grazing incidence. In order to get information on the morphology of the samples, transmission electron microscopy (TEM) was performed. Magnetic characterization of these samples was performed by Superconducting Quantum Interference Device (SQUID) magnetometry and magneto-optic Kerr effect (MOKE) in our laboratory. Polarized neutron reflectivity (PNR) under small angles has been performed with the HADAS reflectometer at the Jülich research reactor FRJ-2 (DIDO). Various magnetic microscopies have been carried out on the DMIM systems. Magneto-optic Kerr microscopy was done in our laboratory, while synchrotron radiation based photoemission electron microscopy (XPEEM) was performed at the Advanced Light source (ALS) at Berkeley, USA.

Second, we have investigated frozen ferrofluids with different concentrations, containing $Fe_{55}Co_{45}$ nanoparticles dispersed in n-hexane. These samples were prepared by chemical engineering from precursor mixtures of $Fe(CO)_5$ and $Co_2(CO)_8$, by the group of Dr. A. Hütten at Universität Bielefeld, Bielefeld, Germany. Its structural characterization by TEM and magnetic characterization by SQUID magnetometry and Mossbauer spectroscopy were performed at various laboratories of our university. The preparation of these ferrofluids and their structural and magnetic properties will be discussed in Chapter 5.

3.1. Preparation of Discontinuous Metal Insulator Multilayers (DMIMs)

Nanosized particles can be prepared by both physical and chemical preparation methods. A common method to fabricate materials made of metallic nanosized clusters embedded in insulating matrix, is co-sputtering or co-evaporating the metal and the insulator on a suitable substrate. In this process a random distribution of clusters in the matrix can be obtained. The cluster sizes are controlled by varying the substrate temperature and/or postgrowth annealing. However, an alternative approach to prepare three-dimensional (3D) growth of transition and noble metals on insulators is the sequential deposition process [93].

The DMIM samples investigated in this thesis were prepared by focused ion-beam (FIB) sputtering. The FIB sputtering method has advantages compared to magnetron sputtering due to the independent control of beam parameters such as ion kinetic energy
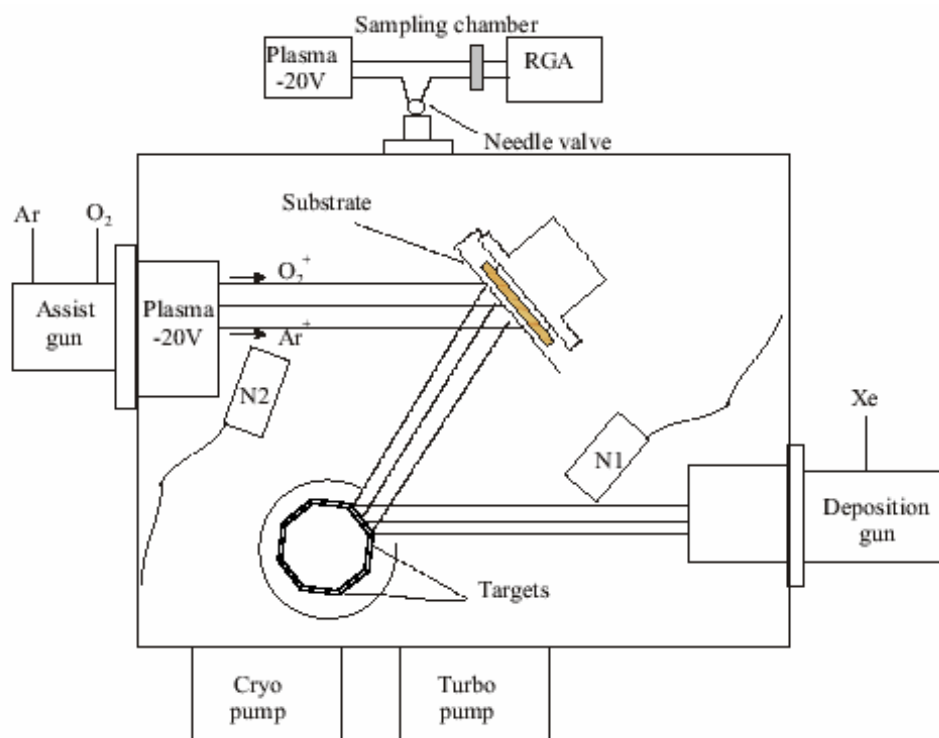

Figure 3.1: Schematic drawing of the FIB system. Pictorial representation of the plasma during the buffer layer oxidation is shown. N1 and N2 are the neutralizers for the deposition and assist guns, respectively. RGA is the residual gas analyzer. Sample distance to assist gun grid and target are 30 cm and 20 cm, respectively.

and deposition pressure. Ion beam sputtering is a versatile tool for the oxidation process and can produce higher quality thin films (with less defects). Samples deposited with this technique maintain the stochiometry of the targets.

The DMIMs are prepared in an automated FIB sputtering system which is equipped with a load-locked chamber (Nordiko N3000), a 10 cm-diameter deposition gun and a 25 cm-diameter assist gun as shown in Fig. 3.1. A quadrupole type residual gas analyzer (RGA) was connected to a sampling chamber for diagnostics of oxygen and argon levels inside the main chamber during the process. The Xe^+-ions within plasma created in the deposition gun are accelerated by applying a voltage of +1450 V and are extracted with a voltage of -300 V. The granular films have been sputtered by Xe ion beam acting alternatively on two separate metallic (CoFe) and insulator (Al_2O_3) targets. A mixed Ar/O_2 beam from a radio-frequency plasma was accelerated by the assist gun by applying a
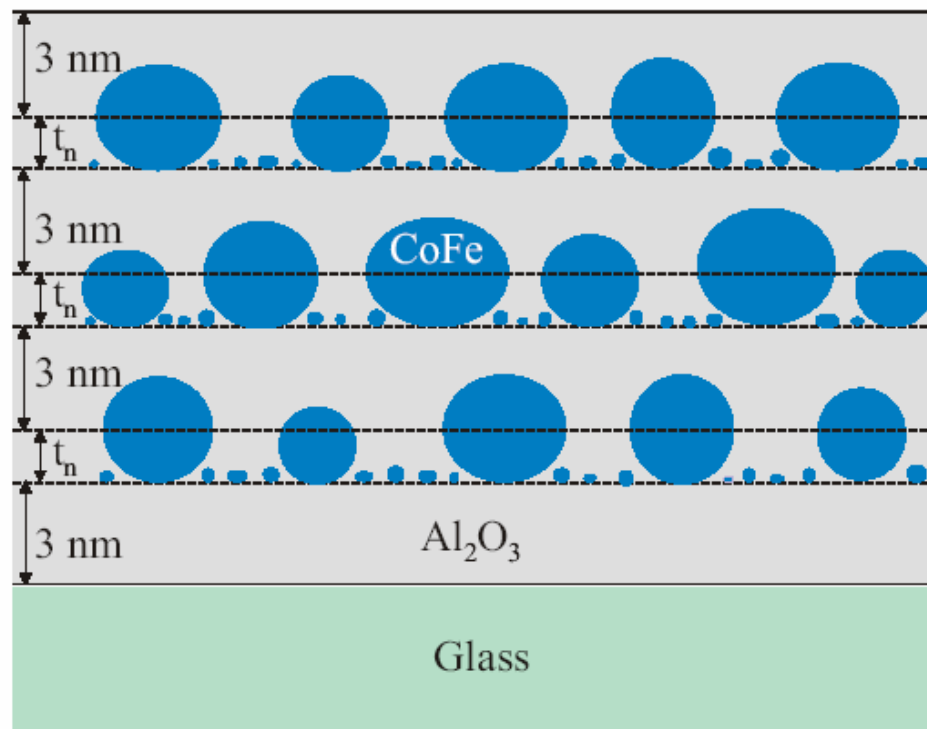

Figure 3.2: Schematic cross section of a DMIM consisting of glass substrate, Al_2O_3 layers (thickness 3 nm) and CoFe layers (nominal thickness t_n) forming quasi-spherical particles. The very small particles present between the big particles are the atomic clusters consisting of only a few atoms and are described in section 4.3.1.1.

potential of +30 V to the assist grids. This beam is meant to form an oxidic film by oxidizing a metallic layer. The design of the FIB system also makes it possible to rotate the

targets for sequential deposition during multilayer growth. The insulating layers were directly sputtered from an Al_2O_3 target providing a deposition rate of 0.012 nm/s and the $Co_{80}Fe_{20}$ was sputtered from a mosaic target (pieces of Fe on a Co plate) with a deposition rate of 0.032 nm/s. The thickness of each layer can therefore be controlled by the time of deposition from the above known deposition rates. Sampling of the chamber atmosphere along the process is performed through a needle valve that assures the RGA operating at $\approx 1 \times 10^{-7}$ Torr during all the steps of the sample deposition. The substrate temperature was maintained at 200 °C during deposition. Details of the sputtering system can be found in Ref [94].

The DMIMs structure is substrate (float glass)/Al_2O_3 (3nm)/[$Co_{80}Fe_{20}(t_n)$/ Al_2O_3 (3nm)]$_m$ where m is the number of CoFe(t_n)/Al_2O_3 bilayers and t_n corresponds to the nominal thickness of CoFe layer, i.e., the thickness that the ferromagnetic CoFe layer would have if it were continuous. The successful preparation of each granular layer is based on the fact that the metallic component has a much higher surface tension than the insulator. Hence, the metal layer does not wet the oxide and, below some thickness, it breaks up into almost spherical nanoparticles. In our case, they possess an average diameter $D \approx 3$nm. $Co_{80}Fe_{20}$ is a soft magnetic alloy with high spin polarization [95]. CoFe-Al_2O_3 is an ideal system from a structural standpoint since the CoFe/Al_2O_3 interfaces are of high quality and there is no evidence of intermixing of the deposited films at room temperature [96]. In particular, it was verified that no CoFe oxide is forming since no trace of exchange bias has been found under various test conditions [96]. Fig. 3.2 shows the schematic cross section of a DMIM consisting of the glass substrate, Al_2O_3 layers (thickness 3 nm) and CoFe layers (t_n) forming quasispherical nanoparticles. As shown in Fig. 3.2, there are some small CoFe spheres which represent small atomic clusters consisting of few atoms and will be discussed in Chapter 4.3. An interesting feature of the DMIMs is that CoFe particle size increases linearly with t_n while the average inter-particle distance monotonically decreases. Like in frozen ferrofluids where the long-range dipolar interaction between the single-domain nanoparticles can be continuously varied by changing the particle concentration, in the DMIMs the inter-particle interaction can be tuned by changing the nominal thickness, t_n.

For magnetic measurements, XRD and PNR, the samples were prepared on float glass substrates of 0.4 mm thickness. For TEM characterization samples were grown on water soluble KBr substrates and on 100 nm thick silicon nitride (SiN_3) membranes, prepared during the same run. Always the top and bottom layers are Al_2O_3, so the number

of Al_2O_3 layers is $m + 1$. The thickness of the Al_2O_3 layer was kept fixed at 3 nm and that of CoFe was varied in the range $0.5 \leq t_n \leq 1.8$ nm.

3.2. X-ray diffraction and diffuse X-ray scattering under grazing incidence

X-ray diffraction (XRD) measurements provide a variety of information on thickness and interfacial properties on the nanometer scale. They provide an ideal method to study nano-structured thin films and superlattices. In recent years the usage of X−ray scattering measurements in specular and nonspecular geometries have been explored for characterization of multilayers (MLs) [97, 98].

The microstructure and the layer quality of the DMIMs were investigated by X-ray diffraction and diffuse X-ray scattering under grazing incidence using a Bruker AXS D8 diffractometer with Cu K_α ($\lambda = 0.154$ nm) radiation equipped with Göbel mirrors for the incident and reflected beams. Fig. 3.3 shows the set-up for the X-ray experiments.
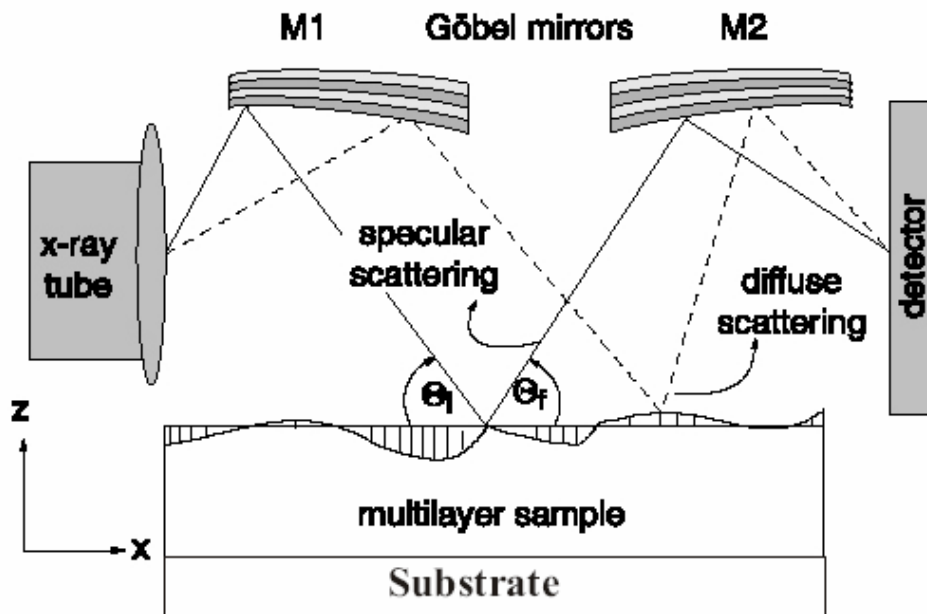

Figure 3.3: XRD scattering geometry at grazing incidence and exit angles in real space. M1 and M2 are Göbel mirrors, which yield an enhanced intensity and suppress the K_b radiation.

We measured the samples in specular geometry with the angle of incidence $\boldsymbol{q}_i$ equal to the exit angle $\boldsymbol{q}_f$ as well as in off-specular geometry with an offset of $\Delta\boldsymbol{w}$ between $\boldsymbol{q}_i$ and

q_f. In a scan with an offset Δw, one measures the diffuse scattering as a function of the component of the momentum transfer vector normal to the sample plane, q_z. True specular reflectivity is obtained by subtracting the off-specularly reflected intensity from the specular one. Diffuse scattering as a function of the in-plane component of the momentum transfer vector, q_x, is measured by keeping the scattering angle $2q$ fixed and rocking the specimen around $q_i = q_f$. In the following the principles of X-ray reflectivity in thin films is briefly described.

First of all let us discuss the refractive index of X-rays and the conditions of total reflectivity. Assuming that the frequency of the radiation w is much larger than any internal characteristic frequency, the refractive index for X–rays can be expressed as [99]

$$n^2(w) = 1 - \frac{w_p^2}{w^2}.$$
(3.1)

where $w_p = 4pe^2E_e/m_e$ is the plasma frequency treating all electrons in the material as free m_e is the electron mass, $E_e = \sum_i N_i Z_i$ is the electron number density, where N_i and Z_i are the atomic (ionic) number density and the atomic (ionic) number, respectively. The sum is taken over all components in the sample. The refractive index may also be expressed as a function of the magnitude of the scattering vector $|Q_0| = |k_{0,f} - k_{0,i}| = Q_0$, which is more appropriate for scattering experiments:

$$n(Q_0) = 1 - \frac{2p r_0}{k_0^2} \sum_i \left[f_i(Q_0) + \Delta f_i \right] - \frac{im}{2k_0}$$

$$= 1 - d - ib$$
(3.2)

Here $|k_{0,i}| = |k_{0,f}| = k_0 = 2p/l$ is the vacuum wavenumber for elastic scattering, r_o is the classical electron radius (2.818×10^{-15} m), $f(Q_0)$ is the atomic form factor ($\cong Z$ for small angles), Δf and m are strongly wavelength dependent close to absorption edges. Since the real part of d is positive and on the order of 10^{-5}, total external reflection of the X-ray beam penetrating into a medium of higher electron density E_e occurs at the critical scattering vector:

$$Q_c^2 = 16p E_e r_0 = 4k_0^2 (1 - n^2).$$
(3.3)

Q_c is a property of the material and does not depend on the wavelength of the radiation. For typical materials Q_c is of the order of 0.5 nm^{-1}. Specular reflectivity is observed, when the

incident and reflected angles q_i and q_f of the beam to the surface are identical. Here the scattering vector is given by $Q_0 = 2k_0 \sin q$. Inside of the material the scattering vector changes according to:

$$Q_1^2 = Q_0^2 - Q_c^2 . \tag{3.4}$$

Above Q_c the reflectivity drops off approximately with Q^{-4}, which is usually referred as Fresnel reflectivity. The reflectivity from a thin multilayer shows interference fringes above Q_c, which are due to the interference of waves scattered from the surface and from the interface to the substrate. These fringes, referred to as Kiessig fringes [100], and from the separation of the maxima ΔQ, the film thickness can be estimated via $d = 2p/\Delta Q$.

In the case of thin films and superlattices one has to deal with several or many interfaces. The boundary conditions must be fulfilled at each individual interface and the reflectivities and transmittivities add together to provide an overall reflectivity for a stratified medium. The reflectivity may then be calculated by the optical transfer matrix or by the recursion scheme described by Paratt [101]. Details of this formalism can be found in Ref. [102].

As mentioned earlier in this section, when the angles of incidence and reflection are identical, the condition of specular reflectity is fulfilled. Also in specular reflectivity measurements, the momentum transfer is perpendicular to the sample surface, $q = q_z$. This type of measurement provides information about the individual layer thicknesses and an estimate of the laterally averaged (rms) roughness of the layers.

In the following X-ray diffuse scattering will be discussed. It is known that scattering of electromagnetic radiation from non-ideal surfaces (rough surfaces) and interfaces results in a loss of specular reflectivity and gives rise to non-specular reflectivity. For a rough surface the transmittivity is larger than for a smooth one, enhancing thereby the intensity of the interference fringes. On the other hand, for a smooth surface the transmittivity is smaller because of its high reflectivity which reduces the amplitude of the Kiessig fringes. If both surface and interface are rough, the reflected intensity drops off drastically with increasing Q and the amplitudes of the Fringes are highly damped. Also in a multilayer consisting of alternating layers of different materials may lead to interdiffusion. This causes a lateral roughness with no particular length scale. Therefore, the diffuse scattering intensity I_{diff} is constant or zero for a homogenously

graded or abrupt (flat) interface, respectively. However the other extreme is an interface with a rms roughness which steadily increases as a function of a lateral distance in the surface, i.e. a roughness without cut-off. In this case all scattering is diffuse and no specular reflectivity remains. But usually the most interfaces lie between these two extremes. The interface can be described by a rms roughness $\boldsymbol{s}$, a lateral coherence length$\boldsymbol{x}$, and the jaggedness of the interface h $(0 < h < 1)$, where $h = 1$ describes a smooth interface. The parameter h is also related to the fractal dimensionality D of self-affine surfaces via $D = 3 - h$ [97]. The roughness correlation length $\boldsymbol{x}$ is inversely proportional to the frequency of interface irregularities and is assumed to be smaller than the coherence length of the radiation projected into the surface, such that interference is possible. For an example, an interface with a sinusoidal waviness with one particular wavelength $\boldsymbol{l}$ would be characterized by an amplitude $\boldsymbol{s}$, a correlation length $\boldsymbol{x} = \boldsymbol{l}$, and a jaggyness parameter $h = 1$. From such an interface, the off-specular scattering function would exhibit satellite peaks at distances $\Delta Q_{\parallel} = \pm 2\boldsymbol{p}/\boldsymbol{l}$ off the specular ridge. This approximation is valid in case of stepped interfaces with regular ledge lengths. However, usually there is a distribution of wavelengths describing the interfacial roughness and giving rise to off-specular diffuse scattering. Since, this diffuse scattering is weak, it is appropriate to use the kinematical approach of the scattering theory (Born approximation) [103]. In this approach the scattering function S(Q) is represented as the space Fourier transform of the pair correlation function g(r):

$$S(Q) \propto \int g(r)\exp(iQ \cdot r)dr.$$

Furthermore, because of the proximity of the total reflection regime, a distorted wave Born approximation [97, 104] has to be used in order to take the optical properties of the waves into account, yielding for the diffuse intensity

$$I_{diif}\left(Q_{\parallel}\right) = I_0 A \, |t(k_i)|^2 \, |t(k_f)|^2 \, S\left(Q_{\parallel}\right)$$

where $t(k_i)$ and $t(k_f)$ are the transmittivity coefficients [105]; I_0 is the incident intensity, and A collects all constants including geometrical factors. A single rough interface may be described by a height-height correlation function $C\left(r_{\parallel}\right) = \left\langle z(0)\, z\left(r_{\parallel}\right) \right\rangle$ [97], which relates a point at 0 and height $z(0)$ above the average surface to a point at distance $r_{\parallel}$ and at height $z\left(r_{\parallel}\right)$.The angular brackets indicate an ensemble average over all in-plane distances, where

in-plane isotropy way assumed. The scattering function for a single rough surface can be expressed as [97]

$$S\left(Q_{\parallel}\right)=\frac{e^{-|Q_{\perp}|^2 s^2}}{|Q_{\perp}|^2}\int\left(e^{-|Q_{\perp}|^2 C(\eta_{\parallel})}-1\right)e^{iQ_{\parallel}\eta_{\parallel}}d\eta_{\parallel}\,.$$

It should be noted that for a constant $Q_{\perp}$, the scattering function solely depends on the form of $C\left(\eta_{\parallel}\right)$. So for a single rough interface with cut-off, the height-height correlation function can be expressed as [97],

$$C\left(\eta_{\parallel}\right)=s^2 e^{-\left(\eta_{\parallel}/x\right)^{2h}}\,.$$

In case of thin films an additional correlation enters the problem, relating the roughness at the top and bottom. So in general, for a multilayer system, the correlation between the roughness at interface i and j may be described by [106]

$$C_{i,j}\left(\eta_{\parallel}\right)=\left\langle z_i\left(0\right)z_j\left(\eta_{\parallel}\right)\right\rangle\,.$$

If $C_{i,j}\left(\eta_{\parallel}\right)>0$, any interfacial irregularities are replicated from layer to layer to some extent, and this is referred to as conformal roughness. In X-ray reflectivity measurements the conformal roughness can be recognized in scans parallel to the specular ridge. If the longitudinal diffuse scattering follows the shape of the specular intensity including the Kiessig fringes and the Bragg reflections from multilayers then the pattern of any irregularities is replicated from interface to interface. Therefore, in case of conformal roughness the diffuse intensity will form ridges of scattering extending perpendicular to the specular ridge, whereas for a roughness without interfacial correlation the diffuse scattering is the incoherent superposition from the diffuse scattering of all interfaces and will not be structured in the direction parallel to the specular ridge. Experimental data obtained on DMIM samples will be shown later in this thesis and the correlated roughness will be analysed accordingly. Detailed description of X-ray reflectivity is described in Ref. [102, 97].

3.3. Transmission electron microscopy

Transmission electron microscopy (TEM) yields information on the morphology, composition and crystallographic information on a very fine scale. TEMs work the same way as a slide projector where a beam of electrons (like the light) is being shined through

the specimen (like the slide) and whatever part is is transmitted is projected onto a phosphor screen to yield an image from where the morphology can be extracted. A crystalline material interacts with the electron beam mostly by diffraction rather than absorption, although the intensity of the transmitted beam is still affected by the volume and density of the material through which it passes. The intensity of the diffraction depends on the orientation of the planes of atoms in a crystal relative to the electron beam. At certain angles the electron beam is diffracted strongly, sending electrons away from the axis of the incoming beam, while at other angles the beam is largely transmitted. A high contrast image can therefore be formed by blocking electrons deflected away from the optical axis of the microscope and by placing the aperture to allow only unscattered electrons through. This produces a variation in the electron intensity that reveals information on the crystal structure, and can be viewed on a fluorescent screen, or recorded on photographic film or captured electronically. More technical details of typical TEMs and their application can be found in Ref. [107].

The morphology of DMIMs and of the FeCo nanoparticle in hexane was investigated by transmission electron microscopy performed on a Philips CM 12 (in collaboration with Dr. M. Spasova, Experimentalphysik, Universität Duisburg-Essen). The microscope has the following specifications:

Electron gun = LaB_6 rods

Electron energy = 120 keV

Condenser (focusing) system = twin lens arrangement

Point resolution = 0.25 nm

Magnification range = 2650 – 660,000 ´

The TEM is attached with an energy-dispersive X-ray (EDX) Si detector (Oxford). The technique is based on the detection of characteristic X-ray peaks that are generated when an energetic electron beam interacts with the specimen. Since energy levels in all elements are different, element-specific, or characteristic, X-rays are generated. By comparing the relative intensities of X-ray peaks, the relative concentrations of each element in the specimen can easily be determined. Elements with an atomic number less than that of carbon ($Z = 5$) are generally not detectable.

3.4. Resistance and magnetoresistance

Current-in-plane (CIP) resistance measurements were performed in order to structurally characterize the DMIM samples or, in other words, to find out at which nominal thickness the samples become physically and laterally percolated. CIP resistance measurements were made using in line two-probe or four-probe contacts. In the beginning gold contacts were evaporated on the top Al_2O_3 layer using a homemade mask where the contacts were separated by 4.35 mm. After that the two-probe contacts were made on these gold deposited points and on one electrode current was injected and on the other the voltage drop was measured. In this way the resistance was measured. The electrical resistance R was measured in CIP geometry for different samples with varying nominal thickness (1.3nm $< t_n <$ 1.8 nm), and in a temperature range 10–300 K. For measuring the magnetoresistance a magnetic field of (0–1 T) was applied parallel to the current direction.

The resistance measurements were performed in co-operation with Mr. Frank Stromberg, at Universität Duisburg-Essen.

3.5. Ferromagnetic resonance

FMR is a unique tool for the study of magnetic anisotropy of ultrathin films [108]. Different essential parameters which describe the magnetic properties of thin films such as magnetic anisotropy, magnetic moment, Curie temperature, magneto-elastic coupling coefficients and relaxation mechanisms of the magnetization can be measured by this powerful technique. In magnetic superlattices quantitative information on the sign and magnitude of the interlayer exchange coupling strength can be obtained. This technique has certain advantages like its high sensitivity such that FMR signals of 10^{10}–10^{14} magnetic moments (ferromagnetically ordered) can be measured in a few minutes and relaxation times of the magnetization on the order of 10^{-7}–10^{-10} s are accessible.

The principle of ferromagnetic resonance in ferromagnetic materials is similar to electron spin resonance [109] and is based on the transition between Zeeman components of the electronic level. The splitting at a given external magnetic field yields information on the magnetic moment of the ferromagnetic or paramagnetic entities (atoms or ions) involved in the resonance transitions. In the simplest case, the energy difference between a two-level system (S = $\pm$ ½) is given by

$$\Delta E = g m_B B_0 \qquad\qquad (3.5)$$

where g is the Landé g-factor (also called the spectroscopic splitting factor), B_0 is the externally applied magnetic field and m_B is the Bohr magneton. In Fig. 3.4(a) the Zeeman splitting is illustrated. In a magnetic resonance experiment, the total magnetization of a sample precesses around the direction of the local magnetic field $B_{eff} = m_0 H_{eff}$ at the Larmor frequency. The energy of a weak transverse microwave rf (radio frequency) field is absorbed when the rf frequency coincides with the precession frequency. In FMR the local magnetic field can be shifted upto Teslas from the value of the externally applied field. The motion of the magnetization vector around its equilibrium position (the direction of an effective static magnetic field) is described by the Landau–Lifshitz–Gilbert equation of motion [110]

$$\frac{d\vec{M}}{dt} = -g\left(\vec{M} \times \vec{B}_{eff}\right) + \frac{a}{M}\left(\vec{M} \times \frac{d\vec{M}}{dt}\right), \tag{3.6}$$

where $M = M(T,H)$ denotes the temperature and field dependent magnetization, a is the dimensionless damping parameter, g is the gyro-magnetic ratio defined as $g = g\,m_B/\hbar$ and B_{eff} is the effective magnetic field which includes (i) the external magnetic field, (ii) the rf magnetic field of frequency n, and (iii) the anisotropy field. The second term on the right hand side of Eq. 3.6 denotes the relaxation of the magnetization towards the direction of the magnetic field B_{eff}. Thus the linewidth of the resonance signal can be modeled [111, 112, 29, 113].

Usually, the equation of motion is expressed in terms of the total free energy density F, instead of effective fields [114, 111]

$$dF = \vec{B}_{eff} \cdot d\vec{M} \tag{3.7}$$

where F is the free energy density and can be expressed as

$$F = F_{Zee} + F_{dem} + F_{anis} + F_{ex} \tag{3.8}$$

where F_{Zee} is the Zeemann energy contribution due to external magnetic field, F_{dem} is the demagnetizing energy of the sample, F_{anis} is the crystallographic magnetic anisotropy energy which depends on the crystalline structure of the sample and F_{ex} is the exchange energy. The minimum of the free-energy density determines the easy axis of magnetization. For example, in a thin film with tetragonal symmetry and an additional in-plane uniaxial anisotropy $K_{2||}$, the free energy density per unit volume has the expression [111]

$$F = -MB\left[\sin\boldsymbol{q}\sin\boldsymbol{q}_B\cos(\boldsymbol{f}-\boldsymbol{f}_B)+\cos\boldsymbol{q}\cos\boldsymbol{q}_B\right]-\left(\frac{\boldsymbol{m}_0}{2}M^2-K_{2\perp}-K_4\right)\sin^2\boldsymbol{q}$$

$$-\frac{K_4}{8}(7+\cos4\boldsymbol{f})\sin^2\boldsymbol{q}+K_{2\parallel}\sin^2\boldsymbol{q}\cos^2(\boldsymbol{f}-\boldsymbol{d}),\qquad(3.9)$$

where $\boldsymbol{d}$ is the angle between the easy axis of the twofold in-plane anisotropy with respect to the easy axis of the fourfold anisotropy, $\boldsymbol{f}_B(\boldsymbol{q}_B)$ is the azimuthal (polar) angle of the
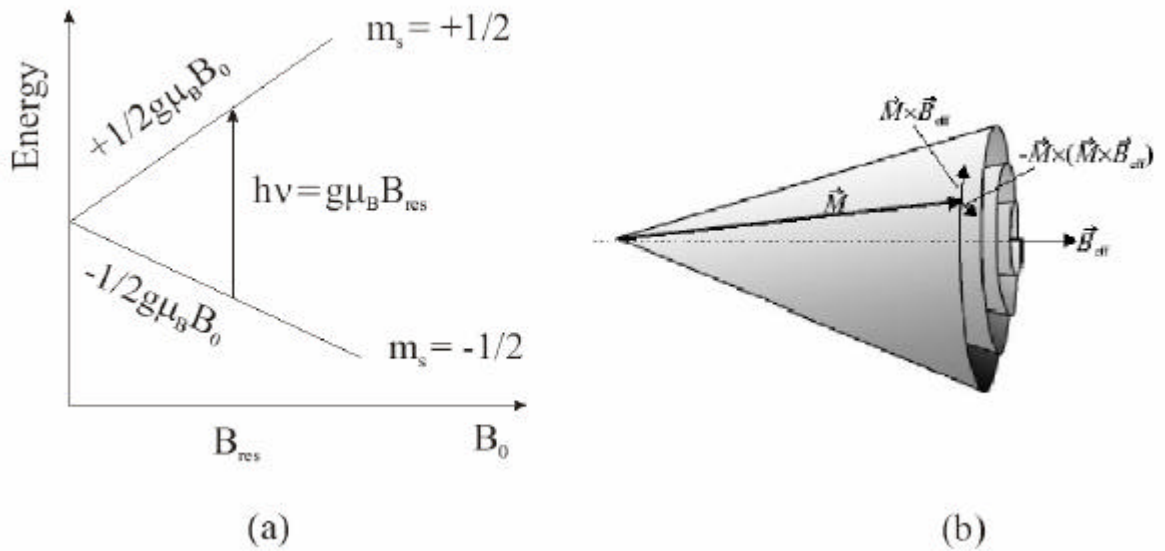
Figure 3.4: Principles of an FMR experiment of a two-level system (a). In an external magnetic field B_0, the electron from the lower energy level will be excited into the upper one by absorbing, radiation quanta $h\boldsymbol{n}_0 = E_2 - E_1 = g\,\boldsymbol{m}_B\,B_{res}$. Precession of the magnetization around the effective field axis is shown in (b). The Landau-Lifshitz-Gilbert equation describes both the precession around and the relaxation towards the effective field axis.

external field B, with respect to $[001]\left(\left[1\bar{1}0\right]\right)$-direction, $\boldsymbol{f}\,(\boldsymbol{q})$ are the azimuthal (polar)

angle of magnetization with respect to $[001]\left(\left[1\bar{1}0\right]\right)$-direction. $K_{2\perp}$ and $K_{2\parallel}$ are the

perpendicular and in-plane uniaxial anisotropy energy densities and K_4 is the cubic one. Considering the equilibrium condition of the magnetization under a steady field and

neglecting magnetic damping effects, the resonance condition for the out-of-plane geometry when the external field is varied from the film normal $[001]$ to the $[1\bar{1}0]$-direction is given by the following equation: [115]

$$
\left(\frac{w}{g}\right)^2 = \left\{ \; B_{res}\frac{\cos\left(q_B - q_{eq}\right)}{\sin q_{eq}} + \left(M_{eff} - \frac{2K_4}{M}\right)\times\frac{\cos 2q_{eq}}{\sin q_{eq}} \right.
$$
$$
\left. + \frac{K_4}{M}\left[3\sin^3 q_{eq} - 9\sin q_{eq}\cos^2 q_{eq}\right] \right.
$$
$$
\left. -2\frac{K_{2\parallel}}{M}\times\frac{\cos 2q_{eq}}{\sin q_{eq}}\cos\left(\frac{p}{4} - d\right) \right\}
$$
$$
\times\left\{ \; B_{res\perp}\sin q_B - 2\frac{K_4}{M}\sin^3 q_{eq} + \frac{2K_{2\parallel}}{M}\sin q_{eq}\sin 2d \; \right\}
$$
$$
-\left[\frac{2K_{2\parallel}}{M}\cos q_{eq}\cos 2d\right]^2 . \tag{3.10}
$$

Here $M_{eff} = \frac{2K_{2\perp}}{M} - m_0 M$ denotes the effective out-of-plane anisotropy field and $\Delta q = q_{eq} - q_B$. For $M_{eff} < 0\ (> 0)$, the easy axis of the system lies in (normal to) the film plane. The resonance condition for the in-plane configuration and $q_B = \frac{p}{2}$ becomes [115]

$$
\left(\frac{w}{g}\right)^2 = \left(B_{res\parallel}\cos\Delta f + \frac{2K_4}{M}\cos 4f_{eq} + \frac{2K_{2\parallel}}{M}\cos 2\left(f_{eq} - d\right) \right)
$$
$$
\times\left(B_{res\parallel}\cos\Delta f_{eq} - M_{eff} - \frac{2K_4}{M} + \frac{K_4}{2M}\left[7 + \cos 4f_{eq}\right] + \frac{2K_{2\parallel}}{M}\cos^2\left(f_{eq} - d\right) \right), \tag{3.11}
$$

where $\Delta f = f_{eq} - f_B$, B_{res} is the resonance field, and $f_{eq}\left(q_{eq}\right)$ is the azimuthal (polar) equilibrium angle of the magnetization with respect to the film normal ($[001]$-direction) which is determined by the minimum of the free energy density (Eq. 3.9).

The FMR measurements were done together with Dr. Jürgen Lindner and Mrs. Anastassia Trounova in the group of Prof. M. Farle at the University Duisburg-Essen. The measurements were done at different temperatures, in a wide range of microwave frequencies with an externally applied magnetic field. The experimental setup is described

in Ref. [116]. Within this setup waveguide systems were mounted allowing an external field orientation in the plane of the sample (parallel configuration) or perpendicular to the sample plane (normal configuration) at different frequencies. From the derivative of the absorptive part of the complex rf susceptibility as a function of the applied magnetic field at a constant microwave frequency, the resonance fields (the zero crossing of the absorption derivative) can be derived. The resonance field of a ferromagnetic sample is shifted from its paramagnetic value by its intrinsic anisotropy fields resulting from different anisotropies. Thus a precise determination of the easy axis of the magnetization is possible.

3.6. Superconducting Quantum Interference Device (SQUID) Magnetometry

Magnetometers based on the SQUID technology are presently the most sensitive instruments to measure magnetic moments of liquid or solid state samples. State of the art systems are capable of measuring magnetic moments in the order of 10^{-7} emu (10^{-10} Am^2) and even below. Essentially two modes of operation exist. First, as a magnetometer, it measures the static magnetic moment, m, at various applied fields, H, and temperatures, T. When normalized to the volume of the sample one obtains the average magnetization, M. Second, as an *ac* susceptometer additionally a small alternating magnetic field is applied and the time dependent response, $m(t)$, is recorded. From these data one can then extract the complex *ac* susceptibility, $c(f) = c' - ic''$, at an *ac* frequency, f. SQUID magnetometers are used in various fields of research such as in the study of superconductors, biological materials, thin magnetic films, magnetic nanostructures, magnetic fluids and geological materials.

The operating principles of SQUIDs is based on the phenomenon of Josephson junction, a device based on a Nobel prize winning tunneling effect proposed in theory by B. D. Josephson in 1962 and observed experimentally in 1964 by Anderson and Rowell. A SQUID device consists of a closed superconducting loop including one or two Josephson junctions in the loop's current path.

The superconducting state, first observed in mercury by Heike Kamerlingh-Onnes in 1911, is a phase in a material for which, below some critical temperature T_c, the electrical resistance of that material falls abruptly to zero. Many metals exhibit this phase change at various temperatures ranging from less than 1 K for zinc to about 23 K for an alloy of niobium and germanium (Nb_3Ge). Beyond the niobium compounds there is a new

class of ceramic materials- an example being the yitrium barium copper oxides (YBCO), which are known as high T_c superconducting materials. They are now quite common in the construction of supermagnetic magnets.

The system used in our laboratory is a SQUID magnetometer manufactured by Quantum Design (MPMS 5S) [117]. The MPMS system includes several different superconducting components:

- a superconducting **magnet** to generate large magnetic fields,

- a superconducting **detection coil** which couples inductively to the sample,

- a **S**uperconducting **QU**antum **I**nterference **D**evice (**SQUID**) connected to the detection coil,

- a superconducting **magnet shield** surrounding the SQUID.

3.6.1. Principle of SQUID operation

The SQUID magnetometer measures the longitudinal magnetic moment of a sample, *i.e.* along the direction of the applied magnetic field. In the regular configuration of the MPMS 5S system the magnetic field can be set in the range $-5 \leq m_0 H \leq 5$ T using a superconducting solenoid and in the range $-0.45 \leq m_0 H \leq 0.45$ mT using a small copper coil with much higher resolution. The homogeneity of the field decreases with increasing distance from the center of the coil. The temperature at the sample location can be set in the range $2 \leq T \leq 400$ K and the temperature stability of the magnetometer is better than 50 mK. For measurements at higher temperatures it is necessary to install an oven, which is available from Quantum Design (QD-M102) and extends the range to 800 K. The diameter of the cylindrical sample space is nominally 9 mm. However, when the oven is in place, the diameter of the sample space is severely reduced to 3.5 mm [118]. The atmosphere in both the regular and the oven configuration is low-pressure helium gas.

The sample space is located within a superconducting detection coil ("pick-up" coil). It is a single piece of superconducting wire wound in a set of three coils configured as a second order (second-derivative) gradiometer as shown in Fig. 3.5. The upper coil is a single turn wound clockwise, the center coil comprises two turns wound counter-clockwise, and the bottom coil is again a single turn wound clockwise. In this configuration the pick-up coil is only sensitive to the magnetic stray fields of the sample, whereas homogeneous contributions from any external fields are canceled out. Centered

around the pick-up coil is the superconducting magnet capable of producing a uniform
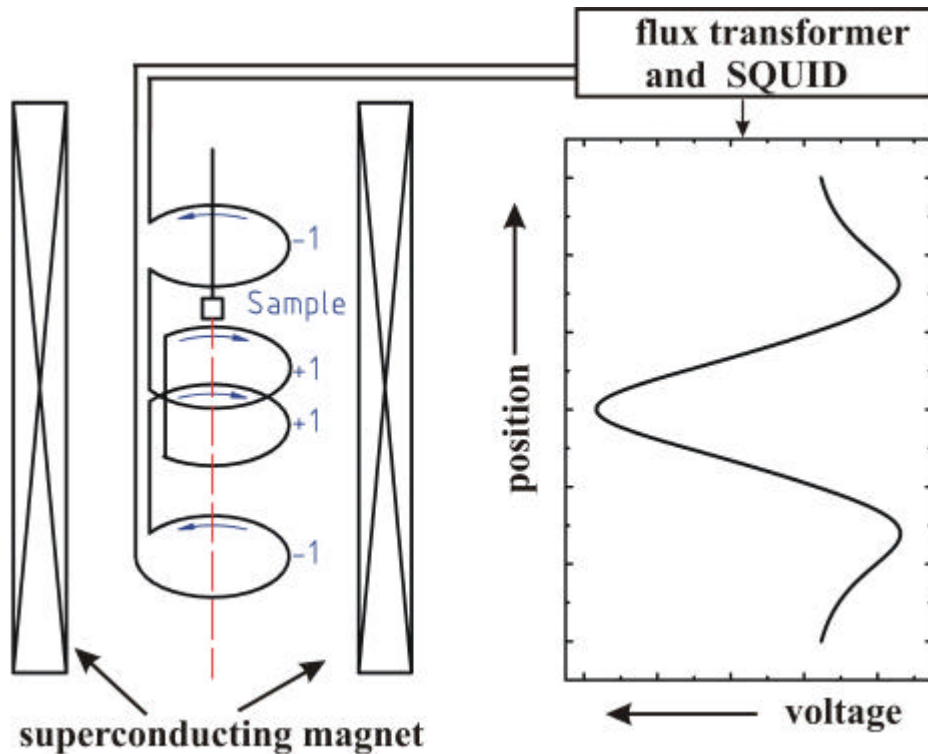constant magnetic field over the entire coil region. The sample is suspended from a rod

Figure 3.5: Pick-up-coil geometry and theoretical response signal of an ideal dipole
vs. scan length in a MPMS SQUID magnetometer.

mounted at the top of the cryostat to a transport mechanism. As the sample is moved
vertically through the detection coil, the magnetic moment of the sample induces an
electric current in the detection coils. Since the detection coil, the connecting wires, and
the SQUID input coil form a closed superconducting loop, any change of magnetic flux in
the detection coil produces a change in the persistent current in the detection circuit, which
is proportional to the change in magnetic flux. Since the SQUID acts as a highly linear
current-to-voltage converter, the variations in the current in the detection coil produce
corresponding variations in the SQUID output voltage. Eventually, the output signal, V, is
recorded as a function of scan length, z. A curve-fitting algorithm of the MPMS software
fits the measured $V(z)$ data points to the theoretical curve of an ideal dipole and thus
extracts the magnetic moment, m [119].

Fig. 3.5 shows the voltage signal produced by an ideal dipole as a function of the
scan length, $V(z)$. It is worth mentioning that the detector coil configuration is sensitive

only to point-like flux discontinuities as a sample is scanned. Samples or sample holders being magnetically homogeneous beyond the length of the detector coil, *i.e.* > 3 cm, do not contribute to the measured voltage response. Consequently, in order to obtain accurate results, it is necessary to use specimens of vertical length less than 5 mm [119, 120].

3.6.2. AC Susceptibility

Magnetic *ac* measurements, in which an *ac* field is applied to a sample and the resulting *ac* moment is measured, are an important tool for characterizing magnetic materials. Since the induced moment is time-dependent, *ac* measurements yield information about magnetization dynamics which are not obtained in *dc* measurements, where the sample moment is constant during the measurement time.

A standard measurement of the *ac* susceptibility of a sample is a two-point measurement. The first part of the measurement nulls all *ac* signals, including the sample signal and the signal generated by the *ac* field coupling to the gradiometer imbalance. The second part of the measurement uses the sample signal, which the nulling waveform now increases by three-fold, to determine the sample´s *ac* susceptibility. Details of the *ac* susceptibility measurement procedures can be found in Ref. [121].

3.6.3. Sample holder for high temperature oven option for MPMS system

For our high temperature measurements in the range of 300K < *T* < 700 K, we have used the oven option (Part Nr. QD 1027-100A) for our MPMS system. For this temperature range a special sample holder design is required. We have designed and constructed a simple sample holder, which is suitable to be used in virtually any magnetometer of similar geometry [122]. However, it is specifically designed for the Quantum Design oven option as described in the following.

A sample holder being suitable for magnetic measurements at elevated temperatures has to fulfil essentially three criteria. (i) It must be mechanically and thermally stable up to 800 K. (ii) The magnetic background signal of the empty sample holder has to be minimal, and (iii) in our particular case the outer diameter has to be less than 3.2 mm in order to fit into the oven [123]. All three criteria are well met by our sample holder design as shown in Fig. 3.6. The main part, denoted as "QR" (quartz rod), is fabricated from fused silica (quartz glass) with a length of 150 mm and a diameter of 3 mm. Quartz glass exhibits an extremely small linear thermal expansion coefficient,

$a = 4.5 \cdot 10^{-7} \deg^{-1}$ (at 295 K), a relatively small magnetic susceptibility, $c = -1.25 \cdot 10^{-5}$ [124] and a sufficiently high transformation temperature, $T_g = 1353$ K [124].
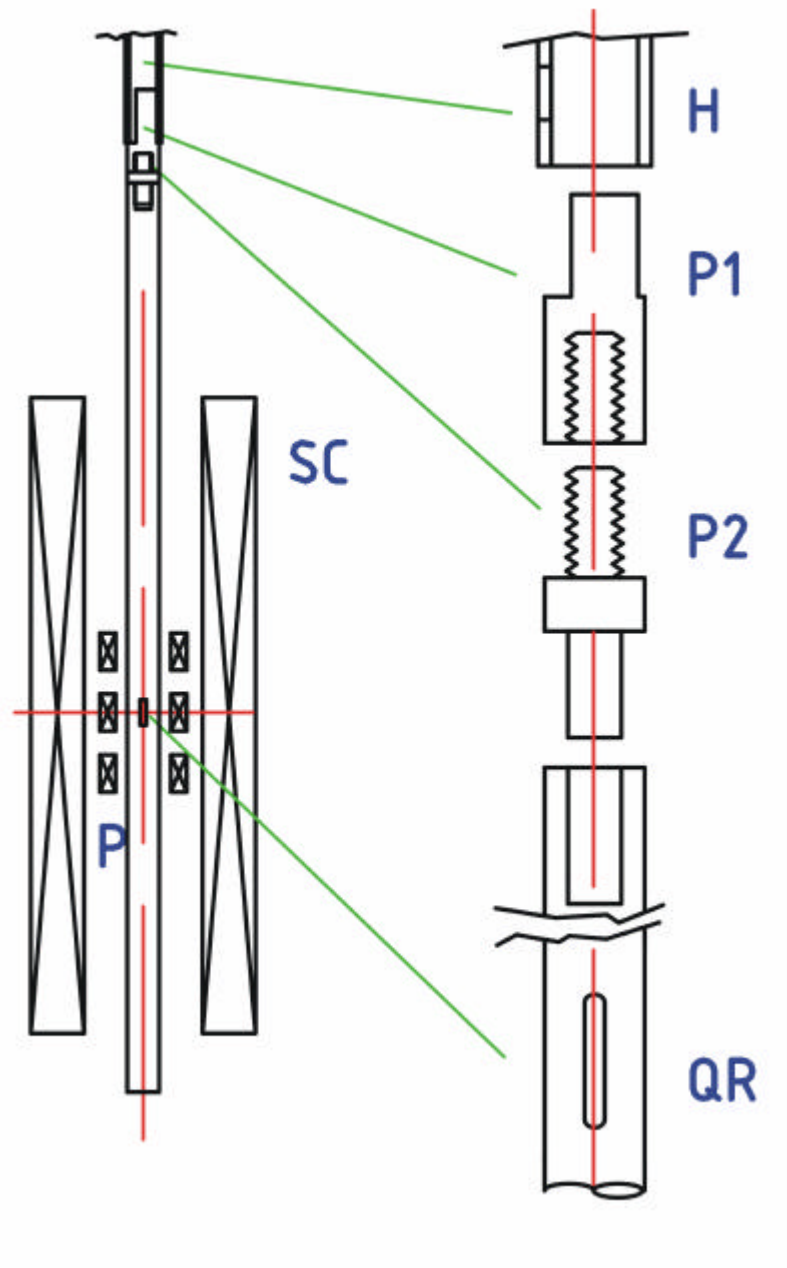

Figure 3.6: Schematic sample holder design. A cross-sectional view of the sample holder (P1−P2−QR) together with the regular sample rod (H) between the pick-up coils (P) and the superconducting coils (SC) is shown on the left hand side. The individual parts of the sample holder, *i.e.* the brass parts, P1 and P2, and the quartz rod, QR, are presented on the right hand side [122].

The sample is inserted into a rectangular slit at a distance of 104 mm (46 mm) from the top (bottom) of the quartz glass rod. This minimizes the influence of the magnetic stray fields

from the two ends of the rod on the measurement. The slit has a height of 5 mm and a width of 0.8 mm, where samples approximately of size $4.5 \times 3.0 \times 0.5$ mm^3 fit. Any horizontal movement of the sample is prevented by the walls of the sample space, which leave only a small gap of 0.25 mm to the quartz rod. Consequently, for exactly fitting samples no glue is required. In this case, the only magnetic contribution from the sample holder is due to the magnetic moment of the missing diamagnetic quartz material in the hole. This slit geometry is specifically designed for thin film samples, where the in-plane component of the magnetization has to be measured. However, there is virtually no other constraint than the space limitations for other geometries, *e.g.* a horizontal slit for measurements of the polar magnetization component.

The quartz rod (QR) is fixed to the regular metal sample holder tube (H) using two brass parts, P1 and P2 (Fig. 3.6) fitted together by threads. Part P1 is permanently glued with its cylindrical shaft to H. The shaft is reduced on one side in order to ensure gas pressure equilibration with the inside of H through a small vent hole at the lower end of H. Part P2 is glued to QR, with a cylindrical shaft fitting exactly into a cylindrical hole at the top of QR. P2 can then be connected to P1 by a thread [122]. This construction ensures easy mounting and de-mounting of the sample holder. For the glue connections we used high-temperature glue "DK-27NF" [125] for the temperature working range $250 \leq T \leq 800$ K. Prior to usage, the glued parts H-P1 and P2-QR were baked out at 700 K with a slow gradual increase of the temperature over several days. The rectangular and the cylindrical holes in QR were fabricated by the company QGT [126] using a CO_2 Laser.

In order to test the magnetic signal of the sample holder, measurements on a DMIM sample $[Co_{80}Fe_{20}(1.6nm)/Al_2O_3(3nm)]_9$ were performed. Fig. 3.7 shows measurements of the magnetic moment, *m vs.* applied field, m_0H, at temperatures $T = 300, 500,$ and 700 K of the empty sample holder (open symbols) and together with the sample (solid symbols). At 300 K the empty sample holder shows a relatively weak moment $< 10^{-8}$ Am^2 (10^{-5} emu) varying linearly with the field and a positive slope resembling a paramagnetic signal. This is due to the fact that the quartz rod itself is diamagnetic. Consequently, the slit will produce an inverted diamagnetic signal. However, the calculated magnetic moment of the slit at $m_0H = 10$ mT and $T \approx 300$ K, using the values above, yields $1.2 \cdot 10^{-9}$ Am^2. The discrepancy to the measured moment of the sample holder, $m \approx 1.3 \cdot 10^{-8}$ Am^2, can be explained by additional paramagnetic impurities on the slit edges. With increasing temperature one observes a systematic downshift of both the background moment and the

hysteresis loop of the sample. Moreover, the slope of the background curve also changes. We exclude any effects of the sample and rather assume an artifact due to incompletely compensated inhomogeneous stray fields of the oven heater wires [127].
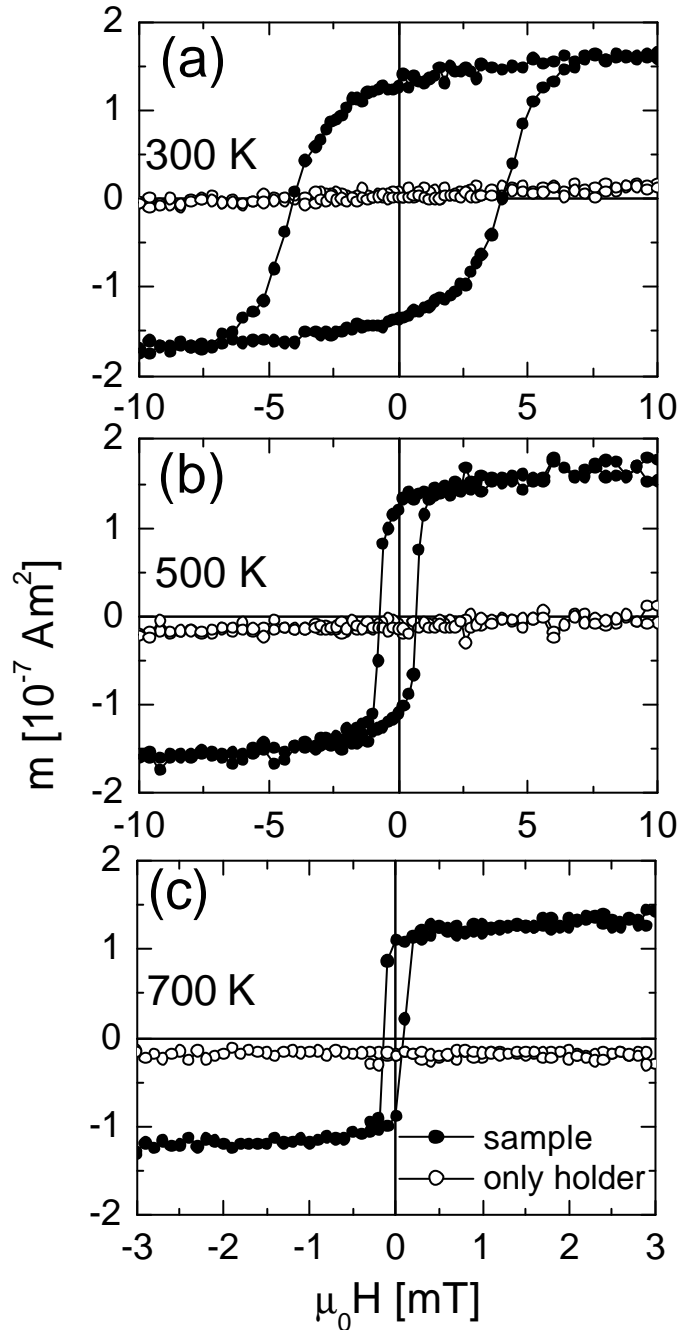

Figure 3.7: Magnetic moment, *m* vs. *μ_0H*, at *T* = 300 (a), 500 (b) and 700 K (c) of the sample holder without (open circles) and with a [$Co_{80}Fe_{20}$(1.6nm)/Al_2O_3(3nm)]$_9$ sample (solid symbols) after correction of the holder contribution.

Obviously, measurements up to 700 K are possible without reduction of the signal quality. Several series of temperature cycles heating up to 700 K and cooling down to 300 K were carried out with no apparent destruction or aging of the components.

3.7. Polarized Neutron Reflectometry

3.7.1. Fundamental Properties of the Neutron

The neutron was discovered by James Chadwick when analyzing the following nuclear reaction

$$_4^9Be + _2^4He \rightarrow _6^{12}C + _0^1n$$
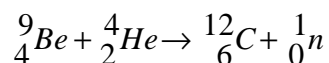
where $_0^1n$ represents the neutron [128]. Neutrons have distinct particle properties, which influence the experimental scattering results. They have nearly no electrical properties: "no" electrical charge, "no" electrical dipole momentum. Neutrons mainly obey nuclear interaction. However, their magnetic moment couples to the local magnetic field of magnetic atoms and ions. Neutrons also exhibit weak interaction which is responsible for the neutron decay.

Neutron scattering is a useful source of information about the positions, motions, and magnetic properties of solids. Due to the following properties neutrons are widely used in science

- Neutrons are **neutral** particles. Therefore they
(i)   are highly penetrating.
(ii)   can be used as nondestructive probes, and
(iii)   can be used to study samples in different environments.

- Neutrons have a **spin**. Therefore they can be
(i)   formed into polarized neutron beams,
(ii)   used to study nuclear (atomic) orientation, and
(iii)   used for coherent and incoherent scattering.

- Neutrons have a **magnetic** moment. So they can be used to
(i)   study microscopic magnetic structure, and
(ii)   study magnetic fluctuations,

- The **energies** of thermal neutrons are similar to the energies of elementary excitations in solids. Therefore, they can be used to study
(i)   molecular vibrations,
(ii)   lattice modes,

(iii)   dynamics of atomic motion and

(iv)   spin waves.

•   The **wavelengths** of neutrons are similar to atomic spacings. They can determine

(i)   crystal structures and atomic spacings,

(ii)   structural information from 10^{-15} to 10^{-6} m, and

•   Neutrons interact with **nuclei**. So they

(i)   can explain isotopic substitution, and

(ii)   can use contrast variation to differentiate complex molecular structures for example

          hydrogen (H)/ deuterium (D) substitution.

Table 3.1: Neutron properties

Mass	$m = 1.675\times10^{-27}$ kg
Spin	$s = 1/2$
Magnetic moment	$\mu_n = -9.5\times10^{-27}$ JT^{-1}
β-decay lifetime	$t = 885.9 \pm 0.9$ s
Confinement radius	$R = 0.7$ fm
Quark structure	udd

The neutron magnetic moment interacts with homogeneous fields B, according to the magnetic potential:

$$V_m = -m_n B,$$

where the minus sign reveals the antiparallel orientation between the spin and the magnetic field.

3.7.2. Polarized Neutron Reflectivity (PNR) from magnetic thin film

Neutrons can provide similar information as X-rays, but in addition give magnetic information. Neutrons have both nuclear and magnetic scattering amplitude. The nuclear amplitudes can be quite different even for adjacent elements (in contrast with the X-ray case), or even for different isotopes of a single element. Thus the contrast between layers may be considerably larger than for X-rays, or could be made larger by appropriate isotopic substitution (notably light with heavy hydrogen). Neutrons are also scattered by magnetic moments and the refractive index at a depth z from the surface is proportional to

the local magnetic induction $\mathbf{B}(z)$. The magnetic term in the refractive index [129] has a sign, which depends on the relative orientation of $\mathbf{B}$ with the neutron spin.
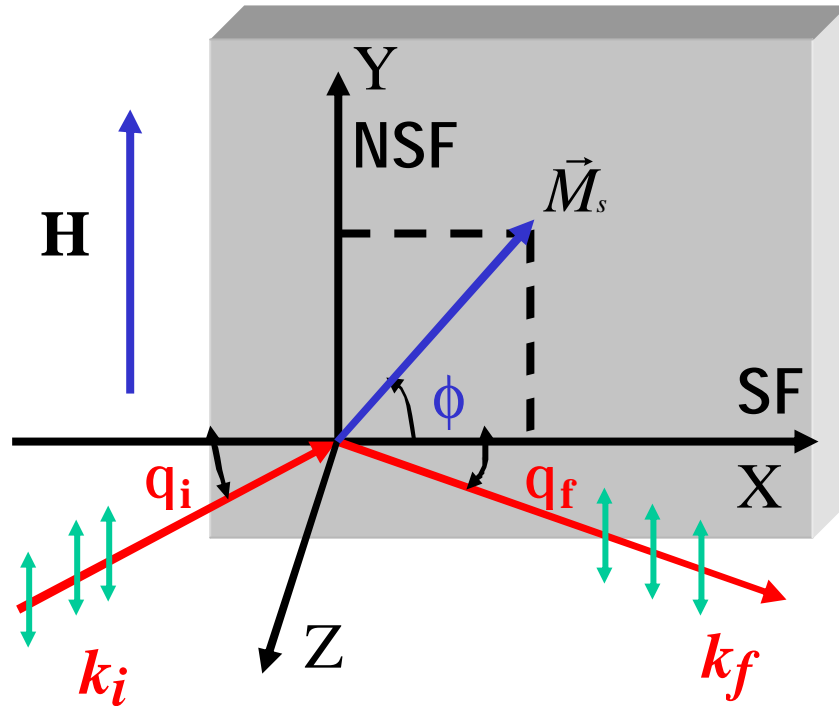

Figure 3.8: Schematic outline of the scattering geometry for spin polarized neutron reflectivity using a continuous and monochromatic neutron beam. The Y-axis is the quantization axis for the neutrons and the non-spin-flip axis and the X-direction is the spin-flip axis.

In PNR the partially reflected neutron intensity is measured, most simply, as a function of the incident spin state and incident wave vector as shown schematically in Fig. 3.8 with the incident and final wave vectors k_i and k_f, respectively, and the scattering vector $Q = k_i - k_f = (4\pi \sin(\phi)/\lambda)\,\hat{z}$ pointing normal to the film plane in the Z-direction, where λ is the neutron wavelength and $\hat{z}$ is a unit vector along the Z-direction. The incident wave vector k_i is varied either by rotating the sample with fixed incident wavelength $\mathbf{l}_i$ or by employing a time of flight method with a fixed incident angle $\mathbf{q}$ [130].

For maximum interaction of the neutron magnetic moment $\mathbf{m}_n$ with the sample magnetization $\mathbf{m}_i$ in the ith layer of a stratified medium, or, more precisely, with the magnetic induction $\mathbf{B}_i$ on the sample it is advantageous to orient the polarization of the incident neutron beam parallel to the film plane.

After reflection from a supermirror in the incident beam (not shown in the above figure), the neutrons are polarized parallel to the Y-direction in the spin-up state (+). By activating a *p*-flipper in front of the sample, a spin-down state is activated. A second *p*-flipper after the sample verifies whether or not the neutron spin has been flipped during the reflectivity process, together with a supermirror in the exit beam acting as a spin up filter. Therefore, if both flippers are deactivated, the non-spin-flip (NSF) scattering cross-section for the (+,+) states is measured; alternatively, if both are activated the NSF (-,-) cross section, and if one flipper is on and the other off the spin-flip (SF) cross-sections (+,-) and (-,+) are measured.

An ideally reflecting (ferromagnetic) medium can be represented by a one-dimensional (1D) optical potential $V(z)$ where the direction normal to the surface of the film defines the Z axis. A multilayer can be described by a sequence of layers (i.e. a stratified medium) each with a constant interaction potential [131, 132]. For the ith layer, the in-plane spatially averaged optical potential $V_{eff, i}$, may be approximated by

$$V_{eff, i} = V_{n, i} \pm V_{m,i}, \tag{3.12}$$

where V_n, V_m are the usual neutron-nuclear pseudo-potential and magnetic neutron-sample interaction, respectively, and the $\pm$ sign refers to the spin-up and spin-down states of the incident neutrons. V_n is given by

$$V_{n, i} = \frac{2p\hbar^2}{m_n} r_i b_i, \tag{3.13}$$

where m_n is the neutron mass, r_i is the atomic density, b_i is the bound coherent neutron scattering length of the material. The magnetic neutron-sample interaction V_m for the ith layer is given by

$$V_{m, i} = -\mathbf{m_n} \times \mathbf{B_i} \tag{3.14}$$

where m_n is the neutron mass, $\mathbf{m_n}$ is the neutron magnetic moment, $\mathbf{B_i}$ is the total magnetic induction in the medium and the suffix i labels the medium. $\mathbf{B_i}$ arises from the magnetically aligned atomic moments. In this description each ferromagnetic layer (medium) is assumed to be uniformly magnetized with the spins in-plane and held parallel to the Y-direction by the external magnetic field. Therefore Eq. 3.12 can be written as

$$V_{eff, i} = \frac{2p\hbar^2}{m_n} r_i b_i - \mu_n \cdot B_i \tag{3.15}$$

The case of nonaligned spins is described below [130, 133, 134, 135]. Nonmagnetic media have no magnetic term. Assuming that the X-component of the wave vector is

conserved, the perpendicular wave vector component (i.e., along the Z-direction) of the neutron is given for the jth medium by

$$q_j = \sqrt{q_i^2 + q_{ci}^2 - q_{cj}^2}$$ (3.16)

and with the critical wave vector q_{cj} for the jth medium given by

$$q_{cj}^2 = \frac{2m_n}{\hbar^2} V_i .$$ (3.17)

Total reflection therefore occurs for $q_i^2 < q_{cj}^2 - q_{ci}^2 = k^2 \sin^2 \boldsymbol{q}_{cij}$, where $\boldsymbol{q}_{cij}$ is the critical angle for the i,j interface [132].

The neutron plane waves for the (+) or (-) states are solutions of the one-dimensional Schrödinger equation

$$\begin{pmatrix} \partial_z^2 + a_1 & b \\ b & \partial_z^2 + a_2 \end{pmatrix} \begin{pmatrix} \psi_+ \\ \psi_- \end{pmatrix} = 0 ,$$ (3.18)

where

$$a_{1,2} = \frac{1}{4} Q^2 - 4\pi N (b_i \pm p_i \sin(\boldsymbol{q}_i))$$ (3.19)

and $$\boldsymbol{b} = 4\pi N p_i \cos(\boldsymbol{q}_i).$$ (3.20)

Here Q is the magnitude of the scattering vector, N is the atomic or nuclear number density, b_i is the nuclear coherent scattering amplitude including imaginary parts from absorption, and p_i is the magnetic scattering amplitude $p_i = (2.695 \times 10^{-4} \text{nm}/\boldsymbol{m}_B) |\boldsymbol{m}|$ in the ith layer, where $\boldsymbol{m}_B$ is the Bohr magneton. The diagonal matrix elements describe the NSF scattering, the off-diagonal elements the SF scattering. The plane wave functions $\boldsymbol{\psi}_+$ and $\boldsymbol{\psi}_-$, which are solutions of the Schrödinger equation (3.18) for the optical potential Eq. (3.15) for the ith medium, is given by the sum of a forward (amplitude A_i) and backward traveling (amplitude B_i) wave. Applying the boundary condition that the wave function and its derivative is conserved at each interface permits the reflection and transmission coefficients $r_{12.....N}$, $t_{12.....N}$ to be calculated by the Parratt recursion formalism, from a multilayer system composed of media 1.......N as indicated by the subscripts. Using a matrix method, these coefficients have been calculated in Ref. [133, 134, 135]. Straightforward approach in multilayer optics can be followed in which the amplitude of successively reflected beams is added in a geometric series [136].

For the case of non-collinear structures, a four component vector for the neutron wave within each medium of the form $(A_i^+, B_i^+ A_i^-, B_i^-)$ where the superscripts refer to the

spin-component with respect to the applied magnetic field, can be used to explain the (+) and (-) reflectivities. In this case of non-spin aligned layers both the reflectivities are dependent on both of the in-plane components of the magnetization vector as described by a reflectivity matrix. Thus in this case the flipping ratio $F = R^+/R^-$ versus wave vector curve is changed dramatically depending on the spin configuration in the multilayer. Therefore in PNR the layer selectivity results from the spatial variation of the wave within the solid. This is distinct from the case of diffraction, which occurs at higher wave vector, where the Fourier component of the spin configuration is probed [137, 138, 139]. From the above discussions it is clear that in a multilayer film, PNR is able to determine the orientation of each layers.

From above it is seen that only the *Y*-component of the sample magnetization contributes to the change of the effective potential the neutron experiences in the sample. The *X*-component of the magnetization vector, although not changing the potential, causes a perturbation of the polarization, which may flip the neutron spin from the (+) to the (-) state or vice-versa over some optical path length. So, in short, the *Y*-axis is the NSF-axis, along which the potential is Zeeman split, while the *X*-axis is the SF-axis, which may flip the neutrons from one potential to the other. Spin-flip scattering is a purely magnetic property and does not interfere with the nuclear scattering.

Now let us briefly discuss how from a PNR experiment, one can extract the magnetization-vector profile of a multilayer system of known layer thickness and layer density, in which the magnetizations of individual magnetic layers need not be parallel [140]. By comparing the results of experiment with simulations, the magnetization vector in each layer can be determined, provided these vector magnetizations are the only unknown variables. The appropriate experimental procedure is as follows: PNR reflectivity should be initially measured for a given sample in an in-plane applied field greater than the saturation field. With the moment in each layer thus aligned, it is then possible to adjust the estimates of the values of layer thicknesses, layer densities, and layer moments to obtain the best fit to the measured reflectivity pattern. In subsequent measurements at lower applied fields, the moments in each layer will no longer be necessarily aligned, leading to different reflectivity pattern. The only remaining adjustable parameters in fitting this data are the directions of the magnetic moments in each layer, and by comparing reflectivity calculated for a range of angular orientations $\boldsymbol{f}_i$, the different reflectivity components can be fitted.

Just for an example, if we consider that the magnetization in the sample is completely parallel to the externally applied magnetic field i.e. $f = 0°$, then in the reflectivity patter there will not be any spin-flip scattering other than the flipping ratio between the different polarizations. It should be kept in mind that the non-spin-flip intensities (R^{++} and R^{--}) contains the structural and magnetic information, whereas the spin-flip intensities (R^{+-} and R^{-+} are degenerate) are purely of magnetic origin. Therefore, in this fully aligned spin structure the significant reflectivities are the NSF reflectivites. However, in this case there will be a strong intensity contrast between the NSF reflectivites because of the potential difference the up and down neutrons experience in the sample. This will be described in more detail in the section 4.3.2.1.3. In a reflectivity pattern the difference in scattering wave vectors between Bragg peaks gives the thickness of individual layers, and the difference between the small oscillations (Kiessig fringes) gives the total multilayer thickness. It should be noted that the magnetized state of the sample can be recognized by the splitting of the reflectivity edges since the refractive indices and therefore the critical scattering vector Q_c for the (+,+) and (-,-) states are different and given by

$$Q_c = \left[16 \boldsymbol{p} N \left(b \pm p \sin \boldsymbol{f}\right)\right]^{1/2},\qquad\qquad (3.21)$$

where b is the nuclear coherent scattering amplitude including imaginary parts from absorption, and p is the magnetic scattering amplitude. Therefore for a non-magnetic sample, the scattering vector turns out to be $Q_c = \left[16 \boldsymbol{p} N b\right]^{1/2}$. However, in a multilayer sample composed of magnetic and non-magnetic layers, for the superlattice Bragg peak the contrast is determined by the difference between $(b + p)$ and $(b - p)$ of the magnetic layer compared to b of the non-magnetic layer. This will also be discussed for the DMIMs in section 4.3.2.1.3.

As mentioned earlier, the NSF intensities depend on the nuclear potential and the magnetization component parallel to Y-direction (Fig. 3.8), and the SF intensities depend on the X-component of the magnetization. This can also be expressed as the difference of the two NSF components

$$R^{++} - R^{--} = R = 2p \sin \boldsymbol{f} = 2p_y \propto M_y,\qquad\qquad (3.22)$$

which is proportional to the y-component of the magnetization M_y, whereas the SF

intensities $R^{+-} = R^{-+}$ are degenerate and

$$R^{+-} + R^{-+} = r = 2p\cos \boldsymbol{f} \propto M_x^2 \qquad (3.23)$$

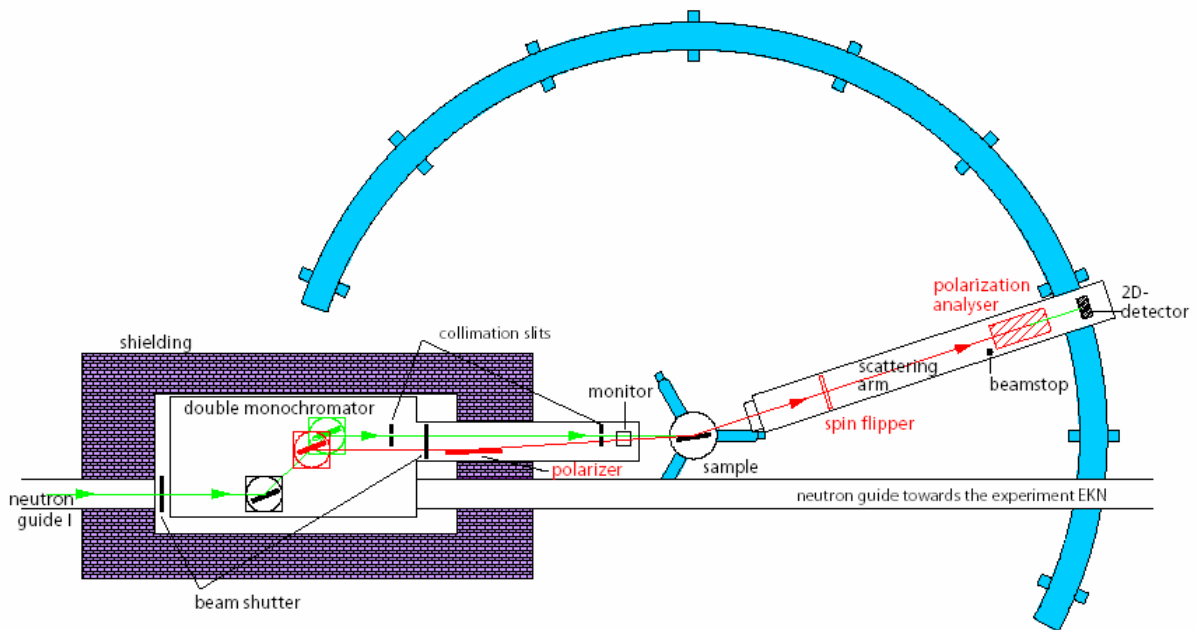is proportional to the square of the x-component M_x [141].

Figure 3.9: A schematic top view of the HADAS reflectometer. Spin polarization is achieved via a supermirror in the incident neutron beam, and the final polarization state is tested via a second supermirror in the exit beam (not shown here), $\boldsymbol{p}$-spin flippers before and after the sample allow to measure non-spin-flip and spin-flip reflectivities.

The PNR measurements were performed with the HADAS reflectometer at the Jülich research reactor FRJ-2 (DIDO) [142, 143]. The main feature of this instrument is that it permits a simultaneous polarization analyzer over the entire range of scattering angles $(q \leq 3°)$. A schematic top view of this instrument is shown in Fig. 3.9. With a specially constructed cryostat, the sample temperature during measurement can be varied between 4.2 and 350 K. Also a magnetic field can be applied using a pair of Helmholtz

coils. The field is homogeneous at the sample position and special care was taken to maintain the initial polarization of the neutron beam.

3.8. Photoemission electron microscopy (PEEM)

Imaging of the magnetic microstructure on a nanometer scale is an outstanding challenge. That is why various powerful imaging techniques have been established so far. Modern techniques to study both static and dynamic properties of magnetic domains with high spatial resolution down to several nanometers, such as Bitter pattern imaging, scanning electron microscopy with polarization analysis (SEMPA), Lorentz microscopy, magnetic force microscopy (MFM), spin-polarized low-energy electron microscopy (SPLEEM), electron holography and scanning Hall and SQUID microscopies are established. In view of the systems of interest, imaging techniques should meet high spatial resolution, high sensitivity combined with huge contrast, element selectivity and imaging in applied fields. X-ray microspctroscopy can yield much finer resolution than visible light imaging, even with low numerical aperture optics. Using the concept of X-ray magnetic circular dichroism (XMCD), which was first observed at the Fe K edge in 1987 [144], in the soft X-ray region two complementary real space imaging techniques have been realized. The first one is photoemission electron microscopy (PEEM) [145], offering surface sensitivity due to the limited escape depth of the secondary electrons of about 5 nm. The second one is transmission X-ray microscopy (TXM) [146], providing depth information of the volume up to about 15 nm [147], given by the limited penetration depth of soft X-rays in matter.

First of all let us discuss the principles of XMCD and how it can be used as a contrast mechanism to image magnetic domains. XMCD is a magneto-optical effect which relates the spectroscopic spectra measured in transmission or absorption geometries to the magnetic properties of a given material. XMCD can be defined as the dependence of the absorption of circularly polarized X-rays in ferro(i)magnets on the projection of the sample magnetization onto the helicity of the photons. It therefore changes sign by reversing either the sample magnetization or the helicity of the light. The physical origin of XMCD in the X-ray absorption is based on angular momentum conservation and spin−orbit interaction mainly of the initial states and the spin-splitting of the final states of the absorption process. If the energy of the absorbed photon equals the binding energy of a particular inner-core level (e.g $P_{3/2}$) the photoelectron is excited into an unoccupied state of d

symmetry above the Fermi level obeying dipolar selection rules. As the initial states are well-defined atomic inner-core levels, the XMCD effect is inherently element selective. According to the Pauli principle the photoelectron can be considered as a local probe for the spin and orbital polarization of the absorbing atom. Also following from Fermi´s Golden Rule, the transition probability of the absorption process is related to the density of the unoccupied states. Since for a ferromagnet the final density of states exhibits a spin
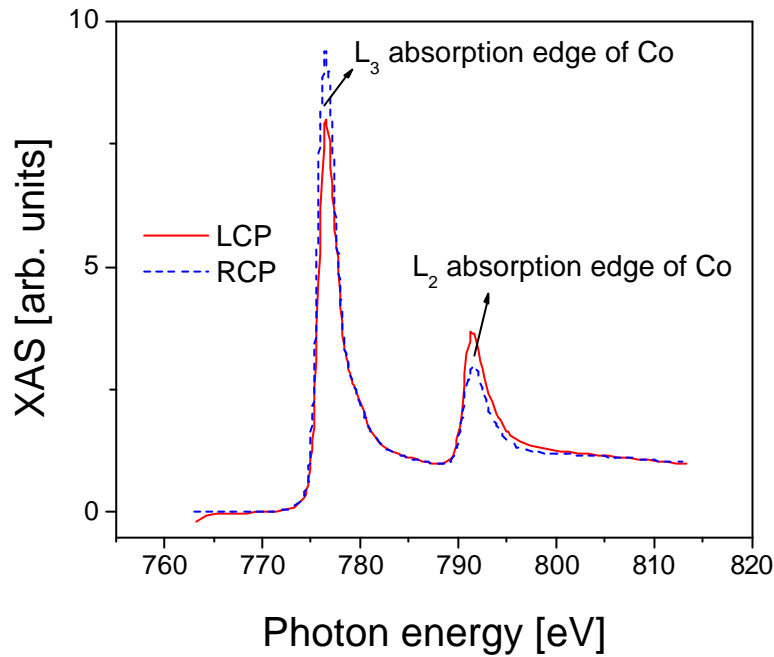
Figure 3.10: XMCD spectra for Co metal measured on a DMIM [$Co_{80}Fe_{20}$ (1.3 nm)/Al_2O_3 (3nm)]$_{10}$ at room temperature.

polarization due to the exchange interaction, the transition probability of the absorption process depends on the polarization of the final states. Therefore the XMCD signal is directly proportional to the magnetic moment of the absorbing atom. This makes XMCD effect a sensitive technique to probe magnetization of a sample. By relating data from spin-orbit split initial states, *e.g.*, the L_2 and L_3 edges and by applying the so-called sum rules [148], XMCD has the unique feature to extract magnetic moments, separated into corresponding spin and orbital contributions. So, circularly polarized X-rays probe the direction of the atomic magnetic moment in a ferromagnet. The angle and magnetization dependence of XMCD in the total absorption signal is given by $I_{XMCD} \sim \cos \boldsymbol{a} \langle M \rangle_T$, with $\boldsymbol{a}$ denoting the angle between X-ray helicity vector $\vec{\boldsymbol{s}}$ (parallel to the X-ray propogation

direction) and the magnetization $\vec{M}$ of the sample. The maximum dichroism effect is observed when the photon spin direction and the magnetization directions are parallel and antiparallel. Strong XMCD effects of opposite sign appear at the L_3 and L_2 $2p \rightarrow 3d$ resonances of the transition metal ferromagnets Fe, Co, and Ni. Therefore XMCD can be used to provide a large, element-selective and quantitative magnetic contrast in all synchrotron based imaging techniques in which the absorption coefficient is involved.

Fig. 3.10 shown the X-ray absorption spectra for Co metal measured on a DMIM [$Co_{80}Fe_{20}$ (t_n)/Al_2O_3]$_m$ at room temperature. The peaks refer to the different absorption edges indicated in the figure. The dichroism is measured by the differential absorption of left- and right-handed circularly polarized light.

Let us now discuss how the secondary photoelectrons accompanying the X-ray absorption differences are proportional to the XMCD. To understand this let us consider a transition metal whose d shell has a spin moment. This moment is given by the imbalance of spin-up and spin-down electrons. The number of d holes with up and down spin can be measured by making the X-ray absorption process spin-dependent [149]. This can be achieved by using left- or right- circularly polarized light denoted as LCP or RCP, respectively. The LCP or RCP transfer their angular momentum $-\hbar$ or $+\hbar$, respectively to the excited photoelectron. The transferred angular momentum is being carried by the photoeletrons as a spin or an angular momentum or both [150]. If the photoelectron originates from a spin-orbit-split level, *e.g.* the $P_{3/2}$ level (L_3 edge), then the angular momentum of the photon can be transferred in part to the spin through the spin-orbit coupling. LCP photons transfer the opposite momentum to the electron from RCP photons, and hence photoelectrons with opposite spins are created in both cases. Since the $P_{3/2}$ (L_3) and $P_{1/2}$ (L_2) levels have opposite spin-orbit coupling ($l+s$ and $l-s$, respectively), the spin polarization will be opposite at these two edges [149]. In the absorption process, "spin-up" and "spin-down" are defined relative either to the photon helicity or photon spin. It is known that spin flips are forbidden in electric dipole-transitions governing X-ray absorption. Therefore spin-up (spin-down) photoelectrons from the p core shell can only be excited into spin-up (spin-down) d hole states. Hence the spin-split valence shell acts as a detector for the spin of the excited photoelectron and the transition intensity is simply proportional to the number of empty d states of a given spin [149].

From above it is discussed that PEEM is an X-ray absorption technique, because contrast is generated by lateral variations in the X-ray absorption cross-section. Therefore

electron yield techniques like PEEM measures the absorption coefficient indirectly, collecting the emitted secondary electrons generated in the electron cascade that follows the creation of the primary core hole in the absorption process. In this case, the total electron yield is proportional to the number of absorbed photons in a near surface region of the sample, whose depth is given by the mean free path of the low energy secondary electrons. It is well known that the probing depth of electron yield detection is typically a few nanometers [151] and this is much smaller than the X-ray penetration length, which explains the surface sensitivity of PEEM [152]. The absorption coefficient from a measured spectrum can be extracted by correcting the saturation effects caused by the finite X-ray penetration depth, and the application of suitable normalization and background subtraction procedures [153, 154]. As mentioned before, in magnetic PEEM,
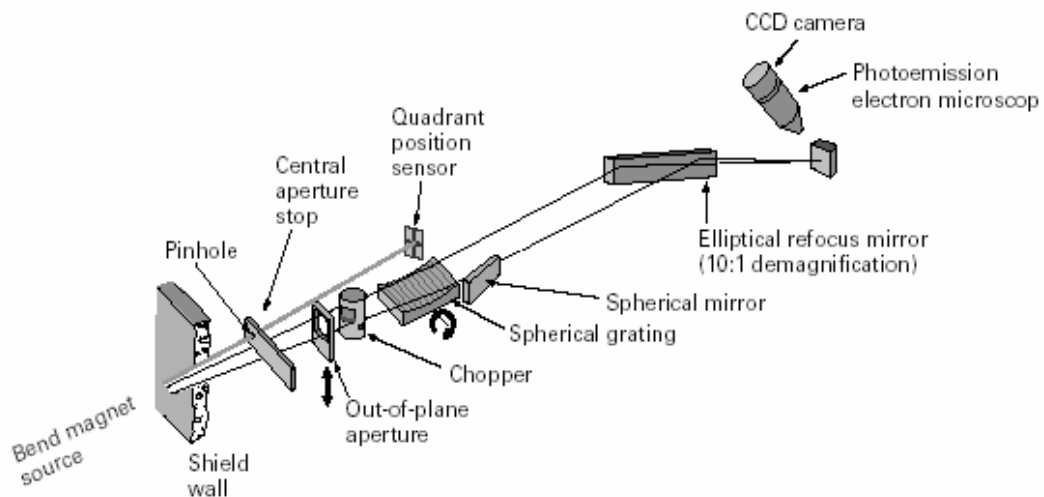
Figure 3.11: Schematic layout of the PEEM-2 instrument at the ALS facility at Berkeley, USA.

the contrast arises from the asymmetry in photon-absorption cross sections of atomic core levels that depend on the orientation of local magnetization relative to the optical helicity of incident circularly polarized soft X-rays. Therefore the most powerful feature of this technique is that magnetic domains can be imaged in an element-specific manner. An advantage of X-ray detection techniques is their insensitivity to external magnetic fields. Therefore imaging in external applied magnetic fields can be done in a PEEM instrument by using very localized fields generated by micro coils.

The PEEM measurements on the DMIMs were performed at the beamline 7.3.1.1 (PEEM-2) at the Advanced Light Source (ALS) facility, Berkeley, USA. A schematic drawing of the PEEM-2 facility is shown in Fig. 3.11. These microscopy measurements were performed in collaboration with Dr. Thomas Eimüller from Ruhr-Universität Bochum, and Dr. A. Scholl from ALS, Berkeley.

In this setup the electrons emitted from the sample are accelerated by a strong electric field (typically 15-20kV) toward the electron optical column, which forms a magnified image of the local electron yield. The spatial resolution in PEEM is solely determined by the resolution of the electron optics, while the intensity is proportional to the X-ray flux density. The PEEM-2 instrument uses bending magnet radiation. The polarization is selected by moving a mask vertically in the beam. Radiation in the plane of the storage ring is linearly polarized, while above and below the plane the radiation is left or right circularly polarized. The sample is at high negative potential for this design, and electrons emitted from the sample are imaged using an all-electrostatic four-lens electron optical system [152]. The spatial resolution in this instrument is around 50−100 nm. The details of this microscope can be found in Ref. [155].

3.9. Mössbauer Spectroscopy

Mössbauer spectroscopy can give very precise information about the chemical, structural, magnetic and time-dependent properties of a material. Key to the success of the technique is the discovery of recoilless gamma ray emission and absorption, now referred to as the 'Mössbauer Effect', after its discoverer Rudolph Mössbauer, who first observed the effect in 1957 and received the Nobel Prize in Physics in 1961 for his work.

The Mössbauer effect provides information about the local magnetic and electronic environment of Mössbauer nuclei (i.e. ^{57}Fe or ^{119}Sn) in a sample. Since this technique does not require the application of an external field, it is possible to observe very weak magnetic interactions, without the perturbing effect of the external field [156, 157].

The principle of the Mössbauer effect is essentially the observation of fine structure in the transition between different nuclear energy levels, *e.g.* of ^{57}Fe or ^{119}Sn nuclei, by means of nuclear resonance absorption or fluoroscence radiation. In the experiment a source containing ^{57}Co nuclei provides a convenient supply of excited ^{57}Fe nuclei, which decay into the ground state accompanied by a gamma ray emission. When the gamma ray energy matches precisely the energy gap in the sample being studied, a nuclear transition occurs in absorption. For this purpose the source moves with a certain velocity *v* and the frequency of the gamma ray can be slightly adjusted because of the Doppler effect. Because of the high frequency of the gamma photon, the Doppler shifts can be quite significant. In this way one can probe any splitting in the ground state in the source or absorber nucleus which might result from magnetic or other interactions.

Fig. 3.12 shows the absorption peak occurring at *v* = 0, where the absorption peak occurs at *v* = 0, since source and absorber are identical. The energy levels in the absorbing nuclei can be modified by their environment in three main ways: by the Isomer Shift, Quadrupole Splitting and Magnetic Splitting.

3.9.1. Isomer Shift

The isomer shift arises due to the slight change in the Coulomb interaction between the nuclear and electronic charge distributions over the nuclear volume which is associated with the slight increase of the ^{57}Fe nucleus in the $I = \dfrac{3}{2}$ state. In a Mössbauer spectrum the isomer shift is the velocity of the center of gravity of the spectrum with respect to zero-velocity. As the isomer shift is proportional to the s-electron density of the nucleus, this

can be used to gain information about the valence state of the Mössbauer atom or of charge transfer, and is also useful to detect lattice expansion/compressions, as these also change the electronic density. The hyperfine splitting scheme for the ^{57}Fe Mössbauer transition induced by Coulomb interaction (isomer shift) is shown in Fig. 3.12 (a).
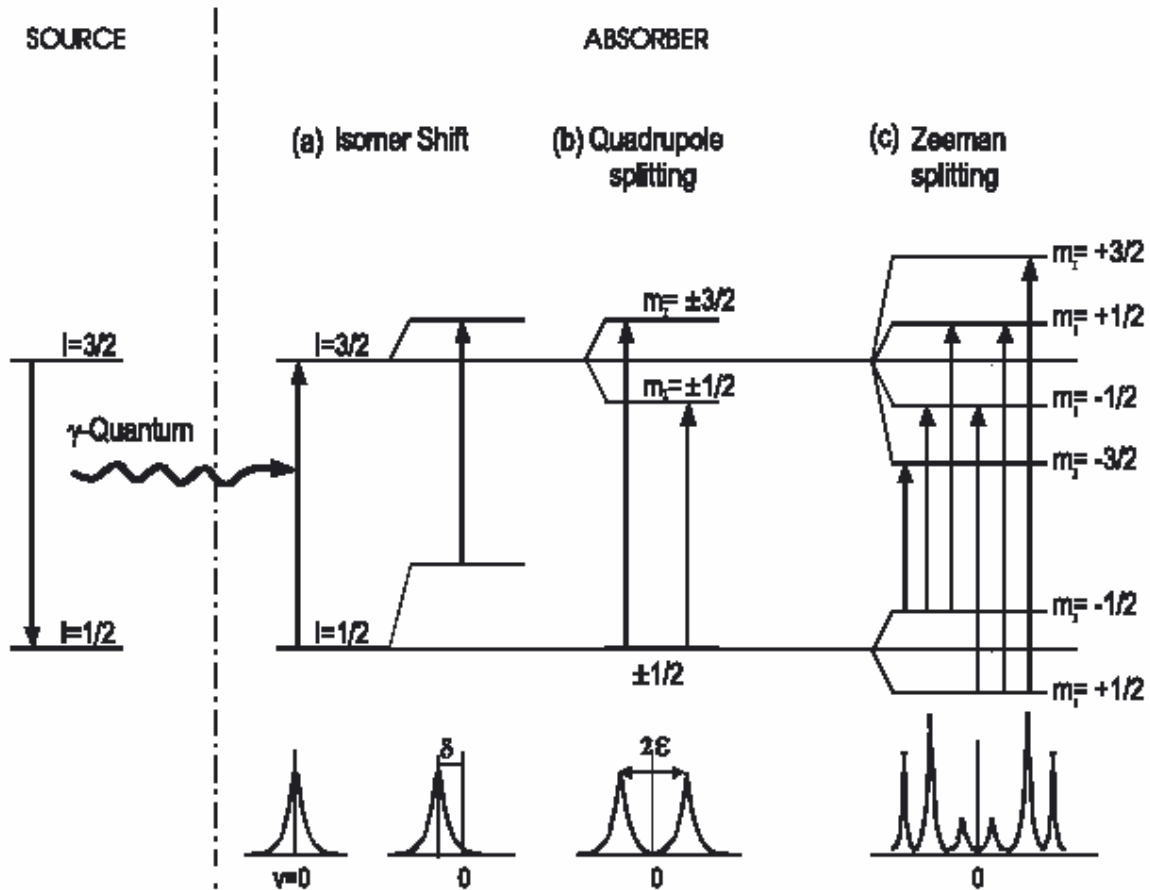

Figure 3.12: Hyperfine splitting scheme for the ^{57}Fe Mössbauer transition induced by (a) Coulomb interaction (isomer shift), (b) quadrupole interaction and (c) magnetic dipole (Zeeman) interaction between the nucleus and the electrons. The corresponding conversion electron Mössbauer (CEMS) spectra are shown schematically [From Ref. 158].

3.9.2. Quadrupole Splitting

If the nucleus is subjected to an electric field gradient, the interaction between the nuclear quadrupole moment and the electric field gradient splits the excited $I = \frac{3}{2}$ state into a doublet, and a two line Mössbauer spectrum is produced and the splitting is called quadrupole splitting. Its applications are the investigations of local symmetry around the

Mössbauer atom and the configuration of its valence electrons. The quadrupole splitting scheme for the ^{57}Fe Mössbauer transition induced by Coulomb interaction (isomer shift) is shown in Fig. 3.12 (b).

3.9.3. Magnetic or Zeeman splitting

In the presence of a magnetic field the nuclear spin moment experiences a dipolar interaction with the magnetic field ie Zeeman splitting. There are many sources of magnetic fields that can be experienced by the nucleus. The total effective magnetic field B_{eff} of the Mössbauer nucleus is given by:

$$B_{eff} = (B_{contact} + B_{orbital} + B_{dipolar}) + B_{applied},$$

the first three terms being due to the atom's own partially filled electron shells. $B_{contact}$ is due to the spin on those electrons polarising the spin density at the nucleus, $B_{orbital}$ is due to the orbital moment on those electrons, and $B_{dipolar}$ is the dipolar field due to the spin of those electrons. This effect can be used to detect magnetic exchange interactions and local magnetic fields. This kind of splitting is illustrated in Fig. 3.12(c).

Mössbauer experiments on the ferrofluid samples (FeCo nanoparticles/n-hexane) were performed together with Dr. R. A. Brand at Universität Duisburg-Essen.

3.10. Magneto-optic Kerr effect and Kerr microscopy

3.10.1. Magneto optics

Magneto optics describes the interaction of electromagnetic radiation with magnetized matter. The magneto-optical Kerr effect (MOKE) and the Faraday effect correspond to a change in the intensity or polarization state of the light either reflected from (Kerr) or transmitted through (Faraday) a magnetic material. A conventional MOKE set-up is depicted in Fig. 3.13.

The light beam from a base is polarized using a linear polarizer, while a photo elastic modulator (PEM) superimposes periodic quarter-wave retardation ($\pm l/4$) to this beam, before it reaches the sample. After the beam is reflected, the light beam again passes through a linear analyzer and then the signal is collected at the detector.
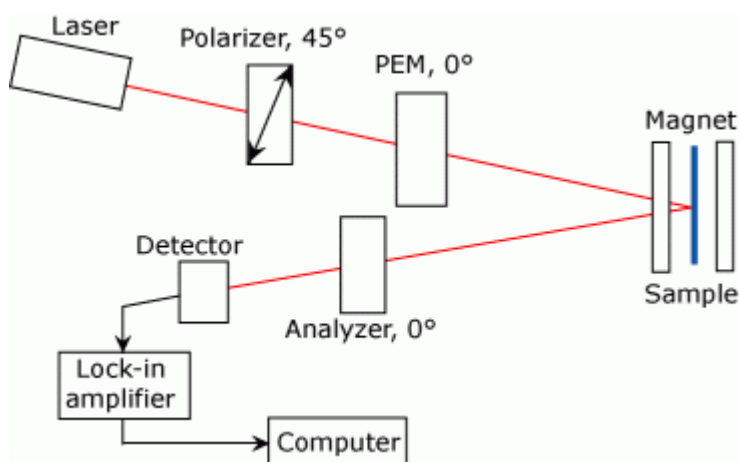
Figure 3.13: Schematic drawing of MOKE set-up in our laboratory.

In principle there are three different optical and magnetic geometries of the Kerr effect:
(a) longitudinal MOKE provides a signal proportional to the component of magnetization that is parallel to the film plane and the plane of incidence of the light. In this geometry (Fig. 3.14(a)) the magnetic field is applied parallel to the plane of the film and the plane of incidence of the light. The longitudinal effect is characterized by a rotation of the plane of polarization, the amount of rotation being proportional to the component of magnetization parallel to the plane of incidence.
(b) transverse MOKE, in which the signal is proportional to the component of magnetization that is parallel to the film plane but perpendicular to the plane of incidence of the light. This effect involves a change in the reflectivity of the light polarized parallel to the plane of incidence and not a rotation of the polarization. Therefore transverse

MOKE only affects the amplitude of the incident polarization (for *p*-polarized incident light only). In this geometry (Fig. 3.14(b)) the magnetic field is applied perpendicular to the plane of the incidence of the light.

(c) polar MOKE, in which a signal proportional to the component of magnetization that is perpendicular to the film plane is measured and often performed at normal incidence. Here the magnetic field is applied to perpendicular to the plane of the film ((Fig. 3.14(c)).
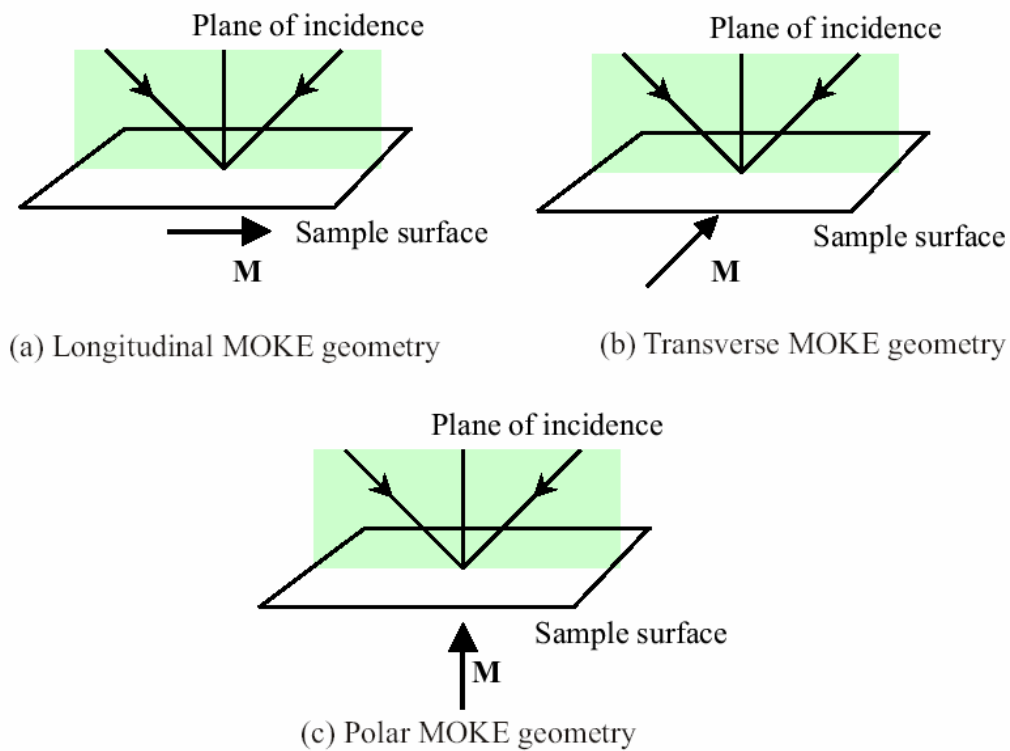

(a) Longitudinal MOKE geometry   (b) Transverse MOKE geometry

(c) Polar MOKE geometry

Figure 3.14: Scattering geometries of different kinds of MOKE

Magneto-optics is described in the context of either macroscopic dielectric theory or microscopic quantum theory [159]. Microscopically, magneto-optic effects arise from the coupling between the electrical field of the light and the electron spin within a magnetic medium which occurs through the spin-orbit interaction [160]. However, macroscopically these magneto-optic effects arise from the antisymmetric, off-diagonal elements in the dielectric tensor. The dielectric tensor in case of a magnetic material can be written as

$$\tilde{e} = e \begin{pmatrix} 1 & iQ_z & -iQ_y \\ iQ_z & 1 & iQ_x \\ iQ_y & -iQ_x & 1 \end{pmatrix}$$

where Q_x, Q_y and Q_z are proportional to the three components of the magnetization vector in the material. The reflection and transmission coefficients thus depend on these terms as well. Details of the MOKE technique can be found in Ref. [160, 161, 162].

Kerr microscopy is also based on the same phenomena only with the difference that here domains are directly imaged. A schematic picture of this setup is shown in Fig. 3.15 [163]. Here the light from a source passes through a polarizer which transmits only plane polarized light. This polarized light is then incident on the sample. Let us consider the simplest case of two domain state in the sample which are anti-parallel to each other as indicated by arroes in Fig. 3.15. After reflection from the sample, the plane of polarization of beam 1 is rotated one way by certain angle –*q* and that of beam 2 the other way rotated by angle +*q*, because they have encountered oppositely magnetized domains. The light then passes through an analyzer and into a camera to make images. Here the analyzer is now rotated until it is crossed with respect to the reflected beam 1, this beam is therefore extinguished and the lower domain appears dark. But in this position the analyzer is not crossed with respect to that of beam 2. Therefore beam 1 is not extinguished and the upper domain appears light. This is the mechanism to find contrast between two different domains.
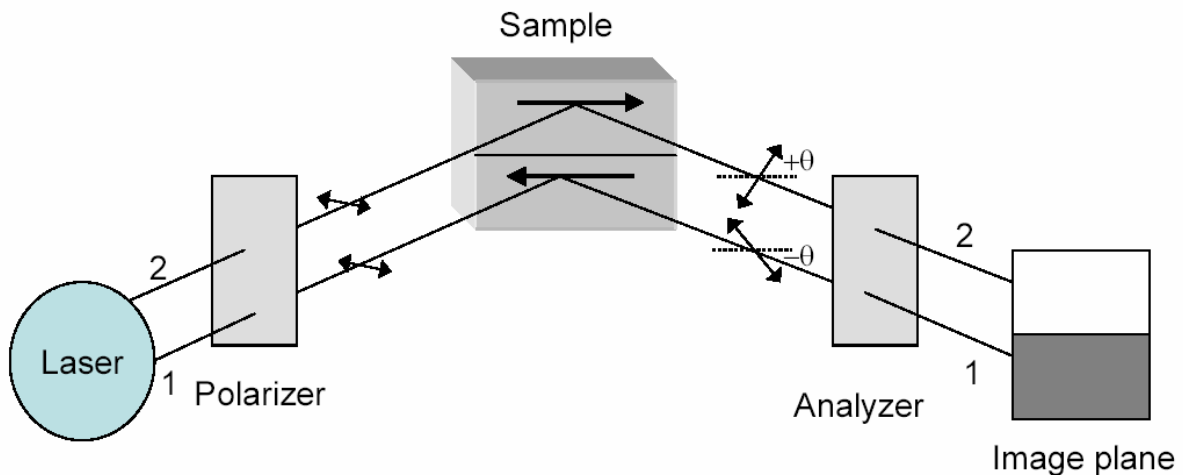
Figure 3.15: A conventional MOKE-microscopy setup.

The DMIMs studied in this thesis have an in-plane uniaxial anisotropy (for details see section 4.2), therefore we have measured the Kerr magnetometry and Kerr microscopy in the longitudinal geometry. The measurements were performed in our group laboratories together with Dr. T. Kleinefeld and Mr. J. Rhensius.

Chapter 4

Structural and magnetic properties of $Co_{80}Fe_{20}/Al_2O_3$ DMIMs

In this section the structural and magnetic properties of discontinuous metal insulator multilayers (DMIMs) $[Co_{80}Fe_{20}(t_n)/Al_2O_3(3nm)]_m$ will be discussed in detail. By changing the nominal thickness t_n of the magnetic CoFe layer, both the magnetic and structural properties can be changed significantly. From structural investigations, it is found that the average diameter of CoFe particles increases linearly with the nominal thickness t_n of the CoFe layers, while their average clearance monotonically decreases. Hence, with increasing t_n the inter-particle interaction increases which can lead to different magnetic states.

In section 4.1, the structural properties of DMIMs determined by different methods such as TEM, X-ray diffraction (XRD), and transport measurements will be discussed. TEM studies on DMIMs reveal that the granules turn out to be nearly spherical having an average diameter in the range of 1.8 nm $\leq t_n \leq$ 5 nm for different DMIMs with increasing t_n. It will also be shown quantitatively how the inter-particle distance decreases with increasing t_n. The microstructure and the layer quality of the samples were investigated by XRD and diffuse X-ray scattering under grazing incidence. The XRD analysis indicates good vertical correlation in the multilayer stacks. Electrical conductivity measurements are carried out to find the physical percolation limit. Magnetotransport measurements reveal the existence of two different particle size distributions, which is later confirmed in this section by magnetometry analysis.

In section 4.2, the existence of an in-plane uniaxial anisotropy in DMIMs is verified by SQUID magnetometry and ferromagnetic resonance measurements.

In section 4.3 the magnetic properties of DMIMs will be addressed for different samples with increasing t_n. In section 4.3.1, a crossover from non-collective blocking to collective superspin glass freezing will be discussed. The sample with the lowest t_n, behaves like a usual superparamagnet because the magnetic interactions between the particles are almost negligible. However by increasing t_n to 0.7 nm, the dipolar interactions becomes relevant and this makes collective freezing and behaves like a spin glass. Also in

these low nominal thickness samples, an additional paramagnetic signal was found which comes from atomically dust particles, also called "glue particles". These glue particles have a significant role to mediate tunnelling exchange interaction between the nanoparticles. This tunnelling exchange interaction in addition to dipolar interactions at higher nominal thickness can lead to a ferromagnetic long-range order between the discontinuous nanoparticles. This state is called superferromagnetic (SFM) and will be discussed in detail in section 4.3.2 for a DMIM sample with $t_n = 1.3$ nm. The SFM domain state will be evidenced by different techniques such as magnetometry, dynamic hysteresis by magneto-optic Kerr effect, Cole-Cole plots of the *ac* susceptibility and polarized neutron reflectivity. The SFM domains are imaged by two different magneto-optic microscopies such as Kerr microscopy and X-ray photoemission electron microscopy. Furthermore the magnetic properties of DMIMs in the percolated regime, $t_n \geq 1.4$ nm, will be discussed in section 4.3.3. By polarized neutron reflectivity measurements on these percolated samples, a modulated magnetization depth profile from CoFe layer to CoFe layer was observed with certain periodicity. By micromagnetic simulations it will be shown how the competition between dipolar coupling, roughness induced Néel coupling and externally applied field can lead to such an unusual modulated magnetization depth profile. The magnetic phase diagram of the DMIMs will be presented at the end of this section.

4.1. Structural properties of DMIMs

The structural properties of the samples are investigated by transmission electron microscopy, X-ray diffraction and electrical resistance measurements. In-plane TEM images are obtained on single CoFe layers sandwiched between Al_2O_3 layers which are deposited either on KBr (water soluble) or on Silicon Nitride substrates. The films on KBr substrates are dissolved in water and the films are collected on circular Cu grids of diameter 3.05 mm and mesh width 100 μm. TEM images are recorded on the Cu grids. Details can be found in Ref. [73]. Also during sample preparation in the ion-beam chamber, films are deposited directly on SiN_3 membranes simultaneously. These SiN_3 membranes are directly inserted into the transmission electron microscope.

TEM images of a Al_2O_3(3 nm)/$Co_{80}Fe_{20}$($t_n = 0.5$ nm)/ Al_2O_3(3 nm) trilayer and for a Al_2O_3(3 nm)/$Co_{80}Fe_{20}$($t_n = 0.9$ nm)/ Al_2O_3(3 nm) trilayer are shown in Fig. 4.1(a) and (b), respectively. These two samples come from the same 2nd batch. The top view structure

of a Al_2O_3(3 nm)/$Co_{80}Fe_{20}$(t_n = 1.4 nm)/ Al_2O_3(3 nm) trilayer on SiN_3 substrate as imaged by transmission electron microscopy (TEM) is shown in Fig. 4.1(c). One should note that the t_n = 1.4 nm sample on which the TEM measurements were performed comes from another batch (3rd batch DMIM). From these plan-view images, it is easily observed that, at all these nominal thicknesses (below percolation) the CoFe granules turn out be nearly spherical and well separated from each other. For the t_n = 0.5 nm sample, the TEM image shows that the particles are nearly spherical with an average diameter of $d \approx 1.8$ nm. These particles are embedded randomly inside the amorphous Al_2O_3 matrix, where the mean distance between two nearest particles is $D \approx 10$ nm. However increasing the nominal thickness to t_n = 0.9 nm, the TEM image shows that the CoFe particles are quasi-spherical with an average diameter $d \approx 2.8$ nm within a Gaussian distribution width of $\boldsymbol{s}_v = 0.95$ nm. In this sample the inter-particle clearance is almost constant and amounts approximately to 3 nm [73, 96]. However in case of the t_n = 1.4 nm sample the average particle size is of the order of 5 nm [164].
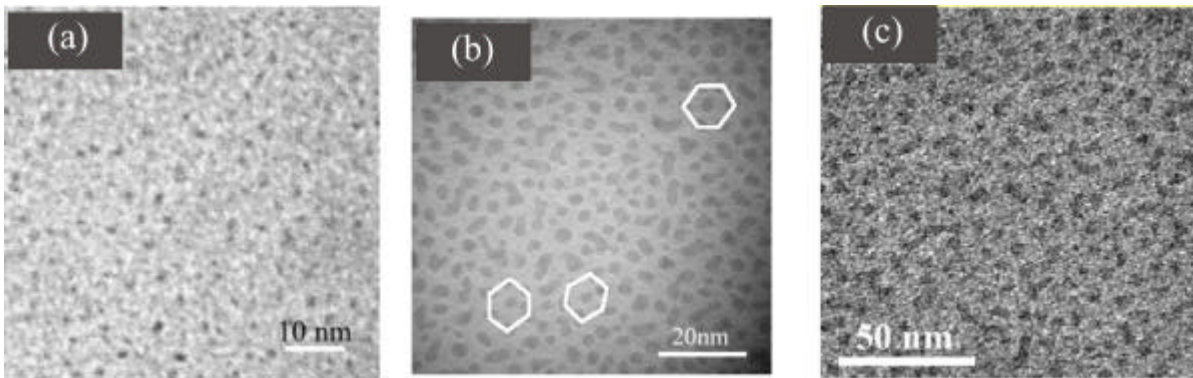
Figure 4.1: TEM top view micrographs of three different nominal thicknesses with $t_n = 0.5$ nm (a), 0.9 nm (b) and 1.4 nm (c). The sample with t_n = 1.4 nm comes from the 3rd batch. The sketches in the image (b) show some quasi-self-organized structures of a triangular lattice [73, 96].

From these TEM micrographs, it is clearly seen that the granule size increases linearly with CoFe layer thickness t_n while their average clearance monotonically decreases until reaching 3D percolation at t_n =1.4 nm for the 2nd batch DMIMs [165]. The formation of isolated particles in the DMIMs indicates a Vollmer-Weber-type growth mode where the deposits are nucleating heterogeneously at sites with invariant aerial

density and tend to form three-dimensional dots. Similar growth mechanisms have also been observed in Co/Al_2O_3 multilayers [166, 167, 168, 169]. In Fig. 4.1(b), it is further noticed that the granules tend to occupy the sites of hexagons as shown by a few sketches, thus forming quasi-self organized structures of a tringular lattice. The elemental composition of the DMIMs has been verified by analyzing the energy dispersive X-ray (EDX) spectrum obtained during transmission electron microscopy. From EDX spectrum analysis, the fractions of 82 % and 18 % for Co and Fe, respectively was obtained, hence, revealing a good stoichiometry of the metallic $Co_{80}Fe_{20}$ nanoparticles [73].
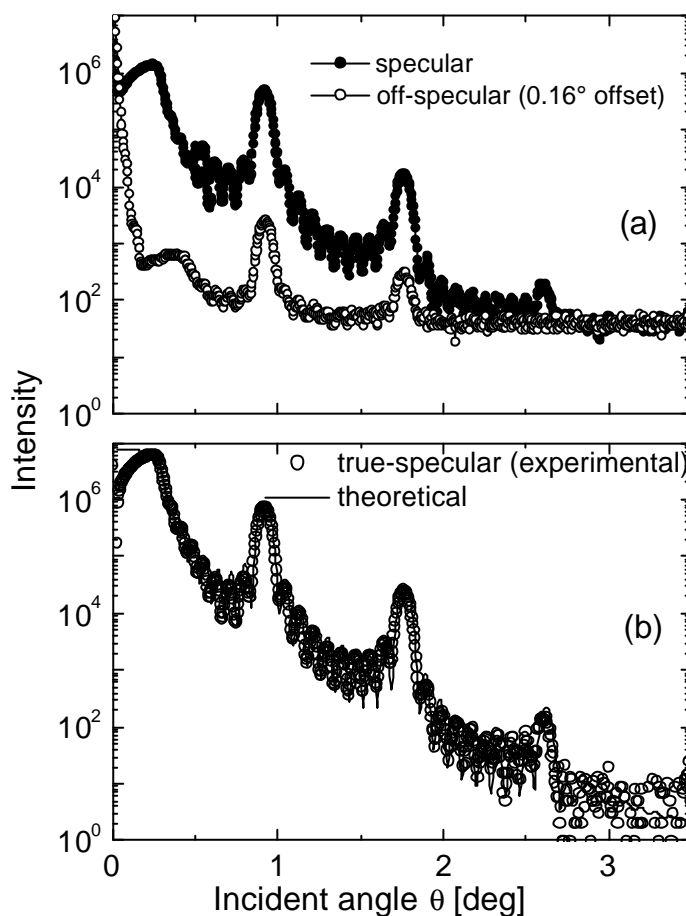
Figure 4.2: (a) X-ray specular reflectivity and longitudinal diffuse scattering $\left(q - 2q + 0.16° \right)$ of a $[CoFe(1.3 \ nm)/Al_2O_3(3 \ nm)]_{10}$ multilayer. (b) The true-specular scan along with the best simulated curve for the multilayer is shown as a function of the angle of incidence.

The microstructure and the layer quality were investigated by low angle X-ray diffraction (XRD) and diffuse X-ray scattering under grazing incidence using a Bruker-

AXS D8 diffractometer with CuKa (l = 0.154 nm). Fig. 4.2(a) shows the scattered intensity measured both in the specular (q - $2q$) and in the longitudinal-diffuse (q - $2q$ + $0.16°$) geometry on a [CoFe(t_n = 1.3 nm)/ Al_2O_3(3 nm)]$_{10}$ multilayer. The longitudinal diffuse scattering peaks at the Bragg peak positions indicate a good vertical correlation in the multilayer stack [43, 106].
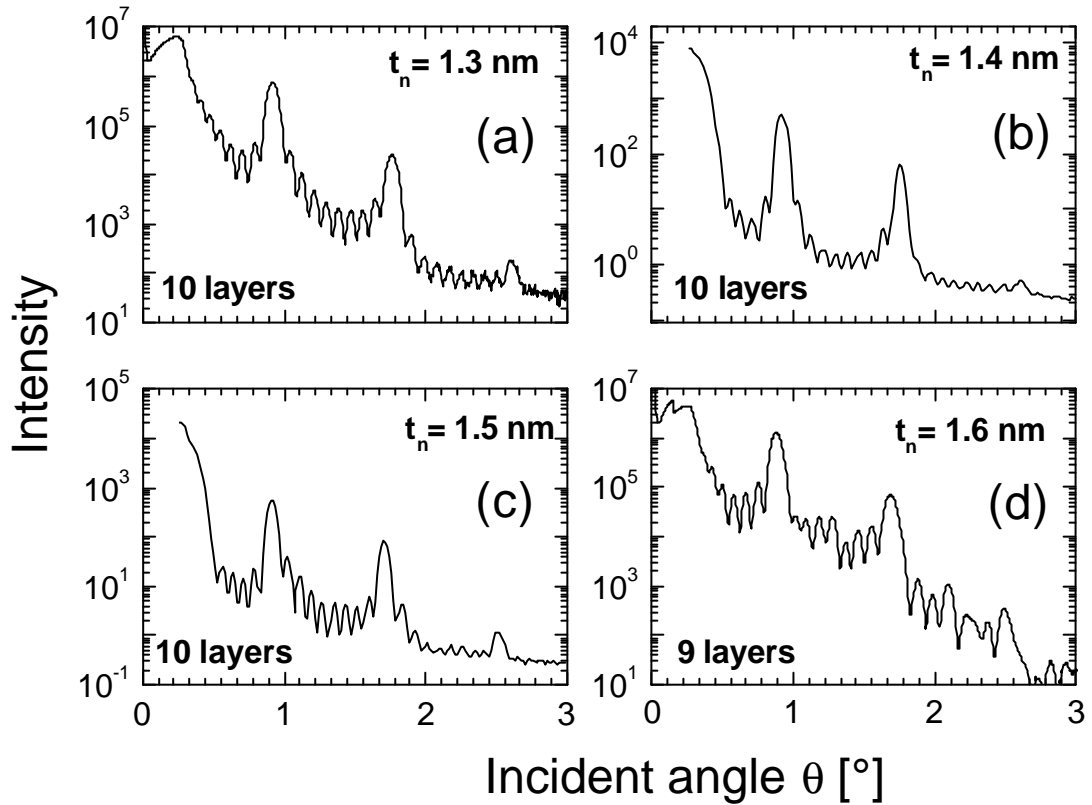

Figure 4.3: Small-angle XRD in [CoFe(t_n)/Al_2O_3(3nm)]$_m$ multilayered films.

Fig. 4.2 (b) shows the true-specular (specular minus off-specular) reflectivity curves along with their fit. One finds well-defined Bragg peaks up to the third order. The presence of well defined finite-thickness higher-frequency oscillations (Kiessig fringes) clearly indicates the presence of ten uniform bilayers. Simulations of the true-specular curve (solid line) yield 1.32 ± 0.02 nm and 3.66 ± 0.02 nm for the thicknesses of the CoFe and Al_2O_3 layers, respectively, with a rms roughness of 0.56 ± 0.02 nm for both Al_2O_3 and CoFe [43]. Similar analysis was performed for the other samples. For example the fitting of the XRD spectra of t_n = 1.6 nm yields 1.61 ± 0.02 nm and 3.66 ± 0.02 nm for the thicknesses of the CoFe and Al_2O_3 layers, respectively, with a rms roughness of 0.42 ±

0.02 nm for both Al_2O_3 and CoFe. From XRD analysis, it is found that the thickness of CoFe remains the same as the nominal thickness but the thickness of Al_2O_3 is slightly different from its expected value defined by the preparation conditions. Further studies have to be done in order to understand this discrepancy between the actual and expected thickness of Al_2O_3.

Fig 4.3 shows small angle XRD curves for different nominal thicknesses from the same 2nd batch DMIMs. The interface quality imrpoves with increasing CoFe layer thickness, producing better defined superlattice Bragg peaks. With increasing nominal thickness, more pronounced Kiessig fringes are visible indicating improvement of the structural quality and flatness of the external surface. In fact, as will be seen below from the electrical resistance measurements, CoFe layers become continuous at $t_n > 1.4$ nm while below this thickness they remain discontinuous giving rise to spin dependent tunnelling transport between CoFe nanoparticles.
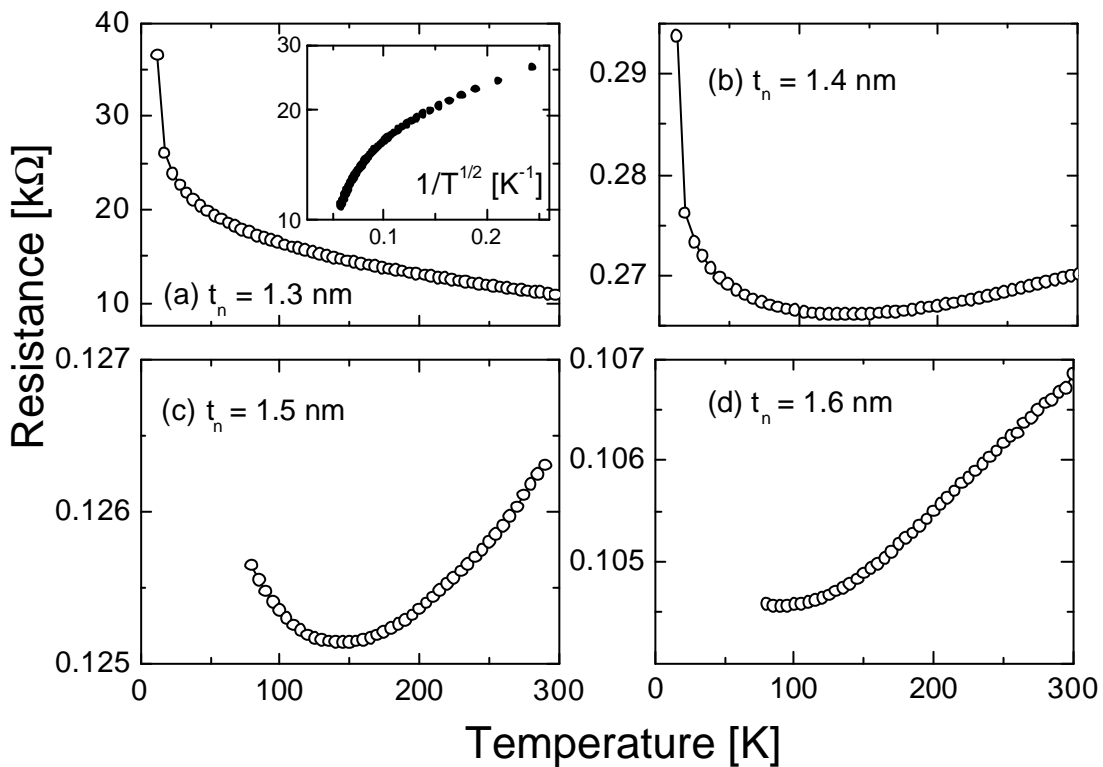

Figure 4.4: Temperature dependence of the electrical resistance of [CoFe(t_n)/Al_2O_3(3nm)]$_m$ multilayered films. Inset of panel (a) shows the temperature dependence of electrical resistance *lnR vs. $T^{-1/2}$*.

Fig. 4.4 shows the electrical resistance R was measured as a function of temperature for different layer thickness t_n measured by current in plane (CIP) geometry. The electrical resistance of the $t_n = 1.3$ nm sample decreases with temperature showing dielectric behavior similar like the results reported earlier [170]. The change from dielectric to metallic regime occurs at $t_n = 1.4$ nm [165]. However a slight upturn is still observed at low enough temperatures (< 50 K, Fig. 4.4(b) and (c)), indicating the presence of a remanent tunnel contribution, likely associated with a few tunnel bridges between the continuous parts of the metallic network within the CoFe granules [170].
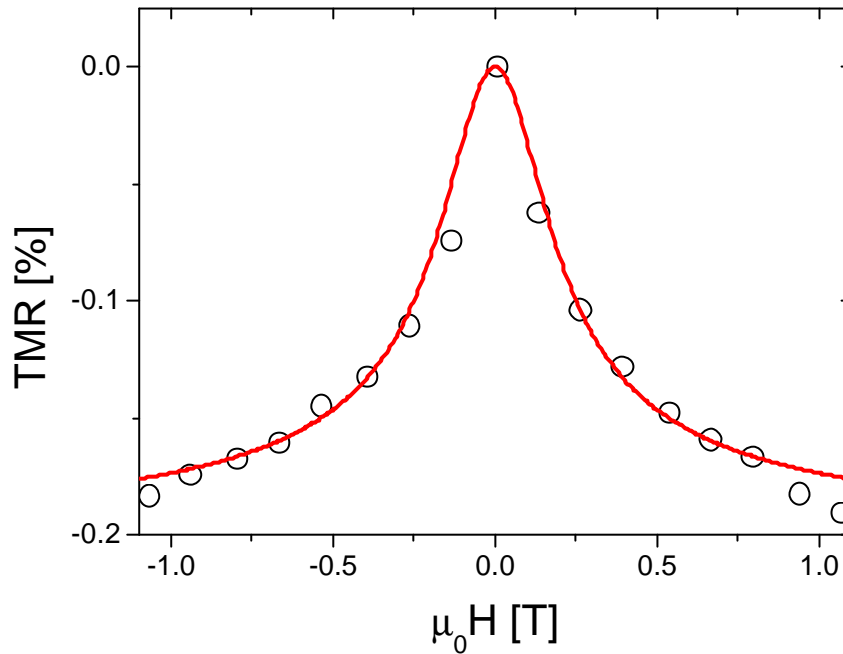
Figure 4.5: Magnetic field dependence of the CIP tunneling magnetoresistance, TMR, at room temperature for a $[Co_{80}Fe_{20}(1.3$ nm$)/Al_2O_3(3$ nm$)]_{10}$ DMIM sample. Full line is a best to the model theory [173] to the data.

The bimodal distribution of CoFe particles as depicted in Fig. 3.2 (in section 3.1) is mirrored by the temperature (T) dependence of the electrical tunneling resistance R of an insulating DMIM sample $[Co_{80}Fe_{20}(1.3$ nm$)/Al_2O_3(3$ nm$)]_{10}$. This bimodal size distribution will be discussed in detail in section 4.3.1 and later in this thesis. When plotting lnR versus $T^{1/2}$ in Fig. 4.4(a) (inset) we do not observe the usual linear relationship, which results from the broad log-normal size distribution of the metallic nanosized granules including the Coulomb blockade effect [171]. The strongly decreasing slope when cooling to low

temperatures hints at an increasing dominance of higher order tunneling processes due to the large fraction of extremely small particles [172].

As a consequence, the higher order tunneling gives rise to a fairly small tunneling magnetoresistance (TMR) [172] of only about 0.2 % in a magnetic field of $B = 1$ T at room temperature (Fig. 4.5). In addition, the different magnetic saturation properties of both kinds of granules are reflected by the shape of the TMR curve. A best fit of a recent model theory [173] to our data (full line in Fig. 4.5) yields reasonable parameters, *viz.* $m_1 \approx 5000$ m_B, $<d_1> \approx 4.1$ nm and $m_2 \approx 14$ m_B, $<d_2> \approx 0.5$ nm, for the nano- and the ultrasmall "glue" particles, respectively. These numbers comply with those magnetometrically obtained which will be discussed in detail in section 4.3.1 [174]. Remanent magnetization at zero magnetic field also diminishes the TMR.

Finally, any oxidation of the CoFe granules can be excluded because of the absence of unidirectional exchange anisotropy in these films. This has precisely been tested on a t_n = 0.9 nm sample by measuring the hysteresis after zero-field cooling and comparing this to the hysteresis measured after a field cooling in 1 T from 300 K to 10 K. It has been reported that the two hysteresis loops were identical. Therefore no exchange-bias effect was found in these films thus proposing the absence of any core-shell FM-AF structure [96].

4.2. Evidence of uniaxial anisotropy in DMIMs

Uniaxial magnetic anisotropy in thin films induced either via an oblique angle of deposition [175, 176] or via a magnetic field during deposition [177] has long been established. Self-shadowing effects lead to areas in the growing film that do not have direct line of sight to the deposition flux and are subject to limited adatom mobility. These sites remain as voids in the growing sample. So this kind of growth by oblique angle of deposition results in uniaxial anisotropy observed in different thin films. In this section, the uniaxial anisotropy observed in DMIMs will be discussed. It is studied by magnetometry and also by ferromagnetic resonance measurements.
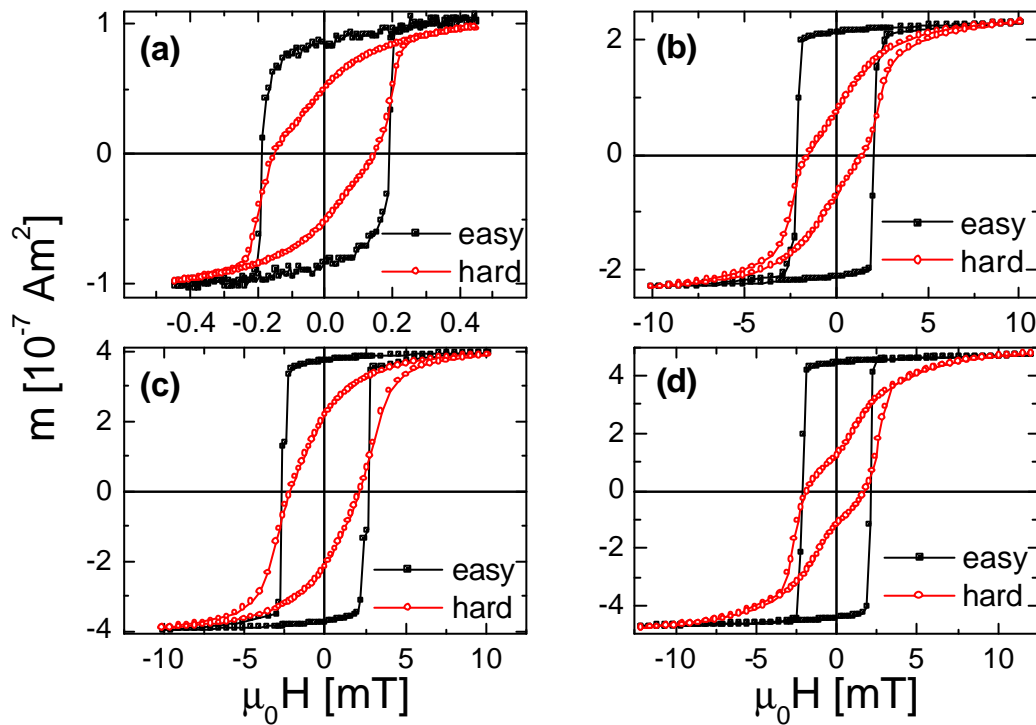
Figure 4.6: Easy- and hard-axis hysteresis measured at room temperature of different DMIM samples $[Co_{80}Fe_{20}(t_n)/Al_2O_3(3nm)]_m$ with t_n = 1.3 (a), 1.6 (b), 1.7 (c) and 1.8 nm (d), respectively.

Fig. 4.6 shows the hysteresis measurements of different DMIMs at room temperature measured by SQUID magnetometry. As mentioned already in section 3.1, a magnetic field of 10 mT was always used to be applied during the sample growth. This direction along which the magnetic field was applied is assumed to be the easy axis of the samples. In the following this hypothesis is verified. In the SQUID magnetometer, we have

measured the hysteresis by applying the magnetic field either along the easy in-plane direction or along the in-plane perpendicular direction. As can be seen in Fig. 4.6, we see square like hysteresis measured in the easy direction, while rounded and distorted loops are measured in the hard direction for four different DMIMs. Thus it is confirmed that in our DMIMs an easy in-plane uniaxial anisotropy exists. For the DMIM samples with $t_n = 1.7$ and 1.8 nm, a step is observed in the hysteresis measured along the easy axis. This will be discussed in detail in section 4.3.3. Hysteresis measured by magneto-optic Kerr effect (data not shown) also revealed the same results concerning the easy and hard axis in DMIMs.

The uniaxial anisotropy is further confirmed by ferromagnetic resonance measurements. By considering the equilibrium condition of the magnetization under a steady field and neglecting magnetic damping effects, the resonance condition for the out-of-plane geometry when the external field is varied from the film normal to the easy in-plane and to the hard in-plane direction is given by the following equations [115]

$$\left(\frac{w}{g}\right)^2 = \left\{ B_{res\perp}\frac{\cos(\Delta q)}{\sin q_{eq}} + M_{eff}\times\frac{\cos 2q_{eq}}{\sin q_{eq}}\right\}\times\left\{B_{res\perp}\sin q_B\right\} - \left[\frac{2K_{2\parallel}}{M}\cos q_{eq}\right]^2. \quad \text{(4.1. (a))}$$

and

$$\left(\frac{w}{g}\right)^2 = \left\{ B_{res\perp}\frac{\cos(\Delta q)}{\sin q_{eq}} + M_{eff}\times\frac{\cos 2q_{eq}}{\sin q_{eq}} - \frac{2K_{2\parallel}}{M}\times\frac{\cos 2q_{eq}}{\sin q_{eq}}\right\}$$

$$\times\left\{B_{res\perp}\sin q_B\right\} - \left[\frac{2K_{2\parallel}}{M}\cos q_{eq}\right]^2 \quad \text{(4.1(b))}$$

respectively.

Here $M_{eff} = \frac{2K_{2\perp}}{M} - m_0 M$ denotes the effective out-of-plane anisotropy field and $\Delta q = q_{eq} - q_B$. For $M_{eff} < 0 \,(> 0)$, the easy axis of the system lies in (normal to) the film plane. The resonance condition for the in-plane configuration and $q_B = \frac{p}{2}$ becomes

$$\left(\frac{w}{g}\right)^2 = \left(B_{res\parallel}\cos\Delta f - \frac{2K_{2\parallel}}{M}\right)\times\left(B_{res\parallel}\cos\Delta f_{eq} - M_{eff}\right) \quad \text{(4.2.)}$$

where $\Delta f = f_{eq} - f_B$, B_{res} is the resonance field, and $\mathbf{q}_{eq}(f_{eq})$ is the polar (azimuthal) equilibrium angle of magnetization with respect to the film normal [115].
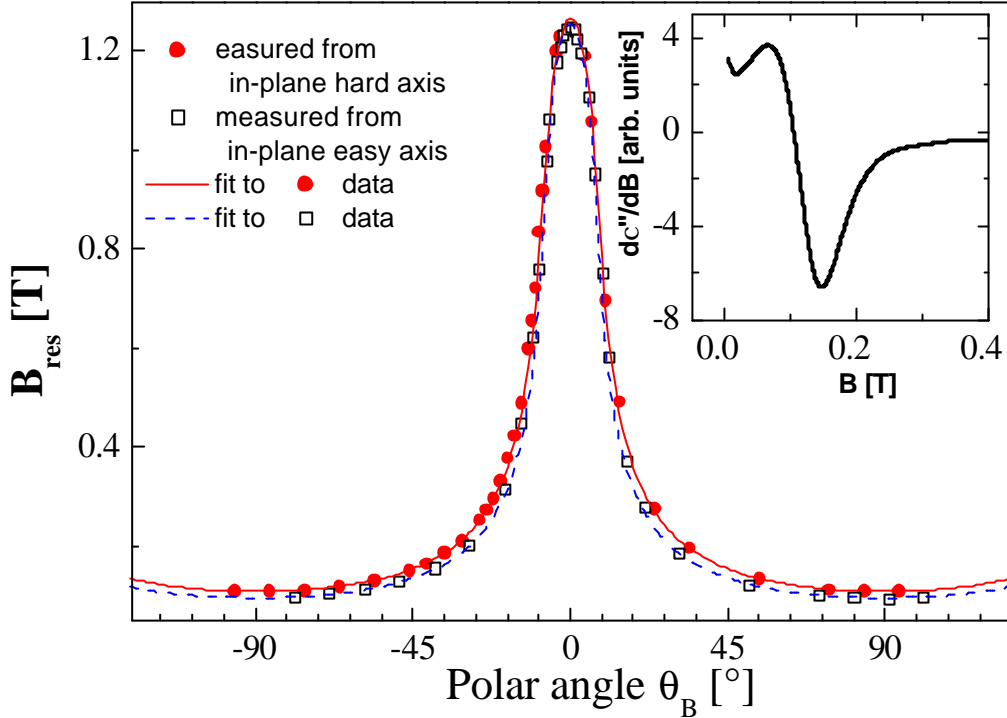

Figure 4.7: Polar angular dependence of the resonance field for a DMIM sample $[Co_{80}Fe_{20}(t_n)/Al_2O_3(3\ nm)]_m$ with t_n = 1.3 nm measured at room temperature with a frequency f = 9.78 GHz. The inset shows typical FMR spectra measured at $\mathbf{q}$ = 90°. The solid and dashed lines in the main panel are the fits according to Eq. 4.1 (a) and (b) respectively.

FMR measurements were performed on different DMIMs at room temperature by applying the magnetic field under different angles to the easy in-plane axis. Fig. 4.7 (inset) shows the FMR spectra at 9.781 GHz with the external field parallel to the in-plane direction for a DMIM sample with t_n = 1.3 nm. The polar angular dependence of the saturated resonance field B_{res}, for the DMIM sample with t_n = 1.3 nm measured at room temperature is shown in Fig. 4.7. The solid and dashed lines are fits using Eq. 4.1 (a) and (b) respectively which yields, g = 2.12, $K_{2\perp}/M$ = -468 mT, $K_{2\parallel}/M$ = -2 mT [178]. The maximum of the resonance field along the film normal indicates that the magnetization of the films favors an in-plane alignment. Also, looking at the two different curves which are

measured from the in-plane easy and in-plane hard axis, one can easily see a splitting between these two curves at $q_B = 90°$. This also clearly shows the in-plane uniaxial anisotropy present in this film. This is again corroborated by the in-plane FMR measurements sweeping the field from the easy-axis to the in-plane hard axis direction.
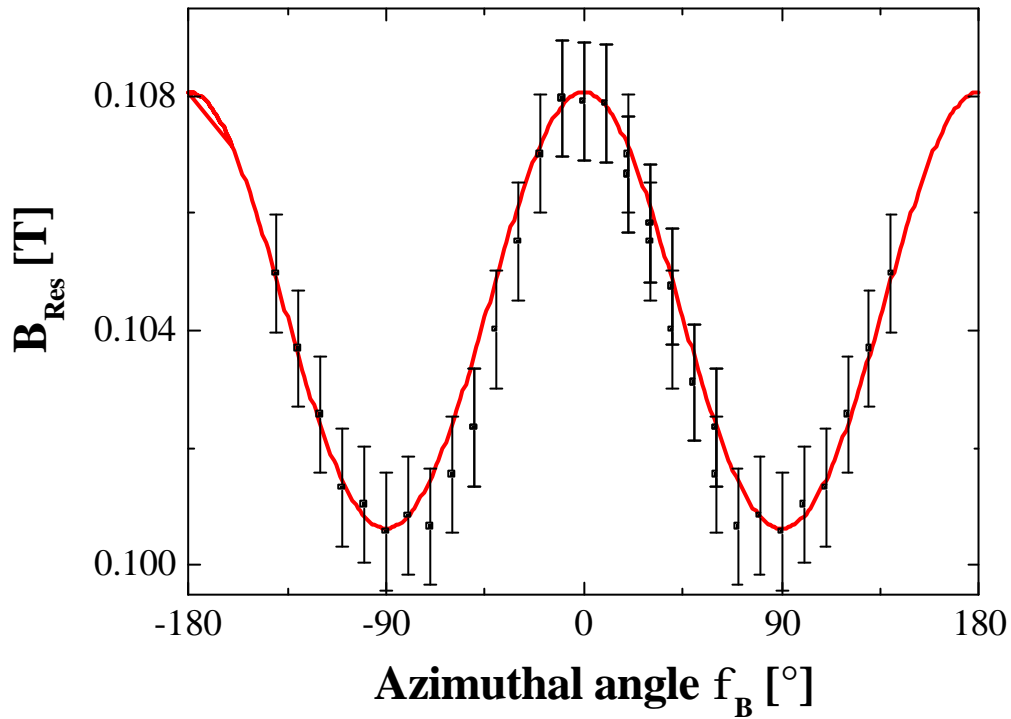

Figure 4.8: Azimuthal angular dependence of the resonance field for a DMIM sample $[Co_{80}Fe_{20}(t_n)/Al_2O_3(3 \text{ nm})]_m$ with $t_n = 1.3$ nm measured at room temperature with a frequency $f = 9.78$ GHz. The solid line is a fit to Eq. 4.2.

The resonance fields for different azimuthal angles are plotted in Fig. 4.8. Here $f_B = 90°$ means that the field is applied to the assumed in-plane easy direction. It is clearly seen that the film has an in-plane easy axis with a minimum resonance field. The same analysis was performed for other DMIMs where the uniaxial in-plane anisotropy has also been verified [178].

4.3. Magnetic properties of DMIMs

The magnetic properties of DMIMs from dilute to higher concentrations will be discussed in this section. At the lowest concentration, $t_n = 0.5$ nm, single particle blocking is observed whereas upon increasing the concentration to $t_n = 0.7$ nm, superspin glass like collective freezing is observed. Further increasing the particle density by increasing the nominal thickness to $t_n > 1.1$ nm, a collective ferromagnetic domain state is encountered which is called superferromagnetic. Finally, physical percolation occurs at $t_n \geq 1.4$ nm and usual ferromagnetism is observed. In these percolated DMIM thin films, a novel modulated magnetization depth profile is observed. Finally this section will be concluded with a magnetic phase diagram of DMIMs.

4.3.1. Crossover from modified superparamagnetism to superspin glass states in DMIMs at low concentration (0.5 nm $< t_n < 1$ nm)

In the following we will focus on the weak interaction limit, as represented by two low coverages, $t_n = 0.5$ and 0.7 nm. We first focus on the strong paramagnetic contributions at low temperatures observed in the temperature dependence of magnetizations. The observations will be explained to be due to atomically small magnetic clusters, which are undetectable in transmission electron microscopy and surround nanoparticles with saturating field-cooled magnetization [174].

After that we will focus on the individual blocking observed in the DMIM sample with $t_n = 0.5$ nm. In the DMIM sample with $t_n = 0.7$ nm, collective SSG freezing will be addressed. In other words it will be shown that a magnetic phase transition occurs from high temperature superparamagnetic (SPM) state to low temperature superspin glass (SSG) state below a well-defined glass temperature T_g [174]. In this context, the relaxational behaviour of the particle assembly will be contested within the framework of Arrhenius-Néel-Brown type law (transition at $T = 0$) and that of a critical power law, characteristic of a phase transition at finite T_g. Furthermore the very existence of zero field memory effects will unequivocally discriminate between superspin glass and superparamagnetic behaviour.

4.3.1.1. Evidence of "dark matter" or "glue particles"

The zero-field-cooled (ZFC) and field-cooled (FC) magnetic moments, m^{ZFC} and m^{FC}, of the $t_n = 0.5$ and 0.7 nm samples are measured in a field $m_0 H = 10$ mT after cooling the

samples in zero field and in $m_0H = 10$ mT, respectively. The temperature dependences of m^{ZFC} and m^{FC} are shown in Fig. 4.9 for the samples with $t_n = 0.5$ nm (a) and for 0.7 nm (b) within the range $2 \leq T \leq 120$ K. At difference with experience on DIMMs with higher coverages, where $m^{ZFC}(T) \approx 0$ and $m^{FC}(T) \approx const.$ at very low temperatures [179], m^{ZFC} and m^{FC} increase rapidly on cooling to very low T for both samples. Intermediate peaks are
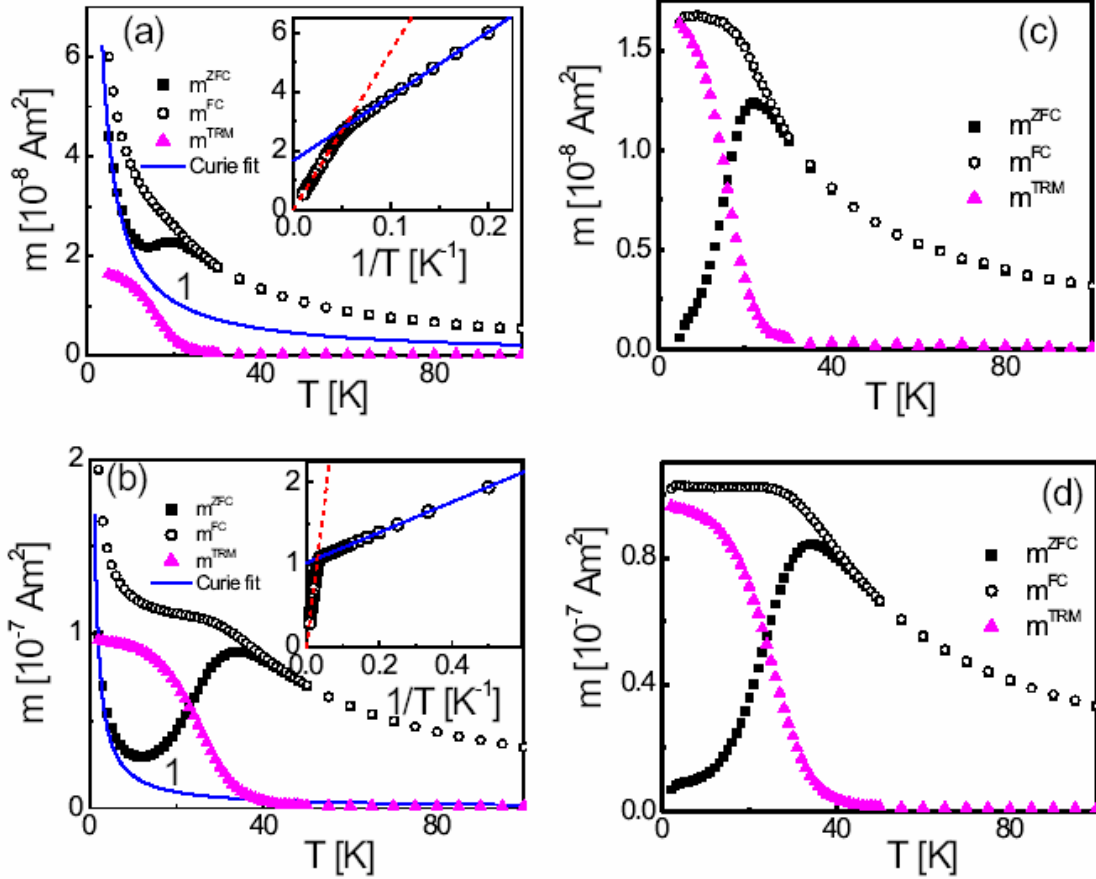

Figure 4.9: Temperature dependence of m^{ZFC}, m^{FC} and m^{TRM} measured in $m_0H = 10$ mT of [Co$_{80}$Fe$_{20}(t_n)$/Al$_2$O$_3$ (3nm)]$_{10}$ samples with $t_n = 0.5$ nm (a) and 0.7 nm (b), respectively. The inset shows m^{FC} plotted vs T^{-1}, where two straight lines are fitted at high (red dashed line) and low (blue solid line) temperatures. Temperature dependence of m^{ZFC}, m^{FC} and m^{TRM} after subtracting the paramagnetic contibution for $t_n = 0.5$ nm (c) and 0.7 nm (d), respectively.

observed in $m^{ZFC}(T)$ at 19 K for the $t_n = 0.5$ nm sample and 34 K for $t_n = 0.7$. These temperatures roughly determine the blocking (T_b) or the glass temperature, (T_g) respectively, and will be discussed below. At high temperature, Curie laws are observed. Two different regions can be distinguished, if we plot m^{FC} versus T^{-1} as shown in the insets

of Fig. 4.9 (a) and (b). The broken lines represent the Curie laws, $m^{FC}(T) = C/T$, for high temperatures, where $C = (5.37 \pm 0.03) \times 10^{-7}$ Am^2 K (a) and $3.51 \pm 0.01) \times 10^{-6}$ Am^2 K (b). At low temperature one can fit with another straight line (solid line) containing a Curie law with an offset m_0^{FC}, i.e. $m^{FC}(T) = C'/T + m_0^{FC}$, where $C' = (2.18 \pm 0.01) \times 10^{-7}$ Am^2 K, m_0^{FC} $= (1.66 \pm 0.01) \times 10^{-8}$ Am^2 (a) and $C' = (1.84 \pm 0.01) \times 10^{-7}$ Am^2 K, $m_0^{FC} = (1.024 \pm 0.001)$ $\times 10^{-7}$ Am^2 (b).

From the above analysis it seems that the magnetization contains two contributions, one of which is paramagnetic down to lowest temperatures, while the other one levels off into a plateau-like contribution at low T. The latter one (shown by the open circles in Fig. 4.9 (c)) becomes apparent after subtracting the paramagnetic Curie function C'/T (solid lines 1 in Fig. 4. 9 (a)) from $m^{FC}(T)$. In addition we show the ZFC curves after subtracting C'/T from the corresponding $m^{ZFC}(T)$ in Fig. 4.9 (c) and (d). Now it becomes clear that the high-T Curie characteristics, C/T, denotes the asymptotic behavior of systems whose particles undergo a blocking or freezing transition at 29 K (a) and 44 K (b), respectively, where $m^{ZFC}(T)$ and $m^{FC}(T)$ split apart. Based on this simple decomposition, we propose that there are two uncoupled subsystems in the samples: one particle subsystem with N_1 big particles each having a magnetic moment $\mathbf{m_1}$, and the other particle subsystem with N_2 small particles each having a magnetic moment $\mathbf{m_2}$. These small particles retain their paramagnetic behavior or have a very low blocking temperature, $T_b < 2$ K. The big ones have SPM behavior, but become frozen at low temperatures and thus contribute to m_0^{FC}. Based on the semiclassical model of paramagnetism, we express the asymptotic Curie constants as

$$C = \frac{\mathbf{m_0} H \left(N_1 \mathbf{m_1^2} + N_2 \mathbf{m_2^2} \right)}{3 k_B}, \tag{4.3}$$

and

$$C' = \frac{\mathbf{m_0} H N_2 \mathbf{m_2^2}}{3 k_B}, \tag{4.4}$$

where k_B is the Boltzmann constant.

In order to determine the four unknown quantities N_1, N_2, $\mathbf{m_1}$ and $\mathbf{m_2}$, we need other relationships in addition to Eq. 4.3 and 4.4. To this end, we analyze the magnetization curves, $m(\mathbf{m_0} H)$, which can be described by Langevin functions, $L(y) = \coth(y) - 1/y$, in the unblocked regime at high enough temperatures, where $y = \mathbf{m_1} \mathbf{m_0} H / k_B T$. If one chooses T far above T_b (≈ 30 K), the Langevin description is justified for the big particles, while the

small particles obey already an asymptotic linear behavior, $m_2 = c_2 V_2 H$, where c_2 and V_2 are the *dc* susceptibility and the volume of the small particle subsystem. Then the total moment reads

$$m = N_1 \boldsymbol{m}_1 L\left(\frac{\boldsymbol{m}_1 \boldsymbol{m}_0 H}{k_B T} \right) + c_2 V_2 H . \tag{4.5}$$

On the other hand, at low temperatures the big particle subsystem becomes saturated at high field, $|m_1| = m_{s1}$, where m_{s1} is the saturated magnetic moment of the big particles. Its contribution is independent of $\boldsymbol{m}_0 H$, but depends on the sign of $\boldsymbol{m}_0 H$. Hence, at low temperatures and high fields one has

$$m = m_{s1} \frac{H}{|H|} + N_2 \boldsymbol{m}_2 L\left(\frac{\boldsymbol{m}_2 \boldsymbol{m}_0 H}{k_B T} \right). \tag{4.6}$$

Fig. 4.10 shows the $m(\boldsymbol{m}_0 H)$ curves for the $t_n = 0.7$ nm sample at $T = 100$ K (a) and at 5 K (b). The solid lines are the best fits to Eq. (4.5) in (a) and to Eq. (4.6) in (b). Note that only data at $|\boldsymbol{m}_0 H| \geq 1.5$ T, i.e. outside the low-field hysteresis, are used to fit Eq. (4.6) in Fig. 4.10 (b). One obtains the parameters $N_1 = (4.46 \pm 0.17) \times 10^{13}$ and $\boldsymbol{m}_1 = (1619 \pm 68)$ $\boldsymbol{m}_B$ for the big particles, and $N_2 = (2.512 \pm 0.004) \times 10^{17}$ and $\boldsymbol{m}_2 = (6.03 \pm 0.02)$ $\boldsymbol{m}_B$ for the small particles. Additionally, $c_2 V_2 = (2.63 \pm 0.02) \times 10^{-13}$ and $m_{s1} = (5.2 \pm 0.3) \times 10^{-7}$ Am^2. Substituting these values into Eq. (4.3) and (4.4), one obtains $C = (2.6 \pm 0.3) \times 10^{-6}$ Am^2 K and $C' = (1.88 \pm 0.02) \times 10^{-7}$ Am^2 K. Comparing to the experimental results from Fig. 4.9 (b), one finds that C' is nearly the same within errors, while C is 31% smaller. The latter deviation is probably due to the finite size distribution of the big particles, which is neglected in the present analysis and enters with different weights into Eq. (4.3) and (4.5), respectively. Under the assumption of an effective atomic moment of the Co$_{80}$Fe$_{20}$ alloy, $\boldsymbol{m}_{CoFe} \approx 1.9$ $\boldsymbol{m}_B$ [180], the average number of atoms per particle is $n_1 \approx 850$ and $n_2 \approx 3$. Hence, a bimodal distribution of nanoparticles (diameters $d_1 \approx 2.6$ nm when assuming the lattice parameters of bulk fcc Co$_{80}$Fe$_{20}$) and "molecules" Co$_{3-n}$Fe$_n$ ($n = 0$-3) is encountered.

The same analysis performed is now on the $m(\boldsymbol{m}_0 H)$ curves of the $t_n = 0.5$ nm sample. Fig. 4.11 shows the $m(\boldsymbol{m}_0 H)$ curves for the $t_n = 0.5$ nm sample at T = 100 K [Fig. 4.11(a)] and at 5 K [Fig. 4.8(b)]. With the same procedure, the analysis yields $N_1 = (4.31 \pm 0.14) \times 10^{13}$, $\boldsymbol{m}_1 = (561 \pm 12)$ $\boldsymbol{m}_B$, $d_1 \approx 1.8$ nm, and $N_2 = (2.791 \pm 0.001) \times 10^{17}$, $\boldsymbol{m}_2 = (6.04 \pm 0.01)$ $\boldsymbol{m}_B$. Remarkably, $d_1 \approx 1.8$ nm of the TEM estimate (Fig. 4.1 (a)) is comfirmed by

magnetometry. Further, as expected [96, 170], the magnetic moment of the big particles, $\boldsymbol{m_l}$, decreases as the nominal thickness t_n decreases, whereas $\boldsymbol{m_s}$ remains constant. From the latter value one can conclude that the small particles are indeed clusters containing only few atoms which cannot be observed in TEM. One might even envisage isolated single Co or Fe atoms or ions (Co^{2+} and Fe^{2+} or Fe^{3+}) bonded to the amorphous oxide environment with magnetic moments in the order $\boldsymbol{m_s} \approx 6\ \boldsymbol{m_B}$ as expected for the $^4F_{9/2}$, $^5D_4$ ($^6S_{5/2}$) ionic
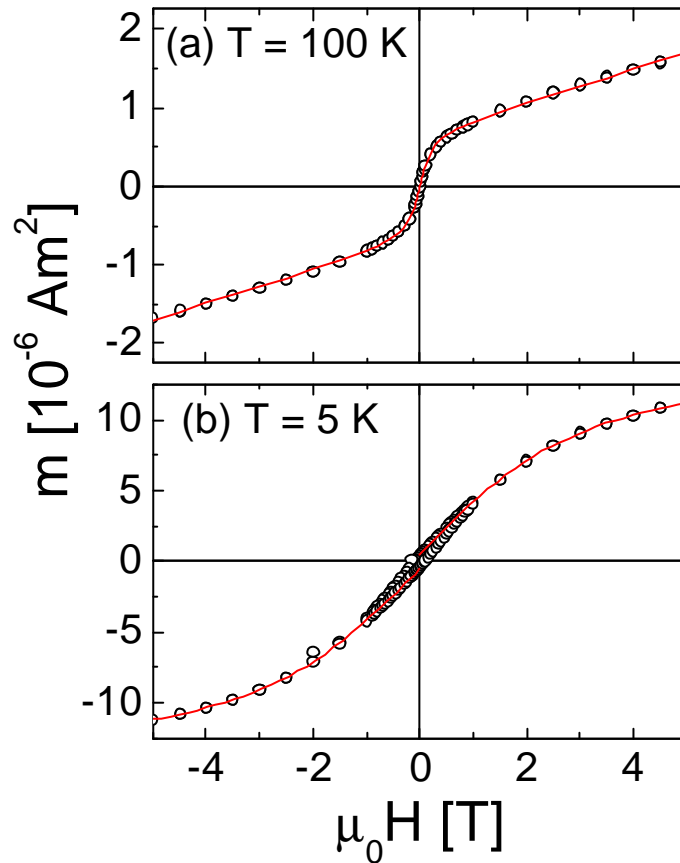

Figure 4.10: Hysteresis loops $m\left(\boldsymbol{m_0}H\right)$ of a $[Co_{80}Fe_{20}(0.7\ nm)/Al_2O_3(3\ nm)]_{10}$ sample at $T = 100$ K (a) and 5 K (b). The solid lines are the best fits to Eqs. 4.5 in (a) and 4.6 in (b), respectively (see text).

ground states [69]. A similar system, $Al_2O_3/Co(t_n)/Al_2O_3$ trilayers, was studied by Maurice *et al.* with TEM and extended X-ray absorption fine structure (EXAFS) [166]. The main particle sizes estimated from TEM were much larger than the sizes calculated from EXAFS spectra for $t_n \leq 0.7$ nm (61% and 47% larger for $t_n = 0.4$ nm and 0.7 nm, respectively). They assumed that TEM misses an appreciable fraction of very small

particles, which are also suggested by Monte Carlo simulations on the growth processes [181].

This conjecture is confirmed by the present investigation, where these TEM-undetectable "dark" or "glue" particles have a large contribution to the magnetic moment, which offers a chance to "see" them in detail by magnetic measurements. Future experiments, *e.g.*, by using Mössbauer spectroscopy of ^{57}Fe, will have to unravel the presently unsolved question, if single ions like Fe^{3+} ($m = 5.9$ m_B) or — less probably— metallic molecules $Co_{3-n}Fe_n$ (e.g,. $m = 8\text{-}9$ m_B for n = 1–2) [182] are at the origin of the newly detected ``dark" or "glue" particles.
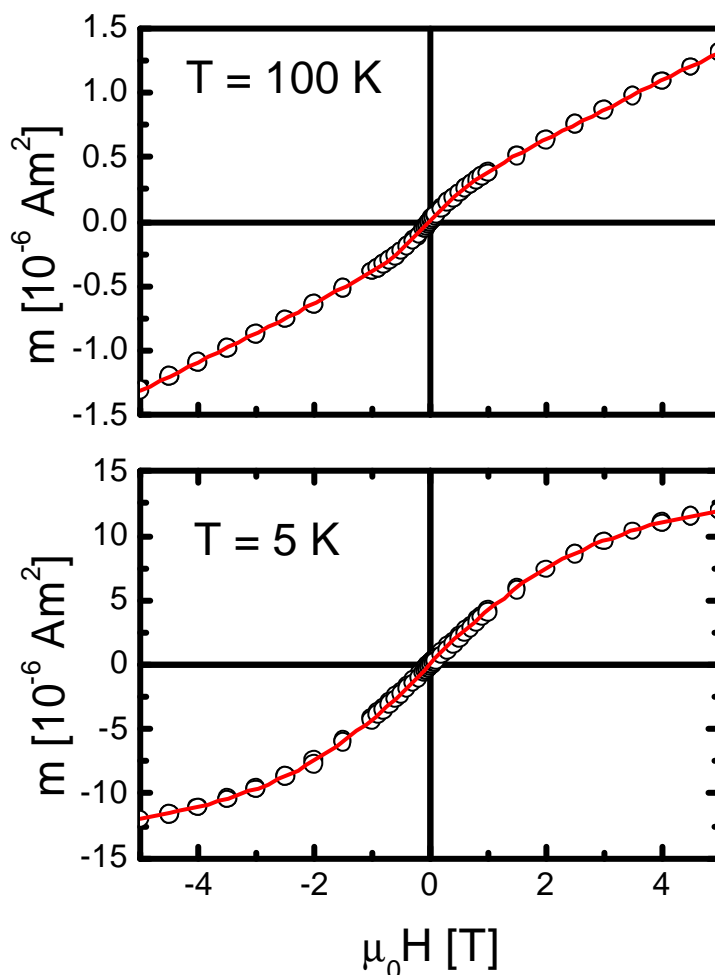
Figure 4.11: Hysteresis loops $m(m_0 H)$ of a $[Co_{80}Fe_{20}(0.5 \text{ nm})/Al_2O_3 \text{ (3nm)}]_{10}$ sample at $T = 100$ K (a) and 5 K (b). The solid lines are the best fits to Eqs. 4.5 and 4.6, respectively (see text).

From the analysis of these two samples, it is found that within errors N_1 remains constant while t_n increases, i.e. the number densities of the big particles is independent of t_n. This is an evidence of a Volmer-Weber-Type growth mode in our CoFe/Al$_2$O$_3$ system [96, 170]. With increasing t_n, starting from a constant concentration of nuclei, the big particles grow. Because of the large distance between particles ($\approx$ 10 nm), the particles do not touch each other during growth at low concentration. Hence the density of the big particles does pratically not change. A similar kind of growth mechanism has often been observed for metals grown on oxide surfaces [166, 167, 168, 169, 181]. On the other hand as a result of Volmer-Weber-Type growth, the ultrasmall particles might refer to the metal atoms being deposited on the oxide surface, but do not have enough time to move to the nucleation sites, where the large particles grow.
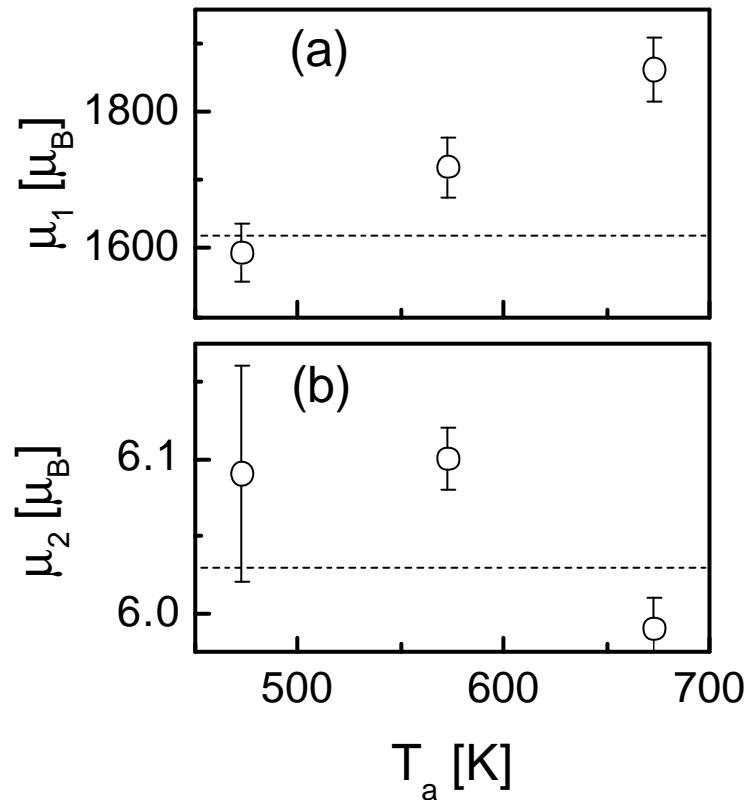

Figure 4.12: Dependence of the moments of big particles m_1 (a) and of the ultrasmall or glue particles m_2 (b) on the annealing temperature T_a for the sample [Co$_{80}$Fe$_{20}$(0.7 nm)/Al$_2$O$_3$(3 nm)]$_{10}$. The dashed lines indicate the magnetic moment values before annealing.

A slight increase of the number of small particles N_2 by about 10 % is observed when decreasing t_n from 0.7 to 0.5 nm. This might be due to the increase of the average diffusion paths of the ultrasmall particles and a decreasing impingement at the big particles owing to their smaller cross section.

Annealing has been carried out in order to gain deeper insight into the growing process. The $t_n = 0.7$ nm sample was annealed in nitrogen atmosphere for 10^4 seconds at T_a = 473, 573 and 673 K respectively. After each annealing step, m^{FC} vs. T and m vs. m_0H were measured and analyzed as previously (see above). Fig 4.12 (a) and (b) show the dependences of m_1 and m_2 on T_a, respectively. As expected, m_1 increases by approximately 10% as T_a increases, while m_2 remains virtually constant. Obviously at higher temperature enhanced diffusion of the ultrasmall particles is activated, which helps the large particles growing. On the other hand, the ultrasmall particles do obviously not aggregate to become larger.

Hence from the above discussions it is clear that in DMIMs a bimodal size distribution exists. The ultrasmall "glue" particles containing few atoms are paramagnetic down to 2K and have dominant magnetic signal. The low temperature increase of the m^{ZFC}, m^{FC} magnetizations are observed in all DMIM samples. Therefore these glue particles are present in all DMIMs but their density decreases as the nominal thickness increases.

4.3.1.2. Low temperature magnetic properties: modified SPM at t_n = 0.5 nm vs. cooperative SSG glass freezing at $t_n = 0.7$ nm

Now let us address the low temperature magnetic properties of the DMIM samples with the lowest nominal thickness, i.e. $t_n = 0.5$ nm in our case. To be more precise we have to analyze, if the particles in this sample are *interacting* or *non-interacting*. For this purpose one can calculate the dipole-dipole interparticle interaction energy between adjacent big particles by using the approximating formula $E_{d-d}/k_B = (m_0/4\pi k_B) m_1^2/D^3$. Considering $D = 10$ nm, $m_1 \approx 561 \, m_B$ for the $t_n = 0.5$ nm sample, one obtains $E_{d-d}/k_B \approx 0.2$ K. Again considering twelve nearest neighbors for each particle, the dipolar interaction energy yields $E_{d-d}/k_B \approx 2.4$ K which is much smaller than $T_b \approx 29$ K (Fig. 4.9 (c)). Therefore in this sample the dipolar interaction is not strong enough to produce a collective state and individual SPM behavior being more favourable.

However performing the same calculation on the $t_n = 0.7$ nm sample, the dipole-dipole interparticle interaction energy between adjacent big particles turns out to be ≈ 20 K,

which is in the order of T_g (see below) ≈ 34 K (Fig. 4.9 (d)). Therefore, quite strong interparticle interactions exist in this sample, which might give rise to a collective state rather than individual SPM behaviour.
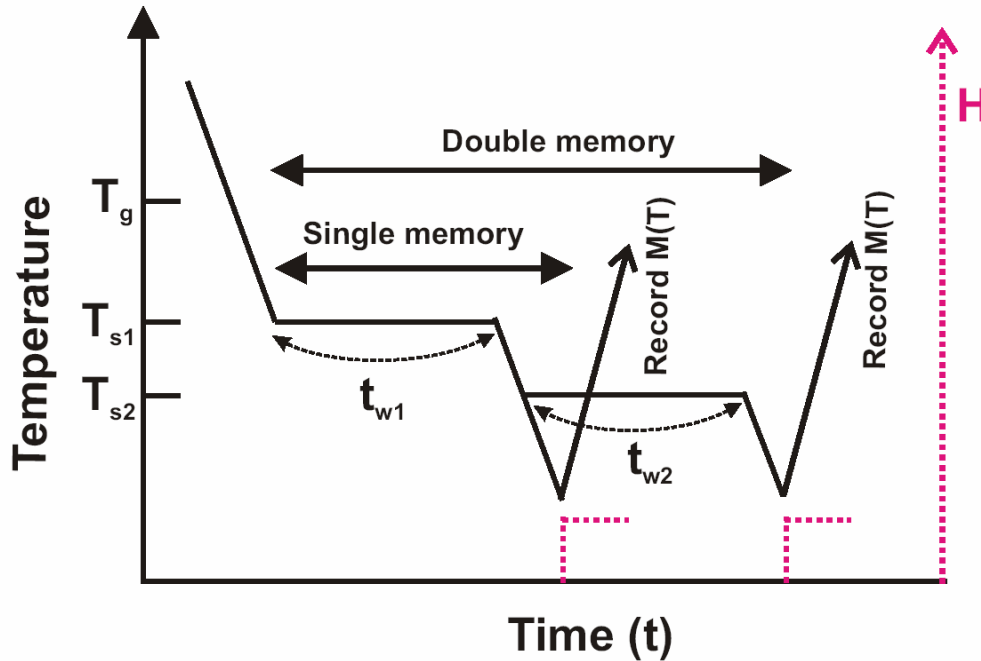

Figure 4.13: The experimental procedures in a single and double memory experiment. T_{s1} and T_{s2} are the two waiting temperatures for their corresponding waiting times t_{w1} and t_{w2}.

In order to check this conjecture, a dynamical study is performed with the aim to clarify our nanoparticle systems to be either blocked SPM or collective SSG. It is well known that both of these states have very slow dynamics, which are very difficult to be distinguished from each other. However, Sasaki *et al.* [62] demonstrated that the memory effect found in the ZFC magnetization is an unequivocal signature of SSG behavior. In the SPM case, no memory is imprinted during a ZFC process below T_b, since the occupation probabilities of spin up and spin down states are always equal to 0.5 (two-state model). However, in the SSG case the sizes of glassy droplets are growing even during the ZFC process as time elapses in the collective SSG state below T_g. This gives rise to a well-defined memory effect.

In a memory experiment, the sample is zero-field-cooled from $T > T_g$ to a stop temperature $T_s < T_g$ (T_{s1} and $T_{s2} < T_{s1}$ in a double memory experiment), where the system is aged for a certain duration (t_w in a single memory effect and t_{w1} and t_{w2} in a double memory effect) before further cooling down to lower temperatures and the field-induced

magnetization is recorded during heating. This is referred to as a stop-and-wait protocol. The memory effects can also be performed in magnetic relaxation measurements [183]. The usual experimental protocol to observe memory effect is shown in Fig. 4.13.
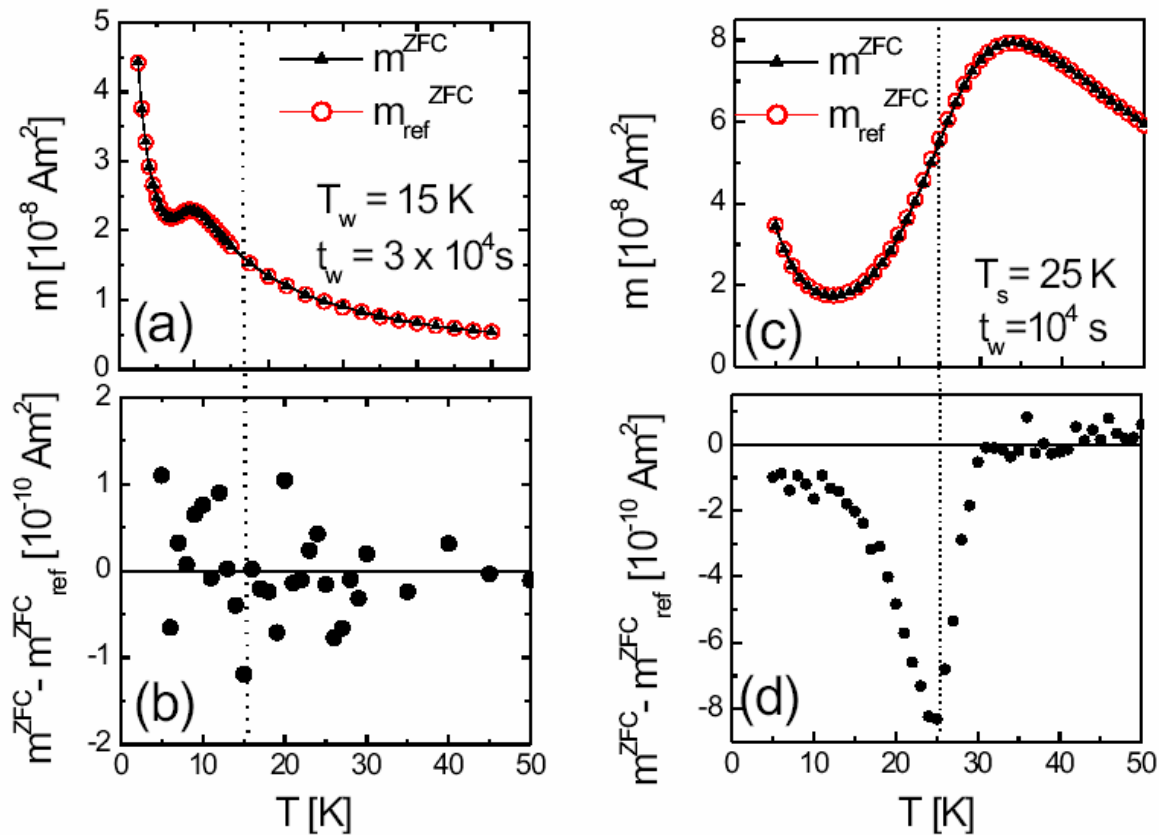

Figure 4.14: Temperature dependence of the reference $m^{ZFC}(T)$ and of the magnetization with a stop-and-wait protocol, $M(T)$, at a magnetic field of $m_0 H = 10$ mT of $[Co_{80}Fe_{20}(t_n)/Al_2O_3\ (3nm)]_{10}$ samples with $t_n = 0.5$ nm (a) and 0.7 nm (c), respectively. Here $m^{ZFC}(T)$ is measured in a magnetic field of $m_0 H = 10$ mT after ZFC from 100 to 5 K with a stop at $T_s = 15$ K for 3×10^4 s (a) and $T_s = 25$ K for 10^4 s (c) (vertical broken lines), while the reference m^{ZFC}_{ref} is measured in the same way, but without any stops. Difference curves of $m^{ZFC}(T)$ with and without intermittent stop T_s are plotted for $t_n = 0.5$ nm and 0.7 nm in Fig. (b) and (d), respectively.

Memory effects are studied on both samples being cooled in zero magnetic field from high temperature with and without an intermittent stop at $T_s < T_b$ (or T_g) for a waiting time t_w respectively. $m^{ZFC}(T)$ is recorded during subsequent heating in a field of 10 mT. Fig. 4.14 illustrates $m^{ZFC}(T)$ with and without intermediate waiting for the $t_n = 0.5$ nm sample (Fig. 4.14 (c)) and for the $t_n = 0.7$ nm sample (Fig. 4.14(c)). The difference curves

between $m^{ZFC}(T)$ with and without intermittent stop are plotted in Fig. 4.14(b) and (d). A memory effect shown as a dip at $T \approx T_s = 25$ K is clearly observed for the 0.7 nm sample (Fig. 4.14 (d)). This difference indicates that the magnetic moment configuration in the system spontaneously rearranges towards equilibrium via growth of equilibrium domains, when the system is left unperturbed at the constant waiting temperature T_s. These equilibrated domains become frozen-in on further cooling and are retrieved on reheating. Therefore we observe a minimum in $\Delta M = M(T) - M_{ref}(T)$ at about T_s in Fig. 4.14(d).

Another interesting feature is that the reference and stop-and-wait curves coalesce at low temperatures and only start to deviate as T_s is approached from below and this clearly indicates that rejuvenation [184] of the system occurs as the temperature is decreased away from T_s in the stop-and-wait protocol. Hence, we conclude that this sample with $t_n = 0.7$ nm is a SSG system. However, in Fig. 4.14 (b) no ZFC memory effect is found beyond noise for the 0.5 nm sample, which most probably implies a non-collective SPM blocking state. Obviously the crossover from SPM to SSG occurs at $0.5 < t_n < 0.7$ nm.

The SSG nature of the $t_n = 0.7$ nm sample is corroborated by *ac* susceptibility measurements as shown in Fig. 4.15. Here χ' vs. T is measured after ZFC to 5 K with an amplitude $\mu_0 h_{ac} = 0.4$ mT and frequencies $10^{-1} \leq f \leq 10^{+3}$ Hz. The peaks, $T_m(f)$, are observed to shift towards a finite glass temperature T_g as f decreases. As observed for other SSG-type DMIMs [179], the critical behavior of the average relaxation time, $\tau = (2\pi f)^{-1}(T_m) = \tau_0 \epsilon^{-z\nu}$, is obtained from the best fit shown in the inset to Fig. 4.15, where $\epsilon = T_m/T_g - 1$ is the reduced temperature with $T_g = 31.9 \pm 1.4$ K. The relaxation time for an individual particle $\tau_0 = (1.2 \pm 0.5) \times 10^{-6}$ s and the critical exponent $z\nu = 8.9 \pm 1.1$ are similar to the values obtained for a SSG with $t_n = 0.9$ nm [96].

The temperature dependence of the *ac* susceptibility of the $t_n = 0.5$ nm sample has also been measured and is shown in Fig. 4.16. Analysis of the peak position of χ' vs. T yields the fitting parameters $T_g = 23.4 \pm 1.1$ K, $\tau_0 = (4.2 \pm 2.6) \times 10^{-6}$ s and $z\nu = 6.0 \pm 1.5$ when fitting to an algebraic law, $\tau = \tau_0 \epsilon^{-z\nu}$. While the values of $z\nu$ and T_g still seem reasonable, the fitting parameter $\tau_0(t_n = 0.5$ nm) being larger than $\tau_0(t_n = 0.7$ nm) contradicts expectation, where the smaller particles should relax faster than the larger ones. Further, the $\tau(T_m)$ data of the $t_n = 0.5$ nm system comply better with an Arrhenius

law, $t = t^* \exp(E/k_b T)$, for weakly interacting magnetic particles with modified relaxation time t^* and activation energy barrier E [2]. First, $\log_{10} t^*/_s = -17.1 \pm 0.8$ confirms the predicted value, $\log_{10} t^*/_s = -17$ to -18. Second, $E/k_B = 448 \pm 23$ K seems to reveal the
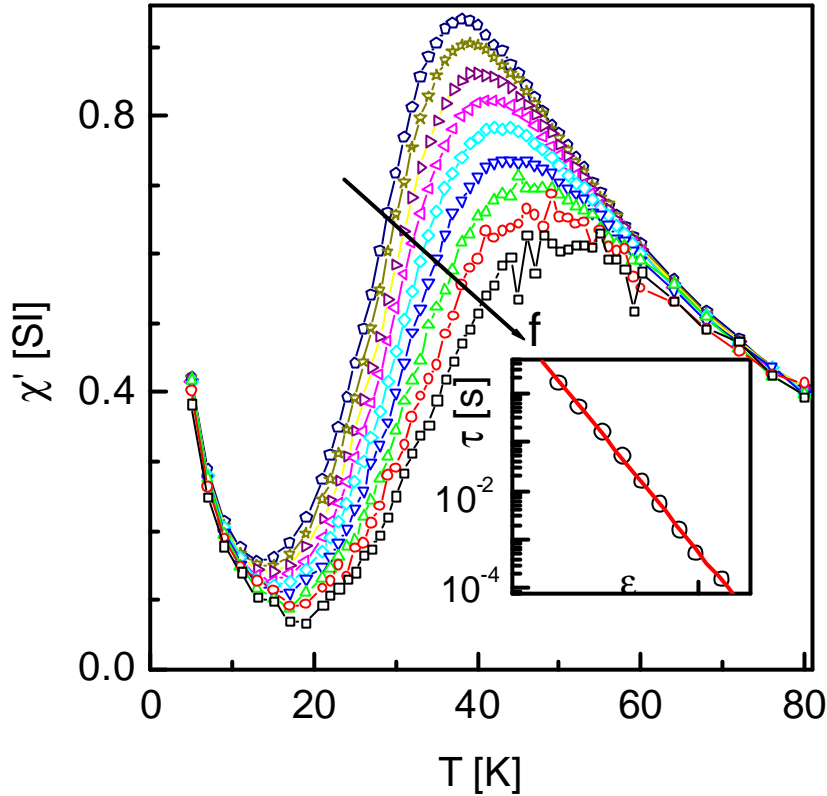

Figure 4.15: Temperature dependence of the real part of the ac susceptibility c' of $[Co_{80}Fe_{20}(0.7 \text{ nm})/Al_2O_3(3 \text{ nm})]_{10}$ measured at an ac amplitude $m_0 h_{ac} = 0.4$ mT with frequencies $f = 0.1, 0.3, 1, 3, 10, 30, 100, 300,$ and 1000 Hz, respectively. The inset shows a double logarithmic plot of t vs. e (open circles) and the best fit to a critical power law (solid line).

expected enhancement due to the dipolar interaction [2], since an energy barrier $KV/k_B \approx 150$ K is expected for isolated particles possessing bulk Co anisotropy. Together with the obvious lack of memory effects, we believe that the $t_n = 0.5$ nm sample does not represent a generic (super)spin glass system, but rather marks the crossover into the regime of dipolarly interacting SPM nanoparticles. It should be noticed that a tentative Arrhenius fit of the $t(T_m)$ data of the $t_n = 0.7$ nm system fails to show the expected increase of the
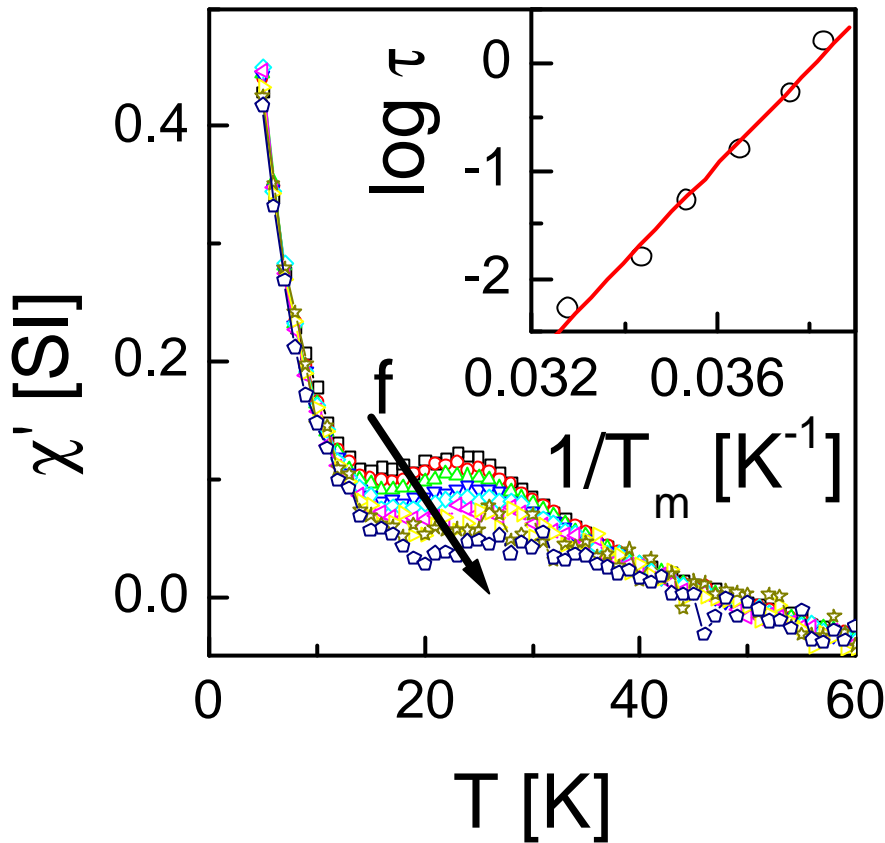
Figure 4.16: Temperature dependence of the real part of the ac susceptibility c' of [Co$_{80}$Fe$_{20}$(0.5 nm)/Al$_2$O$_3$(3 nm)]$_{10}$ measured at an ac amplitude $m_0 h_{ac}$ = 0.4 mT with frequencies f = 0.1, 0.3, 1, 3, 10, 30, 100, 300, and 1000 Hz, respectively. The inset shows a double logarithmic plot of t vs. e (open circles) and the best fit to an Arrhenius law (solid line).

energy barrier in proportion to the particle volume when assuming the same interaction-based increase as in the case t_n = 0.5 nm. Instead of $E/k_B \approx$ 1300 K the fit merely yields $E/k_B \approx$ 700 K, which clearly disproves a possible description as a dipolar interaction-modified nanoparticle system. Needless to say that the very existence of the memory effect in this case is much more convincing of cooperative glassy behavior than any fit of $t(T_m)$ selected out of the wide spectrum of relaxation times. SSG freezing has also been observed in a DMIM sample with t_n = 0.9 nm from the same batch with a spin-glass freezing temperature $T_g \approx 44K$ [73, 96].

To conclude this part, all of our representative experiments have unequivocally discriminated between the individual SPM blocking and collective SSG freezing in two DMIM samples with $t_n = 0.5$ nm and 0.7 nm, respectively. Dipolar interaction and random distribution of anisotropy axes of single domained ferromagnetic nanoparticles in the DMIM system $[Co_{80}Fe_{20}(t_n)/Al_2O_3 (3nm)]_{10}$ with $0.5 < t_n \leq 1.05$ nm, give rise to superspin glass behaviour. The collective SSG behaviour has been evidenced by *ac*-susceptibility measurements, memory-imprint and rejuvenation effects. Another significant discovery was the TEM-undetectable "dark" or "glue" particles surrounding the CoFe big nanoparticles. Contributions of atomic clusters (glue particles) have been observed in all of our DMIM samples at lower temperatures [185].

4.3.2. Superferromagnetic (SFM) domain states in DMIMs at intermediate concentration (1.05 nm < t_n < 1.4 nm)

In this section the focus will be on the DMIM samples with intermediate concentrations. At these concentrations the particle diameters slightly increase implying smaller inter-particle distances. However, the samples do not   display the physical 3D percolation yet, but have a close packing of nanoparticles. Due to the strong inter-particle interaction a collective ferromagnetic long-range order can be established, which is called superferromagnetic (SFM). This SFM state will be evidenced by several techniques, and SFM domain images will also be shown in this section.

4.3.2.1. Evidence of domain state

In the following the SFM domain state will be evidenced by several unique techniques such as SQUID magnetometry and *ac* susceptometry, dynamic hysteresis by magneto-optic Kerr effect, magnetic relaxation along with aging and memory effects and polarized neutron reflectivity.

4.3.2.1.1. Static and dynamic hysteresis

The samples studied in this thesis are very soft magnetic as can be seen from the *dc* magnetization curves M vs the magnetic field m_0H at different temperatures, T (between 150 and 520 K) shown in Fig. 4.17. Both the coercive field, H_c, and remanence, M_r, decrease monotonically as T increases, the latter reaching zero at $T_c \approx 510$ K. Rounded hysteresis loops indicate soft ferromagnetism, which partly demagnetizes in zero field either via domain formation as in permalloy or m metal or via spin fanning due to random anisotropy [186].

The thermoremanent magnetization, M^{TRM}, shown in Fig. 4.18 is recorded after field cooling (FC) in 0.44 mT from 520 to 380 K, then switching off the field and measuring upon heating. Since $M^{TRM}(T)$ qualitatively reflects the behavior of the ferromagnetic order parameter, the curve hints at a critical temperature, $T_c \approx 510$ K, confirming the previous result from M vs. m_0H measurements (Fig. 4.17) [43]. The data shown here have been corrected for the diamagnetic moment of the sample holder and a systematic vertical shift being probably an artefact of the thermal expansion of our sample holder (See section 3.6) [122].
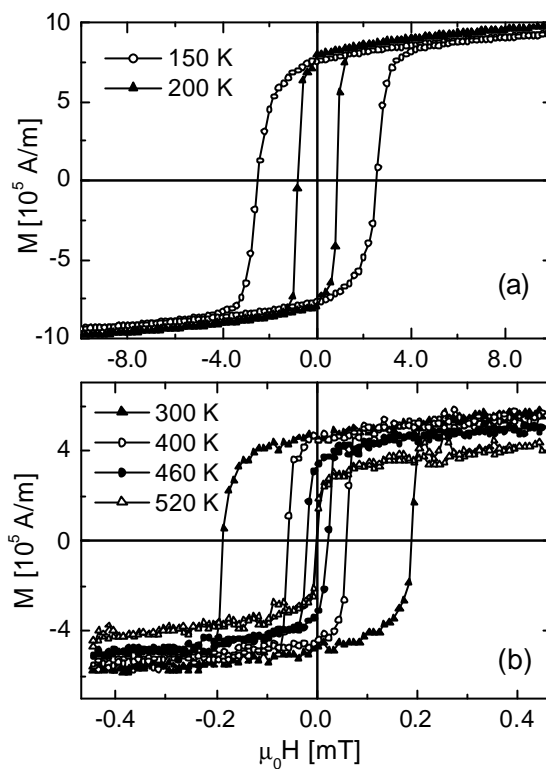
Figure 4.17: Magnetization vs. applied field for a DMIM sample [$Co_{80}Fe_{20}$(1.3 nm)/Al_2O_3(3 nm)]$_{10}$ at T = 150 and 200 K and (b) at 300, 400, 460 and 520 K. The magnetization curves shown here are measured on two different pieces of the same sample, which might explain the different saturation magnetization values.
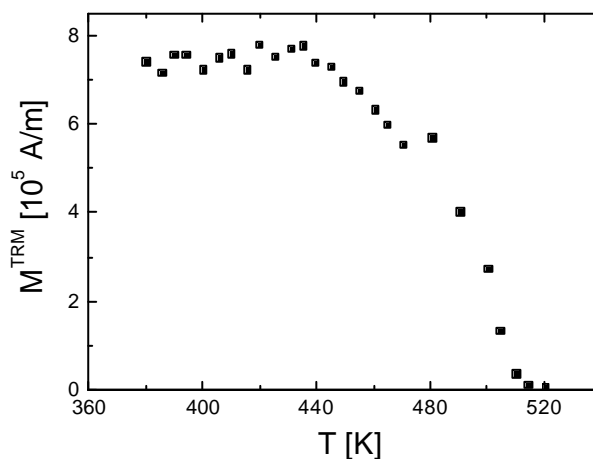

Figure 4.18: Thermoremanent magnetization (M^{TRM}) of a DMIM sample [$Co_{80}Fe_{20}$(1.3 nm)/Al_2O_3(3 nm)]$_{10}$ measured after field cooling in $\mu_0 H$ = 0.44 mT vs. temperature.

The dynamical stabilization of the hysteresis is verified by dynamic MOKE loops as shown in Fig. 4.19 measured at room temperature and frequencies $0.005 \leq f \leq 10$ Hz. The area of the hysteresis loop and the coercive field H_c increase as the frequency of magnetization reversal is increased similarly to dynamic hysteresis loops observed on conventional ferromagnetic ultrathin films, *e.g.*, Fe/GaAs [187]. As will be discussed later, relaxation processes are involved, which are controlled by time dependent domain
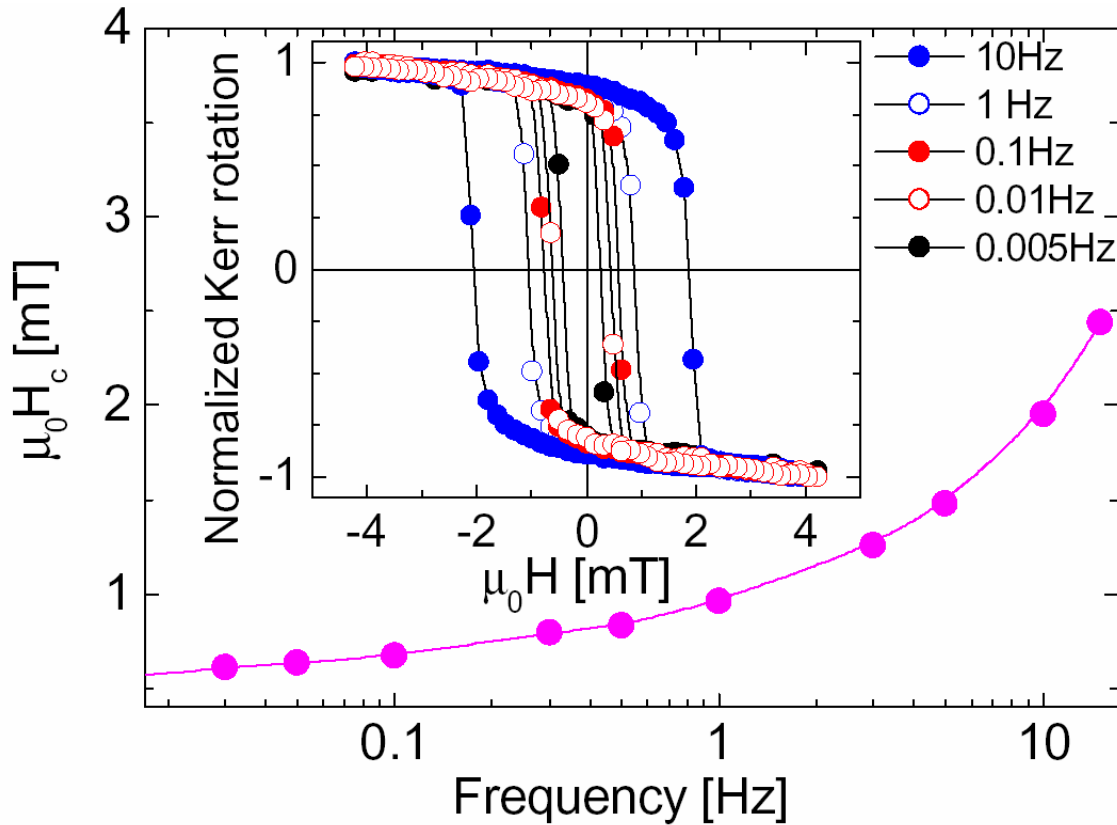

Figure 4.19: Frequency dependence of the dynamic coercive field including the quasistatic SQUID result at $f = 0.001$ Hz of a DMIM sample [Co$_{80}$Fe$_{20}$(1.3 nm)/Al$_2$O$_3$(3 nm)]$_{10}$. Inset: Normalized longitudinal magneto-optic Kerr effect loops obtained at room temperature and $f = 0.005, 0.01, 0.1, 1$ and 10 Hz, respectively.

nucleation and growth. The coercive field is best described by the function $\mu_0 H_c(f) = \mu_0 H_{c0} + b f^a$ with the static coercivity $\mu_0 H_{c0} = 0.20 \pm 0.02$ mT and the dynamic exponent $a = 0.5 \pm 0.1$ (solid line). Obviously, for fields smaller than $\mu_0 H_{c0}$,

switching is inhibited for arbitrarily low frequencies, $f \to 0$, as confirmed by Kerr microscopical imaging (see section 4.3.2.2.).

4.3.2.1.2. *ac* susceptibility measurements and Cole-Cole plots

Magnetic systems exhibiting relaxational phenomena can be characterized by the complex *ac* susceptibility, $c(w) = c'-ic''$. The time dependent complex *ac* susceptibility is defined as

$$M(t) = \tilde{c}(t)\tilde{H}(t), \tag{4.7}$$

with the *complex* external *ac*-field $\tilde{H}(t) = -iH_0 e^{iwt}$, where $h(t) = \text{Re}(\tilde{H}(t))$, and the complex magnetization $M(t)$. In this section, we study the time-independent term of the Fourier series for $\tilde{c}(t)$

$$\tilde{c}_n = \frac{1}{t_c} \int_0^{t_c} dt\, \tilde{c}(t) e^{i\Omega_n t}, \tag{4.8}$$

with $\Omega_n = 2pn/t_c$ and $t_c = 2p/w_0 = 1/f$, namely:

$$c \equiv c'-i\,c'' = \tilde{c}_0 = \frac{1}{t_c} \int_0^{t_c} dt\, \tilde{c}(t). \tag{4.9}$$

This defines the real and imaginary part of c, c' and c'', respectively, as follows

$$c'(w) = \frac{1}{H_0 t_c} \oint_0^{t_c} dt M(t) \sin(wt), \tag{4.10}$$

$$c''(w) = \frac{1}{H_0 t_c} \oint_0^{t_c} dt M(t) \cos(wt), \tag{4.11}$$

Or equivalently, if we define $\tilde{c}(t) = dM(t)/d\tilde{H}(t) = \dot{M}(t) \times (d\tilde{H}/dt)^{-1}$, then the real and imaginary part of susceptibility can be written as

$$c'(w) = \frac{1}{2pH_0} \int_0^{t_c} dt \dot{M}(t) \cos(wt), \tag{4.12}$$

$$c''(w) = \frac{1}{2pH_0} \int_0^{t_c} dt \dot{M}(t) \sin(wt), \tag{4.13}$$

where $\dot{M}(t) \propto v(t)$, the (mean) domain wall velocity, which is a function of the external field h and temperature T [42, 188].
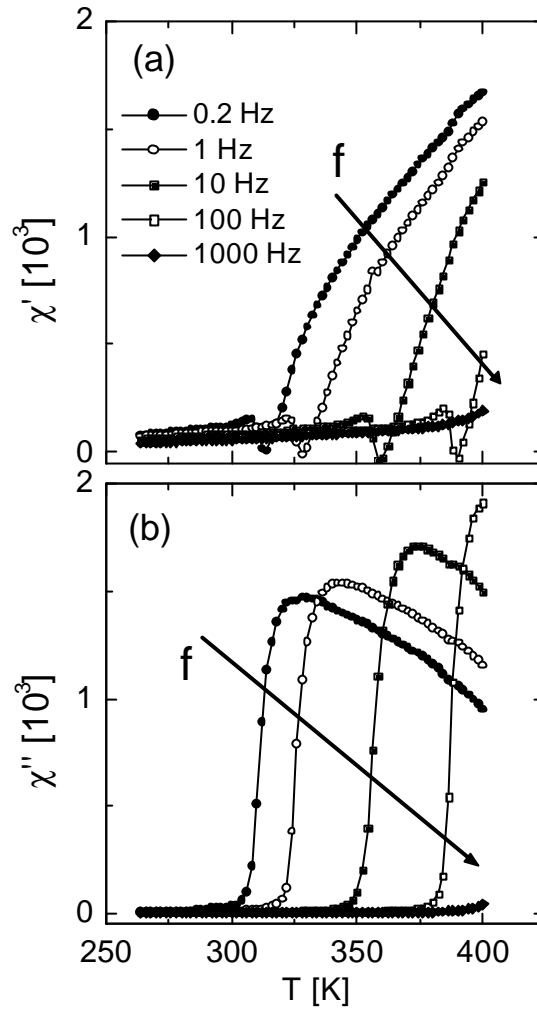
Figure 4.20: c' (a) and c'' (b) vs. *T* of [Co$_{80}$Fe$_{20}$(1.3 nm)/Al$_2$O$_3$(3 nm)]$_{10}$ measured at *ac* amplitudes $m_0 H_{ac}$ = 0.4 mT and frequencies 200 mHz ≤ *f* ≤ 1 kHz. The arrow directions indicate increasing frequency.

Fig. 4.20 shows the *ac* susceptibility components c' and c'' vs. *T* taken with amplitudes $m_0 H_0$ = 0.4 mT at frequencies 0.2 ≤ *f* ≤ 10^3 Hz for the DMIM [Co$_{80}$Fe$_{20}$(1.3nm)/Al$_2$O$_3$(3 nm)]$_{10}$ sample. In the real part Fig. 4.20 (a) one finds virtually no response at low temperatures. Only above a characteristic temperature, $T_w = T_w(f)$, c' strongly increases. Interestingly, near T_w an undershooting of the signal to negative values is observed. This behavior reflects the dynamic transition region between flat minor hysteresis and high switching loops, where parts of the loop show still an increase of the magnetization, while the field is already decreasing and vice versa. This corresponds to the

observed negative susceptibility contributions. Hence the total c' signal is reduced or even negative. The imaginary part c'' in Fig. 4.20 (b) shows a maximum near T_w corresponding to the largest area of the dynamic hysteresis loop and to the point of inflexion of the real part.
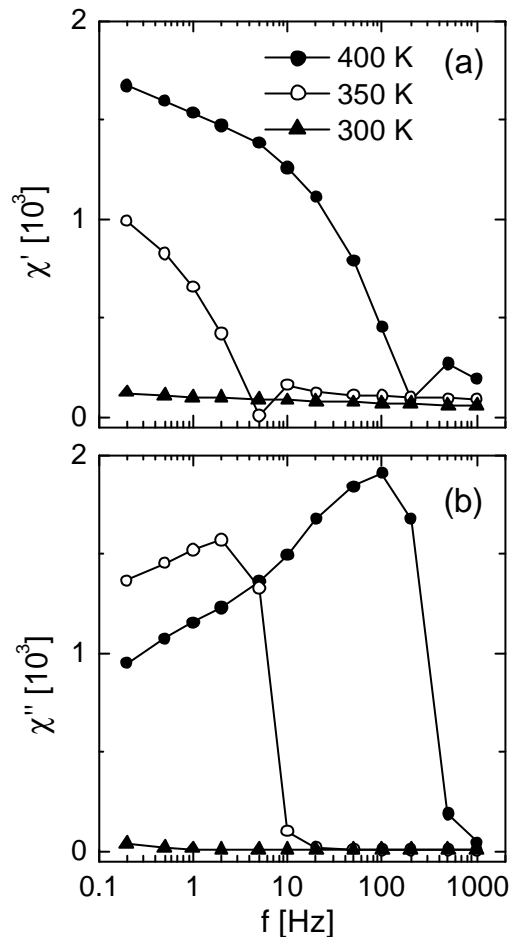
Figure 4.21: c' (a) and c'' (b) vs. frequency of $[Co_{80}Fe_{20}(1.3\ nm)/Al_2O_3(3\ nm)]_{10}$ measured at an *ac* amplitude $m_0 H_{ac} = 0.4$ mT at $T = 300$, 350 and 400 K. Data points are connected by lines.

Plotting these data as frequency spectra in Fig. 4.21 (c' and c'' vs f)) reveals a behavior being close to that found from simulations of a field-driven domain wall (DW) in a random medium [42]. Here the real part, c', shows a sharply rising response below a certain threshold frequency $f_c = f_c(T)$, while the imaginary part, c'', exhibits a peak near to f_c.

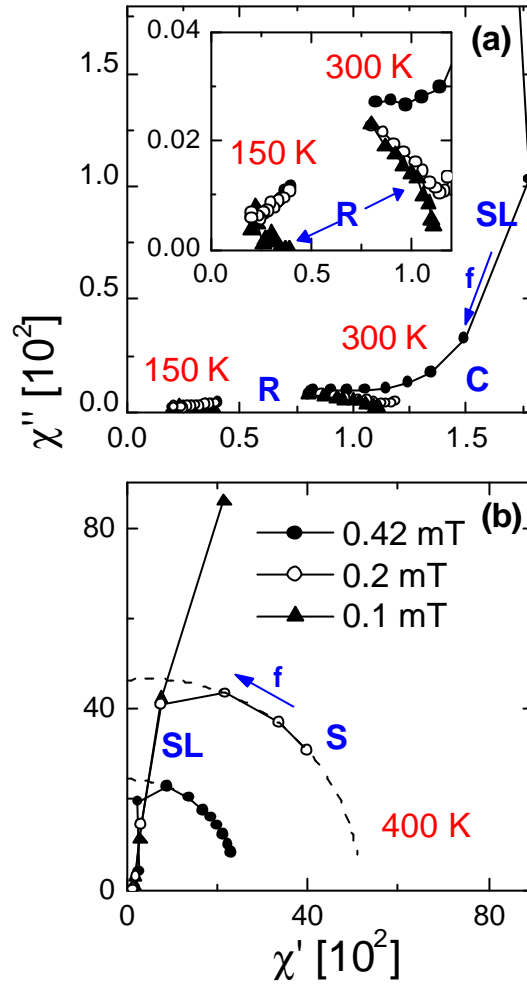Figure 4.22: Cole-Cole plots, c'' vs. c' of $[Co_{80}Fe_{20}(1.3nm)/Al_2O_3(3nm)]_{10}$ measured at *ac* amplitudes $m_0H_{ac} = 0.1$, 0.2 and 0.42 mT at 10 mHz $\leq f \leq 1$ kHz (order indicated by arrows) at $T = 150$ and 300 K (a) and 400 K (b). Data points are connected by solid lines. The data referring to 0.2 and 0.42 mT in panel (b) are fitted to quarter circles as represented by dashed lines. Dynamic regimes referring to relaxation, creep, sliding and switching are marked by R, C, SL and S, respectively. Inset in (c) shows the relaxation regime observed at 150 K.

The spectra can also be presented as Cole-Cole plots, c'' vs. c' [189], which were shown previously to be a more adequate and unequivocal method of characterizing the dynamical behavior of randomly pinned domain wall systems [13, 42]. Fig. 4.22 shows Cole-Cole plots at amplitudes $m_0H_{ac} = 0.1$, 0.2, and 0.42 mT of the *ac* susceptibility data taken at three different temperatures, $T = 150$, 300 and 400K. We are able to observe four

distinct dynamic regions: (i) relaxation, as seen from the flattened partial semi-circles at T =150 and 300 K in (a) for high frequencies designated as "R". It should be noticed that in this context the term "relaxation" means a kinetic state of motion, where the external field is not able to displace the centre of gravity of the domain walls, but merely gives rise to local hopping between adjacent free energy double wells. This mode is absent in *dc* field excitations. (ii) Creep, as found from the linear increase at 300K in (a) designated as "C". This region refers to thermally activated non-adiabatic motion of a DW. (iii) Slide, from the almost vertical parts observed at 400K in (b) designated as "SL". "Slide" is also known as the adiabatic viscous motion of the DW. Finally, (iv) switching as seen from the quarter circles in (b) designated as "S". Here the magnetization is flipped from negative to positive saturation and vice-versa. Region (i) is well understood in ferroelectric systems [190], where the DW shows a polydispersive response, while no net movement of the center of gravity of the DW is encountered. This occurs for small field amplitudes and/or high frequencies, which do not allow the DW to be released from local pinning energy potentials. Upon increase of the field amplitude the DW is locally depinned and enters the "creep" regime, which is clearly seen in (a) for $m_0 H_{ac}$ = 0.42 mT. Due to our technical limitation of $m_0 H_{ac}$ to 0.45mT, the only possibility to enter also the slide and switching regimes is to increase the temperature, *e.g.* to T= 400 K (b) [43].
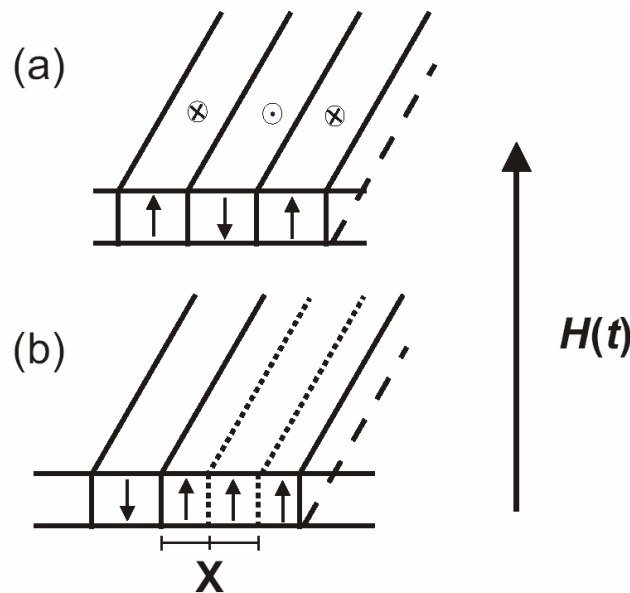

Figure 4.23: (a) Schematic drawing of up and down stripe domains of width d. (b) Displacement of domain wall by an excitation $H(t)$ [73].

The dynamic response in the four regions can be described phenomenologically as follows. Let us consider a simple stripe domain model related to up and down domains

with initial uniform width, d and magnetization, $\pm M_s$ as shown in Fig. 4.23. The sidewise motion of the domain wall by a harmonic excitation $h(t) = h_0 \exp(iwt)$ along the coordinate x will yield a time dependent magnetization,

$$M(t) = (2M_s/d)x(t). \tag{4.14}$$

Therefore the rate of the domain wall displacement can be written as

$$\frac{M(t)}{dt} = (2M_s/d)\mathbf{m}_w h(t) \tag{4.15}$$

where the wall mobility $\mathbf{m}_w$ and $h(t)$ determine the wall velocity, $dx/dt = \mathbf{m}_w h(t)$. Assuming constant $\mathbf{m}_w$ at weak fields (above the depinning threshold [191, 192]), in a constant field H, one finds a linear time dependence of the magnetization,

$$M(t) = (2\mathbf{m}_w M_s/d)Ht \tag{4.16}$$

However in a harmonic field, Eq. 4.15 can be written as

$$M(t) = (2\mathbf{m}_w M_s/iwd + \mathbf{c}_\infty)h_0 \exp(iwt). \tag{4.17}$$

Here the second term refers to the "instantaneous" reversible domain wall response occurring on shorter time scales. Weak periodic fields thus probe a linear *ac* susceptibility $\mathbf{c}^* = \mathbf{c}_\infty\left[1 + 1/(iwt_i)\right]$ with $\mathbf{c}_\infty/t_i \equiv (2\mathbf{m}_w M_s/d)$ where t_i denotes the time, in which the interface contribution to the magnetization equals the instantaneous one, $\Delta M = \mathbf{c}_\infty h$.

Further we have to account for the nonlinearity of v vs h in the creep regime of thermally excited viscous motion, $h_w < h < h_{t1}$ (= depinning field) [191, 192]. Taking the time integral of Eq. 4.15, one obtains

$$M(t) = \left(\frac{2\mathbf{m}_w M_s}{iwd} + \mathbf{c}_\infty\right)h_0 \exp(iwt) \equiv \left(\frac{\mathbf{c}_w}{iwt_w} + \mathbf{c}_\infty\right)h_0 \exp(iwt), \tag{4.18}$$

where $\mathbf{c}_w/t_w \equiv 2\,\mathbf{m}_w M_s/\mathbf{m}_0 d$ and therefore the complex susceptibility can be written as

$$\mathbf{c}^* = \mathbf{c}' - i\mathbf{c}'' = \mathbf{c}_\infty + \frac{\mathbf{c}_w}{iwt_w}. \tag{4.19}$$

Now introducing a phenomenological exponent $\mathbf{b} < 1$ and an effective relaxation time t_{eff} and considering a distribution of different domain widths, viz. d values, the complex susceptibility can be written as

$$c^* = c_\infty \left[1 + \frac{1}{\left(iwt_{eff} \right)^b} \right]. \tag{4.20}$$

The real and imaginary parts can be decomposed by multiplying Eq. 4.20 with its complex conjugate,

$$c' = c_\infty \left[1 + \cos\left(bp/2 \right) \middle/ \left(wt_{eff} \right)^b \right] \tag{4.21}$$

and

$$c'' = c_\infty \sin\left(bp/2 \right) \middle/ \left(wt_{eff} \right)^b. \tag{4.22}$$

This yields the observed linear relationship

$$c'' \middle/ \left(c' - c_\infty \right) = \tan\left(pb/2 \right). \tag{4.23}$$

The sliding regime has asymptotically a purely imaginary response c'' and can be described by $b = 1$ [13]. Both types of behavior correspond well to the results obtained from simulations of a DW in an impure FM, where $b = 1$ in case of an adiabatic and $b < 1$ in case of a non-adiabatic motion of the DW [42].

Furthermore the relaxation and switching regimes are well characterized by a Cole-Cole type expression [189]

$$c\left(w \right) = c_\infty + \frac{c_0 - c_\infty}{1 + \left(iwt \right)^{1-a}} \tag{4.24}$$

where the exponent a with $0 \leq a < 1$ is again a phenomenological exponent reflecting the polydispersivity of the system. The case $a = 0$ yields the standard Debye-type relaxator with one single relaxation time. This is applicable to the switching regime, where the dynamic behavior of the system can be understood as a monodisperse relaxation process. The relaxation time t is characterized by the total time of motion of (in the simplest case) one DW across the sample during half a field cycle. For values of $w = 2pf$ larger than $1/t$ the half-period of the field cycle becomes smaller than the intrinsic 'relaxation time' of the switching, i.e. the time the DW needs to move from one side to the other. Hence, in this frequency regime the system does not switch and enters the slide region, where both c' and c'' rapidly decrease as w increases (SL regions in Fig. 4.22 (b)). However, for $w < 1/t$ complete hysteresis loops are travelled through. They become narrower and higher

as w decreases. This is described by the right half of the Debye semi-circles ("S" regions in Fig. 4.22 (b)), whose apices correspond to $w = 1/t$ [43].

In contrast to switching the relaxation regime is described by Eq. 4.24 using $a \neq 0$, which yields a flattened semi-circle in the Cole-Cole presentation [189]. This corresponds well to the result found in experiment, Fig. 4.22 (a), where data referring to the decreasing low-f branches of the flattened circles are observed at 150 and 300 K. One should note, that the crossovers relaxation-to-creep, creep-to-slide and slide-to-switch as found in Fig. 4.22 (a) and (b) are necessarily smeared, since the applied field during the cycle naturally covers different field values and hence mixes the different modes of motion.

4.3.2.1.3. Polarized neutron reflectivity (PNR) measurements: $2q$ scans and relaxation data

As already mentioned in section 3.7, in a PNR experiment, the intensity of the neutrons reflected from a surface is measured as a function of the component of the momentum transfer that is perpendicular to the surface, $q_z = 4\pi \sin q / l$, where θ is the angle of incidence (and reflection) and λ is the neutron wavelength. We have measured reflectivity data with polarization analysis of the neutron beam, providing two cross-sections for non-spin-flip (NSF), R^{++}, R^{--}, and two for spin-flip (SF), R^{+-} and R^{-+}, reflectivities. The NSF data, R^{++} and R^{--}, depend on the chemical structure, as well as on the projection of the in-plane magnetization parallel to the applied field. The SF cross sections, R^{+-} and R^{-+}, arise solely from the projection of the in-plane magnetization perpendicular to the applied field [193].

Polarized neutron reflectivity (PNR) under small angles has been performed with the HADAS reflectometer at the Jülich research reactor FRJ-2 (DIDO) [142, 143]. Our PNR measurements were performed at 150 K with polarization analysis simultaneously over the whole range $q \gg 3°$ of scattering angles. At this temperature the coercive field is $m_0 H_c \approx 2.5$ mT, while the sample almost saturates at 10 mT (Fig. 4.17(a)). The wavelength of the neutron beam is 0.452 nm and the magnetic field was always applied parallel to the sample plane and to the easy axis.
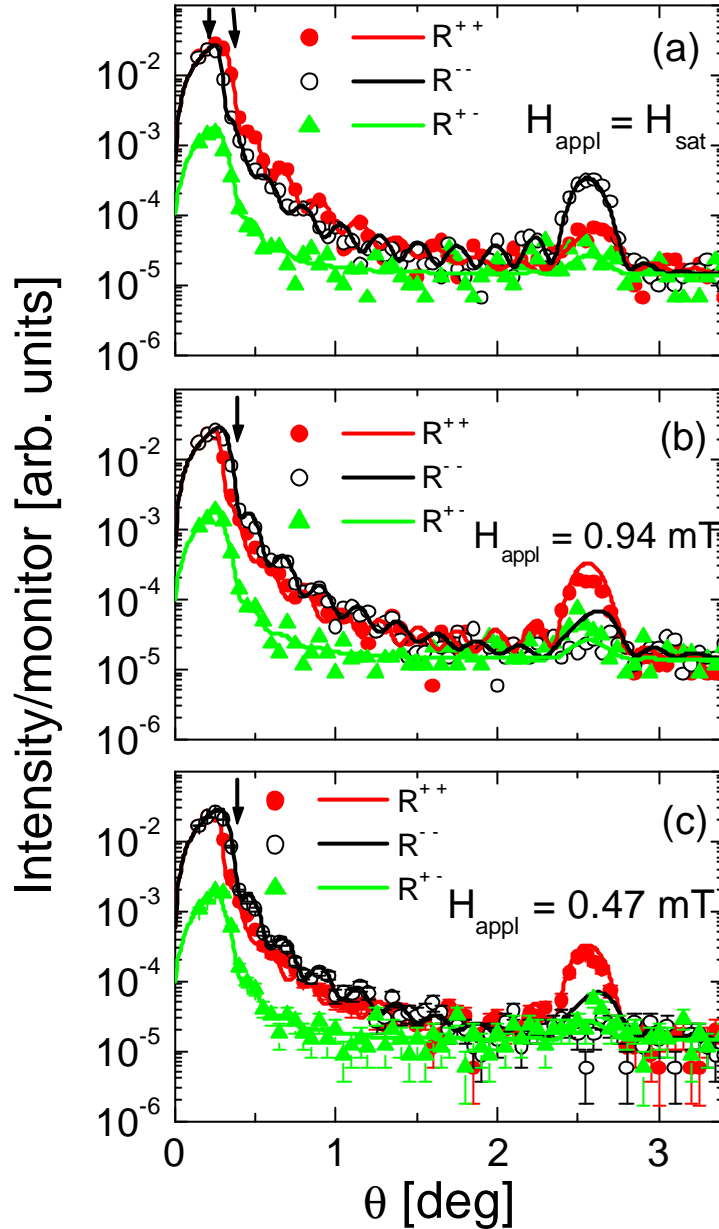
Figure 4.24: PNR reflectivities R^{++} in red (dark gray), R^{--} in black and R^{+-} in green (light gray) vs. q measured at $T = 150$ K and $m_0 H = 12$ mT (saturation) (a) and close to remanence at the guiding field of the neutrons, $m_0 H = 0.94$ mT (b) and at $m_0 H = 0.47$ mT (c), after negative saturation measured on a DMIM sample $[Co_{80}Fe_{20}(1.3 \text{ nm})/Al_2O_3(3 \text{ nm})]_{10}$. The limits of total reflection, Q_c^{++} and Q_c^{--} are designated by vertical arrows in (a). The vertical arrow at $q = 0.35°$ in (b) refers to the scattering data in Fig. 4.25. Errors bars (not shown) are smaller than 0.001 arb. units and removed for sake of clarity.

The PNR data shown in Fig. 4.24(a) were taken at positive saturation (12 mT). The FM state of the sample can be recognized by the splitting of the reflectivity edges where $R^{++}(\boldsymbol{q})$ is shifted to higher angles in comparison to $R^{--}(\boldsymbol{q})$. This can be explained as follows. The critical scattering vectors Q_c, below which the neutrons are totally reflected, are different for the (++) and (- -) states according to [141]

$$Q_c = \left[16\boldsymbol{p}N\left(b \pm p\sin\boldsymbol{f}\right)\right]^{1/2} , \tag{4.25}$$

where b and p are the nuclear and magnetic scattering lengths, respectively. N is the atomic or nuclear number density. For a non-magnetic matrix Q_c is $\left(16\boldsymbol{p}Nb\right)^{1/2}$. $\boldsymbol{f}$ is the angle between the direction of magnetization of the sample to the spin-flip axis as shown in Fig. 3.8 [141]. When the magnetization in the sample is parallel to the guiding field, corresponding to $\boldsymbol{f} = 90°$, we arrive at $Q_c^{++} = \left[16\boldsymbol{p}N\left(b + p\right)\right]^{1/2}$ and $Q_c^{--} = \left[16\boldsymbol{p}N\left(b - p\right)\right]^{1/2}$, respectively. Inserting the nuclear scattering lengths of CoFe and Al_2O_3, i.e. 4.4 and 5.1 fm, [194] respectively, and the magnetic scattering length of CoFe, i.e. 1.7 fm [195], one obtains $Q_c^{++} > Q_c^{--}$ (see arrows in Fig. 4.24 (a)). For the superlattice Bragg peak the contrast is determined by the difference between $(b+p)$ and $(b-p)$ of CoFe compared to b of Al_2O_3. Hence in the positively saturated state the superlattice Bragg peak occurs in the R^{--} channel. This is seen in Fig.4.24 (a) where the first order structural superlattice Bragg peak at $\boldsymbol{q} = 2.56°$ is dominant in the R^{--} channel. Its position corresponds to a bilayer thickness $d \approx 5$ nm in agreement with the X-ray results shown in Fig 4.2. The presence of a weak signal in the two SF channels R^{+-} and R^{-+} is primarily due to the finite flipping ratio of 18 corresponding to a limited efficiency of 94 % for the polarization analysis.

The PNR data shown in Fig. 4.24 (b) and (c) were taken at weak magnetic fields of 0.94 mT and 0.47 mT, respectively, after negatively saturating the sample. They correspond to the negative remanence as confirmed by the small angle data close to the plateau of total reflection, *e.g.* at $\boldsymbol{q} = 0.35°$ (arrow), where $R^{--} > R^{++}$. The first-order structural superlattice peak at $\boldsymbol{q} = 2.56°$ is here dominant in the R^{++} channel, confirming that the net magnetization in the sample is antiparallel to the external field. As there is no significant spin-flip scattering, there is obviously no magnetization component perpendicular to the applied field. It is worth mentioning that PNR measurements

performed at various other points of the hysteresis loop yield no spin-flip scattering, which hints at the absence of any in-plane transverse magnetization component in the sample.
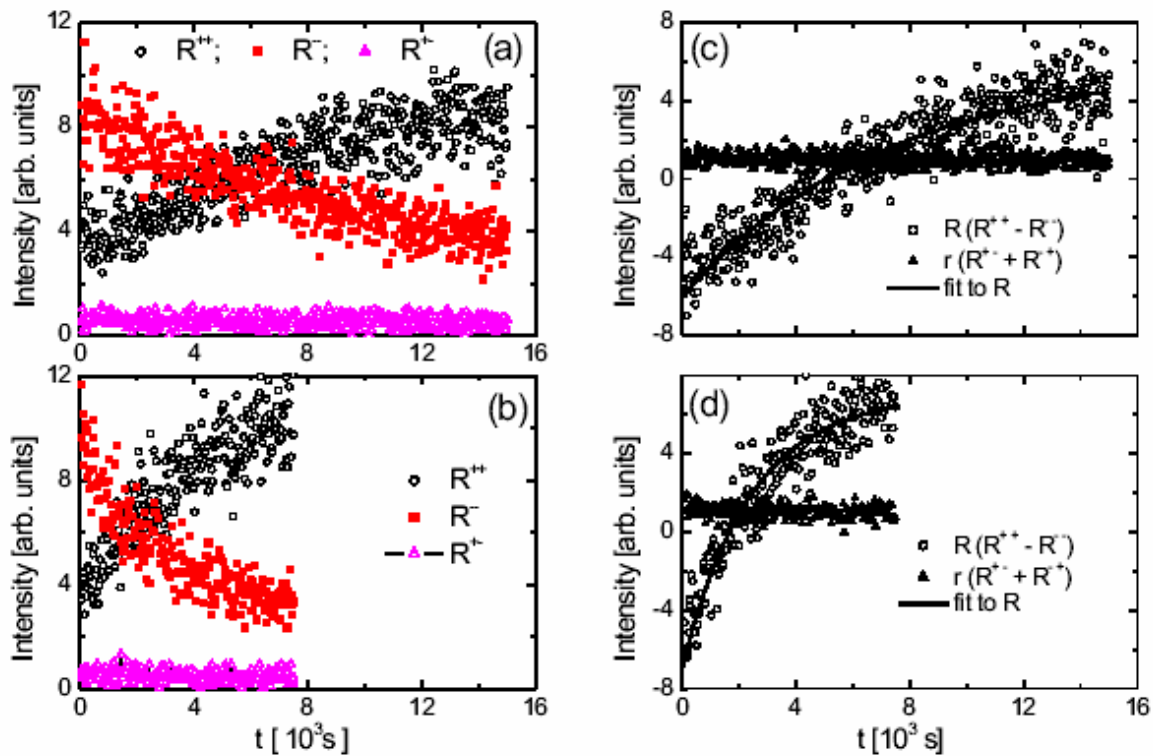

Figure 4.25: Relaxation of the neutron reflectivity components R^{++}, R^{--}, and R^{+-} vs. t of $[Co_{80}Fe_{20}(1.3\ nm)/Al_2O_3(3\ nm)]_{10}$ measured at 150 K and $2q = 0.7°$ with $m_0H = 1.7$ mT (a) or (c) and 1.9 mT (b) or (d) (close to coercivity) applied parallel to the sample plane. The spin-flip scattering component R^{-+} is omitted, since it coincides with R^{+-} (open stars). Statistical errors (not shown) are smaller than 0.001 a. u. The solid lines are best fitted to R according to Eq. 4.26 (see text).

Fig. 4.25 shows the temporal relaxation of the net magnetization at $m_0H = 1.7$ mT (a) and 1.9 mT (b) respectively, (close to the coercive field) parallel to the sample plane after coming from negative saturation as measured at $2\theta = 0.7°$, where $R^{--} > R^{++}$ (see Fig. 4.25). Hence, at the beginning of the experiments the net magnetization of the sample is still antiparallel to the applied field, but an interchange of R^{-} and R^{++} occurs after about 4×10^3 s (a) and 2×10^3 s (b), respectively [196]. Another way of expressing these relaxation data is by showing the NSF intensities as $R = R^{++} - R^{--}$ and the SF intensities

$r = R^{+-} + R^{-+}$ as shown in Fig. 4.25 (c) and (d). The NSF intensities are satisfactorily fitted by exponential decay laws,

$$R(t) = R_\infty [1 - 2\exp(-t/t)], \qquad (4.26)$$

(solid lines) with $R_\infty = 6.0 \pm 0.1$, $t = (7.2 \pm 0.1) \cdot 10^3$s and $R_\infty = 7.0 \pm 0.1$, $t = (2.40 \pm 0.06) \cdot 10^3$s, respectively. On the other hand there is no significant temporal change of r.

Within the Fatuzzo-Labrune model [197] the observed exponential magnetization reversal, Eq. 4.26, under near coercive fields seems to indicate nucleation dominated aftereffects. This appears reasonable, since domain walls in superferromagnets are presumed to cost merely stray field, but virtually no exchange energy. However, the large error bars of the relaxation curves cannot exclude deviations towards non-exponential (*e.g.* logarithmic) behavior. Indeed, both processes are clearly demonstrated by real space domain imaging using Kerr microscopy and XPEEM in section 4.3.2.2.

In order to motivate the use of R and r instead of the original data, R^{++} (t) etc., let us assume that the magnetization vector M lies in the sample plane with an angle f with respect to the horizontal X-axis (Fig.3.8). Hence, it will be perpendicular to the scattering vector Q. Next we consider [141] that a monochromatic and polarized neutron beam is incident onto the sample at a scattering angle q and that the magnetic moments of the incoming monochromatic neutrons are aligned normal to the scattering plane and parallel to the sample surface, i.e. parallel to the transverse component of magnetization M_y. Let us define V_m as the magnetic potential which the neutron experiences in the sample, which can be expressed as

$$V_m = -mB_{eff\parallel} = \left(2p\hbar^2/m\right)N_A p \qquad (4.27)$$

where m is the neutron magnetic moment, $B_{eff\parallel}$ the effective magnetic flux density in the sample plane, m the neutron mass, N_A the atomic density and p the magnetic scattering length. Then the difference of the two non-spin-flip components

$$R = 2p\sin f = 2p_y \propto M_y \qquad (4.28)$$

is proportional to the y-component of the magnetization M_y, whereas the SF reflectivities $R^- = R^{++}$ are degenerate, and

$$r = 2p\cos f \propto M_x^2 \qquad (4.29)$$

is proportional to the square of the x-component M_x.

Fig. 4.25 (a) and (b) clearly show only changes in the NSF intensities, while the SF intensities are almost constant during the measurements. Therefore one can conclude that only the longitudinal magnetization component parallel to the applied field is present in the sample whereas the transverse magnetization component is negligible. This hints at the absence of magnetization rotation and corroborates the suspected domain wall nucleation and growth processes during switching near the coercive field [13].

Similar PNR data were observed on thin films of Fe exchange coupled to antiferromagnetic FeF_2 [198], where a field close to the coercive field was applied parallel to the sample plane. The absence of SF signals during magnetization reversal was attributed to mere nucleation and growth processes of magnetic domains, which also applies to our SFM sample.

Unfortunately we did not observe any off-specular scattering, from which one could calculate the mean domain size in the sample. This might be due either to the limited scattering intensity or to the resolution limit of this PNR experiment, which cannot resolve domains being larger than $x = 30$ μm.

4.3.2.2. Observation of domains by X-ray photoemission electron microscopy (X-PEEM) and Kerr microscopy

Hitherto the SFM domain state has indirectly been evidenced by several methods such as *ac* susceptibility, dynamic MOKE hysteresis, aging, memory effects and polarized neutron reflectometry. In this section we show in a direct way homogeneously magnetized superferromagnetic domain patterns of a non-percolating DMIM imaged by means of X-ray photoemission electron microscopy and magneto-optic Kerr microscopy. Owing to the small coercive fields in the order $\mu_0 H_c \sim 0.5$ mT the search for these domains was cumbersome and necessitated very carefully prepared nucleation procedures.

Fig. 4.26 a – f shows domain images of a $[Co_{80}Fe_{20}(1.3 \text{ nm})/Al_2O_3(3nm)]_{10}$ sample at room temperature under a constant magnetic field of $\mu_0 H = 0.65$ mT, imaged by longitudinal Kerr microscopy. The magnetic field was always applied along the sample plane and the easy axis. The images were taken after negatively saturating the sample and then subsequently exposing the sample to a super-coercive field of $\mu_0 H = 0.65$ mT. Here super-coercive means that the coercive field in a dynamic hysteresis is involved, which is of course bigger than the static coercive field. In the images the dark and bright colors represent the negative and positive magnetized states of the sample.
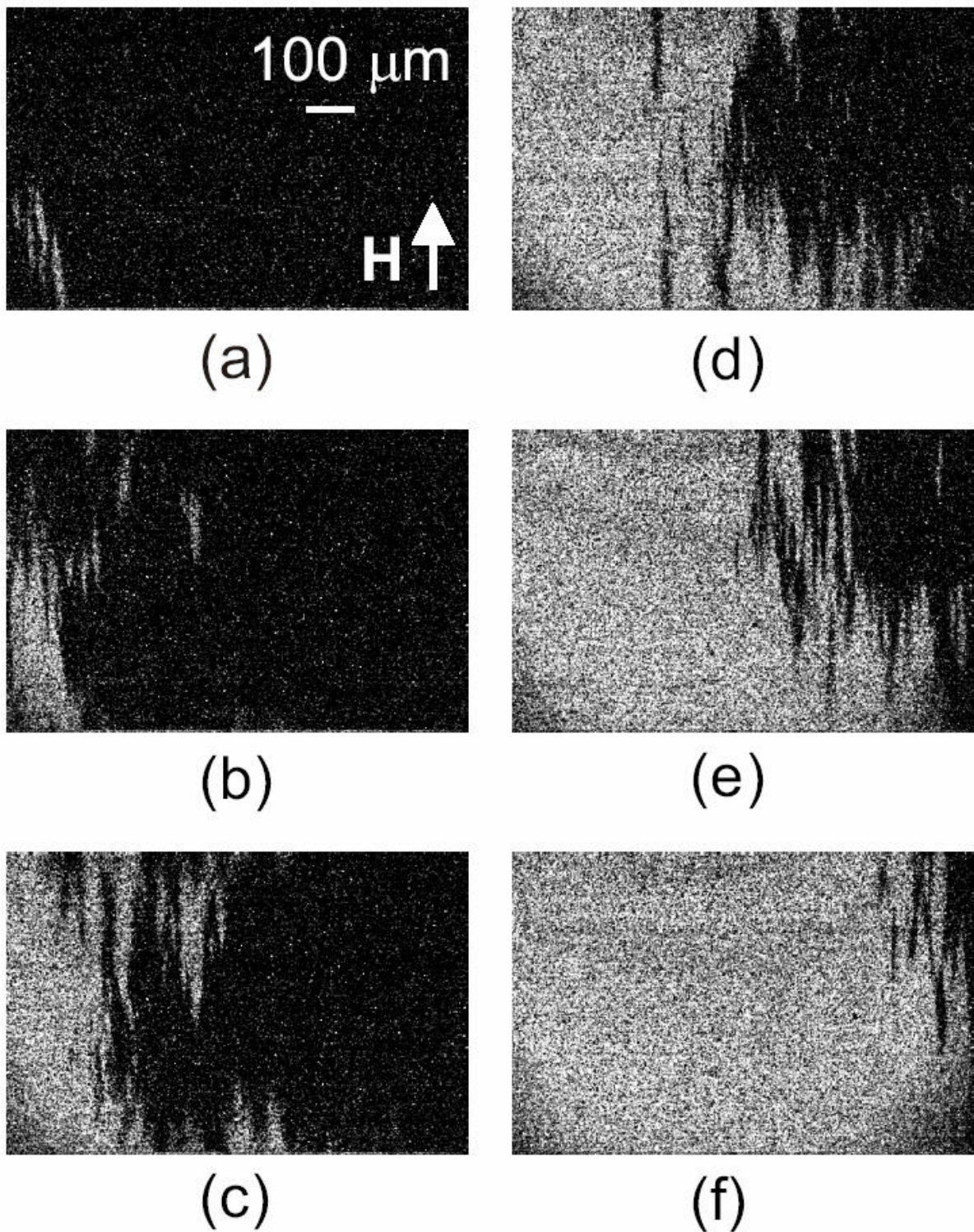
Figure 4.26: Longitudinal Kerr microscopy domain images of initially remanent $[Co_{80}Fe_{20}(1.3 \text{ nm})/Al_2O_3(3 \text{ nm})]_{10}$ at room temperature under a super-coercive field, $m_0H = 0.65$ mT, at $t = 1.5$ (**a**), 2.5 (**b**), 3.5 (**c**), 4.5 (**d**), 5.5 (**e**), and 7 s (**f**). The dimensions of the images are 980 x 700 mm^2.

The first stripe-like domains with reversed magnetization (light) appear at time $t \approx$ 1.5 s (a). In the next few seconds they are observed to extend simultaneously sideways and along the easy (= field) direction, while further domains nucleate at other sample regions. This domain growth process can be called the "sliding" [13, 43] motion as already discussed in section 4.3.2.1.2. These sideways sliding [13] and nucleation processes continue under the same constant field, until all of the down-magnetization is reversed after 9 seconds. The dimensions of the images are 980 x 700 μm^2.

As can be seen the size of the SFM domains are in the order of several tens of microns and extend upto hundreds of microns. Systematic investigations have shown that the domain nucleation rate and the velocity of subsequent wall motion can accurately be controlled by the magnitude of the external field. SFM domain images were also taken by constantly increasing the magnetic field above the super-coercive field by Kerr microscopy (not shown).

In order to study the magnetization reversal with a higher lateral resolution we performed X-ray photoemission electron microscopy (X-PEEM) at room temperature. The spatially and temporally varying magnetic fields of an electrical discharge prepared the sample into a demagnetized state, which shows an equal distribution of up magnetized (light) and down magnetized (dark) domains in the absence of an external magnetic field (Fig. 4.27 a). Lamellar domains with an irregular (probably fractal) structure oriented along the easy direction can be observed. The lamellae appear at different length scales and are similar to those shown in Fig. 4.26, *i.e.*, they show self-similarity and hole-like internal structures ("domains in domains") within the studied length scale of 0.1 - 100 µm. Reversal of the SFM domains has been probed by sweeping a current through a wire being transversely placed underneath the sample, thus generating magnetic fields $0.12 \leq \mu_0 H \leq 0.20$ mT along the easy axis. The images in Fig. 4.27 b – f (individual exposure time 120 s) show the creep-like expansion of the light domains with respect to the dark background as expected in a longitudinal sub-coercive magnetic field [13, 43].

Similar irregular domain structures have been observed in hard magnets, *e. g.* Alnico alloys [88], $Nd_2Fe_{14}B$ [199] or $Sm_2Fe_{17}N_3$ [87], consisting of precipitated single domain nanoparticles, which are only weakly exchange coupled across their grain boundaries. It has been argued that these domains are largely defined by the dipolar stray
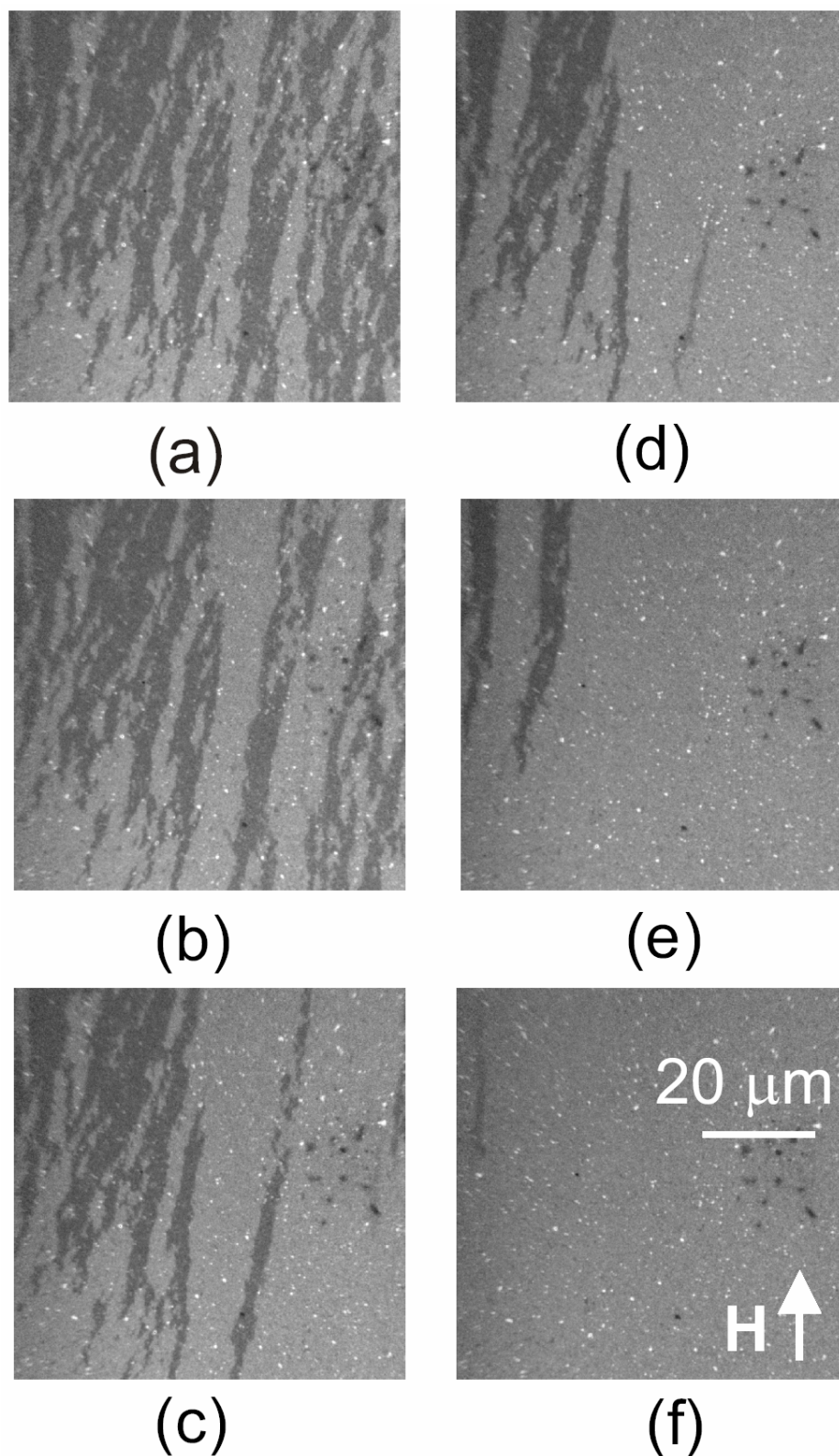
Figure 4.27: X-PEEM domain images of an initially demagnetized sample of $[Co_{80}Fe_{20}(1.3 \text{ nm})/Al_2O_3(3 \text{ nm})]_{10}$ at room temperature under sub-coercive fields, $m_0H = 0$ (**a**), 0.12 (**b**), 0.14 (**c**), 0.15 (**d**), 0.18 (**e**), and 0.2 mT (**f**). The dimensions of the images are 70 x 70 μm^2.

fields of their constituents, the ferromagnetic nanoparticles and were henceforth named "interaction domains" [88]. Qualitatively saying, in these materials after thermal demagnetization the random selection of one of the two easy directions in each grain leads to a relatively high degree of frustration between the magnetization of neighbouring grains. In contrast, the saturation of the sample selects the direction in each grain, which is closest to the applied field direction. By applying an opposite magnetic field of well defined amplitude make the sample demagnetized by creating a configuration with regions ("interaction domains") magnetized around the directions parallel and anti-parallel to the field, which makes a smaller degree of frustration [87].

4.3.2.3. Origin of SFM domains

It is quite well known that in nanoparticle assemblies, dipolar interaction being always present and being most relevant due to their long-range nature can form collective magnetic states. It has been predicted that dipolar interactions can give rise to ferromagnetic and antiferromagnetic ground states, if the particles are positioned in face centered and body centered cubic lattice sites, respectively [66]. In a system of randomly distributed magnetic particles a competition of different spin alignments can be expected. Thus, the nature of the low temperature state of such a frustrated system will resemble that of a spin glass state in many respects. Indeed, very recently the seemingly clear indication of a remanent moment in a random superspin ensemble after FC [63] has been cast in doubt by Bunde and Russ [67], who found that finite size artefacts might have been responsible for the SFM signature in their previous calculations [63].

In this new situation it should be noticed that the suspected glassiness of the ground state of a concentrated dipolarly coupled spin system [65] can be lifted when adding, *e.g.*, a small ferromagnetic interaction between the particles. This was shown by Kretschmer and Binder [68], who predicted a ferromagnetic ground state in a simple cubic dipolarly coupled Ising system upon introducing weak positive nearest neighbor exchange, $J > 0$, in addition to the dipolar long-range interactions. This idea motivates us to believe that some exchange interaction in addition to dipolar interaction might be the key ingredient to form a stable SFM ground state as found experimentally [12, 13, 43]. This idea is corroborated by the discovery of atomically small magnetic clusters (consisting of one atom or ion, or just a few atoms) surrounding the magnetic nanoparticles in discontinuous $Co_{80}Fe_{20}/Al_2O_3$-multilayers as described in section 4.3.1. They were undoubtedly identified by the Curie-

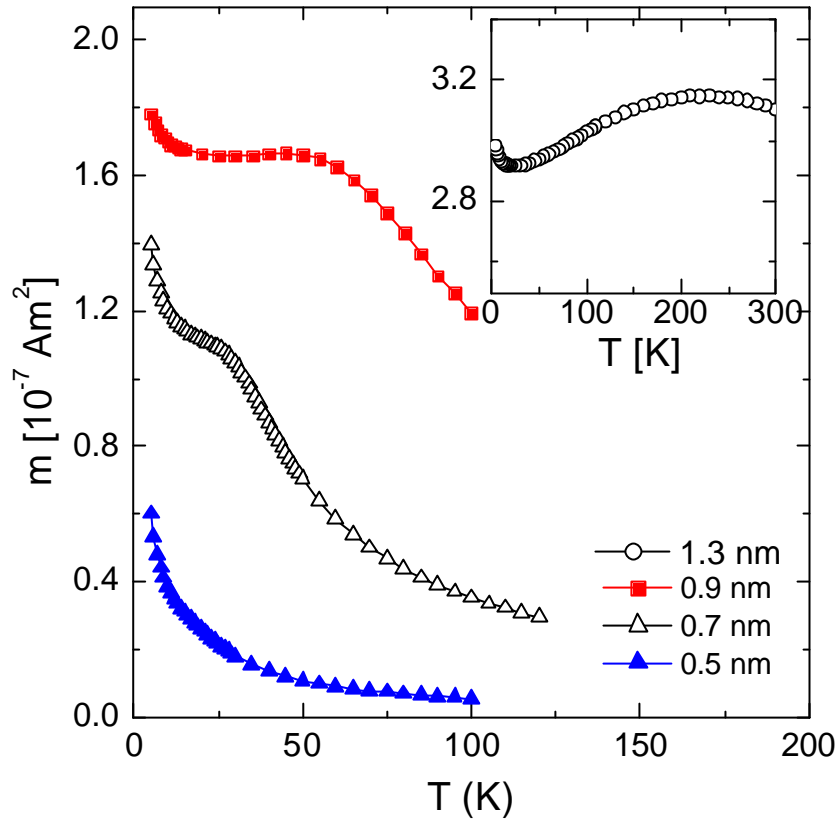Figure 4.28: Temperature dependence of m^{FC} of $[Co_{80}Fe_{20}(t_n)/Al_2O_3(3\ nm)]_{10}$ with $t_n = 0.5$ (solid triangle), 0.7 (open triangles), 0.9 (solid squares), and 1.3 nm (open circles in the inset) respectively, measured in $\mu_0 H = 10\ mT$.

type behavior of their magnetization and could be counted according to their Langevin behavior in a magnetic field as already discussed in section 4.3.1 [174]. It is preliminarily argued [200] that these "dark" or "glue" particles - invisible to transmission electron microscopy (TEM) - might be at the origin of superferromagnetism via transferred tunneling exchange interaction.

Fig. 4.28 shows the temperature dependence of m^{FC} measured in $\mu_0 H = 10\ mT$ of $[Co_{80}Fe_{20}(t_n)/Al_2O_3(3\ nm)]_{10}$ with different nominal thickness such as 0.5, 0.7, 0.9 and 1.3 nm samples, respectively. The low temperature increase of m^{FC} in the superferromagnetic sample (inset of Fig. 4.28) is also clearly seen similar to the samples with small t_n. This finding is supported by preliminary FMR measurements on these samples. Additional paramagnetic signal has been observed at lower temperatures for DMIM samples with $t_n = 0.9$ and 1.3 nm (data not shown). Further FMR measurements have to be performed in order to study the effects of these glue particles [178].

The findings of these glue particles made us believe that the weak exchange, mediated by these ultrasmall ("glue") particles, is the additional key ingredient to dipolar interaction which leads to the SFM domain state. Therefore these SFM domains grow during the magnetization reversal under the constraint of very weak interparticle exchange coupling and dominating dipolar coupling. While the weak exchange, mediated by ultrasmall particles (see above), warrants collinearity of the magnetization under saturating external field conditions, a reversing opposite magnetic field tends to cancel the weak exchange field and thus activates the competing forces of the dipolar interaction. At coercivity the SFM single domain, hence, easily breaks up into antiparallel stripes, which obviously minimize the magnetostatic energy of magnetized chains along the easy direction (Fig. 4.26 and 4.27).

It will be interesting to model this SFM scenario with realistic parameters. In the future, Monte Carlo simulations are to be performed with a simple model for magnetic nanoparticles in which we consider the anisotropy energy, the field energy, the dipolar interaction, the polydispersivity of randomly distributed single particles of different size ("superspin") and an additional exchange interaction between nearest neighbor nanoparticles (mimicking the exchange transferred by ultrasmall magnetic particles) to find possible SFM ground states.

4.3.2.4. Nature of the SFM state

There has been a long-standing and heavily disputed debate on a possible collective ferromagnetic state building up in a system of single domained ferromagnetic nanoparticles. Indirectly such a collective superferromagnetic domain state has been evidenced in non-percolated DMIMs by several means such as dynamic hysteresis, *ac*-susceptibility and the corresponding Cole-Cole plots, magnetic aging, memory effects, and polarized neutron reflectivity. Finally, the domains have been imaged by magneto-optic Kerr microscopy and X-ray photoemission electron microscopy. The SFM phase is single-domained in the field range between saturation and remanence as visualized by magneto-optic microscopies. Its magnetization reversal is controlled by the interplay of dipolar, exchange and external magnetic fields involving fuzzy-shaped "interaction domains". As being classic for ferromagnets all along [15], domain visualization has provided an ultimate proof of the long suspected [56, 82] state of "superferromagnetism".

4.3.3. DMIMs beyond percolation (1.4 nm < t_n < 1.8 nm)

In this section we will discuss the magnetic properties of the percolated DMIM systems [CoFe(t_n)/Al$_2$O$_3$(3nm)]$_9$ where t_n = 1.6 and 1.8 nm. As already discussed in section 4.1, physical percolation occurs at t_n = 1.4 nm evidenced by electric resistance measurements. It is already mentioned that with increasing nominal thickness, the size of the particles grow and therefore the inter-particle distance decreases. Similar growth mechanism has been studied in other DMIM systems such as Co/Al$_2$O$_3$ granular multilayers [166]. There, it has been found that at certain nominal thickness before physical percolation, the height of the nanoparticles does not increase and the particles only grow laterally. Assuming similar mechanism, in our DMIM samples the average diameter will be around 3-5 nm and at percolation the sample structure will be a network of elongated particles. As expected, the percolated samples will behave like continuous thin ferromagnetic thin films. However, the main point of discussion in this section will be the interlayer coupling. Because of the presence of Al$_2$O$_3$ layers between consecutive CoFe layers, RKKY interaction is excluded. But due to its long-range nature the dipolar interaction will be the dominating interaction between the CoFe layers. Additionally we expect another interaction between adjacent CoFe layers. It is called "Néel coupling" and mainly arises due to correlated roughness. It is well known that dipolar interaction tries to make an anti-parallel arrangement between adjacent layers, whereas Néel coupling is ferromagnetic and tries to make a parallel arrangement. So in a system of two layers there will be a competition between these two interactions when finding out the stable ground state. The situation will look more complex when taking a system consisting of many layers. To find a better understanding of this scenario, we have performed PNR measurements on DMIM samples with t_n = 1.6 and 1.8 nm, and also performed some micromagnetic simulations to understand the phenomena.

4.3.3.1. Magnetization hysteresis

Fig.4.29 (a) shows the *dc* moment *m* vs. the magnetic field m_0H of a DMIM sample [CoFe(1.6 nm)/Al$_2$O$_3$(3nm)]$_9$ measured at T = 150 K. Here the magnetic field was applied parallel to the film plane and to the easy axis. The measurement reveals a square-like hysteresis as expected for a ferromagnetic thin film. To check, if there is any polar component of magnetization present in the sample, magneto-optic Kerr magnetometry was performed at room temperature. Fig.4.29 (b) displays the magneto-optic longitudinal (open triangles) and polar (solid triangles) Kerr rotation intensity at T = 300 K. As can be seen,

the polar component of magnetization in the sample is absent, i.e. the sample magnetization lies in the film plane. However, any in-plane transverse component can be present, but this is also excluded by polarized neutron reflectivity measurements which will be described next.
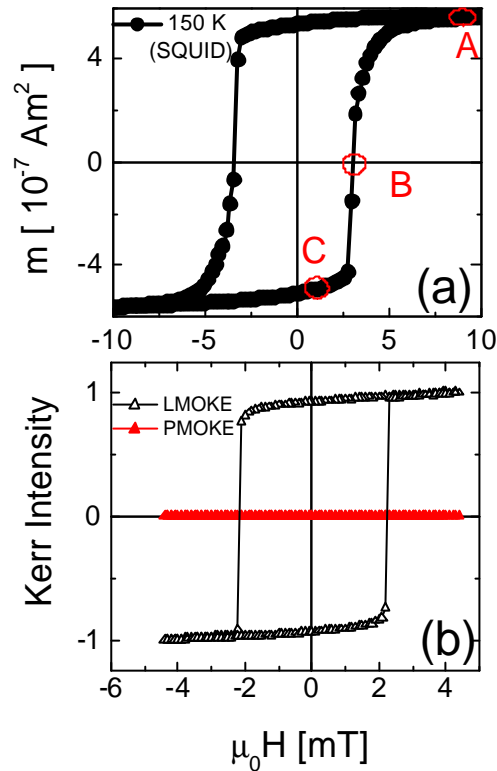

Figure 4.29: (a) Magnetic hysteresis of the ferromagnetically interacting nanoparticle system $[Co_{80}Fe_{20}(1.6 \text{ nm})/Al_2O_3(3 \text{ nm})]_9$ at $T = 150$ K measured by SQUID magnetometry. (b) The normalized longitudinal (open triangles) and polar (solid triangles) MOKE intensity. The labels (A), (B) and (C) mark the points on the hysteresis, for which PNR measurements are shown in Fig. 4.30.

4.3.3.2. Modulated magnetization depth profile observed by polarized neutron reflectometry

PNR measurements under small angles were performed with the HADAS reflectometer at the Jülich research reactor FRJ-2 (DIDO) [142, 143]. We measured all four cross sections, R^{++}, R^{--}, R^{+-}, and R^{-+} for specular and off-specular (*i.e.*, diffuse) conditions. As it has been already mentioned before the non-spin-flip (NSF) data, R^{++} and R^{--}, depend on the chemical structure, as well as on the projection of the laterally averaged in-plane magnetization parallel to the neutron polarization and the spin-flip (SF) cross sections, R^{+-}

and R^+, arise solely from the projection of the in-plane magnetization perpendicular to the neutron polarization. We note that the efficiencies of the HADAS neutron polarizers were larger than 94% in external fields as small as 0.47 mT. Our PNR measurements were performed at 150 K with polarization analysis. At this temperature the coercive field is $m_0 H_c \approx 3.1$ mT and the sample almost saturates at 12 mT (Fig. 4.29(a)). The wavelength of the neutron beam is 0.452 nm and the magnetic field was always applied parallel to the sample plane and to the easy axis. The PNR data are fitted with the program based on Paratt formalism [101] is developed by Dr. E. Kentzinger and Dr. B. P. Toperverg at Forschungszentrum Jülich. Details of the PNR fitting program can be found in Ref. [201].

Fig. 4.30(a) shows PNR data taken at positive saturation (12 mT). The FM state of the sample can be recognized by the splitting of the reflectivity edges, where $R^{++}(\theta)$ is shifted to higher angles in comparison to $R^{--}(q)$ [43]. The first order structural superlattice Bragg peak at $q = 2.45°$ is dominant in the R^{--} channel. Its position corresponds to a bilayer thickness $d \approx 5.4$ nm in agreement with X-ray results (Fig. 4.3 (d)) [202]. The presence of a weak signal in the two SF channels R^{+-} and R^{-+} is primarily due to the finite flipping ratio of 18 corresponding to the limited efficiency of 94 % for the polarization analysis. The oscillatory behavior (Kiessig fringes) of R^{++} and R^{--} is due to the multilayer structure of the sample.

The PNR data shown in Fig. 4.30(c) were taken at a weak guiding field (0.47 mT) of the neutrons after negatively saturating the sample. They correspond to the negative remanence as confirmed by the small angle data close to the plateau of total reflection, *e.g.* at $q = 0.35°$, where $R^{--}(q) > R^{++}(q)$. As there is no significant spin-flip scattering, there is definitely no magnetization component perpendicular to the applied field.

Fig. 4.30(b) shows the PNR components measured at the coercive field after negatively saturating the sample. They correspond to the demagnetised state as confirmed by the small angle data close to the plateau of total reflection, where $R^{--}(q) \approx R^{++}(q)$. Interestingly, two enhanced satellites evolve around the first structural superlattice Bragg peak. Here no significant spin flip scattering was observed, which proves the absence of any in-plane transverse magnetization component in the sample. The PNR measurements performed at $m_0 H_{appl} \approx m_0 H_c + 0.04$ mT, also shows similar enhanced satellites around the first Bragg peak, except that the intensity of the R^{++} and R^{--} are slightly changed. The data are successfully fitted with a modulated magnetization depth profile from CoFe layer to
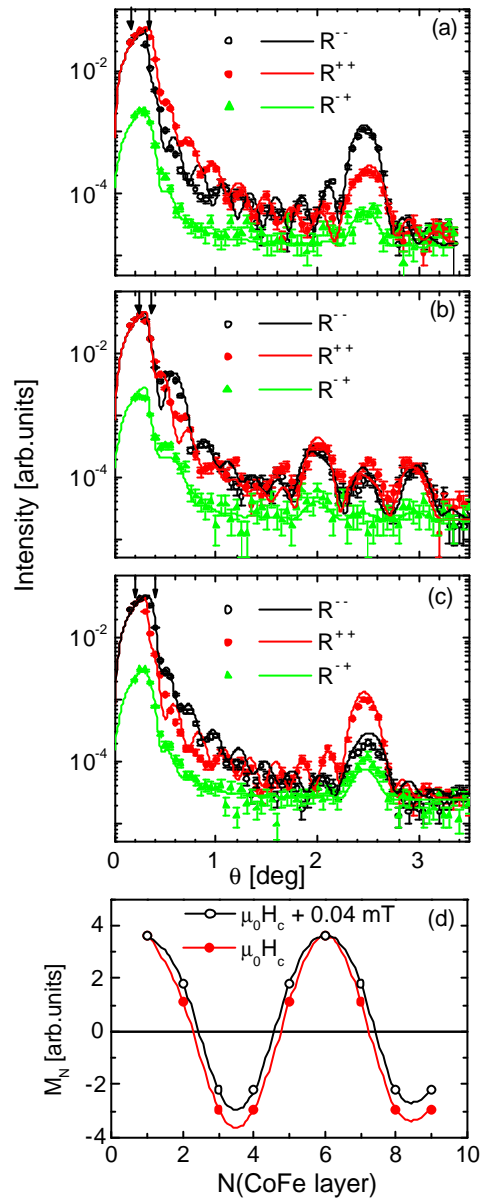
Figure 4.30: PNR reflectivities R^{++} in red (dark gray), R^{--} in black and R^{+-} in green (light gray) *vs.* angle of incidence, $\boldsymbol{q}$, of [Co$_{80}$Fe$_{20}$(1.6 nm)/Al$_2$O$_3$(3 nm)]$_9$ sample measured at $T = 150$ K and $\boldsymbol{m}_0 H = 12$ mT (saturation) (a), close to the coercive field $\boldsymbol{m}_0 H = 3.8$ mT (b), and close to remanence in the guiding field of the neutrons, $\boldsymbol{m}_0 H = 0.47$ mT, after negative saturation (c) – see Fig. 4.29. The plateaus of total reflection, Q_c^{++} and Q_c^{--}, are designated by vertical arrows. (d) Magnetization of individual CoFe layers in the multilayer stack, numbered $N = 1, \dots, 9$ and extracted from the fitting to the PNR data at H_c (b, red), and to similar data for $\boldsymbol{m}_0 H_c + 0.04$ mT (black).

CoFe layer with a periodicity of five layers (Fig. 4.30 (d)). This model is thought to be realized by different multidomain states in each CoFe layer.

Unfortunately we did not observe any off-specular scattering, from which one could estimate the average domain size in the sample. This might be due either to the limited scattering intensity or to the resolution limit of this PNR experiment, which cannot resolve domains being larger than $x \approx 30$ µm [203]. Domains bigger than few tens of micrometers are observed by Kerr microscopy which will be described in section 4.3.3.4.

Further, it is worth mentioning that PNR measurements performed at various other points of the hysteresis loop never yield SF scattering, which hints at the absence of any in-plane transverse magnetization component in the sample. Finally, the occurrence of a modulated magnetization profile as evidenced by a splitting of the first structural superlattice Bragg peak has also been observed in related samples, *e.g.*, at larger CoFe coverages in $[Co_{80}Fe_{20}(1.8nm)/Al_2O_3(3nm)]_9$ (not shown) [204]. The step observed in hysteresis loops for the DMIM samples with $t_n = 1.7$ and 1.8 nm as shown in Figure 4.6 can be also explained by the above mentioned layer-by-layer magnetization reversal [205].
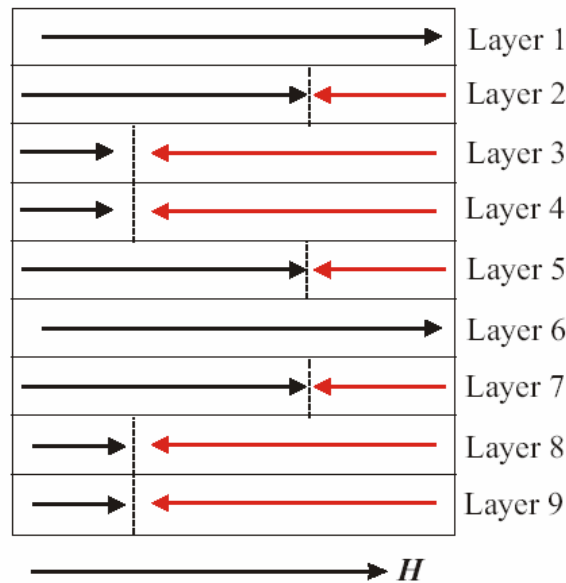

Figure. 4.31. A simple minded domain model in the multilayer stack leading to the oscillating magnetization (see Fig. 4.30(d)).

Let us discuss different interlayer coupling mechanisms responsible for this unusual modulating magnetization in magnetic multilayers. For trilayers consisting of two magnetically saturated pinhole free metallic layers separated by a conductive spacer layer,

the Ruderman-Kittel-Kasuya-Yosida (RKKY) oscillatory exchange provides a major coupling mechanism. In systems with insulating spacer layers and flat interfaces, dipolar interactions are dominant. They favor antiparallel orientation of the intraplanar magnetization between adjacent layers. For rough interfaces the so-called Néel- or orange peel interlayer coupling has to be considered in addition [206, 207, 208]. In 1962, Néel [206] pointed out that there should be ferromagnetic coupling between adjacent films due to magnetic dipoles at the interface induced by a correlated morphological corrugation. Finally, if one considers the domain structure within each layer, a magnetostatic interaction could arise between the domain-wall stray fields in a FM / N / FM structure, where N can be a non-magnetic metallic or insulating layer. Recently Lew *et al*. [209] have shown that interlayer domain-wall coupling can induce a mirror domain structure in a magnetic trilayer system, which can affect the transport properties.

Furthermore, dipolar interaction can lead to frustration effects in magnetic multilayers with in-plane magnetization direction. Generally, the long-ranged dipolar fields from one layer to the nearest layer and to the next-nearest layer will favor antiparallel magnetization. Since the nearest-neighbor interaction usually prevails, an antiparallel alignment throughout the multilayer stack will be stabilized. However, for rough interfaces, the ferromagnetic Néel interlayer coupling [206, 207, 208] must be introduced in addition. Since the next-nearest neighboring layers remain antiferromagnetically coupled a competing interaction can be encountered, which might give rise to modulated incommensurate phases [210]. This has been shown, *e.g.*, for Ising models with competing nearest- and next-nearest-neighbour interactions (**A**xial-**N**ext-**N**earest-**N**eighbour-**I**sing or so called ANNNI models). As will be shown below, our system behaves similarly when superimposing a homogeneous magnetic field, which provides matching conditions.

4.3.3.3. Micromagnetic simulation results

In order to understand the experimental observation of the magnetization reversal process in our multilayer system, micromagnetic simulations have been performed. We begin with the three-dimensional model within the object-oriented micromagnetic modeling framework (OOMMF) public micromagnetic code [211] and extend the expressions of each of its energy terms to account for a variation in thickness from one cell to the next [212]. The lateral sample size for the simulation is chosen to be 480 nm × 480 nm. We have taken 9 magnetic and 9 non-magnetic layers in an alternative arrangement. The thickness is 3.2 nm for both magnetic and non-magnetic layers. The cell size is

$10 \times 10 \times 3.2$ nm^3. For the simulation, we assume a saturation magnetization of 1.44 MA/m, which corresponds to the value for a ferromagnetic Co layer. The roughness parameter being primarily due to the initial Volmer-Weber granular growth of the single layers [12, 96, 170, 174, 213] is mimicked by using a random modulation of the saturation magnetization,
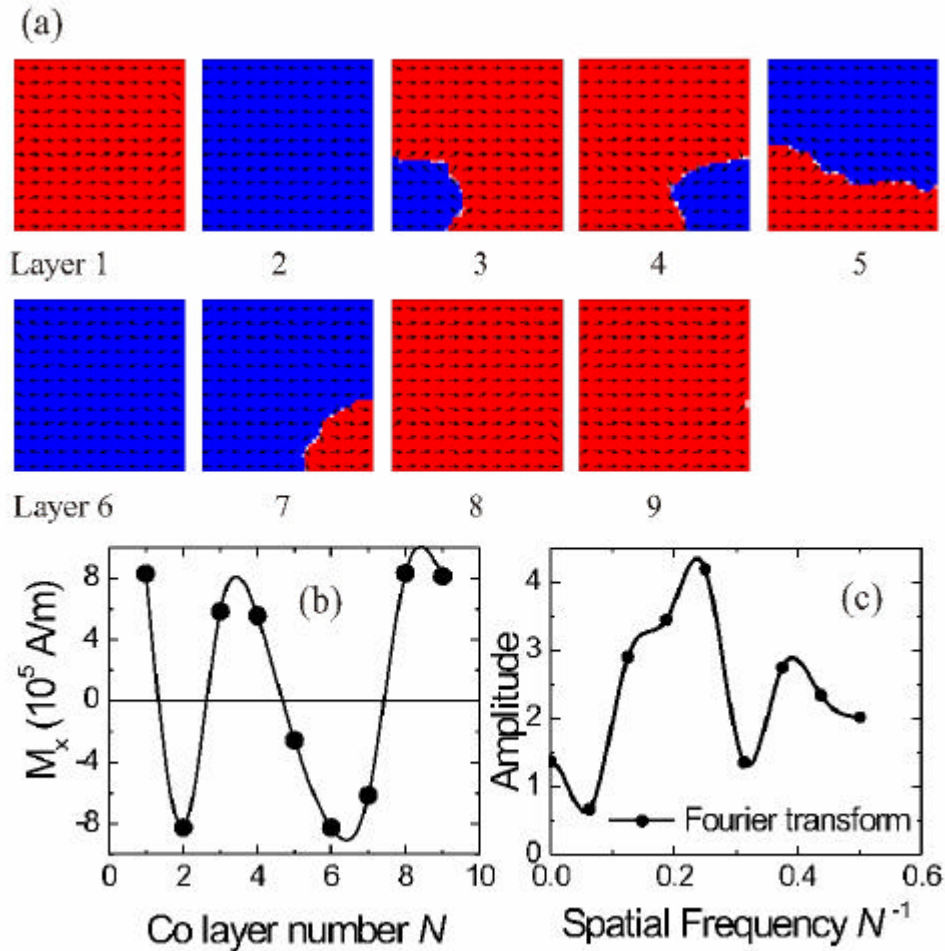
Figure 4.32: (a) Spin structure of the single layers coded M_x in red (light gray) and blue (dark gray) for $M_x > 0$ and < 0, respectively, obtained from micromagnetic simulations (see text). The layer magnetization M_x vs. distance in units of the bilayer thickness $d = 6.4$ nm and the corresponding Fourier transform in units d^{-1} are shown in panels (b) and (c), respectively.

M_s(cell) $= M_s$(Co)$-\Delta M_s \cdot$rand(0,1), where rand(0,1) is a random number between 0 and 1. In the present simulation we chose $\Delta M_s = 1.2$ MA/m. Two in-plane anisotropy terms are incorporated in the simulation (i) $K_1 = 0.05$ MJ/m^3, uniform uniaxial anisotropy expected

for our experimental system and (ii) $K_r = 0.1$ MJ/m^3, random uniaxial anisotropy in order to simulate the still present granularity of the film. The dominant interaction between the layers is dipolar interaction. Néel inter-layer coupling is realized by the roughness in the magnetic layers. The equilibrium magnetization was found by solving the Landau-Lifshitz-Gilbert (LLG) equation [214]

$$\frac{d\vec{M}_i}{dt} = -g\left(\vec{M}_i \times \vec{B}_{eff}\right) + \frac{a}{M}\left(\vec{M}_i \times \frac{d\vec{M}_i}{dt}\right),\qquad(4.30)$$

where M magnetization, a is the dimensionless damping parameter, g is the gyro-magnetic ratio and B_{eff} is the effective magnetic field. The effective field is defined as

$$\vec{B}_{eff} = -\frac{\partial E}{\partial \vec{M}}.$$

The average energy density E is a function of $\vec{M}$ specified by Brown´s equation [215], including anisotropy, exchange, self-magnetostatic (demagnetization), and applied field (Zeeman) terms [211]. Details about OOMMF simulation procedures can be found in Ref. [211].

Fig 4.32 (a) shows the magnetization spin structure in each Co layer near the coercive field, $m_0 H_c = -20$ mT. In Fig 4.32 (b), the x-component of magnetization for each Co layer is shown versus its number N, $1 \leq N \leq 9$. It is seen that the Co layers are not just oppositely magnetized, but display intermediate magnetized states. The simulation results are in agreement with the model adapted to the PNR data (Fig 4.30 (d)). As mentioned earlier, there are mainly two kinds of interactions present in the simulation: the long-ranged dipolar interaction and the Néel coupling due to the roughness of the layers. In zero external magnetic field the latter interaction obviously dominates and stabilizes the global ferromagnetic state of the multilayer. However, when applying a reverse field the ferromagnetic interaction is weakened with respect to the dipolar next-nearest neighbor antiferromagnetic interaction. That is why the multilayer experiences a kind of ANNNI interaction scheme close to the coercive field. That is why an incommensurate magnetization modulation is observed both in the experiment and in the numerical simulation. If the simulation results of the magnetization were described by a fundamental sinusoidal variation, we obtain a periodicity of 4.2d (d = bilayer thickness) in rough agreement with the observed value of $\approx 5d$. This is corroborated by a formal calculation of the Fourier transform of the magnetization in reciprocal space, which yields a peak at about 0.24d^{-1} (Fig. 4.32(c)).

4.3.3.4. Domain imaging by Kerr microscopy

The modulated magnetization depth profile is evidenced by the domain structure of the same sample observed by magneto-optic Kerr microscopy. Fig. 4.33 shows the domain image of the $[Co_{80}Fe_{20}(1.6 \text{ nm})/Al_2O_3(3 \text{ nm})]_9$ measured at room temperature and in an in-plane field of $m_0H = 2.3$ mT (close to the coercive field) parallel to the easy axis.

As seen Fig. 4.33, from the gray scale it seems as if there is one domain structure superimposed to another one (*e.g.* white marked as 2 on gray marked as 3). Since the MOKE contrast mirrors the projected local magnetization of all CoFe layer (total thickness 14.4 nm being small compared to the light wavelength 670 nm) the different gray scales evidence the heterogeneity of the layer-by layer magnetization pattern [216] as was shown by computer simulations for $t_n = 1.6$ nm recently [202].
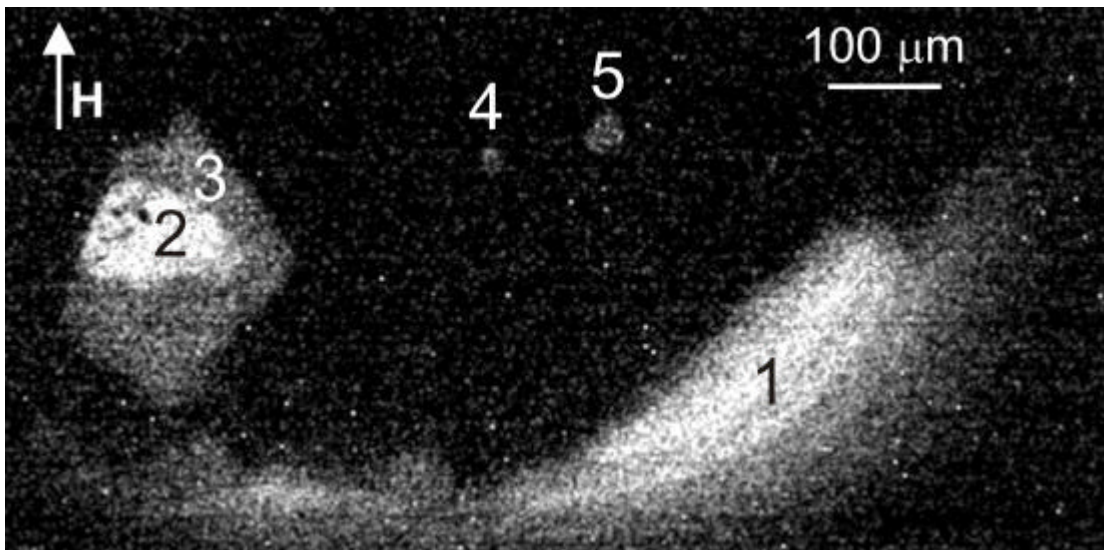
Figure 4.33: Longitudinal Kerr microscopy domain image of the $[Co_{80}Fe_{20}(1.6 \text{ nm})/Al_2O_3 (3 \text{ nm})]_9$ system at room temperature and under coercive field, $m_0H = 2.3$ mT. Different positions marked with numbers *e.g.* 1 and 2 show domains with brighter contrast as compared to less bright areas marked *e.g.* 3, 4, and 5, respectively. Position 4 and 5 show two nucleating small domains.

In summary, by polarized neutron reflectivity we have observed an oscillating magnetization depth profile in a purely dipolarly coupled multilayer. It is found that in

the demagnetized state an oscillating magnetization depth profile from FeCo layer to FeCo layer with a certain periodicity develops along the multilayer stack. Similar results have been found from micromagnetic simulations showing that the competition between ordinary dipolar and Néel coupling can indeed lead to stable domain states with oscillatory net magnetization from layer to layer. However it should be mentioned that the period will change from system to system by changing the thicknesses of the magnetic and non-magnetic layers, also with the separation between the layers and on materials. More simulations are to be done in order to understand the effects of all these parameters on the modulated magnetization depth profile in magnetic multilayers.

4.3.4. Magnetic phase diagram of DMIMs

In this chapter, we have demonstrated that by changing the nominal thickness t_n of the CoFe layer and, hence, changing the magnetic particle concentration, the magnetic properties of DMIMs $[Co_{80}Fe_{20}(t_n \text{ nm})/Al_2O_3(3\text{nm})]_m$ change strongly. As described in section 4.3.1 one finds modified superparamagnetism for a nominal thickness $t_n = 0.5$ nm, while a transition from superparamagnetism to superspin glass occurs at $t_n = 0.7$ nm [174, 186]. The occurrence of this transition from SPM to SSG at intermediate concentrations, results from non-negligible dipolar interaction between the particles and randomness of particle positions. With increase of the nominal thickness t_n, a crossover to a superferromagnetic domain state occurs at $t_n \geq 1.05$ nm [12, 217] as shown in Fig. 4.34 are the exponents obtained from relaxation measurements of DMIMs fitted to the following decay laws

$$m(t) \simeq m_0 \exp\left[-(t/\boldsymbol{t})^{1-n}\right] \quad \text{for } 0 \leq n < 1, \tag{4.31}$$

$$m(t) \simeq m_1 t^{-A} \qquad \text{for } n = 1, \tag{4.32}$$

$$m(t) \simeq m_\infty + m_1 t^{1-n} \qquad \text{for } n > 1, \tag{4.33}$$

where m_0, m_1, m_∞ and $\boldsymbol{t}$ are parameters linked to A, t_0, $m(t = t_0)$ and n [196, 217]. In agreement with predictions [63], it has been found experimentally on DMIMs that with increasing particle concentration the exponent n increases monotonically [196, 217]. In the SSG regime, the exponent n becomes smaller than 1, and in the SFM regime it becomes larger than 1 [196, 217]. It has been shown that at intermediate concentration, $n \approx 1$ in the crossover regime from SSG to SFM ($t_n \approx 1.1$ nm). The value of n is also temperature

dependent. For the DMIM sample with $t_n \approx 1.1$ nm, $n < 1$ and $n = 1$ were obtained from the $m(t)$ relaxation data measured much below the glass temperature $(T_g \approx 84K)$ and measured close to T_g, respectively. Similarly for the DMIM sample with $t_n \approx 1.2$ nm, $n < 1$ and $n = 1$ were obtained from the $m(t)$ relaxation data measured much below the
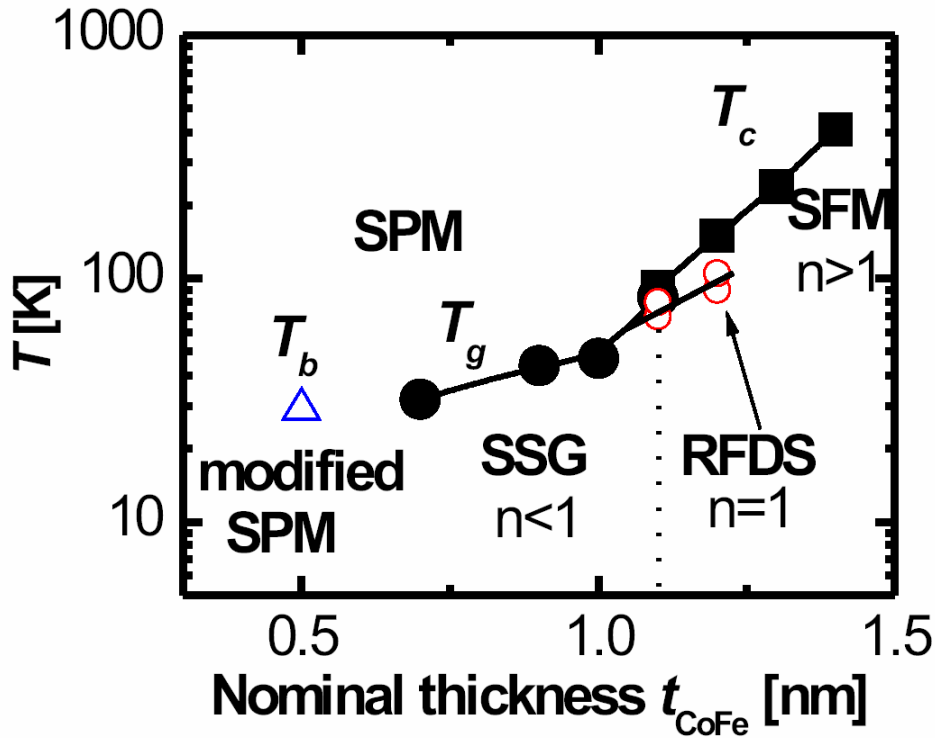

Figure 4.34: Magnetic phase diagram of DMIMs with nominal thickness t_n (shown in the figure as t_{CoFe}) of CoFe . T_b is the blocking temperature (open triangle), T_g is the glass temperature (solid circle), T_c is the critical temperature for the SFM transition (solid squares) and $n \geq$ or < 1 (open circles) (see text). Here the samples with $t_n = 0.5, 0.7$ and 0.9 nm come from the 2nd batch and the rest comes from the 1st Batch of DMIMs.

glass temperature $(T_c \approx 164K)$ and $n > 1$ was obtained when measured close to T_c. It has been analysed in Ref. [196, 217] that the change from $n < 1$ at low temperature to $n > 1$ for T below, but close to T_c only applies to the crossover regime, $t_n = 1.1$ and 1.2 nm. This crossover is explained in terms of superposition of droplet-like growth processes on a nanoscale (as in a spin glass phase) to the domain wall relaxation on a mesoscale. That means, although the sample is in a SFM state some droplet-like growth processes occur. The mechanism of this is probably due to quenched random fields (RFs) [218] originating

from a small fraction of large particles, which become blocked prior to the transition into the collective state. Details of this transition can be found in Ref. [196, 217].
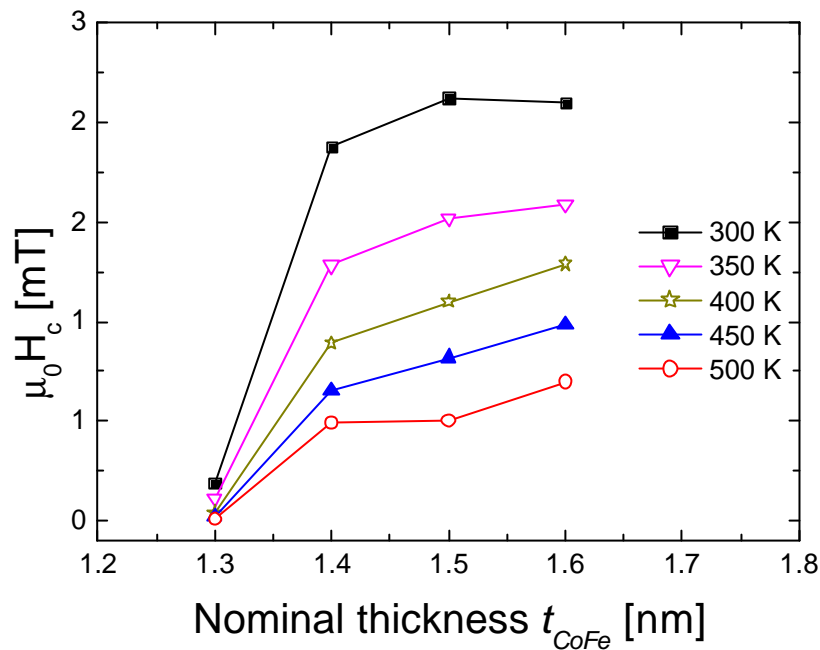

Figure 4.35: Magnetic phase diagram of DMIMs with nominal thickness t_n (shown in the figure as t_{CoFe}) of CoFe showing the transition from non-percolated SFM ($t_n < 1.4$ nm) to percolated FM $t_n \geq 1.4$ nm. The different symbols correspond to different temperatures. Here all the samples come from 2nd batch DMIMs.

The SFM domain state has been evidenced by different methods and imaged by magneto-optic microscopies as already described in this thesis. The weak exchange mediated by the ultrasmall ("glue") particles dispersed between the usual nanoparticles, is the key ingredient in addition to dipolar interaction which leads to the SFM domain state.

By electrical conductivity measurements, the crossover from non-percolating SFM state to percolated FM state is found to occur at $t_n \geq 1.4$ nm [165]. This is also corroborated by the static coercive fields vs nominal thickness at constant temperatures as shown in Fig. 4.35. This reminds of the jump of the Curie temperature of granular Co layers for different coverages [219]. Note that the SFM-FM transition occurs at $1.3 < t_n < 1.4$ nm for the samples represented by Fig. 4.35 (2nd batch), while it occurs at $1.4 \leq t_n < 1.8$ nm for those referring to Fig. 4.35 (1st batch).

Chapter 5

Superferromagnetism in frozen ferrofluids [Fe$_{55}$Co$_{45}$/*n*-hexane]

5.1. Introduction

These days nano sized colloids are an active research subject, *e.g.*, due to their potential for biomedical applications. The recent interests lies in the use of nanosized colloids in antibodies for biological cell separations as well as therapeutic in vivo applications such as drug-targeting, cancer therapy, lymph node imaging or hyperthermia. Iron oxide based particles, *e.g.* magnetite, are commonly used as the magnetically responsive component of commercially available magnetic microspheres [220]. Apart from the technological application point of view, these nanoparticles attract the interests of researchers due to their fundamental interest. Among many nanoparticle systems, frozen ferrofluids are a model system where the long-range dipolar interaction between the single-domain nanoparticles can be continuously tuned by varying the particle concentration. In very dilute ferrofluids, the inter-particle interaction between the particles is almost negligible and therefore the ferrofluid will show single-particle properties. But by increasing the particle concentration the interaction between the particles becomes relevant and single-particle behavior will be dominated by collective behavior as already described in the last chapter. In this chapter we describe the structural and magnetic properties of frozen ferrofluids containing surfactant coated Fe$_{55}$Co$_{45}$ nanoparticles dispersed in *n*-hexane, which consist of strongly disordered hard magnetic shells and soft FM cores. Two ferrofluid samples of different particle-to-liquid volume ratios (1:1) and (1:5) are studied by magnetometry, *ac* susceptometry and Mössbauer spectroscopical measurements. In these concentrated ferrofluids, due to strong interaction, a collective superferromagnetic state consisting of FM cores, will be evidenced by different measurements. However it will be demonstrated that the magnetic shells gradually become blocked below $T_b \gg 30K$, whereas the cores undergo an inter-particle FM phase transition at $T_c \gg 10K$, very probably via dipolar coupling.

5.2. Preparation of Fe$_{55}$Co$_{45}$/*n*-hexane ferrofluids

Fe$_{55}$Co$_{45}$ nanoparticles are prepared by chemical engineering from precursor mixtures of iron pentacarbonyl, Fe(CO)$_5$ and dicobaltoctacarbonyl, Co$_2$(CO)$_8$ [221]. Thus prepared nanoparticles consist of densely packed crystalline metallic nuclei with an average diameter d = (4.6 ± 0.3) nm surrounded by organic surfactants as evidenced by transmission electron microscopy (TEM). The metallic nuclei show an onion-skin-like structure with Fe-rich cores surrounded by shells with increasing Co content [221]. The volume ratios of Fe$_{55}$Co$_{45}$ to hexane are (1:1) and (1:5), which to the best of our knowledge belong to the densest ferrofluids ever studied. Hitherto ferrofluids with volume ratios of at most 1:6 have been studied in order to evidence superspin glass properties [222]. It should be noted that owing to the outer organic shell mutual contact between the metallic nuclei is inhibited. Hence, direct exchange interaction between the nanoparticles is excluded.
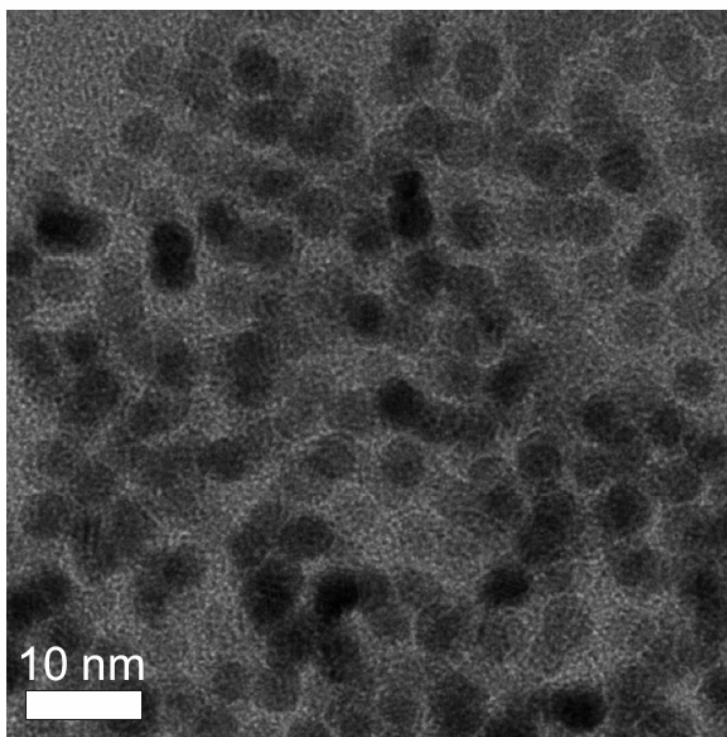
Figure 5.1: Transmission electron microscopy image of Fe$_{55}$Co$_{45}$ nanoparticles.

5.3. Structural properties

Particle size distribution of these nanoparticles is investigated by transmission electron microscopy. 2-4 µl of the colloidal solutions from a (1:100) ferrofluid were dropped onto a carbon coated TEM Cu grid. Fig. 5.1 shows a TEM image revealing nearly spherical FeCo nanoparticles. The average particle diameter is found to be 4.6 ± 0.3 nm. According to

magnetometry analysis these FeCo nanoparticles have an onion like structure with an Fe core surrounded by a shell with increasing Co content [221]. However, from our TEM measurements the detailed particle structure could not be extracted. As will be shown later, magnetization measurements evidence that these nanoparticles have a very small metallic core and heavily disordered surface.

5.4. Magnetic properties and evidence of a collective superferromagnetic state

In this section the magnetic properties of the two ferrofluids with volume ratio (1:1) and (1:5) will be discussed. First magnetization, ac-susceptibility and relaxation measurements will be discussed and then Mössbauer spectroscopy results will be shown.

5.4.1. Magnetization, *ac* susceptibility and relaxation of [Fe$_{55}$Co$_{45}$/*n*-hexane (1:1)] ferrofluid

The magnetic properties of this ferrofluid were investigated by use of SQUID magnetometry and *ac* susceptometry. (MPMS-5S, Quantum Design). Prior to all magnetic measurements, the ferrofluid sample is first zero-field cooled (ZFC) from room temperature to $T = 105$ K, and thereafter either ZFC or field cooled (FC) to the measurement temperature. Fig. 5.2 shows the temperature dependence of the total magnetic moment of the frozen ferrofluid within the range $4.5 \leq T \leq 105$ K as induced after ZFC to $T = 4.5$ K by an external magnetic field $\mu_0 H = 10$ mT upon field heating ($m^{ZFC\text{-}FH}$, solid symbols) and subsequently upon FC again to $T = 4.5$ K (m^{FC}, open symbols). As shown by a bi-directional arrow the latter data are reversible, while $m^{ZFC\text{-}FH}$ is irreversible below $T_b \approx 30 K$ (arrow). Such behavior reminds of superparamagnetic (SPM) single-domain particles, which become blocked below T_b. The unusually smooth separation of the ZFC and FC curves seems to hint at gradual blocking of an extremely wide particle size distribution of freely rotating SPM particles with relaxation times $\tau = \tau_0 \exp\left(KV/k_B T\right)$ [2, 19], where K is the anisotropy energy density and V the particle volume. However, as shown by transmisission electron microscopy (TEM) [221, 223] the size distribution of our particles is quite narrow ($\Delta d/d < 0.1$) and cannot explain the observed smooth separation of the ZFC and FC magnetization data.

As will be discussed in the following, the particles encountered here fall out of the usual scheme of freely rotating moments. The data rather hint at a progressive internal

blocking tendency as T is lowered. At difference with most SPM nanoparticles, but in close agreement with the properties of a-Co-Ni-B alloy nanoparticles [224, 225] a relatively weak moment is induced at T_b. Upon further cooling, however, it increases considerably instead of the usual leveling-off. Most spectacularly, a fairly sharp peak arises in the $m^{ZFC\text{-}FH}$ curve at $T_c \approx 10$ K (arrow), while m^{FC} maximizes as $T \to 0$ (Fig. 5.2). These features indicate a second ordering process, which will be attributed to FM interparticle long-range ordering as indicated by Curie-Weiss -type behavior, $m^{FC} \propto (T - T_c)^{-1}$ [226].
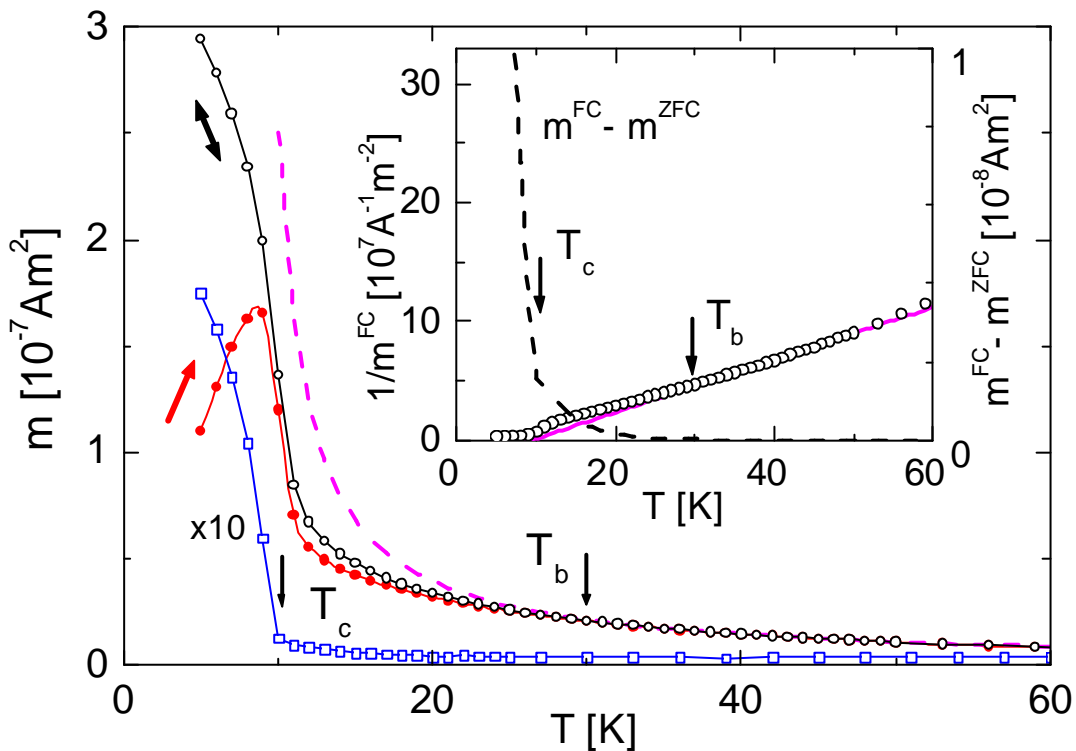
Figure 5.2: Temperature dependence of the ZFC (solid circles; arrow) and FC magnetic moments $m(T)$ (open circles; bi-directional arrow) measured at $\mu_0 H = 10$ mT and of the thermoremanent moment after FC in $\mu_0 H = 0.4$ mT (open squares; magnified $\times 10$) for the ferrofluid [Fe$_{55}$Co$_{45}$/n-hexane (1:1)]. The inset shows an enlarged plot of $m^{FC} - m^{ZFC}$ and $\left(m^{FC}\right)^{-1}$ vs. T best-fitted within $T_b \approx 30$ K (arrow) $< T < 60$ K to the Curie-Weiss law (solid line; broken line in the main panel) with intercept at $T_c \approx 10$ K (arrows).

This Curie-Weiss behaviour is shown in the inset to Fig. 5.2 by the linear behavior of the inverse magnetization, $\left(m^{FC}\right)^{-1}$ in the range $30 \pounds T \pounds 60$ K. The intercept with the T scale (divergence of the broken curve in the main panel of Fig. 5.2) reveals $T_c \twoheadrightarrow 9.4$ K, similar to the peak temperature of $m^{ZFC\text{-}FH}$.
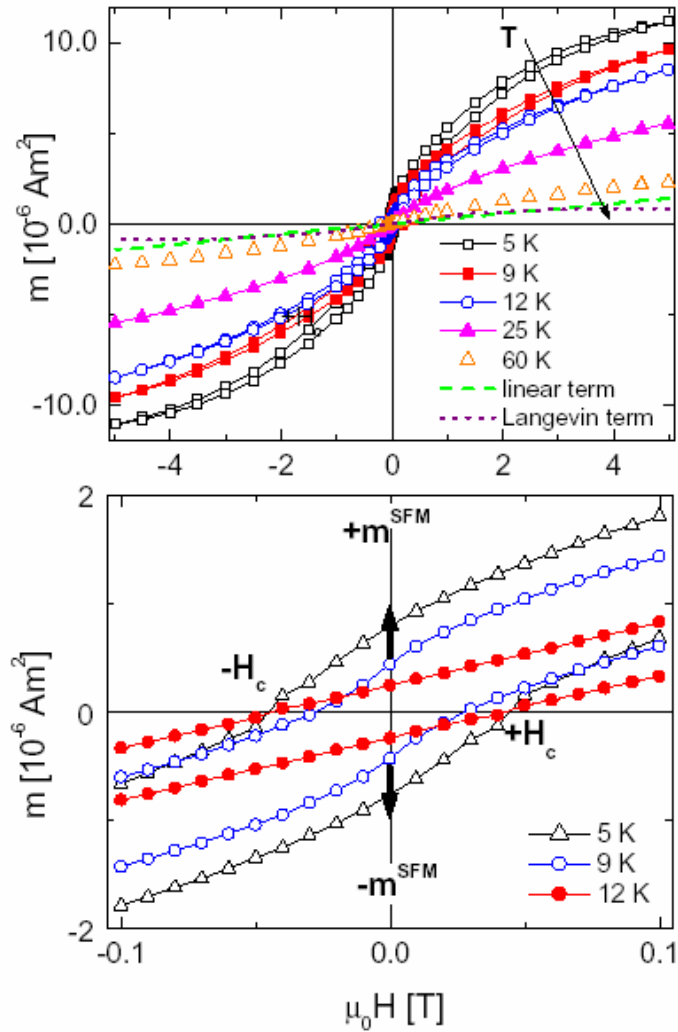
Figure 5.3: Magnetic moment m^{ZFC} vs $m_0 H$ of the ferrofluid [$Fe_{55}Co_{45}/n$-hexane (1:1)] obtained after ZFC from 105K to $T = 5, 9, 12, 25, 60$ K, respectively, interpolated by solid splines except for the 60 K data, which are best-fitted by a Langevin-type plus a linear curve (see text; dotted and broken lines, respectively). Hysteresis is seen in the data at $T < 20$ K. The lower panel shows the hysteresis loops taken at $T = 5$ K (open triangles), 9 K (open circles) and 12 K (solid circles) at low fields. Arrows indicating $\pm m^{SFM}$ refer to the SFM low-T anomaly (see text).

Other pieces of evidence for the suspected low-T phase transition are shown in Fig. 5.3. In the main panel the *dc* moment m vs m_0H is shown for fields $-5 \le m_0H \le 5$ T at different temperatures descending from 60 to 5 K. Each of these curves is obtained after ZFC from 105 K to the measurement temperature. As expected, reversibility without hysteresis is encountered in the unblocked regime at $T > T_b$. At $T = 60$ K, Langevin´s law of large fully rotatable SPM moments complemented by a paramagnetic correction term,

$$m(H) = Nm_0L(m_0H\,m_0/k_BT) + cH$$

with $L(x) = \coth(x) - 1/x$ and c the volume susceptibility due to small SPM moments, is satisfactorily obeyed by a best-fit procedure. The dotted Langevin term yields an average single particle moment $m_0 = (1.1 \pm 0.1) \times 10^{-21}$ Am^2 and a saturation moment $Nm_0 = (1.0 \pm 0.1) \times 10^{-6}$ Am^2 when employing the total particle number $N = (9.1 \pm 0.3) \times 10^{14}$ of our sample with mass $m = 2.24$ mg and average particle diameter $d = (4.6 \pm 0.3)$ nm. The linear term (broken line) yields a volume susceptibility $c = (3.6 \pm 0.2) \times 10^{-13}$ m^3/v, which is only partially due to the above SPM contribution. At high fields, ´sublattice´ rotational processes are probably dominating [224, 225].

Surprisingly the value of m_0 corresponds to only 55 Bohr magnetons, m_B, which largely differs from an estimated number of 3600 ± 230 m_B for a $Fe_{55}Co_{45}$ particle with bulk FM properties. Obviously the moments are nearly completely compensated and thus remind of *superantiferromagnetic* (SAF), i.e. AF nanoparticles with weak ferrimagnetism due to surfacial sublattice imbalance [227]. Indeed, the chemical route of our sample preparation principally encourages oxidic reactions in the outer shell of the particles. However, high resolution TEM has not been able to reveal structural changes due to oxide formation at the particle surfaces. That is why we favor a physically founded core-shell model similar to that proposed for a-Co-Ni-B nanoparticles [224, 225]. We assume strong radially directed surface anisotropy K_s giving rise to a nearly compensated moment in the shell region, while a very small central part forms an SPM particle, which is virtually decoupled from the shell.

In accordance with Monte Carlo simulations [225] the competition between isotropic exchange J and K_s is assumed to be at the origin of the near-compensation of the moment in zero field. This decreases further as T is lowered as can be deduced from Langevin-type fits (see above), which yield $m_0 = 122$, 77 and 55 m_B at $T = 60$, 25 and 12 K, respectively. It should be stressed, however, that simplistic models like the SPM one, even

when completed by an additional linear response term, must fail in view of the highly frustrated situation governing the shell spins. Similarly, corrections for particle size distributions as proposed for SAF particles [228] cannot account for the high-field linearity in core-shell systems like ours.

Interestingly, when cooling the sample in a field of $m_0H = 1$ T from $T = 105$ K to different temperatures below T_b we observe shifts of the hysteresis curve, which reach $m_0H_{shift} \approx 30$ mT as shown for $T = 5$ K in Fig. 5.4. Very probably this effect has nothing to do with unidirectional anisotropy (*exchange bias*) induced at antiferromagnetic (AF)/ferromagnetic (FM) interfaces after proper FC procedures [229]. It is rather due to the properties of so-called minor loops in disordered systems, which memorize the sign of the initial field when performing incomplete hysteresis cycles [230].
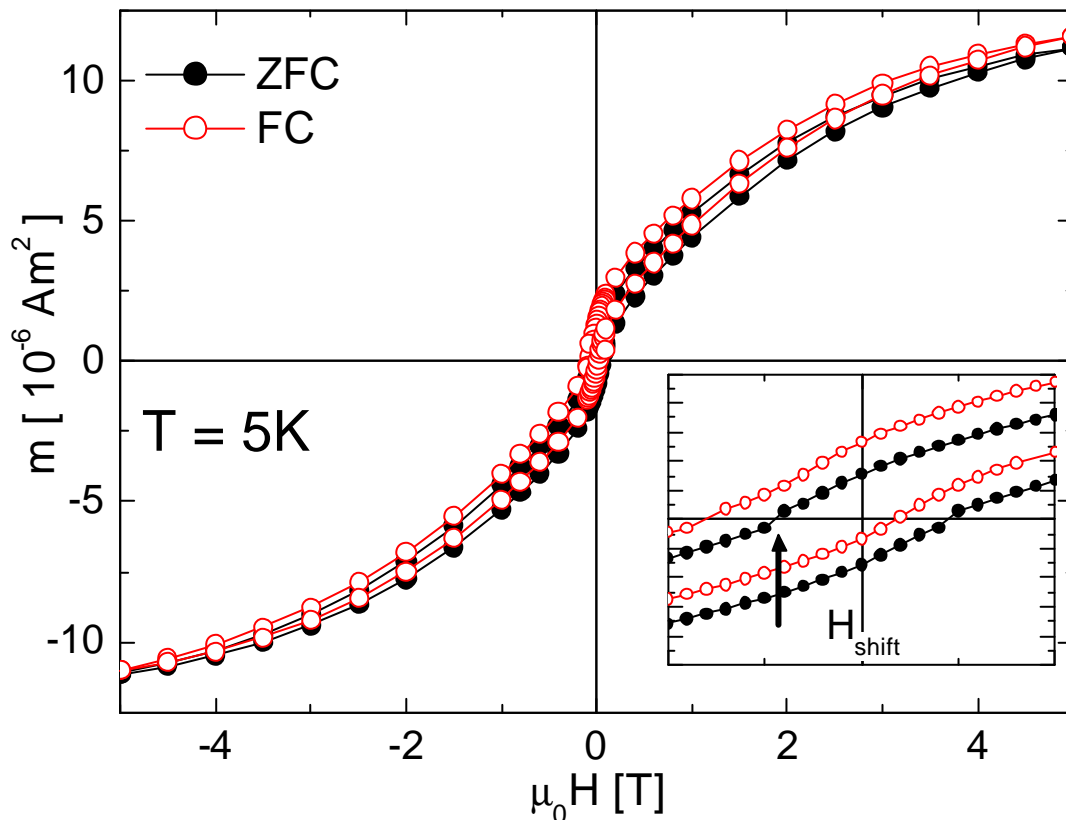

Figure 5.4: ZFC and FC hysteresis loops at 5 K of the ferrofluid [$Fe_{55}Co_{45}/n$-hexane (1:1)] measured after zero-field-cooling or field-cooling in 1 T from 105 K.

Most spectacular is a novel magnetization component, which is announced by its Curie-Weiss-type susceptibility at $T > T_c \gg 10$ K in Fig. 5.2 and steeply rises below T_c. As shown very clearly in the lower panel of Fig. 5.3 it superimposes to the *S*-shaped deviations from the linear behavior (as seen at $T = 12$ K) in the hysteresis cycle in the low-field magnetization curves at $T = 9$ and 5 K. A component denoted as $+m^{SFM}$ (up arrow) adds to the down-branches above $-H_c$ ($\gg$ -50 mT at 5K), while another one subtracts as $-m^{SFM}$ from the up-branches below $+H_c$ (down arrow). After subtraction of the linear asymptotes one obtains complete hysteresis loops with width $2H_c$ and height $2m_r$, where *e.g.* $m_r(T = 5K) = 2.4 \times 10^{-7}$ Am^2 (arrows in Fig. 5.3, upper inset; Fig. 5.5, inset). This value corresponds to a total moment of about $4m_B$, hence, 2 - 3 magnetic atoms per nanoparticle. Clearly, moments of this size remain SPM down to very low temperatures [226].
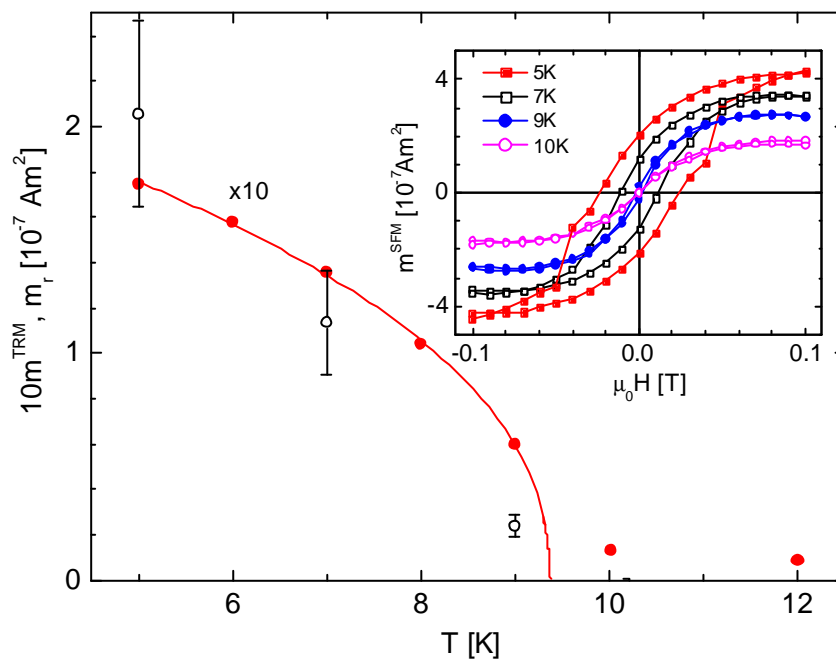

Figure 5.5: Magnetic moments m^{TRM} vs. T (solid circles; see Fig. 5.1) and m_r vs. T (open circles) as extracted from m^{SFM} vs. H (inset; see text) at $H = 0$ of the ferrofluid [Fe$_{55}$Co$_{45}$/n-hexane (1:1)]. The solid line is the best- fit of m^{TRM} to $(T_c - T)^b$ with $T_c = 9.4$ K and $b = 0.43$ (see text).

We argue that m_r is a measure of a spontaneous magnetization arising via a second order phase transition below T_c. Within errors its temperature dependence m_r vs. T as shown in Fig. 5.5 (open symbols) comes close to that of the thermoremanent moment induced by FC in a small field of $\mu_0 H = 0.4$ mT (Fig. 5.1), m^{TRM} (Fig. 5.5; solid circles; note that these data are expanded by a factor of 10).
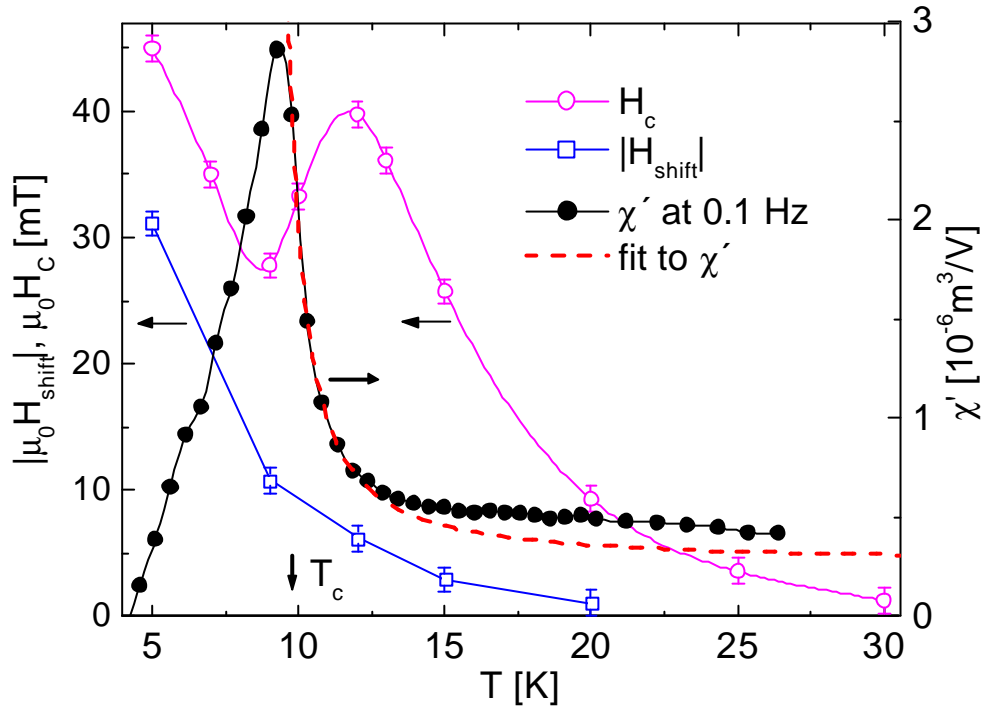
Figure 5.6: Temperature (T) dependencies (data points with eye-guiding lines) of the coercivity H_c (open circles), the loop shift field $\left|H_{shift}\right|$ (open squares) and the *ac* susceptibility χ' ($f = 0.1$ Hz and $\mu_0 h_{ac} = 0.4$ mT) (solid circles with best-fitted power law (broken line)) of the ferrofluid [$Fe_{55}Co_{45}/n$-hexane (1:1)].

The common T dependence of $m_r(T)$ and $m^{TRM}(T)$ is satisfactorily described by conventional order parameter criticality, $m \propto (T_c - T)^b$, with a best-fitted critical temperature $T_c = (9.4 \pm 0.2)$ K and an exponent $b = 0.44 \pm 0.05$, respectively. The value of b is close to the mean-field one, $b = 0.5$, which might be expected for a dipolarly coupled SFM system with long-range interaction forces. A further test of the dipolar character of the low-T phase transition is provided by ac susceptibility data, which are

sharply peaking at T_c as shown in Fig. 5.6 (solid circles). A best-fit of the data taken at frequency f = 0.1 Hz to the power law $c\,\leftarrow\,c_0\,\pm\,\mu\,(T - T_c)^{-g}$ (broken line) yields the background response due to the nearly compensated shell, $c_0 = (2.7 \pm 0.5) \times 10^{-7}$ m^3/V, the critical temperature T_c = 9.2 ± 0.1 K, and an exponent $g = 1.26 \pm 0.20$, which is compatible with the mean field result $g = 1$.

Interestingly, the coercive field, H_c, drops by approximately 30% and attains a minimum when approaching T_c from above (Fig. 5.6; open circles). We propose this to be related to critical fluctuations of the magnetization order parameter of the cores, which couple to the ferrimagnetic moments of the shells (see above) and thus soften their internal pinning forces. Remarkably, the loop shift field, $|H_{shift}|$, as obtained from m^{FC} vs. H curves (Fig. 5.4) and plotted versus T in Fig. 5.6 does not show any anomaly at T_c, but continues to increase monotonically as T is lowered (Fig. 5.6; open squares). This is compatible with the report [230] that minor loops shifts are related to the skewness of the corresponding major loop rather than to its width $2H_c$.

Fig. 5.7 shows the relaxation of the thermoremanent magnetic moment $m^{TRM}(t)$ measured at different temperatures. Before measuring, the sample was cooled in a field of $m_0 H_0$ = 10 mT from 105 K to the measurement temperature T_m where the field was switched off and $m(t)$ was recorded. The solid lines in Fig 5.7 (a) and (b) are fitted to a power law with finite remanence

$$m_0 + m_1 \left(t + t_0\right)^{1-n}, \tag{5.1}$$

where t_0 is some time delay in the beginning of the measurement and n is an exponent whose value depends on the concentration of nanoparticle assemblies [63, 217]. The fittings yield $m_0 \approx 2.1\ (0.9) \times 10^{-7}$ Am^2, $m_1 \approx 1.1\ (1.4) \times 10^{-7}$ Am^2, $t_0 \approx 23\ (13)$ s and $n \approx$ 1.057 (1.034) in Fig. 5.7 (a,b) respectively. The relaxation data measured at 15 K (Fig. 5.7 (c)) can be fitted to a stretched exponential law

$$m_0 \exp\left[-\left((t + t_0)/t_p\right)^{1-n}\right], \tag{5.2}$$

where t_p is the response time depends on temperature. The best fitting to the data (solid line) in Fig. 5.7 (c) yields $m_0 \approx 0.9 \times 10^{-7}$ Am^2, $t_p \approx 2.03 \times 10^{-7}$ s, $t_0 \approx 12$ s and $n \approx 0.97$. It has already been discussed that magnetic relaxation with a power law behaviour is a clear signature of collective superferromagnetic state. [217, 218] Therefore the power law

behaviour of m^{TRM} relaxation in this concentrated ferrofluid is another evidence of SFM state below 10 K. Above 30 K, no magnetic relaxation can be observed as shown in Fig. 5.7 (d) which shows the magnetic moment remains almost constant measured at 35 K.
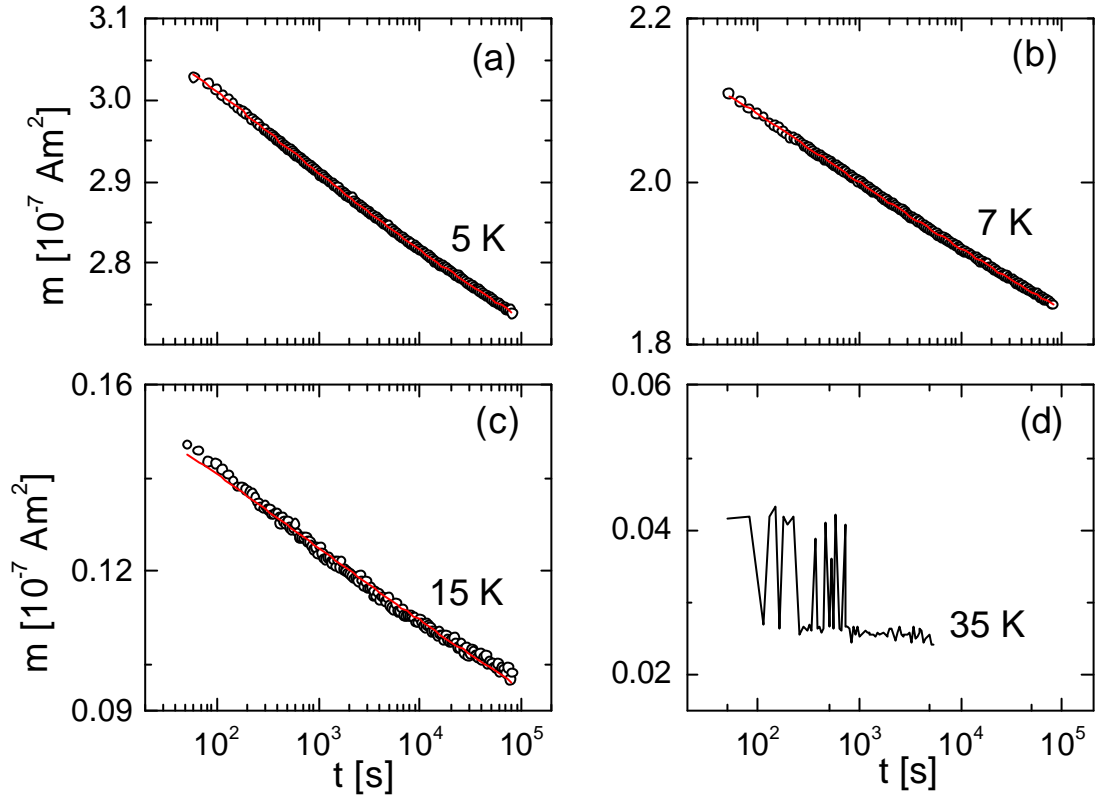
Figure 5.7: Relaxation curves of m^{TRM} vs. t after FC in $m_0 H = 10$ mT from $T = 105$ K to $T_m = 5$ (a) and 7 K (b), 15 (c) and 35 K (d) for the ferrofluid [Fe$_{55}$Co$_{45}$/n-hexane (1:1)]. The solid lines are best fits to Eqn. 5.1 (a,b) and 5.2 (c).

5.4.2. Magnetization and *ac* susceptibility measurements of [Fe$_{55}$Co$_{45}$/n-hexane (1:5)] ferrofluid

In the following the magnetic properties of a less dense ferrofluid [Fe$_{55}$Co$_{45}$/hexane] with volume ratio (1:5) will be discussed. The magnetic properties obtained on this ferrofluid are similar those obtained on the ferrofluid discussed in section 5.4.1. The magnetic properties of this ferrofluid were investigated by use of SQUID magnetometry and *ac* susceptometry. (MPMS-5S, Quantum Design). Prior to all magnetic measurements, the

ferrofluid sample is first zero-field cooled (ZFC) from room temperature to $T = 105$ K, and thereafter either ZFC or field cooled (FC) to the measurement temperature.

In Fig. 5.8 the temperature dependence of m^{ZFC}, m^{FC} and m^{TRM} are measured within the range $4.5 \leq T \leq 105$ K as induced after ZFC to $T = 4.5$ K by an external magnetic field $m_0 H = 10$ mT upon field heating ($m^{ZFC\text{-}FH}$, solid symbols) and subsequently upon FC again to $T = 4.5$ K (m^{FC}, open symbols). These results look similar to those obtained on the other ferrofluid. The m^{ZFC} curve has a peak around 8.5 K. Also m^{FC} curve has a kink at around 9 K similarly shown previously for the other ferrofluid. The inset in Fig. 5.8 shows an enlarged plot of $\left(m^{FC} \right)^{-1}$ vs. T best fitted within $T_b \approx 30$ K (arrow) $< T < 60$ K to the Curie-Weiss law (solid line) with intercept at $T_c \approx 8.7$ K (arrows) [223].
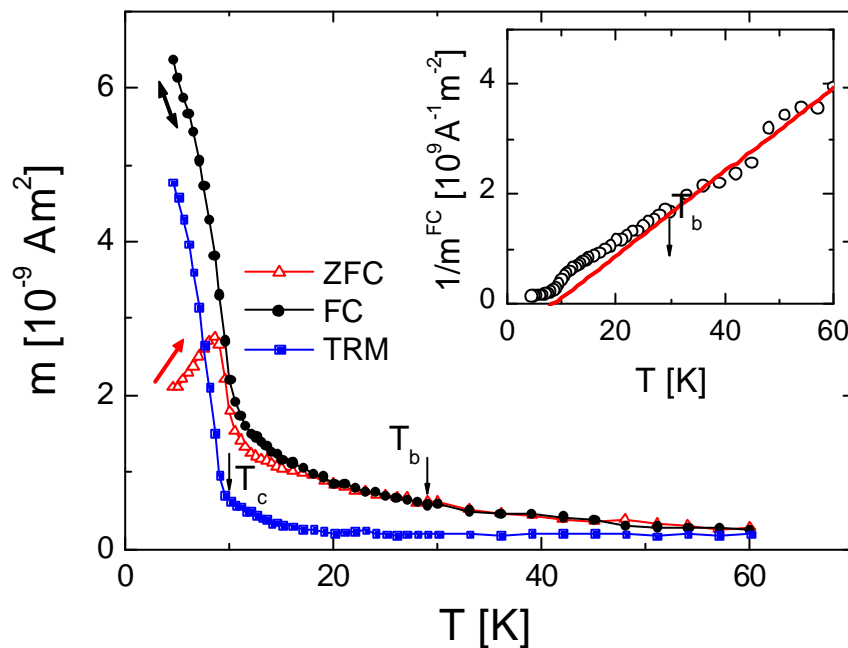
Figure 5.8: Temperature dependence of the ZFC (open triangles, arrow), FC (solid circles; bi-directional arrow) and TRM (solid squares;) magnetic moments $m(T)$ of the ferrofluid [Fe$_{55}$Co$_{45}$/n-hexane (1:5)], measured at $m_0 H = 10$ mT. The inset shows an enlarged plot of $\left(m^{FC} \right)^{-1}$ vs. T best fitted within $T_b \approx 30$ K (arrow) $< T <$ 60 K to the Curie-Weiss law (solid line) with intercept at $T_c \approx 8.7$ K (arrows).
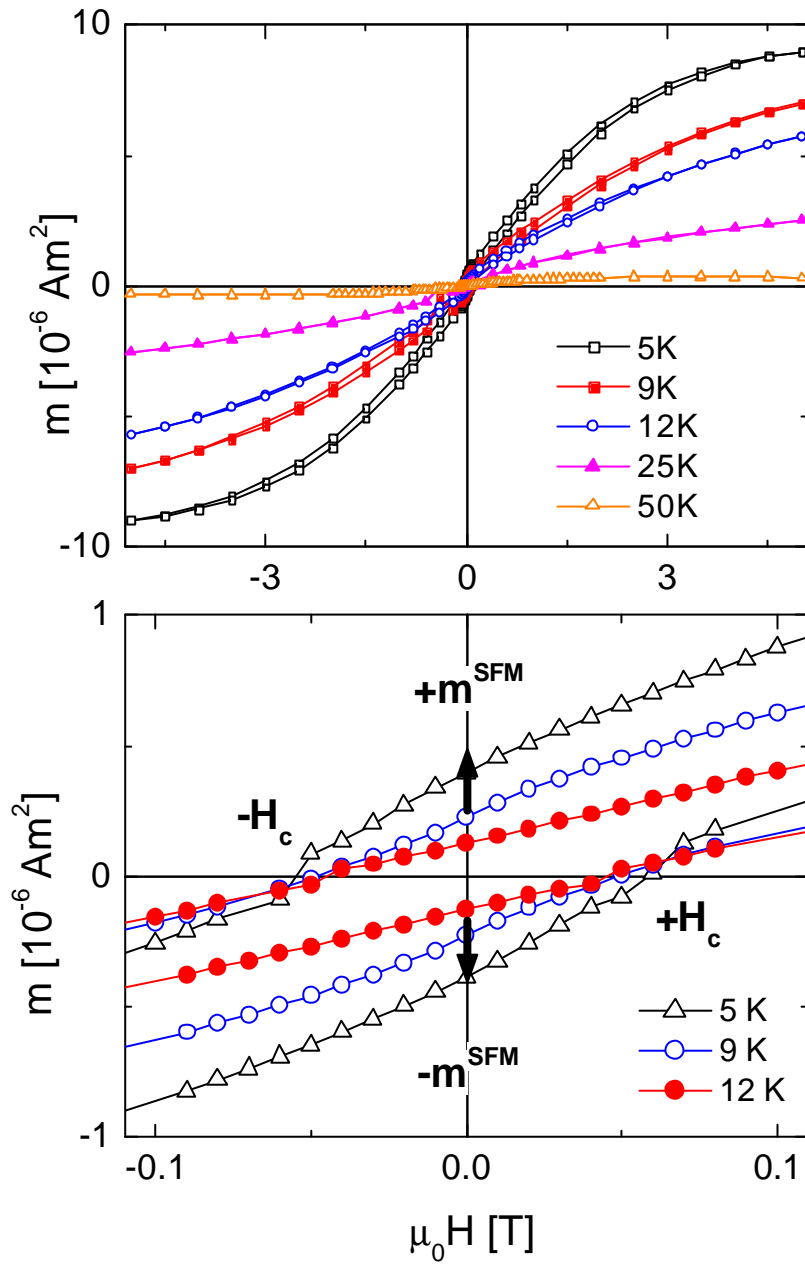
Figure 5.9: Magnetic moment m^{ZFC} vs $\mu_0 H$ of the ferrofluid [$Fe_{55}Co_{45}/n$-hexane (1:5)] obtained after ZFC from 105 K to $T = 5$, 9, 12, 25, and 50 K, respectively. The lower panel shows the hysteresis loops taken at $T = 5$ K (open triangles), 9 K (open circles) and 12 K (solid circles) at low fields. Arrows indicating $\pm m^{SFM}$ refer to the SFM low-T anomaly (see text).

Fig. 5.9 shows the *dc* moment *m* vs $\mu_0 H$ measured after cooling in zero field the sample from 105 K to the measurement temperature. Above 35 K, the moments can be

described by Langevin´s formula similar described for the ferrofluid with concentration (1:1). Minor loop shifts were also observed similar like the other ferrofluid sample after cooling the sample in a field from 105 K (data not shown). Other magnetic properties such as *ac* susceptibility also yield similar results from this ferrofluid compared to the other one [223].

The *ac* susceptibility data taken at frequency $f = 0.1$ Hz and $\mu_0 h_{ac} = 0.4$ mT shown in Fig. 5.10 can be fitted to the power law $\chi' = \chi'_0 + \mu \left(T - T_c\right)^{-g}$. A best fit (broken line in Fig. 5.10) to this power law yields the background response due to the nearly compensated shell, $\chi'_0 = \left(4.8 \pm 0.5\right) \times 10^{-7}\,\mathrm{m^3/V}$, the critical temperature $T_c = 9.0 \pm 0.1$ K, and an exponent $g = 1.21 \pm 0.20$, which is compatible with the mean field result $g = 1$. These analyses are consistent with the ac susceptibility measurements on the other ferrofluid described earlier in chapter 5.4.1. It will be discussed below (section 5.4), why both systems behave so similarly despite their different degrees of dilution.
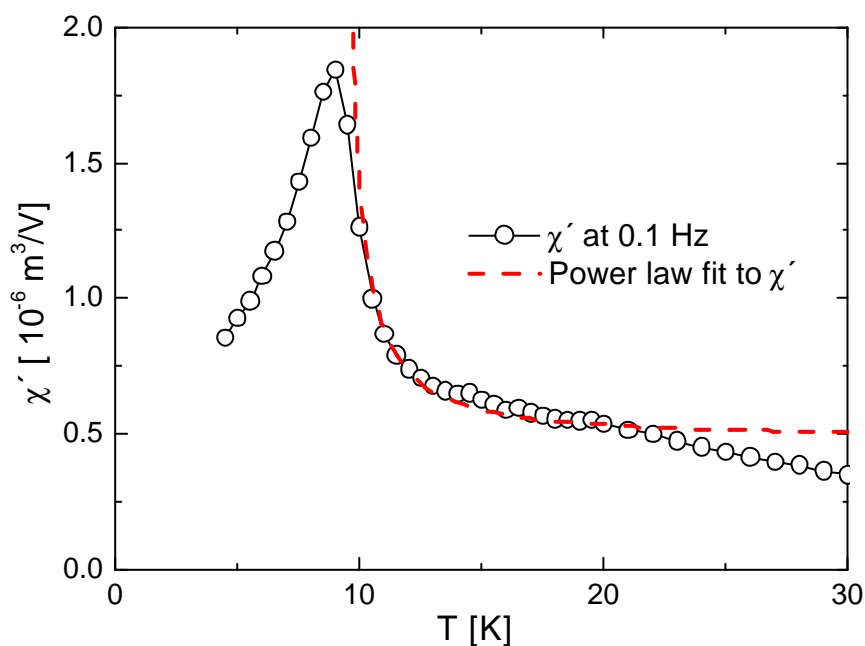

Figure 5.10: *ac* susceptibility χ' of the ferrofluid [Fe$_{55}$Co$_{45}$/n-hexane (1:5)] measured at frequency $f = 0.1$ Hz and field amplitude $\mu_0 h_{ac} = 0.4$ mT. The dotted line is a best fit to the power law.

5.4.3. Mössbauer spectroscopical measurements on [Fe$_{50}$Co$_{50}$/*n*-hexane (1:1)]

Mössbauer spectroscopy was carried out on a similar ferrofluid sample with the concentration (1:1). In this sample the mean diameter <D> of the nanoparticles was ≈ 2.93 ± 0.15 nm. These nanoparticles were prepared under similar conditions as the other two ferrofluid samples described earlier in this chapter. The sample for Mössbauer spectroscopy was sealed in a plexiglass container with thin windows. The spectra were taken from room temperature down to 4 K in a standard helium bath cryostat. We show the spectra up to 45 K in Fig. 5.11. First of all, the spectrum at 45 K shows clearly two electric field gradient (EFG) quadruple doublets. The center shift, the EFG and the relative weights of the sub-spectra are given in Table 5.1. The different parameters, in particular EFG and center shift [231], clearly hint at contributions due to Fe^{2+} and Fe^{3+}. By detail analysis it is found that the majority site has the characteristics of Fe^{3+}, while the minority component those of Fe^{2+}. In Table 1 the % area, center shift and electric field gradient (EFG) are shown for the Fe^{3+} and Fe^{2+} subspectrum analysed from the Mössbauer spectrum at 45 K. The center shift is defined as the center of the spectrum. This is composed of the chemical isomer shift, plus the 2nd order Doppler shift. The EFG is defined as the electric field gradient splitting of the two lines (± 3/2, ±1/2 and ± 1/2, ±1/2 nuclear transitions).

Table 5.1

Temperature 45 K

Subspectrum	area %	center shift (mm/s)	EFG (mm/s)
Fe3+	70.5	0.413	0.805
Fe2+	29.5	1.230	2.572

The spectra at lower temperature show a gradual appearance of magnetic splitting. The spectra from about 25 K to 4.2 K show magnetic splitting with a main component of the hyperfine magnetic field (B_{hf}) near 50 T, typical of iron Fe^{3+} oxides. This is a very typical value of B_{hf} for magnetically ordered Fe^{3+}. The minority component Fe^{2+} is not distinguishable due to the broad lines of the magnetic sextets. The low temperature spectra have been fitted using a distribution of hyperfine fields. The resulting distributions are
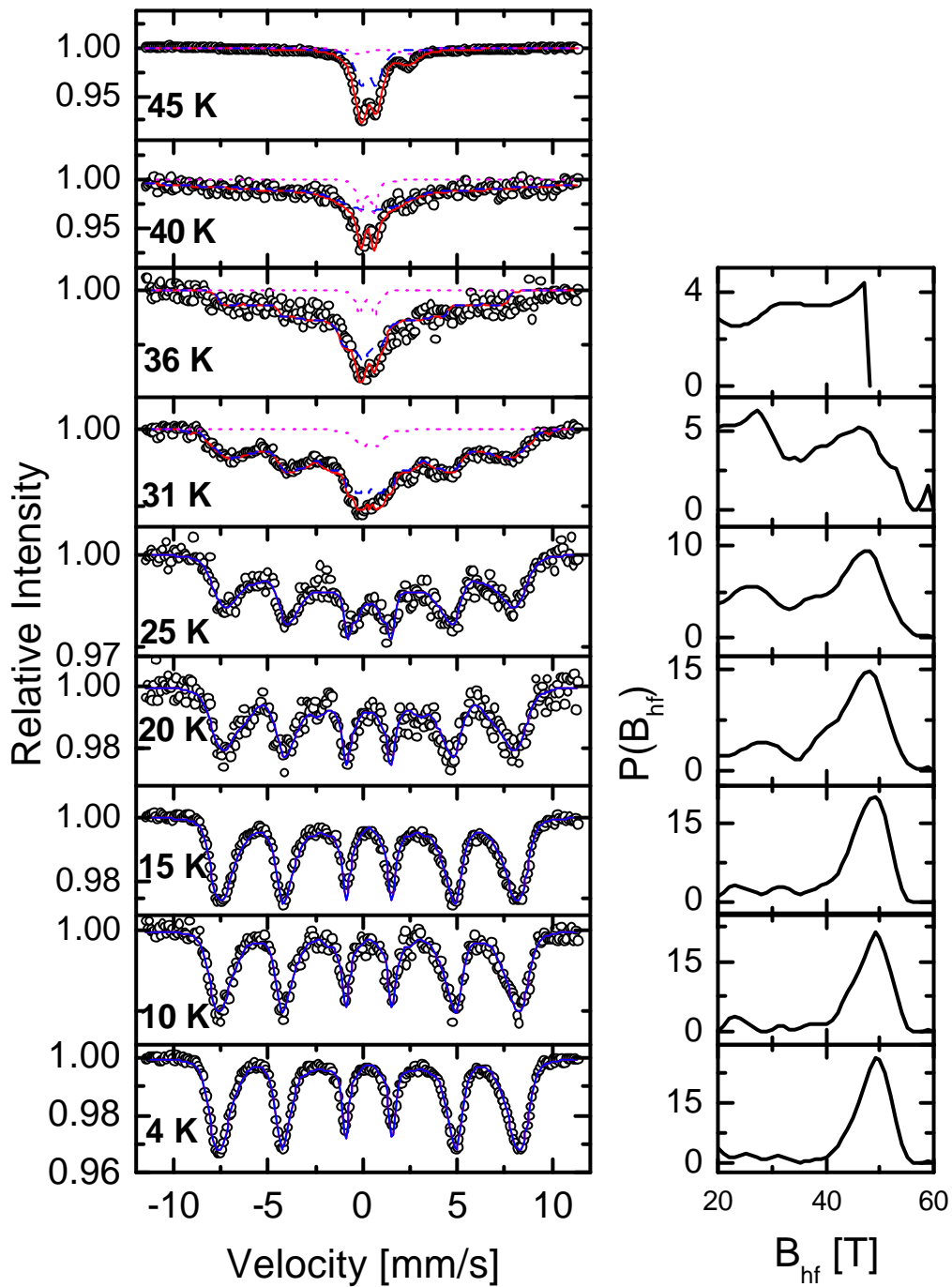
Figure 5.11: Mössbauer spectra of the ferrofluid [Fe$_{50}$Co$_{50}$/n-hexane (1:1)], at different temperatures. The blue lines represent the Fe^{3+} contribution and the magenta coloured lines represent the contribution of Fe^{2+}. Red lines are the sum of Fe^{3+} and Fe^{2+} contributions. The right hand side shows the corresponding hyperfine field distribution at different temperatures corresponding to the spectra shown in the left side.

shown at the right. It should be noted that the maximum field does not change significantly with increasing temperature. Only a tail at low fields develops, leading to a gradual collapse of the magnetic splitting [232]. This kind of broadening of hyperfine field distribution can be interpreted as collective inter-particle interactions which slow the magnetic fluctuations. As the collapse of the magnetic splitting is not abrupt, therefore it does not look like small particles which are suddenly released from their anisotropy axis by thermal activation. It looks like individual regions undergo a gradual transition from a frozen state to (super-) paramagnetism over a range of temperatures. Hence the collective inter-particle SFM state is again evidenced by Mössbauer spectroscopy together with SQUID measurements.

5.4. Conclusion

A superferromagnetic state has been evidenced by different criteria such as temperature dependencies of m^{ZFC}, m^{FC} and m^{TRM} magnetization, hysteresis measurements, *ac* susceptibility measurements, relaxation of thermoremanent magnetization and finally by Mössbauer spectroscopy. The SFM state is consist of small ferromagnetic cores covered by heavily disordered shell of the nanoparticles [226]. These findings are in consistent with previously reported results on these kinds of nanoparticles that FeCo nanoparticles are very sensitive to oxidation [221].

Interestingly for both ferrofluids with different concentrations similar behaviours were found. This might be due to particle agglomeration at lower temperatures yielding similar configuration for both of the ferrofluids [233]. To test this hypothesis small angle neutron scattering (SANS) measurements on two different ferrofluids with concentration (1:1) and (1:5) were performed at the Berlin neutron scattering facility (BENSC) with the SANS instrument V4. Unfortunately these experiments failed, since both samples lost ferrofluid material due to a crack in the glue of the sample container while cooling down. Future SANS measurements are expected to shed light on the structural agglomeration of the nanoparticles and any collective magnetic ordering (SFM) state.

Fig. 5.12 shows a schematic sketch of our picture of the frozen ferrofluid with single particle magnetic core-shell structure coated with organic surfactants. The arrows in the small ferromagnetic core represent the superspin moment. The magnetic shell is heavily disordered covered by the organic ligands which excludes any magnetic contact of the nanoparticles.

Similar magnetic results are also observed in other nanoparticle assemblies which will be discussed briefly here. Three of our criteria for a low-T collective SFM state in the FeCo particle system were also observed on a-Co-Ni-B nanoparticles with diameter $d \approx 3$ nm [225]. All anomalies, viz. a drop of H_c, a sharp peak in $m^{ZFC\text{-}FH}(T)$ and a sharp kink of $m_r(T)$ were found at $T \approx 9$ K. They were explained by ordering processes of FM clusters in the disordered shells at low temperatures, i.e. by a kind of intra-particle phase transition. We cannot accept this interpretation for our particles, since it is unlikely that small systems, viz. particles with less than 10 atoms, exhibit well-behaved phase transitions with bulk critical exponents as observed in our system.

A simple blocking transition of uncoupled SPM moments into a hysteretic state of coherent rotation [7] can also be excluded. This scenario predicts constant amplitudes of

the hysteresis loops with increasing coercivity, H_c, on cooling [234]. This is at difference with the data, which clearly show a critical increase of the spontaneous magneization below T_c (Fig. 5.5, inset). However, the very origin of the SFM interaction remains to be elucidated. An estimate of the dipolar energy between two particles with effective moment $m = 4m_B$ and distance $D = 4.6$ nm yields $E_{d-d}/k_B = \left(m_0/4pk_B\right)m^2/D^3 \gg 10^{-4}$ K. Since this value is by far too small as to explain the ordering temperature $T_c \gg 10$ K, we rather suggest a transferred exchange coupling mechanism via the nearly compensated, but magnetically susceptible shell (*mirror forces*} [209]. Further research will be necessary in order to verify this hypothesis.
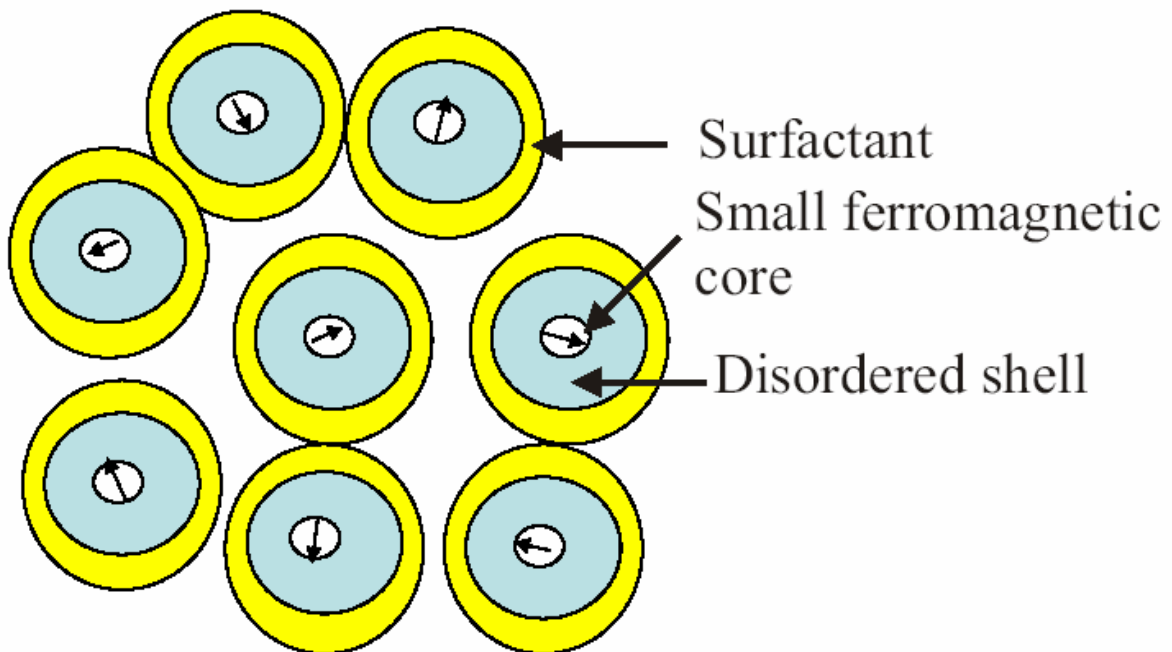

Figure 5.12: A schematic sketch of the frozen ferrofluid with single particle magnetic core-shell structure coated with organic surfactants. The arrows in the small ferromagnetic core represent the superspin moment.

Chapter 6

Summary and Outlook

In this work detailed investigations of the structure and the magnetic properties of two systems have been presented: (i) discontinuous metal insulator multilayers [$Co_{80}Fe_{20}(t_n)/Al_2O_3(3nm)]_m$ with different nominal thickness t_n and (ii) ferrofluids with the general formula [$Fe_{55}Co_{45}/n$-hexane] for two different volume ratios [such as (1:1) and (1:5)]. Various experimental techniques, such as TEM, XRD, transport, FMR, SQUID, PNR, X-PEEM, Mössbauer spectroscopy, MOKE and Kerr microscopy have been employed to study the above systems.

Structural studies performed by TEM on different nominal thickness reveal that the CoFe disassemble into quasi-spherical nanoparticles in the Al_2O_3 matrix. Comparing the TEM images of two sample with different nominal thicknesses *e.g.* $t_n = 0.5$ and 0. 9 nm, it is found that the nanoparticle size increases linearly and their average interparticle distance decreases with CoFe nominal thickness t_n. Small angle X-ray reflectivity measurements on these DMIMs reveal that the samples exhibit regular multilayer structure. Close coincidence of X-ray specular small angle reflectivity and longitudinal diffuse scattering are obtained on the DMIMs, which indicate good vertical correlation in the multilayer stack. Electrical conductivity measurements yields that the structural percolation occurs at $t_n = 1.4$ nm in the second batch DMIMs. Magnetotransport measurements reveal the existence of two different particle size distributions which is later confirmed in this thesis by magnetometry analysis. The existence of an in-plane uniaxial anisotropy in DMIMs induced by an in-plane magnetic field during growth is verified by SQUID magnetometry and ferromagnetic resonance measurements.

In this thesis it has been shown that the DMIM represent a model system to study the effect of inter-particle interactions by varying the nominal thickness which corresponds to the magnetic particle concentration. The DMIM sample with the lowest nominal thickness $t_n = 0.5$ nm experiences single particle blocking because of negligible inter-particle interactions. On the contrary, strong evidence has been found for a collective superspin glass state in the DMIM sample with $t_n = 0.7$ nm. The non-equilibrium collective

dynamics of a superspin glass phase has been evidenced by ac-susceptibility and zero field cooled memory effects.

In all DMIM samples an additional paramagnetic signal was observed at low temperatures. This paramagnetic signal comes from atomically small particles, also called "glue particles". These glue particles have probably a significant role to mediate tunnelling exchange interaction between the nanoparticles. This tunnelling exchange interaction in addition to dipolar interactions at higher nominal thickness leads to the long-range ordered superferromagnetic domain state. In this thesis the SFM domain state has been evidenced by different techniques such as magnetometry, dynamic hysteresis and by magneto-optic Kerr effect, Cole-Cole plots of the *ac* susceptibility and polarized neutron reflectivity. Cole-Cole plots on a SFM sample with $t_n = 1.3$ nm evidenced four dynamic modes of domain walls as in a random ferromagnet. In addition, domain wall motion induced magnetization relaxation in the SFM system is evidenced by polarized neutron reflectivity measurements. SFM domains stretched along the easy in-plane axis, but exhibiting irregular walls and hole-like internal structures ("domains in domains") are revealed by X-ray photoemission electron microscopy (X-PEEM) and Kerr microscopy. They shrink and expand, respectively, preferentially by sideways motion of the long domain walls in a longitudinal field. They show temporal relaxation as evidenced by SQUID magnetometry and polarized neutron reflectometry.

It has to be remarked that magnetic nanoparticles undergoing a transition into the long range ordered SFM state are clearly unsuitable for applications in data storage, which tries to address independent single particles [235] under blocking conditions beyond the superparamagnetic limit [19, 20]. Since the remanent SFM alignment counteracts large TMR values, also magnetic random access memory (MRAM) applications are not promising for DMIMs. However, owing to their ultralow coercivity, high magnetic permeability and high tunneling resistivity, superferromagnets are promising materials for microelectronic, power management and sensing devices designed for high frequencies [236]. By tuning the nominal CoFe film thickness, *viz.* granule size and distance, the specific resistivity (r) and coercivity (H_c) can reliably be controlled. Further research has to be devoted to maximize the uniaxial anisotropy field H_k [236], which is presently controlled by an external field applied during the film growth of the DMIMs. Apart from the application point of view, SFM systems are interesting for fundamental research. In addition to the well-known states of "superparamagnetism" and "superspin glass" our

ultimate proof of "superferromagnetism" completes the fascinating new field of "supermagnetism", which will probably enter future textbooks on magnetism.

The DMIM samples with $t_n \geq 1.4$ nm percolate structurally and behave like bulk ferromagnets. These percolated samples reveal layer dependent magnetization reversal as evidenced by PNR measurements. With the help of micromagnetic simulations we have demonstrated that competition between long and short-ranged dipolar interactions apparently gives rise to a modulated magnetization depth profile in these dipolarly coupled magnetic multilayers. With the help of micromagnetic simulations we demonstrate that the competition between long-range dipolar, short-range Néel and external field interactions apparently give rise to a modulated magnetization depth profile in these dipolarly coupled magnetic multilayers. Future research should be aimed at exploring the essential ingredients which determine the modulation period along the multilayer stacks.

The second system studied in this thesis is ferrofluid consisting of FeCo nanoparticles in liquid hexane. TEM studies reveal that the average particle diameter of CoFe granules is 4.6 nm. Inter-particle SFM ordering between FeCo nanoparticles are evidenced by magnetization measurements and ac-susceptibility measurements. The collective SFM state is also been evidenced by Mössbauer spectroscopy measurements. Interestingly the same kind of magnetic properties are observed in two ferrofluids with different volume ratios. This is explained by structural agglomeration at low temperatures in both the ferrofluids. To confirm this hypothesis small angle neutron scattering measurements should be performed in future to study the structural agglomeration as well as the magnetic correlations at low temperatures.

Bibliography

1. G. A. Prinz and J. H. Hathaway, Physics Today **48** (4), 24 (1995); P. Grünberg, Physics Today **54** (5), 31 (2001); G. A. Prinz, Science **282**, 1660 (1998).

2. J. L. Dormann, D. Fiorani, and E. Tronc, Adv. Chem. Phys. **98**, 283 (1997).

3. F. J. Himpsel, J. E. Ortega, G. J. Mankey, and R. F. Willis, Adv. in Phys. **47,** 511 (1998).

4. J. Frenkel and J. Dorfman, Nature **126**, 274 (1930).

5. C. Kittel, Phys. Rev. **70**, 965 (1946).

6. E. C. Stoner, E. P. Wohlfarth, IEEE Trans. Mag. **27**, 3475 (1947).

7. E. C. Stoner and E. P. Wohlfarth, Philos. Trans. London Ser. A **240**, 599 (1948).

8. W. C. Elmore, Phys. Rev. 54 (1938) 1092; C. G. Montgomery, Phys. Rev. **38**, 1782 (1931).

9. T. Jonsson, J. Mattsson, C. Djurberg, F. A. Khan, P. Nordblad, P. Svedlindh, Phys. Rev. Lett. **75**, 4138 (1995).

10. H. Mamiya, I. Nakatani, and T. Furubayashi, Phys. Rev. Lett. **82**, 4332 (1999).

11. J. L. Dormann, R. Cherkaoui, L. Spinu, M. Nogués, F. Lucari, F. D´Orazio, D. Fiorani, A. Garcia, E. Tronc, and J. P. Jolivet, J. Magn. Magn. Mater. **187**, L139 (1998).

12. W. Kleemann, O. Petracic, Ch. Binek, G. N. Kakazei, Y. G. Pogorelov, J. B. Sousa, S. Cardoso, and P. P. Freitas, Phys. Rev. B **63**, 134423 (2001).

13. X. Chen, O. Sichelschmidt, W. Kleemann, O. Petracic, Ch. Binek, J. B. Sousa, S. Cardoso and P. P. Freitas, Phys. Rev. Lett. **89**, 137023 (2002).

14. C. C. Berry and Adam S G Curtis, J. Phys. D. Appl. Phys. **36**, R198 (2003).

15. P. Weiss, J. de Phys. Rad. **6**, 661 (1907).

16. R. C. O´Handley, *Modern Magnetic Materials*: *Principles and applications*. (John Wiley & Sons, 2000).

17. D. Givord, Q. Lu, and M. F. Rossignol, in *Science and Technology of Nanostructured Materials*, Edited by G. C. Hadjipanayis and G. A. Prinz (Plenum, New York, 1991) p. 635.

18. S. Chikazumi, *Physics of Ferromagnetism* (Oxford University Press, New York, 1999).

19. L. Néel, Ann. Geophys. **5**, 99 (1949).

20.   W. F. Brown, Jr., Phys. Rev. **130**, 1677 (1963).

21.   B. D. Cullity, *Introduction to Magnetic Materials* (Addison-Wesley, Menlo Park, California, 1972).

22.   D. Hinzke, U. Nowak, and K. D. Usadel, in *Structure and Dynamics of Heterogeneous Systems*, Edited by P. Entel and D. E. Wolf (World Scientific, Singapore, 2000).

23.   W. F. L. Brown, J. Appl. Phys. **30**, 130S (1959).

24.   W. T. Coffey, Yu. P. Kalmykov, and J. T. Waldron, *The Langevin Equation* (World Scientific, Singapore, 1996).

25.   Weil, Gruner, and Deschamps, Comp. Rend. **244**, 2143 (1957).

26.   A. Knappwost, Z. Elektrochem. **61**, 1328 (1957).

27.   R. Hahn and E. Kneller, Z. Metallk. **49**, 426 (1958).

28.   A. E. Berkowitz and P. J. Flanders, J. Appl. Phys. **30**, 111S (1959).

29.   M. Farle, Rep. Prog. Phys. **61**, 755 (1998).

30.   S. Chikazumi, *Physics of Magnetism*. Robert E. Kriger Publishing Company Malabar, Florida, (1964).

31.   J. A. Osborn, Phys. Rev. **67**, 351 (1945).

32.   D. A. Garanin and H. Kachkachi, Phys. Rev. Lett. **90**, 65504 (2003).

33.   Y. Labaye, O. Crisan, L. Berger, J. M. Greneche, and J. M. D. Coey, J. Appl. Phys. **91**, 8715 (2002).

34.   F. Bødker, S. Mørup, and S. Linderoth, Phys. Rev. Lett. **72**, 282 (1994).

35.   A. Hubert and R. Schäfer, *Magnetic Domains*, Springer (2000).

36.   L. D. Landau, and E.Lifshitz, Phys. Z. Sowjetunion **8**, 153 (1935).

37.   F. Bloch, Z. Phys. **74**, 295 (1932).

38.   B. A. Lilley, Phil. Mag. **41**, 792 (1950).

39.   R. Rhodes, Proc. Leeds. Phil. And Lit. Soc. (Sci. Sect.), **5**, 116 (1949).

40.   L. Néel, J. Phys. Rad. **12**, 339 (1951).

41.   F. D. Stacey, Austral. J. Phys. **13**, 599 (1960).

42.   O. Petracic, A. Glatz, and W. Kleemann, Phys. Rev. B **70**, 214432 (2004).

43.   S. Bedanta, E. Kentzinger, O. Petracic, W. Kleemann, U. Rücker, Th. Brückel, A. Paul, S. Cardoso, and P. P. Freitas, Phys. Rev. B. **72**, 024419 (2005).

44.   W. Kleemann, Th. Braun, J. Dec, and O. Petracic, Phase Trans. **78**, 811 (2005).

45.   A. Bauer, Habilitationsschrift, Freie Universität Berlin (2000).

46. M. Rao, H. R. Krishnamurthy, and R. Pandit, Phys. Rev. B **42**, 856 (1990); *ibid.* J. Phys.: Condens. Matter **1**, 9061 (1989).

47. M. Acharyya and B. K. Chakrabati, Phys. Rev. B **52**, 6550 (1995).

48. M. Somoza and R. C. Desai, Phys. Rev. Lett. **70**, 3279(1993).

49. Y.-L. He and G.-C. Wang, Phys. Rev. Lett. **70**, 2336 (1993).

50. W. Y. Lee, B.-Ch. Choi, J. Lee, C. C. Yao, Y. B. Xu, D. G. Hasko, and J. A. C. Bland, Appl. Phys. Lett. **74**, 1609 (1999).

51. M. R. Scheinfein, K. E. Schmidt, K. R. Heim, and G. G. Hembree, Phys. Rev. Lett. **76**, 1541 (1996).

52. N. Mikuszeit, E. Y. Vedmedenko, H. P. Oepen, J. Phys. Condens. Matter. **16**, 9037 (2004).

53. X. Batlle, and A. Labarta, J. Phys. D. Appl. Phys. **35**, R15 (2002).

54. C. Djurberg, P. Svedlindh, P. Nordblad, M. F. Hansen, F. Boedker, and S. Moerup, Phys. Rev. Lett. **79**, 5154 (1997).

55. S. Sahoo, O. Petracic, W. Kleemann, P. Nordblad, S. Cardoso, and P. P. Freitas, Phys. Rev. B **67**, 214422 (2003).

56. S. Moerup, M. B. Madsen, J. Franck, J. Villadsen, and C. J. W. Koch, J. Magn. Magn. Mater. **40**, 163 (1983).

57. J. Hauschild, H. J. Elmers, and U. Gradmann, Phys. Rev. B **57**, R677 (1998).

58. V. F. Puntes, P. Gorostiza, D. M. Aruguete, N. G. Bastus, and A. P. Alivisatos, Nature Mat. **3**, 263 (2004).

59. R. V. Chamberlin, G. Mozurkewich and R. Orbach, Phys. Rev. Lett. **52**, 867 (1984).

60. R. Hoogerbeets, W-L Luo and R. Orbach, Phys. Rev. Lett. **55**, 111 (1985).

61. J. Mydosh, *Spin Glasses: An Experimental Introduction* (Taylor and Francis, London, 1993).

62. M. Sasaki, P. E. Jönsson and H. Takayama, Phys. Rev. B **71**, 104405 (2005).

63. M. Ulrich, J. Garcia-Otero, J. Rivas, and A. Bunde, Phys. Rev. B **67**, 024416 (2003).

64. J. O. Andersson, T. Jonsson and J. Mattsson, Phys. Rev. B **54**, 9912 (1996).

65. R. W. Chantrell, N. Walmsley, J. Gore and M. Maylin, Phys. Rev. B **63**, 024410 (2000).

66. P. Politi and M. G. Pini, Phys. Rev. B **66**, 214414 (2002).

67. A. Bunde, S. Russ (private communication).

68.   R. Kretschmer and K. Binder, Z. Physik B **34**, 375 (1979).

69.   S. Blundell, Oxford University Press Inc., New York (2001).

70.   A. Fert and P. M. Levy, Phys. Rev. Lett. **44**, 1538 (1980).

71.   T. Jonsson, P. Svedlindh and M. F. Hansen, Phys. Rev. Lett. **81**, 3976 (1998).

72.   K. Gunnarsson, P. Svedlindh, P. Nordblad, L. Lundgren, H. Aruga, and A. Ito, Phys. Rev. B, **43**, 8199 (1991).

73.   S. Sahoo, Ph. D. thesis, Universität Duisburg-Essen (2003).

74.   P. E. Jönsson, Ph. D. thesis, Uppsala University (2002).

75.   K. Binder, and A. P. Young, Rev. Mod. Phys. 58, 801 (1986).

76.   S. F. Edwards and P. W.Anderson, J. Phys. F. **5**, 965 (1975).

77.   G. Parisi, Phys. Rev. Lett. **43**, 1754 (1979).

78.   M. Mezard, G. Parisi, M. A. Virasoro, *Spin Glass Theory and Beyond*, in *LectureNotes in Physics*, *Vol.* **9** (World Scientific, Singapore, 1987).

79.   D. S. Fisher and D. A. Huse, Phys. Rev. Lett. **56**, 1601 (1986).

80.   D. S. Fisher and D. A. Huse, Phys. Rev. B **38**, 373 (1988); **38**, 386 (1988).

81.   A. P. Malozemoff and B. Barabara, J. Appl. Phys. **57**, 3410 (1985).

82.   D. G. Rancourt, & J. M. Daniels, *Phys. Rev. B.* **29**, 2410 (1984).

83.   S. Sankar, D. Dender, J.A. Borchers, David J. Smith, R.W. Erwin, S.R. Kline, A.E. Berkowitz, J. Magn. Magn. Mater. **221**, 1 (2000).

84.   A. Sugawara, G.G. Hembree, M.R. Scheinfein: J. Appl. Phys. **82**, 5662 (1997).

85.   J. Shen, R. Skomski, M. Klaua, H. Jenniches, S. Sundar Manoharan, and J. Kirschner, Phys. Rev. B **56**, 2340 (1997);

86.   C. Mathieu, C. Hartmann, M. Bauer, O. Buettner, S. Riedling, B. Ross, S. O. Demokritov, B. Hillebrands, B. Bartenlian, C. Chappert, D. Decanini, F. Rousseaux, E. Cambril, A. Müller, B. Hoffmann, and U. Hartmann, Appl. Phys. Lett. **70**, 2912 (1997).

87.   W. Rave, D. Eckert, R. Schäfer, B. Gebel and K.-H. Müller, IEEE Trans. On Magnetics, **32**, 4362 (1996).

88.   D. J. Craik and E. D. Isaac, Proc. Phys. Soc. (Research Notes), **76**, 160 (1960).

89.   J. D. Livingston in "Soft and hard magnetic materials with applications" ed. J. A. Salsgiver et al., ASM Metals Park Ohio, page 71 (1986).

90.   R. K. Mishra and R. W. Lee, Appl. Phys. Lett. **48**, 733 (1986).

91.   E. A. Nesbitt and H. J. Williams, Phys. Rev. **80**, 112 (1950).

92. T. Schrefl, H. F. Schmidts, J. Fidler, H. Kronmüller, J. Magn. Magn. Mater. **124**, 251 (1993).

93. C. T. Campbell, Surf. Sci. Rep. **27**, 1 (1997).

94. S. Cardoso, V. Gehanno, R. Ferreira, and PP Freitas, IEEE Trans. Magn, vol **35** (1999) 2952.

95. D. I. Bardos, J. Appl. Phys. **40**, 1371 (1969).

96. S. Sahoo, O. Petracic, W. Kleemann, S. Stappert, G. Dumpich, P. Nordblad, S.Cardoso, and P. P. Freitas, Appl. Phys. Lett. **82**, 4116 (2003).

97. S. K. Sinha, E. B. Sirota, S. Garoff, and H. B. Stanley, Phys. Rev. B **38**, 2297 (1988).

98. T. Salditt, T. H. Metzger, and J. Peisl, Phys. Rev. Lett. **73**, 2228 (1994).

99. J. D. Jackson; Classical Electrodynamics (Wiley, New York, 1975).

100. H. Kiessig: Ann. Phys. (Leipzig) **10**, 715, 769 (1931).

101. L. G. Paratt: Phys. Rev. **95**, 359 (1954).

102. H. Zabel, Appl. Phys. A. **58**, 159 (1994).

103. W. Marshall, S. W. Lovesey, *Theory of Thermal Neutron Scattering* (Clarendon, Oxford, 1971).

104. G. H. Vineyard, Phys. Rev. B **50**, 4146 (1982) and H. Dosch, Phys. Rev. B **35**, 2137 (1987).

105. L. Névot, P. Croce, Rev. Phys. Appl. **15**, 761 (1980).

106. M. K. Sanyal, S. K. Sinha, A. Gibaud, S. K. Satija, C. F. Majkrzak, H. Homma, IN surface X-ray and Neutron Scattering, ed. By H. Zabel, I. K. Robinson, Springer Proc. Phys., Vol. **61** (Springer-Verlag, Berlin, Heidelberg, 1991) p. 91.

107. L. Reimer, *Transmission Electron Mocroscopy, (Spinger Series in Optical Sciences, Vol. 34),* Ed. D. L. MacAdam, (Springer-Verlag, Berlin, 1984).

108. B. Heinrich and J. F. Cochran, Adv. Phys. **42,** 523 (1993).

109. C. P. Poole. *Electron Spin Resonance*. (Intercience Pulishers, New York, 1967).

110. P. E. Wigen, *Phys. Rev.* **133**, A1557 (1964), B. Heinrich, *Ultrathin Magnetic Structures* vols I and II (Berlin: Springer) (1994), J. Pelzl and U. Netzelmann, *Topics in Current Physics* vol 47 (Berlin: Springer) p 313 (1989).

111. J. Lindner and K. Baberschke, In situ ferromagnetic resonance: an ultimate tool to investigate the coupling in ultrathin films, J. Phys.: Condens. Matter **15**, R193 (2003).

112. R. Meckenstock, PhD Thesis, Ruhr-Universität Bochum (1997).

113. S. V. Vonsovskii, *Ferromagnetic Resonance* (Pergamon Press, London, 1966).

114. J Pelzl, R Meckenstock, D Spoddig, F Schreiber, J Pflaum and Z Frait, J. Phys. Condens. Matter. **15**, S 451 (2003).

115. Kh. Zakeri, Th. Kebe, J. Lindner, and M. Farle, J. Magn. Magn. Mater. **299**, L1 (2006).

116. U. Wiedwald, PhD Thesis, Universität Duisburg-Essen (2004).

117. Quantum Design, Inc., 11578 Sorrento Valley Road, San Diego, CA 92121-1311, USA.

118. Quantum Design, Oven Option manual, QD-M102 (1999).

119. Quantum Design, MPMS 5S manual, Part No. 1004-100A (1999).

120. Correction tables are provided by Quantum Design for different sample sizes.

121. Quantum Design, MPMS 5S manual, Part Nr. 1004-110 A (1999).

122. S. Bedanta, O. Petracic, M. Aderholz, and W. Kleemann, Rev. Sci. Instr. **76**, 083910 (2005).

123. L. H. Lewis and K. M. Bussmann, Rev. Sci. Instrum. **67**, 3537 (1996).

124. F. Kohlrausch, Praktische Physik (B. G. Teubner, Stuttgart 1968).

125. IGP GmbH, Ingenieurbüro Grosse-Perdekamp, Wierlings Busch 42, 48249 Dülmen, Germany.

126. QGT-Quarzglastechnik GmbH & Co.KG, Landstrasse 49, 38667 Bad Harzburg, Germany.

127. Quantum Design, Application Note 2005 (unpublished).

128. J. Chadwick, Proc. Roy. Soc., A **136**, 692 (1932).

129. G. P. Felcher, Phys. Rev B **24**, 1595 (1981).

130. J. A. C. Bland, in *Ultrathin Magnetic Structures*, edited by J. A. C. Bland and B. Heinrich (Springer Berlin, 1994), vol. 1.

131. J. A. C. Bland, J. Vac. Sci. Technol. A **15**, 1759 (1997).

132. J. A. C. Bland, J. Lee, S. Hope, G. Lauhoff, J. Penfold, and D. Bucknall, J. Magn. Magn. Mater. **165**, 46 (1997).

133. S. J. Blundell and J. A. C. Bland, Phys. Rev. B **46**, 3391 (1992).

134. J. A. C. Bland, H. T. Leung, S. Blundell, V. S. Speriosu, S. Metin, B. A. Gurney, and J. Penfold, J. Appl Phys. **79**, 6295 (1996).

135. G. P. Felcher, R. O. Hilleke, R. K. Crawford, J. Haumann, R. Kleb, and G. Ostrowski, Rev. Sci. Instrm. **58**, 609 (1987).

136. S. J. Blundell and J. A. C. Bland, J. Magn. Magn. Mater. **121,**185 (1993).

137. R. Rodmacq, K. Dumesnil, Ph. Mangin and M. Hennion, Phys. Rev. B **48**, 3556 (1993).

138. M. Schäfer, J. A. Wolf, P. Grünberg, J. F. Ankner, A. Schreyer, H. Zabel, C. F. Majkrzak, J. Appl. Phys. **75**, 6193 (1994).

139. M. Schäfer, J. A. Wolf, P. Grünberg, J. F. Ankner, A. Schreyer, H. Zabel et al., Europhys. Lett. **32**, 595 (1995).

140. B. C. Choi, A. Samad, C. A. F. Vaz, J. A. C. Bland, S. Langridge, and J. Penfold, Appl. Phys. Lett. **77**, 892 (2000).

141. H. Zabel and K. Theis-Bröhl, J. Phys. Condens. Matter. **15** (2003) S505.

142. U. Rücker, B. Alefeld, W. Bergs, E. Kentzinger, Th. Brückel, Physica B **276-278**, 95 (2000).

143. U. Rücker, W. Bergs, B. Alefeld, E. Kentzinger and Th. Brückel, Physica B **297**, 140 (2001).

144. G. Schütz, W. Wagner, W. Wilhelm, P. Kienle, R. Zeller, R. Frahm, and G. Materlik, Phys. Rev. Lett. **58**, 737 (1987).

145. J. Stöhr, Y. Wu, B. D. Hermsmeier, M. G. Samant, G. Harp and S. Koranda, Science **259,** 658 (1993).

146. P. Fischer, G. Schütz, G. Schmahl, P. Guttmann and D. Raasch, Z. Phys. B: Condens. Matter. **101**, 313 (1996).

147. W. Chao, B. D. Harteneck, J. A. Liddle, E. H. Anderson and D. T. Attwood, Nature, **435,** 1210 (2005).

148. B. T. Thole, P. Carra, F. Sette, G. van der Laan, Phys. Rev. Lett. **68**, 1943 (1992).

149. J. Stöhr, H. A. Padmore, S. Anders, T. Stammler, & M. R. Scheinfein, *Surf. Rev. Lett.* **5**, 1297 (1998).

150. J. Stöhr and Y. Wu, in New Directions in Research with Third-Generation Soft X-Ray Synchrotron Radiation Sources, eds. A. S. Schlachter and F. J. Wuilleumier (Kluwer, Netherlands, 1994), p. 221.

151. R. Nakajima, J. Stöhr, and Y. U. Idzerda, Phys. Rev. B **59,** 6421 (1999).

152. S. Anders, H. A. Padmore, R. M. Duarte, T. Renner, Th. Stammler, A. Scholl, M. R. Scheinfein, J. Stöhr, L. Séve, and B. Sinkovic, Rev. Sci. Instrum. **70,** 3973 (1999).

153. T. J. Regen, H. Ohldag, C. Stamm, F. Nolting, J. Lüning, J. Stöhr, and R. L. White, Phys. Rev. B **64,** 214422 (2001).

154. J. Lüning, F. Nolting, H. Ohldag, A. Scholl, E. E. Fullerton, M. Toney, J. W. Seo, J. Fompeyrine, H. Siegwart, J.-P. Locquet, and J. Stöhr, **67,** 214433 (2003).

155. A. Scholl, H. Ohldag, F. Nolting, S. Anders, and J. Stöhr, Chapter 2, page 29, Magnetic Microscopy of Nanostructures, Edited by H. Hopster and H. P. Oepen (Springer-Verlag, Berlin Heidelberg, 2005).

156. Ch. Sauer and W. Zinn, in: L.H. Bennet and R.E. Watson (Eds.), *Magnetic multilayers*, (World Scientific, Singapore, 1993).

157. H. Wegener, *Der Mössbauer Effect und seine Anwendung in Physik und Chemie*, (Bibliograph. Institut Mannheim, Mannheim, 1966).

158. B. R. Cuenya, Ph.D. thesis, Gerhard-Mercator-Universität Duisburg, (2001).

159. L. D. Landau and E. M. Lifshtz, *Electrodynamics of Continuous Media* (Pergamon, London, 1960).

160. Z. Q. Qiu and S. D. Bader, Rev. Sci. Instru. **71**, 1243 (2000).

161. C. Daboo, J. A. C. Bland, R. J. Hicken, A. J. R. Ives, M. J. Baird, M. and J. Walker, Phys. Rev. B **47,** 11852 (1993).

162. W. S. Kim, M. Aderholz, and W. Kleemann, Meas. Sci. Technol. **4**, 1275 (1993).

163. B. D. Cullity, *Introduction to Magnetic Materials* (Addison-Wesley, Menlo Park, California, 1972).

164. S. Bedanta, M. Spasova et al., (unpublished).

165. S. Bedanta, F. Stromberg et al., (unpublished).

166. J.-L. Maurice, J. Briático, J. Carrey, F. Petroff, L. F. Schelp, and A. Vaurès, Phil. Mag. A **97**, 2921 (1999).

167. C. Morawe and H. Zabel, J. Appl. Phys. **77**, 1969 (1995); U. Diebold, J. Pan, and T. E. Madey, Surf. Sci. **331-333**, 845 (1995).

168. N. M. Dempsey, L. Ranno, D. Givord, J. Gonzalo, R. Serna, G. T. Fei, A. K. Petford-Long, R. C. Doole, and D. E. Hole, J. Appl. Phys. **90**, 6268 (2001).

169. J.-P. Barnes, A. K. Petford-Long, R. C. Doole, R. Serna, J. Gonzalo, A. Suárez-García, C. N. Afonso, and D. Hole, Nanotechnology **13**, 465 (2002).

170. G. N. Kakazei, Yu. G. Pogorelov, A. M. L. Lopes, J. B. Sousa, S. Cardoso, P. P. Freitas, M. M. Pereira de Azevedo, and E. Snoeck, J. Appl. Phys. **90**, 4044 (2001).

171. B. Abeles, P. Sheng, M. D. Coutts, & Y. Arie, Structural and electrical properties of granular metal films. *Adv. Phys.* **24**, $407 - 461$ (1975).

172. S. Mitani, S. Takahashi, K. Takanashi, K. Yakushiji, S. Maekawa, and H. Fujimori, *Phys. Rev. Lett.* **81**, 2799 (1998).

173. C. Wang, Z. Guo, Y. Rong, and T. Y. Hsu, *Phys. Lett. A* **329**, 236 (2004).

174. X. Chen, S. Bedanta, O. Petracic, W. Kleemann, S. Sahoo, S. Cardoso, and P. P. Freitas, Phys. Rev. B **72**, 214436 (2005).

175. T. G. Knorr and R. W. Hoffman, Phys. Rev. **113**, 1039 (1959).; D. O. Smith, J. Appl. Phys. **30**, Supplement, 264S (1959).

176. G. S. Chang, A. Moewes, S. H. Kim, J. Lee, K. Jeong, C. N. Whang, D. H. Kim and S.-C. Shin, Appl. Phys. Lett. **88**, 092504 (2006).

177. S. Ohnuma, N. Kobayashi, and T. Masumoto, S. Mitani and H. Fujimori, J. Appl. Phys. **85**, 4574 (1999).

178. S. Bedanta, J. Lindner et al. (unpublished).

179. S. Sahoo, O. Petracic, Ch. Binek, W. Kleemann, J. B. Sousa, S. Cardoso, and P. P. Freitas, Phys. Rev. B **65**, 134406 (2002).

180. R. H. Victora and L. M. Falicov, Phys. Rev. B **30**, 259 (1984).

181. J. Briático, J. L. Maurice, J. Carrey, D. Imhoff, F. Petroff, and A. Vaurès, Eur. Phys. J. D **9**, 517 (1999).

182. G. Mpourmpakis, G. E. Froudakis, A. N. Andriotis, and M. Menon, Phys. Rev. B **72**, 104417 (2005).

183. Y. Sun, M. B. Salamon, K. Garnier, and R. S. Averback, Phys. Rev. Lett. 9**1**, 167206 (2003).

184. L. Berthier and J.-P. Bouchad, Phys. Rev. B **66**, 054404 (2002).

185. S. Bedanta, W. Kleemann, X. Chen *et al.*, (unpublished).

186. O. Petracic, X. Chen, S. Bedanta, W. Kleemann, S. Sahoo, S. Cardoso, P.P. Freitas, J. Magn. Magn. Mater. **300**, 192 (2006).

187. W. Y. Lee, Y. B. Xu, S. M. Gardiner, J. A. C. Bland and B. C. Choi, J. Appl. Phys. **8**7, 5926 (2000).

188. A. Glatz, Ph. D. Thesis, Universität Köln (2004).

189. K. S. Cole and R. H. Cole, J. Chem. Phys. **9**, 341(1941); A. K. Jonscher, *Dielectric Relaxation in Solids* (Chelsea Dielectrics Press, London, 1983).

190. Th. Braun, W. Kleemann, J. Dec, and P. A. Thomas, Phys. Rev. Lett. **94**, 117601 (2005).

191. M. V. Feigel´man, V. B. Geshkenbein, A. I. Larkin, and V. M. Vinokur, Phys. Rev. Lett. **63**, 2303 (1989).

192. S. Lemerle, J. Ferré, C. Chappert, V. Mathet, T. Giamarchi, and P. Le Doussal, Phys. Rev. Lett. **80**, 849 (1998).

193. H. Zabel, Physica B **198**, 156 (1994).

194. V.F. Sears, Neutron News, **3**, 26, (1992).

195. C. Fermon, F. Ott, and A. Menelle, Neutron Reflectometry in J. Daillant and A. Gibaud (Eds), "X-ray and Neutron Reflectometry Principles and Applications", Springer (1999).

196. S. Bedanta, X. Chen, S. Sahoo, W. Kleemann, E. Kentzinger, P. Nordblad, S. Cardoso, and P. P. Freitas, Phys. Status Solidi C **1**, 3288 (2004).

197. E. Fatuzzo, Phys. Rev. **127**, 1999 (1962); M. Labrune, S. Andrieu, F. Rio, and P. Bernstein, J. Magn. Magn. Mater. **80**, 211 (1989).

198. M. R. Fitzsimmons, C. Leighton, J. Nogues, A. Hoffmann, K. Liu, C. F. Majkrzak, J. A. Dura, J. R. Groves, R. W. Springer, P. N. Arendt, V. Leiner, H. Lauter, and Ivan K. Schuller, Phys. Rev. B **65**, 134436 (2002).

199. L. Folks, R. Street, and R. C. Woodward, Appl. Phys. Lett. **65**, 910 (1994).

200. S. Bedanta, T. Eimüller, W. Kleemann, F. Stromberg *et al.* (submitted 2006).

201. E. Kentzinger, U. Rücker, and B.P. Toperverg, Physica B, **335**, 82 (2003).

202. S. Bedanta, E. Kentzinger, O. Petracic, W. Kleemann, U. Rücker, Th. Brückel, A. Paul, S. Cardoso, and P. P. Freitas, Phys. Rev. B. **74**, 054426 (2006).

203. A. Paul, E. Kentzinger, U. Rücker, D. E. Bürgler, and P. Grünberg, Eur. Phys. J. B **45**, 249 (2005).

204. S. Bedanta, A. Paul, E. Kentzinger, W. Kleemann *et al.*, (unpublished).

205. S. Bedanta, E. Kentzinger, W. Kleemann, *et al.*, (unpublished).

206. L. Néel, C. R. Acad. Sci. **255**, 1676 (1962).

207. B. D. Schrag, A. Anguelouch, S. Ingvarsson, G. Xiao, Y. Lu, P. L. Trouilloud, A. Gupta, R. A. Wanner, W. J. Gallagher, P. M. Rice and S. S. P. Parkin, Appl. Phys. Lett. **77**, 2373 (2000).

208. S. Tegen, I. Mönch, J. Schumann, H. Vinzelberg, and C. M. Schneider, J. Appl. Phys. **89**, 8169 (2001).

209. W. S. Lew, S. P. Li, L. Lopez-Diaz, D. C. Hatton, and J. A. C. Bland, Phys. Rev. Lett. **90**, 217201 (2003).

210. P. Bak, Rep. Prog. Phys. **45**, 587 (1982); W. Selke, Phys. Rep. **170**, 213 (1998).

211. M. J. Donahue and D. G. Porter, *OOMMF User's Guide*, Version 1.23, National Institute of Standards and Technology, Gaithersburg, MD, USA (1999).

212. D. G. Porter and M. J. Donahue, J. Appl. Phys. **89,** 7257 (2001).

213.	D. Babonneau, F. Petroff, J.-L. Maurice, F. Fettar, and A. Vaure`s, A. Naudon, Appl. Phys. Lett. **76**, 2892 (2000).

214.	A. Aharoni, *Introduction to the Theory of Ferromagnetism*, Clarendon, Oxford, 1996.

215.	W. F. Brown, Jr., *Micromagnetics* (Krieger, New York, 1978).

216.	S. Bedanta, W. Kleemann *et al.*, (Unpublished).

217.	Xi Chen, S. Sahoo, W. Kleemann, S. Cardoso, and P. P. Freitas, Phys. Rev. B **70**, 172411 (2004).

218.	Xi Chen, W. Kleemann, O. Petracic, O. Sichelschmidt, S. Cardoso, and P. P. Freitas, Phys. Rev. B **68**, 054433 (2003).

219.	U. Bovensiepen, P. Poulopoulos, W. Platow, M. Farle, and K. Baberschke, J. Magn. Magn. Mater. **192**, L386 (1999).

220.	A. Hütten, D. Sudfeld, I. Ennen, G. Reiss, W. Hachmann, U. Heinzmann, K. Wojczykowski, P. Jutzi, W. Saikaly and G. Thomas J. of Biotechnology **112**, 47 (2004).

221.	D. Sudfeld, K. Wojczykowski, W. Hachmann, P. Jutzi, G. Reiss, and A. Hütten, J. Appl. Phys. **93**, 7328 (2003).

222.	M. F. Hansen, P. E. Jönsson, P. Nordblad, and P. Svedlindh, J. Phys.: Cond. Matter, **14**, 4901 (2002).

223.	S. Bedanta, M. Spasova, W. Kleemann, A. Hütten *et al*. (unpublished).

224.	E. de Biasi, C.A. Ramos, R.D. Zysler and H. Romero, Phys. Rev. B **65**, 144416 (2002).

225.	R.D. Zysler, H. Romero, C.A. Ramos, E. de Biasi , and D. Fiorani, J. Magn. Magn. Mater. **266**, 233 (2003).

226.	S. Bedanta, S. Sahoo, X. Chen, W. Kleemann, D. Sudfeld, K. Wojczykowski, and A. Hütten, Phase Trans. **78**, 121 (2005)

227.	L. Néel, C. R. Acad. Sciences, Paris **252**, 4045 (1961).

228.	C. Gilles, P. Bonville, K.K.W. Wong, and S. Mann, Eur. Phys. J. B **17**, 417 (2000).

229.	W.H. Meiklejohn and C.P. Bean, Phys. Rev. **105**, 904 (1956).

230.	P. Shukla, Phys. Rev. E **63**, 027102 (2001).

231.	P. Gütlic, R. Link, and A. Trautwein, Mössbauer Spectroscopy and Transition Metal Chemistry, Springer, Berlin (1998).

232.	S. Bedanta, R. Brand, W. Kleemann *et al*. (unpublished).

233.	A. Wiedenmann, Physica B **297**, 226 (2001).

234. D. Kumar, J. Narayan, A.V. Kvit, A.K. Sharma, and J. Sankar, J. Magn. Magn. Mater. **232**, 161 (2000).

235. S. Sun, C. B. Murray, D. Weller, L. Folks, & A. Moser, Science **287**, 1989 (2000).

236. H. Fujimori, S. Ohnuma, N. Kobayashi, & T. Masumoto, J. Magn. Magn. Mater. **304**, 32 (2006).

Acknowledgment

First of all I would like to thank my thesis advisor Prof. Dr. Wolfgang Kleemann for giving me the opportunity to do my Ph.D. work in his group at the University of Duisburg-Essen. I am grateful for his kindness, his motivation, for his valuable suggestions and stimulating discussions. I appreciate his extensive supervision and full support which guides me through in my research work.

I would like to express my gratefulness to Prof. P. Entel and the selection committee for selecting me as a Ph.D. student to the Graduiertenkolleg ``Struktur and Dynamic Heterogener Systeme`` DFG – GK 277 and the financial support through this graduate program. Also I would like to thank DFG for financial support through the project KL/38−2.

I owe many thanks to all members of the research group of Prof. Kleemann and in particular Prof. Christian Binek , Dr. Oleg Petracic, Dr. Xi Chen, Dr. Theo Kleinfeld, Dipl.-Phys. Andreas Hochstrat, Dipl.-Ing. Manfred Aderholz, Mr. Helmut Junge and Mr. J. Rhensius for distinct helpfulness and for creating a pleasant atmosphere in the whole department.

I must show my gratefulness to Dr. Emmanuel Kentzinger for his distinct co-operation for the polarized neutron reflectivity (PNR) measurements at Forschungszentrum Jülich. I would like to thank Prof. Thomas Brückel, Dr. Ulrich Rücker and Dr. Amitesh Paul for their extensive support during work at Jülich.

I express my gratitude to Prof. Paulo Freitas and Dr. Susana Cardoso Freitas from INESC, Lisbon, Portugal for providing the granular multilayer samples.

Many thanks to Dr. T. Eimüller from Ruhr Universität Bochum for the co-operation to make X-ray photoemission electron microscopy (X-PEEM) measurements at Advanced Light Source (ALS), Berkeley, CA, USA.

Also thank Dr. D. V. Berkov from INNOVENT *e.v.*, Jena for valuable discussions.

Curriculum Vitae

Name	Subhankar Bedanta
Date of birth	21.02.1980
Place of birth	Cuttack, India
Nationality	Indian
Marital status	Married

Education:

2002-2006   Ph.D. in applied physics, University of Duisburg-Essen, Duisburg, Germany.

Thesis Title: Supermagnetism in magnetic nanoparticle systems

1999-2001   Master of Science, Utkal University, Bhubaneswar, Orissa, India.

1996-1999   Bachelor of Science, Salipur College, Salipur, Orissa, India.

1994-1996   Intermediate, Salipur College, Salipur, Orissa, India.

1991-1994   High school, Banahara Highschool, Banahara, Orissa, India.

Invention:

"A new sample holder construction for high temperature measurements in superconducting quantum interference device (SQUID) magnetometers" has been made with the co-operation of Prof. W. Kleemann, Dr. O. Petracic, and Mr. M. Aderholz [see Publication 4].

Grants and Fellowships:

(i) Graduate college fellowship from the graduate college "Structure and Dynamics of heterogeneous systems" from May 2002 till April 2005.

(ii) A number of scholarships achieved during school and college.

Publications:

1. S. Bedanta, S. Sahoo, X. Chen, W. Kleemann, D. Sudfeld, K. Wojczykowski, and A. Hütten
    Intra- and interparticle interaction in a dense frozen ferrofluid
    Phase Trans. **78**, 121 (2005)

2. S. Bedanta, X. Chen, S. Sahoo, W. Kleemann, E. Kentzinger, P. Nordblad, S. Cardoso, and P.P. Freitas
    Collective magnetic states of ferromagnetic nanoparticles in the superspin limit
    Phys. Stat. Sol. (c) **1**, 3288 (2004)

3. S. Bedanta, O. Petracic, E. Kentzinger, W. Kleemann, U. Rücker, A. Paul, Th. Brückel, S. Cardoso, and P. P. Freitas
    Superferromagnetic domain state of discontinuous metal insulator multilayer
    Phys. Rev. B. **72**, 024419 (2005)

4. S. Bedanta, O. Petracic, M. Aderholz, and W. Kleemann
    A sample holder design for high temperature measurements in superconducting quantum interference device magnetometers
    Rev. Sci. Instrum. **76**, 083910 (2005)
    Virt. J. Appl. Supercond. **9**, 4 (2005)

5. X. Chen, S. Bedanta, O. Petracic, W. Kleemann, S. Sahoo, S. Cardoso, and P. P. Freitas
    Superparamagnetism vs. superspin glass behavior in dilute magnetic nanoparticle systems
    Phys. Rev. B **72,** 214436 (2005)

6. O. Petracic, X. Chen, S. Bedanta, W. Kleemann, S. Sahoo, S. Cardoso, and P. P. Freitas
    Collective states of interacting ferromagnetic nanoparticles
    J. Magn. Magn. Mater. **300**, 192 (2006)

7. S. Bedanta, E. Kentzinger, O. Petracic, W. Kleemann, U. Rücker, A. Paul, Th. Brückel, S. Cardoso, and P. P. Freitas
    Modulated magnetization depth profile in dipolarly coupled magnetic multilayers
    Phys. Rev. B. **74**, 054426 (2006)

8. S. Bedanta, T. Eimüller, W. Kleemann, J. Rhensius, F. Stromberg, E. Amaladass, S. Cardoso, and P. P. Freitas,

   Superferromagnetism – overcoming dipolar disorder in dense ensembles of CoFe nanoparticles

   Submitted to Phys. Rev. Lett. (2006)

9. S. Bedanta, E. Kentzinger, O. Petracic, W. Kleemann, U. Rücker, A. Paul, Th. Brückel, S. Cardoso, and P. P. Freitas

   Polarized neutron reflectivity studies on granular $C_{80}Fe_{20}/Al_2O_3$ multilayers

   Physica B (accepted, 2006)

Participation in International conferences and schools:

1. Magnetic ordering transition in a dense frozen ferrofluid – Poster presented at DPG 2004 in Regensburg.

2. Polarized Neutron Reflectivity Studies on Discontinuous Metal Insulator Multilayers- Poster presented at Deutsche Neutronenstreutagung 'DN 2004' held in Dresden.

3. Magnetic property of weakly interacting nanoparticle systems- Poster presented at DPG 2005 held in Berlin.

4. Magnetic structures in dipolar coupled multilayers- Poster presented at DPG 2005 held in Berlin.

5. Polarized Neutron Reflectometry and magnetometry studies on granular multilayers- Talk presented at DPG 2005 held in Berlin.

6. From modified superparamagnetism to collective magnetic states of ferromagnetic nanoparticles in the superspin limit- Poster presented at EUROMAT 2005 held at Prague.

7. Interacting ferromagnetic nanoparticles in the superspin limit: from modified superparamagnetism to collective magnetic states- Poster presented at DPG 2006 held at Dresden.

8. Superferromagnetic domains in granular multilayers observed by X-PEEM and transmission x-ray microscopy- Talk presented at DPG 2006 held at Dresden.

9. Magnetic and structural properties of Cr_2O_3 thin film systems- Poster presented at DPG 2006 held at Dresden.

10. Polarized neutron reflectometry studies on Discontinuous Metal Insulator Multilayers- Poster presented at PNCMI 2006 held in Berlin.

11. Modulated magnetization depth profile in dipolarly coupled magnetic multilayers- A talk by O. Petracic has been presented at MMM 07 held in Baltimore, USA.

Invited talks:

1. Polarized neutron reflectometry studies on granular multilayers- Invited talk presented at JCNS 06 held at Jülich, February 2006.

2. Polarized neutron reflectometry studies on granular multilayers- Invited talk presented at Ruhr Universität Bochum, Prof. H. Zabel´s group, May 2006.

Reports

1. Polarized neutron reflectometry on discontinuous metal insulator multilayers

   S. Bedanta, O. Petracic, and W. Kleemann

   Experimental report 2003, Neutron scattering at FRZ-2, (Forschungszentrum Jülich, 2003) p. 147

2. Polarized neutron reflectometry on discontinuous metal insulator multilayers

   S. Bedanta, O. Petracic, and W. Kleemann

   Experimental report 2004, Neutron scattering at FRZ-2, (Forschungszentrum Jülich, 2004) p. 159.

3. Polarized neutron reflectometry on discontinuous metal insulator multilayers

   S. Bedanta, O. Petracic, and W. Kleemann

   Experimental report 2005, Neutron scattering at FRZ-2, (Forschungszentrum Jülich, 2005) p. 275.

4. Small angle neutron scattering on FeCo ferrofluids

   S. Bedanta, O. Petracic, W. Kleemann, A. Hütten, and M. Kammel

   BENSC Experimental report 2005, (Hahn-Meitner-Institut Berlin, 2005) p. 128.

Schools attended:

1. 24th tutorial session on neutron scattering 2003- Held at HMI, Berlin from 17th to 21st February 2003.

2. Laboratory course on neutron scattering 2004- held at Forschungszentrum Jülich from 13th- 24th September 2004.

Research Travels:

(i)   Traveled to Forschungszentrum Jülich several times to perform polarized neutron reflectivity measurements.

(ii) Once traveled to BENSC, Berlin to perform small angle neutron scattering.

(iii) Once traveled to ALS, Berkely to perform synchrotron measurements.